Statistical Analyses of Massive Stars and Stellar Populations

Dissertation
zur
Erlangung des Doktorgrades (Dr. rer. nat.)
der
Mathematisch-Naturwissenschaftlichen Fakultät
der
Rheinischen Friedrich-Wilhelms-Universität Bonn

vorgelegt von
Fabian Schneider
aus
Duisburg

Bonn, Oktober 2014

I, a universe of atoms,
an atom in the universe.

(Richard P. Feynman)

Abstract

Massive stars, i.e. stars more massive than about ten times that of the Sun, are key agents in the Universe. They synthesise many of the chemical elements that are so important for life on Earth, helped reionising the early Universe and end their lives in spectacular supernova explosions that are visible out to large distances. Because of their important role for much of astrophysics, accurate and reliable stellar evolution models are essential. However, recent developments regarding wind mass loss rates, internal mixing processes and duplicity seriously challenge our understanding of massive stars and stellar populations.

It is now established that most, if not all, massive stars reside in binaries or higher order multiple systems such that more than two-thirds of all massive stars are expected to interact through mass transfer with a binary companion during their lives. We investigate the consequences of this finding for coeval stellar populations and show that the most massive stars in star clusters are likely all rejuvenated binary products that may seriously bias the determination of cluster ages. We further find that wind mass loss from stars and binary mass transfer leave their fingerprints in the high mass end of stellar mass functions. Using these fingerprints, we are able to age-date the young Arches and Quintuplet star clusters with far reaching consequences for the stellar upper mass limit that we revise to be in the range 200–$500 \, \mathrm{M}_\odot$. Such an upper mass limit would allow for pair-instability supernovae in the local Universe.

Large spectroscopic surveys such as the VLT-FLAMES Tarantula Survey (VFTS) deliver many atmospheric parameters of hundreds of massive stars that are ideal to probe and calibrate the physics used in stellar models. To make use of such data, we develop the Bayesian code BONNSAI and make it available through a web-interface. With BONNSAI we are able to match all available observables of stars including their uncertainties simultaneously to stellar models to determine fundamental stellar parameters like mass and age while taking prior knowledge such as initial mass functions into account. A key aspect of BONNSAI is that it allows us to identify stars that cannot be reproduced by stellar models. We use BONNSAI to test the Milky Way stellar models of Brott et al. (2011) with eclipsing binaries and find good agreement.

We further use BONNSAI in combination with data from the VFTS to study the massive O and WNh stars in one of the largest starburst regions known to date, 30 Doradus. In particular we investigate their age distributions to learn about their formation history. The VFTS stars in our sample are mostly found outside clusters and associations and we do not find spatially coherent age patterns. The stars either formed continuously over the 30 Doradus field or in clusters and associations from where they were ejected to their current positions. The age distributions of our sample stars are consistent with the existence of at least two to four coeval stellar populations which would imply that most of the VFTS stars in our sample formed in clusters and associations.

Contents

Introduction

> Twinkle, twinkle, little star,
> How I wonder what you are.
> Up above the world so high,
> Like a diamond in the sky.
>
> *(Jane Taylor)*

Since the dawn of mankind, people have looked into the dark night sky, watching the stars and wondering what they are. Stars helped navigating on sea and land, and played a major role in ancient mythology and religion. The movement of stars over the course of a year told people when to plant and harvest. In ancient Egypt, the day when Sirius, the brightest star in the night sky, became visible just before sunrise indicated the annual flooding of the river Nile and was therefore a pivotal element of the Egyptian calender and mythology. The apparent position of the Sun on the celestial sphere still defines the worldwide used Gregorian calender.

But what are these fascinating, twinkling lights in the night sky? This question has kept mankind busy for millennia. For a long time, stars have been considered to be lights fixed on the outermost sphere of a finite universe with the Earth, the Sun and the other planets of our solar system being located inside this sphere. Only in 1584, Giordano Bruno proposed an infinite universe with an infinite number of stars that are like the Sun but far away from us. He even envisioned that many of these stars host planets just like our Earth (Gatti 2002). He was burnt at the stake in 1600 by the Roman inquisition for his views[1]. In 1838, Friedrich Bessell measured the first parallax distance, 293 mas and 11.1 lightyears respectively, to the star 61 Cyg (Unsöld & Baschek 2001), thereby proving that stars are like our Sun but far away. Bessell's parallax measurement is still in excellent agreement with those of the Hipparcos satellite[2].

Bessell not only influenced science in general with his extensive work but also the astronomical research in Bonn. His lectures in 1818 in Königsberg (Kaliningrad) attracted the young Friedrich Wilhelm August Argelander. Fascinated by Bessell's lectures, Argelander switched his field of study from economics to astronomy and later became Bessell's PhD student. In 1836,

---

[1] "Giordano Bruno." *Encyclopaedia Britannica. Encyclopaedia Britannica Online Academic Edition.* Encyclopædia Britannica Inc., 2014. Web. 26 Jun. 2014.
http://www.britannica.com/EBchecked/topic/82258/Giordano-Bruno.

[2] 61 Cyg is actually a wide binary star for which parallaxes of $\pi_A = 286.82 \pm 6.78$ mas and $\pi_B = 285.88 \pm 0.54$ mas are determined from Hipparcos observations for the binary components A and B, respectively (van Leeuwen 2007).

Argelander was offered the directorship of the newly founded astronomical institute at the University of Bonn, which is nowadays named after him. During his time in Bonn, specifically from 1852 to 1863, he and his colleagues Schmidt, Thormann, Schönfeld and Krüger created the first, modern catalogue of stars in the northern hemisphere, the Bonner Durchmusterung (BD). The original catalogue contained about 325,000 stars up to an apparent magnitude of about 9.5 and was extended in the Córdoba Durchmusterung (CD) and the Cape Photographic Durchmusterung (CPD) to also cover stars in the southern hemisphere. These catalogues are still in use and many stars are named after them (the BD-, CD- and CPD-numbers). The Bonner Durchmusterung and the applied techniques made Argelander famous[3].

1.1 Towards a modern picture of stellar evolution

Discovery of the Hertzsprung–Russell diagram   Since Bessell measured the first distance to a star, it took yet further 100 years to establish what stars and particularly the Sun really are and how they work. A great breakthrough in the understanding of stars was accomplished with the discovery of the Hertzsprung–Russell (HR) diagram by E. Hertzsprung in 1909 and independently by H.N. Russell in 1913 (see e.g. Russell 1914b but also Rosenberg 1910 for the very first published HR diagram inspired by ideas of E. Hertzsprung and K. Schwarzschild). When E. Hertzsprung and H.N. Russell plotted the luminosity of stars against their effective temperatures, they found that stars predominantly cluster around a band, the main-sequence, and a region called the red giant branch. These correlations were the starting point in a long and ongoing journey of understanding the evolution of stars. The HR diagram is still the most frequently used diagram to compare the predictions of stellar evolution calculations to observations.

The energy source of stars   A central question was still unanswered: how do stars produce the energy to shine? One idea was that stars shine because they radiate energy released by gravitational contraction. Maybe partly because of that did H.N. Russell suggest that stars evolve down the red giant branch and then down the main-sequence while contracting, cooling and releasing gravitational energy (Russell 1914a). Nowadays we know that stars evolve rather in the opposite direction and are visible as red giants in the end phases of their lives. According to the contraction theory, the lifetime of the Sun, $\tau_\odot$, can be approximated by dividing the total available energy, E_{tot}, by the rate at which energy is being released, $\dot{E}$, i.e. by the solar luminosity, $L_\odot$, such that

$$\tau_\odot \approx \frac{E_{\text{tot}}}{\dot{E}} = \frac{G M_\odot^2}{2 R_\odot L_\odot} \approx 16\,\text{Myr}, \tag{1.1}$$

where G is the gravitational constant, $M_\odot$ the solar mass and $R_\odot$ the solar radius. With the discovery of radioactivity by H. Becquerel, M. Curie and P. Curie and the determination of the age of our solar system to be about 4.5 billion years from the radioactive decay of long-lived isotopes, it soon became clear that gravitational contraction is not the main source of energy of the Sun and other stars.

Already in 1919/1920, J. Perrin and A.S. Eddington suggested that the fusion of hydrogen to helium may provide the required energy to power the luminosity of the Sun. H. Bethe and C.F.v. Weizsäcker further elaborated on this idea and, in 1938, a detailed theory was

---

[3] For more information about Argelander, his life and work see, e.g., Batten (1991) and http://www.astro.uni-bonn.de/~geffert/ge/arg/arg.htm

established explaining how hydrogen is converted to helium either by successive proton captures first forming deuterium and in the end helium (pp-chain) or by proton capture on catalysts such as carbon, nitrogen and oxygen (CNO cycle; Weizsäcker 1937, 1938; Bethe & Critchfield 1938; Bethe 1939). H. Bethe was awarded the Nobel Prize in physics in 1967 partly for this discovery.

Major advances in stellar modelling   Further big steps in the understanding of the interiors of stars have been accomplished by S. Chandrasekhar, F. Hoyle and M. Schwarzschild. The old picture of A.S. Eddington that all the hydrogen in a star is burnt to helium had to be revised. Schönberg & Chandrasekhar (1942) showed that only about 10% of the whole hydrogen content of a star is converted into helium and paved the way to explain the transition from main-sequence to red giant stars. Thanks to the growing computing power and refined numerical methods to solve the stellar structure equations such as the Henyey scheme (Henyey et al. 1959, 1964), stellar evolution models of ever improving accuracy could be computed, boosting our understanding of stars. The Henyey scheme is still state of the art.

The origin of the elements   It was also during that time that Burbidge, Burbidge, Fowler, & Hoyle (1957) in their seminal B^{2}FH paper could explain the formation of the chemical elements in the Universe because of the advanced understanding of nuclear physics and the processes occurring in the interior of stars. After the Big Bang, there was mainly hydrogen, deuterium, helium and some traces of lithium. Burbidge et al. (1957) proposed that all the other elements such as the oxygen we breath every day, the iron in our blood and the carbon constituting the building blocks of life as we know it were once synthesised in the interior of stars and thrown out into space in dramatic supernova explosions and through strong stellar winds. These discoveries and the advances in the theory of stellar evolution led to Nobel Prizes for W.A. Fowler and S. Chandrasekhar in 1983.

Discovery of stellar winds   Besides supernova explosions, stellar winds are crucial to expel the chemical elements synthesised in stellar interiors into the interstellar medium from which new generations of stars and planets form. Massive, hot stars, i.e. main-sequence stars with initially more than $10\,M_\odot$, radiate most strongly in the UV regime which is inaccessible by ground-based observatories because of the, fortunately, strong absorption of the Earth atmosphere. The stellar winds of massive stars were thus only discovered in 1967 when it became possible to investigate UV radiation from outer space with spectrographs on board balloons and rockets (Morton 1967a,b).

Soon after their discovery, the first complete theories of how these strong and fast stellar winds are driven were published by Lucy & Solomon (1970) and Castor et al. (1975). The stellar winds of hot stars are driven by momentum transfer because of the absorption of photons by atoms in the stellar atmosphere. The importance of stellar winds not only for the evolution and fate of stars but also for the evolution and chemical enrichment of galaxies was soon realised (e.g. Chiosi & Maeder 1986). Stellar winds significantly change the evolution of stars, help to understand strange objects such as Wolf–Rayet stars, affect supernova explosions and give rise to strong feedback in terms of kinetic energy imparted into the interstellar medium.

Stellar evolution: a solved problem—or not?   In the 1990s, stellar evolution was, except for some second order effects, thought to be a nearly solved problem: stars are single, slowly rotating spheres of plasma powered by nuclear fusion in their cores. In massive stars, this picture
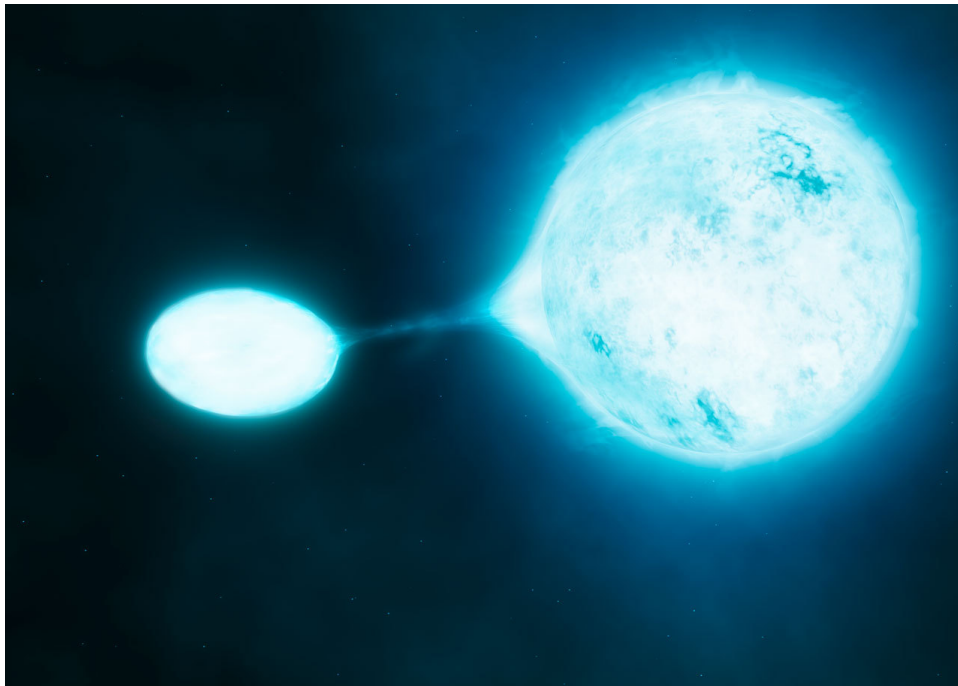
Figure 1.1: Artist's impression of mass transfer in an O-type main-sequence binary. The donor star (right) and accretor (left) have an initial mass of $20\,\mathrm{M_\odot}$ and $15\,\mathrm{M_\odot}$, respectively. The mass gainer is spun up by accretion resulting in significant deformation. Credit: ESO/M. Kornmesser/S.E. de Mink.

was soon revised when realising that several observations are in stark contrast with predictions of stellar evolution. For example, stellar evolution predicts a gap in the HR diagram after the end of the main-sequence evolution, the so-called Hertzsprung gap, but observations of massive stars show that this gap is densely filled with stars (e.g. Fitzpatrick & Garmany 1990; Evans et al. 2006). Another problem is posed by stars whose surfaces are highly enriched in hydrogen burning products such as helium and nitrogen, which was not expected from the theory of stellar evolution at that time (e.g. Herrero et al. 1992). Furthermore, many stars show what is known as the "mass-discrepancy": stellar masses inferred from evolutionary models disagree with those inferred from spectroscopy (e.g. Herrero et al. 1992). Also the ratio of blue to red supergiants as a function of metallicity shows the opposite trend to what models predict (e.g. Langer & Maeder 1995; Eldridge et al. 2008). All these problems persist until today and await a solution.

New challenges It became evident that the interiors of stars are more complex than generally believed and that aspects of stellar evolution widely regarded as second order effects such as rotation and duplicity must be considered (e.g. Langer 1992; Vanbeveren et al. 1998). Rotation and the corresponding rotational mixing was subsequently investigated in detail and led to a revision of massive star evolution. Massive star evolution is considered no longer only a function of initial mass and metallicity but also of rotation (e.g. Maeder & Meynet 2000; Heger et al. 2000).

In 2012, the picture of massive star evolution was once more revolutionised. It was already known that many stars do not live alone but have at least one companion. For example,
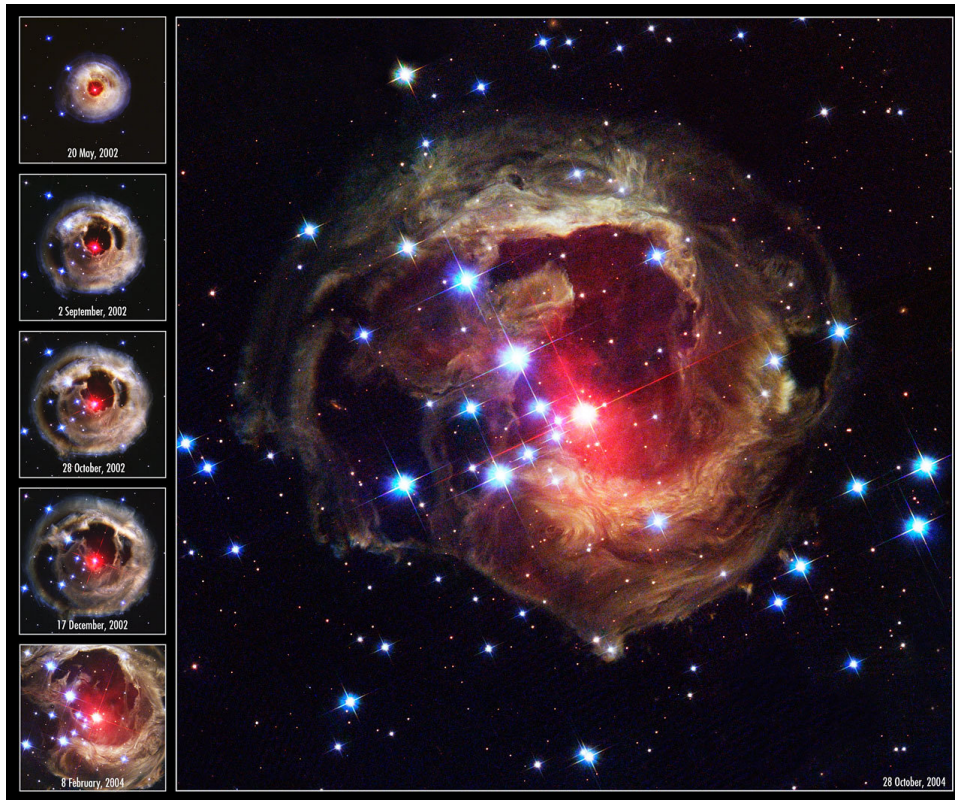
Figure 1.2: Temporal evolution of the light echo of V838 Mon, a good candidate system for a binary star caught in the act of merging. The eruption of the central, reddish object V838 Mon in 2002 released an outward moving flash of light that illuminated subsequently more distant parts of the previously unknown surrounding nebula structure. Credit: NASA, ESA, and The Hubble Heritage Team (AURA/STScI)

α Centaurus, the closest star to Earth, is a multiple system. However, the breakthrough was made when Sana et al. (2012) could show that the fraction of binary stars among the most massive stars in the Universe, i.e. of O stars with an initial mass of $\geq 15\,\mathrm{M}_\odot$, is about 70% and that the orbital period distribution of these binaries is more strongly biased toward short periods than previously thought. The implications of this discovery are far reaching. Sana et al. (2012) estimate that about 71% of all O stars witness a phase where mass is transferred from one star to the other or where both components merge (see Fig. 1.1 for an artist's impression of binary mass transfer). The resulting consequences of binary mass transfer and mergers for stellar evolution are dramatic and not yet fully explored.

Mergers have even been directly observed. In V1309 Sco, the decay of a ~ 1.4 day orbit of a binary in which both stars are in physical contact is seen, implying a merger (Tylenda et al. 2011). The merger is accompanied by an outburst (brightening of about 5 mag in the I-band) of the "V838 Mon type eruption" (Munari et al. 2002), suggesting that also the eruptions of V838 Mon and V4332 Sgr (Martini et al. 1999) were due to stellar mergers (Fig. 1.2). Such transients, typically called luminous red novae, are observed frequently in distant galaxies (Kulkarni et al. 2007; Kasliwal 2011) and future wide field transient surveys such as that using the Large Synoptic Survey Telescope (LSST) are likely to find more of these objects. This will help to shed light onto this interesting evolutionary phase.

Another big challenge for massive star evolution is posed by ongoing large stellar surveys such as the Magnetism in Massive Stars (MiMeS) and the B-fields in OB stars (BOB) projects that investigate the surface magnetic fields in massive stars. Preliminary results show that about 7% of massive, main-sequence stars possess strong (up to several kG), large scale magnetic fields (Wade et al. 2014). The origin of these fields is unknown as is their influence on the final fates of stars but magnetic fields may influence the mixing in the interior of stars and rotational velocities by torquing stars if the magnetic field is coupled to a stellar wind. It is suspicious that only a small fraction of massive stars show such strong fields, implying that something special must have happened to them. One hypothesis is that these fields are produced in strong binary interactions such as stellar mergers (Ferrario et al. 2009; Langer 2012). The discovery of a strong B-field in the mass-accreting secondary star of the O-type binary HD 47129, also known as Plaskett's star, may be a smoking gun for this scenario (Grunhut et al. 2013). Are the highly magnetic neutron stars, the so-called magnetars, the descendants of these massive magnetic main-sequence stars and can they explain some of the newly discovered superluminous supernovae?

1.2 Modern massive star evolution

Today, massive stars are recognised as key agents in the Universe (Langer 2012). Their feedback in terms of chemical elements, ionising radiation and kinetic energy injected by their strong stellar winds and violent explosions drives the evolution of galaxies (Ceverino & Klypin 2009; Schaye et al. 2010; Vogelsberger et al. 2014) and the chemical enrichment of the Universe (Burbidge et al. 1957). Stellar feedback helps to reionise the Universe during the dark ages (Haiman & Loeb 1997; Loeb & Barkana 2001; Conroy & Kratter 2012), triggers the formation of new stars (Elmegreen 2011; Walch 2014) and is essential to explain the structure of disk galaxies (Ceverino & Klypin 2009; Vogelsberger et al. 2014). Massive stars die as the most powerful explosions in the Universe such as gamma-ray bursts (GRBs) and pair-instability supernovae (PISNe), which are visible up to large distances and hence are probes of the early Universe (Savaglio et al. 2009; Tanvir et al. 2009; Cucchiara et al. 2011; Whalen et al. 2013b,a; Kozyreva et al. 2014). Compact objects, i.e. white dwarfs, neutron stars and black holes, are born at the end of a star's life and give rise to spectacular transients such as type Ia supernovae, X-ray binaries, pulsars and magnetars, and allow us to probe fundamental physics like the expansion of the Universe, gravity and the equation of state of ultra-compact matter (Riess et al. 1998; Perlmutter et al. 1999; Lattimer & Prakash 2004; Antoniadis et al. 2013). Mergers of the compact remnants of massive stars are thought to produce gravitational waves that might be detectable with ground-based laser interferometers (Sathyaprakash & Schutz 2009).

Despite the importance of massive stars to a large variety of astrophysical fields, our understanding of their lives is seriously incomplete, mainly because of stellar wind mass loss (Sec. 1.2.1), interior mixing (Sec. 1.2.2) and duplicity (Sec. 1.2.3).

1.2.1 Stellar wind mass loss

Mass loss from single stars is mainly driven in three ways (e.g. Smith 2014): (1) by heating and subsequent evaporation if particles gain enough energy to overcome the gravitational pull of the star, e.g. the solar wind being heated by magnetic reconnection, (2) by absorption of photons which transfer momentum such that particles are accelerated beyond the escape velocity, e.g. by dust in cool giants or by iron atoms in hot massive stars (line-driven wind), and (3) by
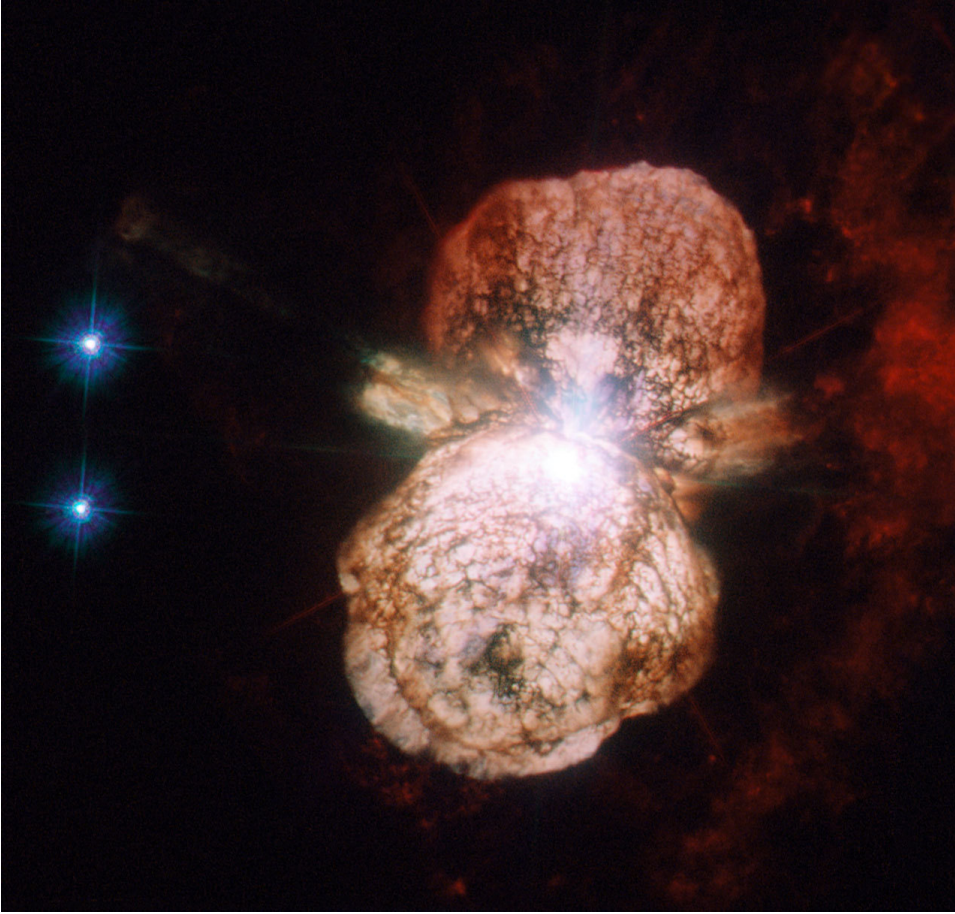
Figure 1.3: Hubble Space Telescope image of the bipolar Homunculus Nebula surrounding the central binary star η Car. The Homunculus Nebula is thought to have been ejected in the "Great Eruption" of η Car in the middle of the 19th century when it became the second brightest star in the night sky. Smith et al. (2003) estimate that η Car may have ejected about 10–20 $M_\odot$ over a timescale of decades in its giant eruption. Credit: ESA/Hubble and NASA

pulsations and eruptions, e.g. in Luminous Blue Variables such as η Car (Fig. 1.3) but also in classical variable stars such as Cepheids. In the massive main-sequence stars dealt with in this thesis, line-driven winds are most important.

The accumulated wind mass loss over the lifetime of stars initially more massive than 20 $M_\odot$, $\Delta M_{\text{loss}} = \int \dot{M} \, \text{d}t$ ($\dot{M}$ being the mass loss rate), can make up a significant fraction of the stellar mass (Chiosi & Maeder 1986). For example, an initially 120 $M_\odot$, non-rotating Milky Way star model of Ekström et al. (2012) loses about 90 $M_\odot$, i.e. three quarters of the initial mass, during its life. Besides mass, angular momentum is also lost from stars in stellar winds (Langer 1998). Given that the mass and angular momentum of stars are deterministic parameters of stellar evolution, wind mass loss has profound consequences for a star's life. Mass loss affects the luminosity, lifetime, core mass and spins of stars and therefore directly their further fates as, for example, Wolf–Rayet stars, supernovae, GRBs or PISNe (e.g. Heger et al. 2003).

The problem with stellar winds is that their rates are quite uncertain. Line-driven winds of O-type stars may be uncertain by about ±30% (Puls et al. 2008; Smith 2014), but, more

importantly, inhomogeneities (clumps) in the wind lead to an observational reduction of inferred mass loss rates for O stars by about a factor of 2–3 (e.g. Smith 2014). This reduction is not yet incorporated in state-of-the-art stellar models of O stars.

Furthermore there is the "weak wind problem" at the lower luminosity end of the O star regime ($\log L/\mathrm{L}_\odot \lesssim 5.2$ corresponding to O7 dwarfs). For these stars, the standard predictions of line-driven wind mass loss rates are larger by up to a factor of 100 than empirically measured rates (e.g. Puls et al. 2008; Muijres et al. 2012; Gvaramadze et al. 2012). Another challenge arises at the high luminosity end of the O star regime, i.e. towards Wolf–Rayet stars ($\log L/\mathrm{L}_\odot \gtrsim 6.0$). These stars approach the Eddington limit and it is found theoretically as well as observationally that their mass loss rates depend on how close they are to the Eddington limit (Gräfener & Hamann 2008; Gräfener et al. 2011; Vink et al. 2011; Bestenlehner et al. 2014). In the most massive and evolved stars, line-driven winds may transition into continuum-driven winds when radiation pressure becomes more and more important. This may result in giant eruptions during which several solar masses of material can be ejected (e.g. giant eruptions in Luminous Blue Variables; cf. Fig. 1.3). The consequences of all of these findings for massive star evolution are yet unexplored and pose a major uncertainty for their evolution and especially final fates.

1.2.2 Interior mixing and rotation

The internal mixing of stars, i.e. the mixing of chemical elements and angular momentum, is a crucial aspect of stellar evolution. For example, mixing occurs because of convection and convective core overshooting and possibly also because of gravity waves, magnetic fields and rotational mixing. Mixing can prolong the life of stars by bringing fresh fuel into the cores and may be essential for the progenitor stars of long duration GRBs. The mixing processes in stars involve turbulence and therefore are inherently complicated. They are incorporated in stellar models in an approximate way, typically by defining diffusion coefficients for all mixing processes that are then plugged into diffusion equations describing the transport of chemical elements and angular momentum through the interior of a star (e.g. Heger et al. 2000).

The mixing of chemical elements and angular momentum is essential to explain the abundances of those stars whose surfaces are enriched with products of core hydrogen burning such as helium and nitrogen, and to explain the rotation rates of the cores of stars as probed by asteroseismology, young white dwarfs and neutron stars. As of today, stellar models have difficulties to explain the surface abundances of some stars with rotational mixing alone (Hunter et al. 2008b; Brott et al. 2011b) as well as the transport of angular momentum through the interior of stars although magnetic fields, which give rise to an extra coupling between the stellar core and envelope, help to explain some observations (Heger et al. 2005; Suijs et al. 2008; Beck et al. 2012; Mosser et al. 2012; Cantiello et al. 2014). Altogether, these shortcomings may imply a substantial lack of knowledge concerning the mixing of the interior of stars but they could also have a different physical origin. In the following we focus on rotationally induced mixing and do not discuss mixing because of other physical processes such as gravity waves, magnetic fields or convective core overshooting.

Rotation influences stars mainly in two ways. First, the associated centrifugal force helps to counteract gravity such that stars behave as if they had less mass and, second, it results in rotationally induced mixing. The latitudinal dependence of the centrifugal force results in the deformation of a star such that the equator feels the centrifugal force strongest, hence is pushed farthest away from the core and is cooler than the poles. Consequently, a thermal imbalance between the poles and the equator arises, leading to mixing (meridional circulation).
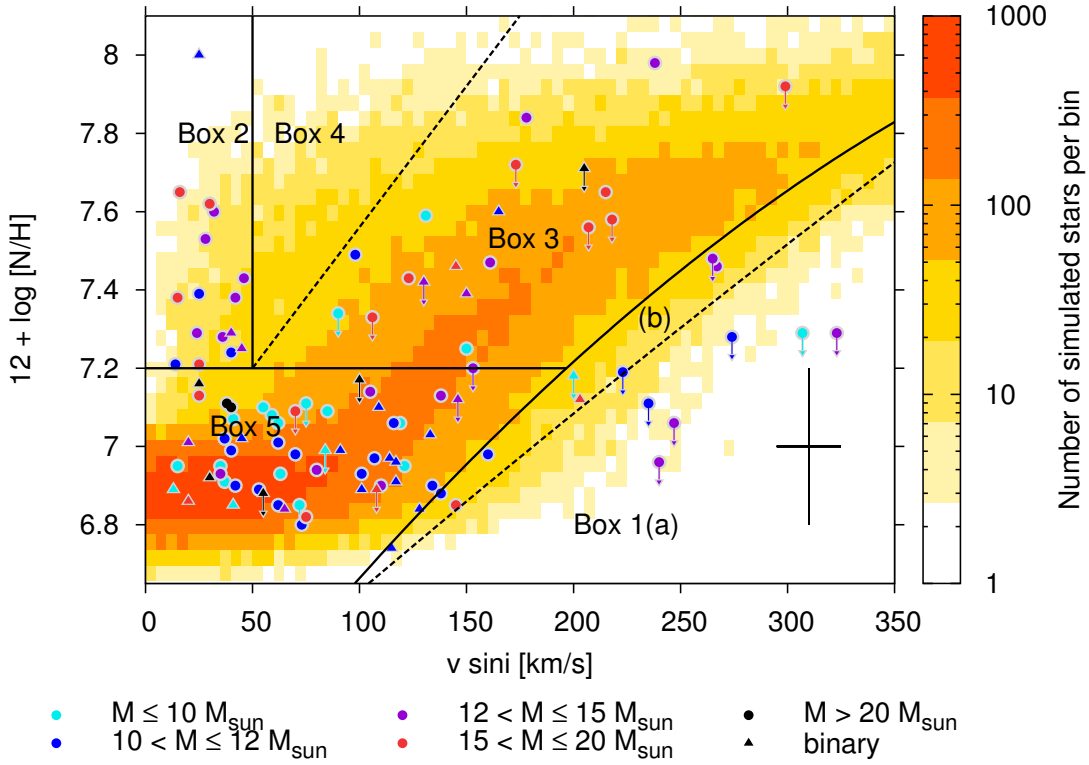
Figure 1.4: Hunter diagram, i.e. surface nitrogen abundance, $\log(N/H) + 12$, as a function of projected rotational velocity, $v \sin i$, of B stars in the Large Magellanic Cloud (Hunter et al. 2008b). The background colour coding shows the expected number of rotating, single stars (Brott et al. 2011b). Triangles denote binary stars, circles are for apparent single stars and the colours indicate the approximate mass ranges of the stars. Two classes of stars, the rapid rotating, nitrogen normal (Box 1) and the slowly rotating, nitrogen enriched stars (Box 2), defy the predictions of rotational mixing in single stars. Figure adopted from Brott et al. (2011b).

During the evolution of a star, the core contracts while the envelope expands. In rotating stars, this leads to differential rotation and hence shear mixing because of friction at the interfaces between differentially rotating layers.

Rotationally induced mixing can bring products of nuclear burning, e.g. helium and nitrogen, formed in the cores of stars to their surfaces. Rotational mixing is expected to be stronger the faster a star rotates. At sufficiently high rotation rates, mixing is faster than nuclear burning such that stars are homogeneously mixed throughout their main-sequence evolution (Maeder 1987; Langer 1992). The helium synthesised in the core and mixed throughout the star reduces the number of free electrons per gram of material and hence the electron-scattering-dominated opacity of the stellar interior. Instead of becoming a cool giant, such stars heat up and become brighter because of a lower opacity and a larger average mean molecular weight. At low metallicity, they may retain enough angular momentum to produce long duration GRBs (Yoon & Langer 2005; Woosley & Heger 2006) when the stellar core collapses to a black hole (collapsar scenario; Woosley 1993). If there is enough angular momentum to form an accretion disc, a powerful jet may be launched giving rise to a fireball exploding the star and producing gamma rays when interacting with the outer layers of the star. If the jet happens to point towards an observer, a long duration GRB is observed.

However, the picture of rotational mixing is seriously challenged by observations of B stars in the Large Magellanic Cloud (LMC; Fig. 1.4) in which 15% of the B stars are found to rotate very quickly while showing no significant chemical enrichment at their surface (Box 1) and another 15% are found to exhibit strong enrichment while rotating slowly (Box 2; Hunter et al. 2008b; Brott et al. 2011b). This puzzle remains unsolved.

1.2.3 Binary star evolution

Stars expand while ageing. This is neither surprising nor worrisome when thinking of single stars. In binary stars, however, this changes everything. In the case of two orbiting stars, the potential describing their mutual attraction, the Roche potential, is given by the gravitational potential of each individual star and the (effective) centrifugal repulsion. The Roche potential limits the growth of a star in a binary to a maximum radius after which the outer layers of a star are more strongly attracted by its companion than by itself. The critical limit is called the Roche lobe radius and corresponds to the radius of a sphere that has the same volume as the Roche lobe of the corresponding star. Eggleton (1983) approximated the Roche lobe radius, R_{L}, by

$$R_{\mathrm{L}} = \frac{0.49q^{2/3}}{0.6q^{2/3} + \ln(1 + q^{1/3})}a, \tag{1.2}$$

where a is the orbital separation and q the ratio of the mass of the star whose Roche radius we wish to compute to the mass of its companion. Once a star fills its Roche volume, i.e. if the radius of a star, R, becomes larger than its Roche lobe radius, $R > R_{\mathrm{L}}$, the outer layers are transferred into the gravitational potential of the companion and a phase of Roche lobe overflow (RLOF) is initiated. Roche lobe overflow can be either initiated by an expanding star or by a decreasing Roche lobe radius, e.g. in orbits decaying because of gravitational wave radiation.

Roche lobe overflow is responsible for a wide variety of spectacular phenomena. For example, in X-ray binaries, stars transfer mass onto a neutron star or a black hole unleashing energy by matter falling into the gravitationally potential of the compact object (Psaltis 2006; Tauris & van den Heuvel 2006) and in type Ia supernovae white dwarfs overcome the Chandrasekhar mass by mass accretion or merging leading to thermonuclear explosions (Hillebrandt & Niemeyer 2000; Podsiadlowski 2010; Maoz & Mannucci 2012; Wang & Han 2012) that are so important for cosmology and lead to the discovery of the accelerated expansion of the Universe (Riess et al. 1998; Perlmutter et al. 1999). Binary stars play also a key role in classical novae (Bode & Evans 2012), the formation of planetary nebulae (Hall et al. 2013), the large variety of supernova classes and probably also in long duration GRBs, PISNe and the newly discovered class of super-luminous supernovae (Podsiadlowski et al. 1992; Langer 2012; Podsiadlowski 2013).

The outcome of mass transfer phases can be diverse and depends critically on the reaction of the donor and the accretor upon mass loss and gain, respectively (see Ivanova 2014, for a review). In the following we briefly discuss our current understanding of the main consequences of initiating RLOF, namely stable mass transfer, merging of binaries and common envelope evolution. In addition we briefly discuss other forms of mass transfer that recently gained more attention (e.g. Mohamed & Podsiadlowski 2007; Abate et al. 2013). However, several aspects of binary evolution are theoretically uncertain and large regions of the binary parameter space, such as mergers, are not yet systematically explored with detailed state-of-the-art models. Altogether this leaves a large gap in our understanding of massive stars and their final fates.

Stable mass transfer During stable mass transfer, mass is flowing from one star to the other (Fig. 1.1). The donor star is stripped of its hydrogen-rich envelope and layers processed by nuclear burning are exposed. If massive enough, the star explodes as a type Ib/c supernova, i.e. as a supernova with no hydrogen or helium lines in its spectrum. The accreting star spins up because, besides mass, angular momentum is transferred as well. The accreted material may be rich in the ashes of nuclear burning that took place in the interior of the donor star. The spin-up of the star may be such that the star starts to evolve chemically homogeneously, leading to a long duration GRB (Cantiello et al. 2007).

Mass transfer episodes are also responsible for the Algol paradox. Algol, the demon star, is a close binary in which the more massive star is a main-sequence star while the less massive companion has already evolved off the main-sequence. This is a paradoxical situation because, according to single star evolution, more massive stars evolve faster and the more massive star in Algol should therefore be the post main-sequence object. This paradox is resolved when realising that mass transfer inverted the mass ratio, i.e. that the currently less massive, post main-sequence star in Algol transferred mass onto the nowadays more massive component.

Contact binaries and stellar mergers It may also happen that both stars fill their Roche lobes such that their surfaces are in direct contact, likely resulting in a merger of both stars because of orbital energy losses, e.g., because of friction or the Darwin instability. A contact phase may arise either if the mass transfer rate is so fast that the accretor is brought out of thermal equilibrium such that it expands until both stars get into physical contact or if the initial orbit is so close that also the accretor overfills its Roche lobe because of its expansion due to nuclear burning (e.g. Pols 1994; Wellstein et al. 2001). According to these studies, binaries with an initial mass ratio of $q = M_2/M_1 \lesssim 0.6$ in which mass transfer is initiated while the donor is a main-sequence star evolve into contact to finally merge. Hence, more than 50% of these binaries are expected to merge, meaning that a substantial fraction of stars in the Milky Way, about 10%, are merger products (e.g. Podsiadlowski et al. 1992; de Mink et al. 2014).

The merger product is expected to rotate rapidly because of the angular momentum contained in the binary progenitor (spin and orbital angular momentum) unless material ejected in the merger takes away the majority of the angular momentum. From detailed merger simulations (e.g. Lombardi et al. 1995; Sills et al. 1997, 2001; Glebbeek & Pols 2008; Glebbeek et al. 2013), it is expected that nuclear burning products such as helium and nitrogen are brought to the surface and that some fresh hydrogen is mixed into the cores of stars, increasing the available fuel and hence prolonging the star's life (rejuvenation). Because of the strong shear, magnetic fields may be generated (Tout et al. 2008; Ferrario et al. 2009; Langer 2012, 2014; Wickramasinghe et al. 2014), which, when coupled to out-flowing material or a stellar wind, may torque the star, spinning it down (magnetic braking). This channel might be able to explain the nitrogen rich, slowly rotating LMC B stars in Fig. 1.4 (Box 2).

Besides the previously mentioned V1309 Sco, V838 Mon and V4332 Sgr systems, the nearby, fast rotating, magnetic O6.5f?p star HD 148937 with its massive, quickly expanding bipolar nebula (Leitherer & Chavarria-K. 1987; Langer 2012) and the over-luminous B[e] supergiant R4 in the Small Magellanic Cloud, which also has a massive bipolar nebula (Pasquali et al. 2000), are promising post merger candidates. In the case of HD 148937, the mass of the nebula is estimated to about $2\,M_\odot$, i.e. to about 5% of the merger mass (Leitherer & Chavarria-K. 1987). The surrounding bipolar nebulae are in both cases enriched with nitrogen and appear to be similar to nebulae of some Luminous Blue Variable stars (cf. Fig. 1.3 Pasquali et al. 2000). Are

some of these objects and their bright eruptions such as the giant eruption of η Car also related to stellar mergers? May it even be that some of these eruptions are the massive counterpart of luminous red novae?

Common envelope evolution   Stars with fully convective envelopes tend to expand upon mass loss, thereby overfilling their Roche lobes even more, resulting in more mass transfer and faster radius expansion and so on—a viscous circle that is thought to lead to an engulfment of the companion by the donor star, a phase called common envelope evolution (Paczynski 1976; Taam & Sandquist 2000). In such a situation, there are two possible outcomes. Either the stars merge or the binary survives after ejecting the common envelope. A leading idea is that orbital energy is injected into the common envelope by the in-spiral of the engulfed star and, if the energy is enough to unbind the envelope, the envelope is ejected and the two stars avoid merging. This process is important to explain the short orbits of binaries with compact objects (e.g. X-ray binaries).

The yellow hypergiant HR 5171 A may be caught in a common envelope phase (Chesneau et al. 2014). From the lightcurve of the binary eclipses a possible contact system is inferred. According to the analysis of Chesneau et al. (2014), the 1304 ± 6 day binary has a total mass of $39^{+40}_{-22}\,\mathrm{M}_\odot$ where the yellow hypergiant is at least 10 times more massive than the companion. This and related systems might turn out to be a key to get a deeper insight into the still uncertain physics of common envelope evolution.

Other forms of mass transfer   Mass can be transferred in a binary not only because of RLOF but also through stellar winds (Boffin 2014). In the classical Bondi–Hoyle–Lyttleton accretion (Hoyle & Lyttleton 1941; Bondi 1952), a star accretes from a homogeneous surrounding medium, e.g. produced by the wind of its companion. If the wind velocity is comparable to the orbital velocity, e.g. in wide binaries with giants having slow winds, the orbital movement is imprinted into the gas flow because the winds are too slow to restore the classical flow before the stars pass by again. In such situations, another form of mass transfer, "wind RLOF", may apply that can be 100 times more efficient than the Bondi–Hoyle–Lyttleton accretion (Mohamed & Podsiadlowski 2007). In wind RLOF, the star itself does not fill its Roche lobe but its slow wind does, if the wind acceleration radius, i.e. the radius at which the wind reaches the terminal velocity, is larger than the Roche radius. The wind is then gravitationally channelled through the inner Lagrangian point into the potential well of the companion. Observational support of this new mass transfer mechanism comes from binaries that show the classical Algol paradox but in which the donor star significantly underfills its Roche lobe (e.g. SS Leporis, Blind et al. 2011). Both, Bondi–Hoyle–Lyttleton accretion and wind RLOF, may be enhanced by tides reducing the effective gravity of stars and thereby enhancing the stellar wind (Tout & Eggleton 1988). Wind mass transfer and tidal wind enhancement also apply to massive stars and may be important for stars close to the Eddington limit and rapidly rotating stars.

1.3 This thesis

As discussed above, mass loss, rotation and duplicity play a major role in massive stars and pose challenges for the theory of stellar evolution. In light of recent developments, we want to advance our understanding of massive stars and stellar populations by confronting state-of-the-art theoretical models with observations. To that end, we investigate the consequences of our
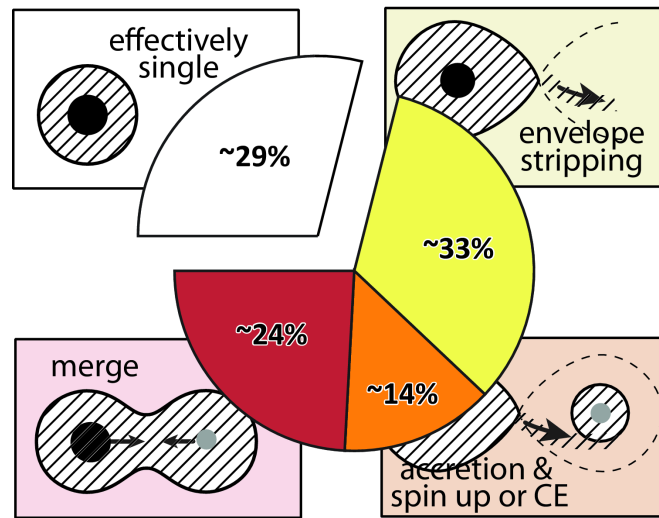
Figure 1.5: Fraction of all Milky Way O stars that end their lives as effectively single stars (either as a genuinely single star or in a wide binary), merge with a companion, accrete & spin-up and are stripped off their envelopes (Sana et al. 2012). The percentages are in terms of all stars born as O-type stars, including genuinely single O stars and O stars in binaries. The insets are artist's impressions of the different evolutionary channels. Figure courtesy of Selma de Mink.

current picture of stars, in particular of duplicity and mass loss, for coeval stellar populations and compare our predictions to observations of Galactic star clusters (Sec. 1.3.1). Furthermore, we develop a Bayesian statistical method to match detailed observations of individual stars to stellar models. This new method allows us to probe, with statistical significance, the physics implemented in stellar evolutionary models and to deepen our understanding of observed stars and stellar populations (Sec. 1.3.2).

1.3.1 Role of binary star evolution in coeval stellar populations

Thanks to recent surveys and large observational campaigns, it is now established that amongst massive stars binaries are way more frequent than previously thought and that they play an important role in stellar evolution and stellar populations. The multiplicity fraction, i.e. the number of multiple systems divided by the total number of systems, is at least 40% in solar like stars and exceeds 70% in the most massive stars (e.g. Bastian et al. 2010; Duchêne & Kraus 2013). The vast majority of O stars undergo a phase of mass transfer, where about 24% of all O stars merge with a companion, about 14% accrete mass thereby spinning up or go through a common envelope phase and about 33% of all O stars are stripped of their envelopes (Fig. 1.5; Sana et al. 2012). As described in the previous sections, mass transfer phases heavily alter the evolution of stars and lead to spectacular phenomena. But what are the consequences of this dominant role of binary star evolution for massive star populations, e.g. in star clusters, and massive stars in general?

Stellar wind mass loss and binary mass transfer heavily alter the masses of individual stars and hence also the distribution of stellar masses in populations of stars, i.e. the mass function. Mass transfer in binaries not only alters stellar masses but also rejuvenates the mass accretors such that they may appear younger than they really are. Central questions are therefore: How does stellar evolution shape stellar mass functions and thereby influences the determination

of the initial mass function, i.e. the birth distribution of stellar masses, that is so important for many areas in astrophysics, and how does rejuvenation affects the ages inferred for star clusters?

State-of-the-art predictions were lacking, so we conducted population synthesis computations to investigate these questions. To that end we equipped the rapid binary evolution code of Izzard et al. (2004, 2006, 2009) with the newest relevant stellar physics and simulated the evolution of millions of single and binary stars to model realistic stellar populations. In this thesis (Chapters 2 and 3), we investigate coeval stellar populations such as those found in star clusters. Stellar populations that formed with a constant star formation rate in the past, e.g. the Galactic stellar population, are studied with the same techniques in de Mink et al. (2014).

For star clusters, we find that stellar wind mass loss creates a peak at the high mass end of mass functions and that binary mass exchange forms a tail that extends the single star mass function by up to a factor of two in mass. Based on these fingerprints of stellar evolution in mass functions, we develop a new method to age-date young star clusters. Classical blue straggler stars, i.e. stars extending the main-sequence turn-off in the HR diagram towards hotter effective temperatures and brighter luminosities, are formed by binary mass transfer and mergers, and primarily populate the mass function tail. We characterise this population of blue stragglers in terms of their frequency, apparent ages and binary fraction, and compare to observations (Chapter 2). The comparison with the observations reveals a fundamental mismatch between the predicted and observed frequency of blue straggler stars as a function of cluster age and we propose modifications to the adopted physics of the evolution of binary stars that may solve this discrepancy. Most importantly, we find that the most massive stars in sufficiently old star clusters are all products of binary mass transfer and that ages derived from these stars significantly underestimate the true cluster age because of rejuvenation arising from binary mass transfer.

Equipped with this knowledge, we probe observed mass functions of the young Galactic Arches and Quintuplet star clusters for signs of massive single and binary star evolution. We are able to find the fingerprints of stellar wind mass loss and binary mass transfer in the mass functions and use our new method to age-date these two clusters. From the features found in the mass functions and additional Monte Carlo experiments, we conclude that the most massive stars in Arches and Quintuplet, the nitrogen and hydrogen rich Wolf–Rayet stars, are likely rejuvenated binary products (Chapter 3). Our findings solve two major problems: (1) the age problem in young clusters in which the most massive stars appear to be younger than less massive cluster members (Martins et al. 2008; Liermann et al. 2012) and (2) the maximum mass problem. Observationally, a tentative stellar upper mass limit of $150\,M_\odot$ is proposed (Figer 2005) whereas more massive stars are observed in 30 Doradus (Crowther et al. 2010; Bestenlehner et al. 2011) and are inferred for the progenitor of supernova 2007bi (Gal-Yam et al. 2009). Our analysis of the Arches cluster questions the $150\,M_\odot$ limit and revises the upper mass limit of stars to be in the range 200–$500\,M_\odot$. Such an upper mass limit allows for pair-instability supernovae in the local Universe that would add yet unaccounted contributions to the chemical enrichment of galaxies and are visible up to large distances.

1.3.2 The Bonnsai project

Large stellar surveys such as the VLT Flames Tarantula survey (VFTS; Evans et al. 2011) and Gaia-ESO (Gilmore et al. 2012) take spectra of thousands of stars. Within the VFTS multi-epoch spectra of more than 1000 OB stars in 30 Doradus (Fig. 1.6), the largest resolved star

Figure 1.6: The central R136 star cluster in the heart of the gigantic starburst region 30 Doradus in the Large Magellanic Cloud. Once hypothesized to be a supermassive single star of $2500\,\mathrm{M_\odot}$ (Cassinelli et al. 1981), R136 is now resolved to be a star cluster that still hosts some of the most massive stars ever observed, e.g. the four stars R136a1-a3 and R136c with inferred initial masses of 165–$320\,\mathrm{M_\odot}$ (Crowther et al. 2010). Credit: NASA, ESA, and F. Paresce (INAF-IASF, Bologna, Italy), R. O'Connell (University of Virginia, Charlottesville), and the Wide Field Camera 3 Science Oversight Committee

forming complex known to date, have been taken. These observations comprise an unprecedented data set that is analysed with detailed atmosphere models to derive stellar parameters such as surface gravity, luminosity, effective temperature, surface chemical abundances etc. for each star. Such plentiful information is ideally suited to, e.g., determine empirical prescriptions for stellar wind mass loss from some of the most massive stars known and to test and calibrate important physics in stellar models such as rotationally induced mixing.

Classically, observations of stars are compared to stellar models in the Hertzsprung–Russell diagram. However, this is no longer possible when many more stellar parameters than just luminosity and effective temperature are known as is the case in modern surveys such as VFTS. To that end, we develop the Bayesian code Bonnsai that is capable of matching all observables simultaneously to theoretical models to derive fundamental stellar parameters such as initial mass and age while taking prior knowledge like the initial mass function into account (Chapter 4). Currently Bonnsai supports the rotating, single star models of Brott et al. (2011a) and Köhler et al. (2014). A key feature of Bonnsai is that we can securely identify stars that cannot be reproduced by stellar models, i.e. we can thoroughly test state-of-the-art stellar evolutionary models. Only with such statistical methods are we able to find shortcomings in current models. We further make our method available through a web interface at http://www.astro.uni-bonn.de/stars/bonnsai.

In a first application, we use Bonnsai to test the stellar models of Brott et al. (2011a) with some of the most accurately measured masses and radii of Galactic eclipsing binary stars. The stellar models reproduce these observations well but we find that the observed temperatures of stars hotter than 25 kK are, on average, warmer by 1.1 ± 0.3 kK (95% CI) than predicted by the models. This systematic discrepancy in temperature results in a systematic offset between observed and predicted luminosities. In cooler stars, the observed and predicted effective temperatures and luminosities are in agreement.

In a second application of Bonnsai (Chapter 5), we match the atmospheric parameters derived for the massive VFTS O and WNh stars to the stellar models of Brott et al. (2011a) and Köhler et al. (2014) to (1) probe the models and (2) determine fundamental stellar parameters such as mass and age to investigate the formation process of these stars in 30 Doradus. The latter is a key step to understand the age structure of this local template of more distant and unresolved starbursts.

With Bonnsai we identify two stars that cannot be reproduced by the models because they are likely binary products. We further find that the models have difficulties in explaining the evolution of the most massive stars. According to the models, more than 50% of the WNh stars must initially rotate faster than $300 \, \mathrm{km \, s^{-1}}$ to simultaneously explain the observed luminosities, effective temperatures and large surface helium mass fractions. We consider such a large fraction of rapid rotators unrealistic given that only less than 20% of the less massive OB stars are observed to rotate that fast. Furthermore, the stellar models predict stars in a region of the HR diagram ($T_{\mathrm{eff}} \lesssim 35$ kK and $\log L/\mathrm{L}_\odot \gtrsim 6.1$) where no stars are observed. Both problems indicate that additional physics is needed to explain the evolution of these massive stars. We propose that stronger stellar winds and the inclusion of binary star evolution may help solving these discrepancies.

The VFTS stars in our sample are mostly field stars that are spread over the whole region. We find no spatially coherent age pattern, meaning that these stars either formed continuously in apparent isolation in various regions of 30 Doradus or in distinct star clusters and associations from where they were then ejected. To further investigate these formation scenarios, we compute age probability distributions of our sample stars to identify potential coeval stellar populations

by their ages. We find two peaks at about 2.7 and 4.5 Myr in the age distributions that may indicate the existence of at least two coeval stellar populations. From independent age estimates for the most active site of recent star formation, the central R136 cluster, we conclude that, if R136 hosts a coeval stellar population whose ejected stars form a peak in our age distributions, it must be associated with the 2.7 Myr group of stars. Stars of the 4.5 Myr group are mainly found 1.2 arcmin outside R136 and may be associated with the second most obvious site of recent star formation, NGC 2060. If these two groups of stars indeed belong to two stellar populations, our age distributions reveal at least two further groups of 3.6 and 5.3 Myr stars. The 3.6 Myr stars are only found in the vicinity of R136 and may belong to the north-east clump suggested by Sabbi et al. (2012) to merge with R136. If true, these findings imply that most of our sample stars formed in clusters and associations from which they ejected. However, in order to prove this scenario, future proper motion measurements are required to trace back the formation sites of stars in the different age groups.

Evolution of mass functions of coeval stars through wind mass loss and binary interactions

F.R.N. Schneider, R.G. Izzard, N. Langer and S.E. de Mink

Abstract   Accurate determinations of stellar mass functions and ages of stellar populations are crucial to much of astrophysics. We analyse the evolution of stellar mass functions of coeval main sequence stars including all relevant aspects of single- and binary-star evolution. We show that the slope of the upper part of the mass function in a stellar cluster can be quite different to the slope of the initial mass function. Wind mass loss from massive stars leads to an accumulation of stars which is visible as a peak at the high mass end of mass functions, thereby flattening the mass function slope. Mass accretion and mergers in close binary systems create a tail of rejuvenated binary products. These blue straggler stars extend the single star mass function by up to a factor of two in mass and can appear up to ten times younger than their parent stellar cluster. Cluster ages derived from their most massive stars that are close to the turn-off may thus be significantly biased. To overcome such difficulties, we propose the use of the binary tail of stellar mass functions as an unambiguous clock to derive the cluster age because the location of the onset of the binary tail identifies the cluster turn-off mass. It is indicated by a pronounced jump in the mass function of old stellar populations and by the wind mass loss peak in young stellar populations. We further characterise the binary induced blue straggler population in star clusters in terms of their frequency, binary fraction and apparent age.

2.1 Introduction

Stellar mass functions are important for population studies, both nearby and at high redshift. Mass functions are not static but change their shape when the frequencies of stars or their masses are altered over time (Scalo 1986; Kroupa et al. 2013). Possible causes include the evaporation of stars and mass segregation in star clusters (de Grijs et al. 2002; McLaughlin & Fall 2008; Harfst et al. 2010; Habibi et al. 2013) and mass loss in the course of stellar evolution (Langer 2012). These mechanisms leave characteristic fingerprints in mass functions from which insights into the evolutionary status of stellar populations and the mechanisms themselves can be gained.

Massive stars are subject to strong stellar wind mass loss, which decreases their masses already on the main-sequence (MS), directly affecting mass functions. Furthermore, it emerges that binary stars play an important role in stellar populations of various ages and even dominate the evolution of massive stars (Sana et al. 2012). The multiplicity fraction, i.e. the number of multiple stars divided by the total number of stellar systems, is larger for higher masses (e.g. Bastian et al. 2010; Duchêne & Kraus 2013): it exceeds 40% for solar like stars (F, G and K stars) and 70% for the most massive stars (O-stars). In close binaries, mass is exchanged between the binary components during Roche lobe overflow (RLOF) or in stellar mergers, directly affecting stellar masses and hence the mass function. The mass gainers are rejuvenated and can appear much younger than they really are. Some mass gainers may also be visible as blue straggler stars (Braun & Langer 1995; Dray & Tout 2007; Geller & Mathieu 2011).

The determination of stellar ages is a fundamental task in stellar astrophysics (Soderblom 2010) that can be biased by rejuvenated binary products. Various methods are used to determine stellar ages. The surface properties of individual stars can be compared with evolutionary model predictions, e.g. luminosity, surface temperature or surface gravity (Holmberg et al. 2007; Schneider et al. 2014a), rotation rates in low mass stars (Barnes 2007) or surface nitrogen abundances in massive stars (Köhler et al. 2012). In star clusters, the most widely used age determination method compares the main sequence turn-off with theoretical isochrones (e.g. Naylor & Jeffries 2006; Monteiro et al. 2010). Close binary evolution such as mass transfer and stellar mergers leads to spurious or inaccurate results in all of these methods. To derive unambiguous age estimates one must be able to distinguish between rejuvenated binary products and genuinely single stars.

In this paper we investigate how the modulation of stellar mass functions by single and binary star evolution can be used both to identify binary products and to derive unambiguous stellar ages. More generally, we explore what can be learned about stellar evolution and the evolutionary status of whole stellar populations from observed mass functions. We also investigate quantitatively how single and binary star evolution influence the determination of initial mass functions. To that end, we perform detailed population synthesis calculations of coeval stellar populations using a rapid binary evolution code.

We describe our method in Sec. 2.2 and present mass functions of coeval single and binary star populations of ages ranging from 3 Myr to 1 Gyr in Sec. 2.3. Through binary interactions, blue straggler stars are formed in our models. We characterise their binary fraction and ages, and compare their predicted frequencies to those found in Galactic open star clusters in Sec. 2.4. Blue straggler stars predominantly populate the high mass end of mass functions and may bias determinations of stellar cluster ages. We show how to use mass functions to overcome such biases when determining cluster ages in Sec. 2.5 and conclude in Sec. 2.6.

2.2 Method

We compute the evolution of single and close, interacting binary stars and construct, at pre-defined ages, mass functions by counting how many stars of certain masses exist. This approach ensures that we factor in all the relevant single and binary star physics to investigate their influence on the present-day mass function (PDMF).

The initial parameter space of binaries is large compared to that of single stars, which essentially consists of the initial mass. In binaries, there are two masses, the orbital separation, the eccentricity of the orbit and the relative orientation of the spin axis of both stars. We apply some standard simplifications to reduce this huge parameter space: we impose circular orbits and that both stellar spins are aligned with the orbital angular momentum. All our models are calculated for a metallicity $Z = 0.02$ (unless stated otherwise). Furthermore we focus on the main-sequence because stars spend typically 90% of their life in this evolutionary stage. Still, we need to follow the evolution of a large number of stellar systems to sample the remaining binary parameter space and to resolve effects at the high mass end of the PDMF. Hence, we work with a rapid binary evolution code.

2.2.1 Rapid binary evolution code

We use the binary population and nucleosynthesis code of Izzard et al. (2004, 2006, 2009) with modifications due to de Mink et al. (2013) which is based on the rapid binary evolution code of Hurley et al. (2002). This code uses analytic formulae (Hurley et al. 2000) fitted to detailed single star evolutionary models (Pols et al. 1998) to approximate the evolution of single stars for a wide range of masses and metallicities.

The fitting formulae of Hurley et al. (2000) are based on detailed stellar model sequences of stars with mass up to $50\,\mathrm{M}_\odot$ (Pols et al. 1998). The evolution of stars with mass in excess of $50\,\mathrm{M}_\odot$ is thus based on extrapolations of the original fitting formulae. The MS lifetime, τ_{MS}, is particularly inaccurately extrapolated by the appropriate fit, so we replace it with a logarithmic tabular interpolation of the main sequence lifetimes taken directly from the models of Pols et al. (1998) in the mass range $20 \leq M \leq 50\,\mathrm{M}_\odot$. More massive than this we extrapolate the final two masses in the grid of detailed models (Pols et al. 1998). This results in a reduction of the MS lifetime of e.g. a $100\,\mathrm{M}_\odot$ star at $Z = 0.02$ from $3.5\,\mathrm{Myr}$ to $2.9\,\mathrm{Myr}$, i.e. in a reduction of 17%, which is in agreement with state-of-the-art non-rotating detailed stellar models of Brott et al. (2011a) and Ekström et al. (2012).

Stellar wind mass loss for stars with luminosities $L > 4000\,\mathrm{L}_\odot$ is given by Nieuwenhuijzen & de Jager (1990). This recipe is modified by a factor $Z^{0.5}$ according to Kudritzki et al. (1989) to mimic the impact of the metallicity Z on wind mass loss rates.

Binary stars can exchange mass either by Roche lobe overflow (RLOF), wind mass transfer or merging. Roche lobe overflow occurs when one star (hereafter the donor) fills its Roche lobe and transfers mass to its companion (hereafter the accretor) through the inner Lagrangian point. Depending on the physical state of the donor star one distinguishes between Case A, B and C mass transfer. Following the definition of Kippenhahn & Weigert (1967), Case A mass transfer occurs during core hydrogen burning, Case B after the end of core hydrogen burning and Case C, defined by Lauterborn (1970), after the end of core helium burning.

Our binary evolution code differs from Hurley et al. (2002) in its treatment of RLOF. For stable mass transfer it is expected that the stellar radius R adjusts itself to the Roche lobe radius R_L, i.e. $R \approx R_\mathrm{L}$. Whenever RLOF occurs ($R > R_\mathrm{L}$) we remove as much mass as

needed to shrink the donor star back into its Roche lobe. The resulting mass transfer and mass accretion rates are capped by the thermal timescales of the donor and accretor, respectively.

We follow Hurley et al. (2002) to determine the occurrence of common envelope evolution and contact phases that lead to stellar mergers. Main-sequence mergers are expected either if the initial orbital separation is so small that both stars fill their Roche lobes and thus come into physical contact or if the mass ratio of the accretor to the donor star falls below a certain limit at the onset of mass transfer, $q = M_2/M_1 < q_{\mathrm{crit}}$, which drives the accretor out of thermal equilibrium and hence results in a contact system (e.g. Ulrich & Burger 1976; Kippenhahn & Meyer-Hofmeister 1977; Neo et al. 1977; Wellstein et al. 2001). The critical mass ratio is approximately $q_{\mathrm{crit,MS}} = 0.56$ for MS stars (de Mink et al. 2007), $q_{\mathrm{crit,HG}} = 0.25$ if the donor star is a Hertzsprung gap star and is given by a fitting formula if the donor star has a deep convective envelope (Hurley et al. 2002).

Mass transfer because of either stable RLOF or during a stellar merger makes the mass gainers appear younger than they really are (Braun & Langer 1995; van Bever & Vanbeveren 1998; Dray & Tout 2007). Such rejuvenated stars may stand out as blue stragglers in Hertzsprung Russell diagrams. Rejuvenation is handled following Tout et al. (1997) and Hurley et al. (2002) but with improvements as described in Glebbeek & Pols (2008) and de Mink et al. (2013). The apparent age T of a star is given by the amount of burnt fuel compared to the total available. For a star with MS lifetime τ_{MS} we therefore have (in a linear approximation) $T = f_{\mathrm{burnt}}\tau_{\mathrm{MS}}$ where $f_{\mathrm{burnt}} = M_{\mathrm{burnt}}/M_{\mathrm{available}}$ is the mass ratio of the burnt to totally available fuel. After mass transfer onto a MS star with a convective core, the mass of the already burnt fuel is given by the fraction of burnt material, f_{burnt}, times the convective core mass before mass transfer, M_{c} (primes indicate quantities after mass transfer). After mass transfer, the convective core and hence the available fuel of the accretor grow in mass, i.e. $M_{\mathrm{c}}' > M_{\mathrm{c}}$, because the total stellar mass increases (and vice versa for the donor star). Thus, the fraction of burnt fuel after mass transfer is $f_{\mathrm{burnt}}' = f_{\mathrm{burnt}}M_{\mathrm{c}}/M_{\mathrm{c}}'$ and the apparent age, $T' = f_{\mathrm{burnt}}'\tau_{\mathrm{MS}}'$, is

$$T' = \frac{M_{\mathrm{c}}}{M_{\mathrm{c}}'}\frac{\tau_{\mathrm{MS}}'}{\tau_{\mathrm{MS}}}T. \tag{2.1}$$

This equation holds for the accretor and also for the donor when setting $M_{\mathrm{c}} = M_{\mathrm{c}}'$ (no burnt fuel is mixed out of the core upon mass loss from the stellar surface) and shows that the accreting stars rejuvenate upon mass transfer ($T' < T$ because $M_{\mathrm{c}}' \geq M_{\mathrm{c}}$ and $\tau_{\mathrm{MS}}' < \tau_{\mathrm{MS}}$) while the donor stars age ($T' > T$ because $\tau_{\mathrm{MS}}' > \tau_{\mathrm{MS}}$). The accretor and donor will have burnt less (more) fuel than a single star of the same mass that did not accrete (lose) mass. If stars do not have convective cores, e.g. stars with initial masses in the range $0.3 \leq M/\mathrm{M}_\odot \leq 1.3$ or Hertzsprung gap stars which have radiative cores, we set $M_{\mathrm{c}} = M_{\mathrm{c}}'$ because no fresh fuel is expected to be mixed into their cores.

To model the rejuvenation of MS mergers we follow de Mink et al. (2013): first, we assume that a fraction f_{loss} of the total mass $M_3 = M_1 + M_2$ is lost during the merger; we adopt $f_{\mathrm{loss}} = 0.1$. Second, we approximate the core mass fraction f_{c} of MS stars according to fitting functions (Glebbeek & Pols 2008) and estimate the apparent age T_3 of the newly formed merged star from,

$$T_3 = \tau_{\mathrm{MS,3}} \cdot \frac{f_{\mathrm{c,1}} \cdot \frac{T_1}{\tau_{\mathrm{MS,1}}} + f_{\mathrm{c,2}} \cdot \frac{T_2}{\tau_{\mathrm{MS,2}}}}{f_{\mathrm{c,3}}^{\mathrm{eff}}}, \tag{2.2}$$

where T_1 and T_2 are the effective ages, $f_{\mathrm{c,1}}$ and $f_{\mathrm{c,2}}$ are the core mass fractions of the progenitor

stars and τ_{MS} denotes the MS lifetime of the corresponding star. The denominator contains the effective core mass fraction $f_{\mathrm{c},3}^{\mathrm{eff}} = f_{\mathrm{c},3} + f_{\mathrm{mix}} \cdot (1 - f_{\mathrm{c},3})$ of the merger product which is given by its core mass fraction modified by an additional mixing of $f_{\mathrm{mix}} = 10\%$ of the hydrogen-rich envelope. The resulting rejuvenation is less than in the original Hurley et al. (2002) code, where it is assumed that the whole star is mixed, and closer to that seen in hydrodynamic and SPH simulations of stellar mergers (e.g. Lombardi et al. 1995; Sills et al. 1997, 2001; Glebbeek & Pols 2008; Glebbeek et al. 2013).

2.2.2 Initial distribution functions

We set up a grid of stellar systems to cover the parameter space of single and binary stars and assign each stellar system j a probability of existence δp_j. The probabilities δp_j are calculated from $\delta p_j = \Psi \delta \ln V$ where Ψ is a distribution function of the initial masses and the initial orbital periods and $\delta \ln V$ is the volume of the parameter space filled by the stellar system j. The initial distribution function, Ψ, reads,

$$\Psi = \begin{cases} \psi(\ln m) & \text{single stars,} \\ \psi(\ln m_1)\,\phi(\ln m_2)\,\chi(\ln P) & \text{binary stars,} \end{cases} \tag{2.3}$$

where m_1 and m_2 are the initial masses of the primary and secondary star in binaries, respectively, and P is the initial orbital period. The functions $\psi(\ln m_1)$, $\phi(\ln m_2)$ and $\chi(\ln P)$ are the initial mass functions of the primary and secondary star and the distribution function of the initial orbital period, respectively. Stellar masses m are given in solar masses.

Single stars and also the primaries of binary stars, i.e. the initially more massive component, are distributed according to a Salpeter initial mass function (IMF) (Salpeter 1955). The initial mass function $\psi(\ln m_1)$ is then

$$\psi(\ln m_1) \equiv \frac{\mathrm{d}p}{\mathrm{d}\ln m_1} = m_1 \frac{\mathrm{d}p}{\mathrm{d}m_1} = A m_1^{\Gamma} \tag{2.4}$$

with $\Gamma = -1.35$ the slope of the mass function and A the normalization constant such that

$$\int_{m_{\mathrm{l}}}^{m_{\mathrm{u}}} \frac{\mathrm{d}p}{\mathrm{d}m_1}\,\mathrm{d}m_1 = 1. \tag{2.5}$$

The lower and upper mass limits are chosen such that we do not exceed the validity of the fitting functions used in the code, hence $m_l = 0.1$ and $m_u = 100$.

Duchêne & Kraus (2013) review stellar multiplicity (multiplicity fractions, mass ratio distributions and orbital separations distributions) and its dependence on primary mass and environment. A complete picture is yet lacking (e.g. for MS primary stars in the mass range 8–16 $\mathrm{M}_\odot$) but it seems that a flat mass ratio distribution,

$$\phi(\ln m_2) = \frac{\mathrm{d}p}{\mathrm{d}\ln m_2} = q\frac{\mathrm{d}p}{\mathrm{d}q} \propto q, \tag{2.6}$$

is reasonable maybe except at the lowest primary masses ($\lesssim 1\,\mathrm{M}_\odot$). We adopt this as the distribution function of the initial mass ratios, meaning that all mass ratios q are equally probable ($\mathrm{d}p/\mathrm{d}q = \text{const.}$). We adopt a minimum mass ratio, $q_{\mathrm{min}} = 0.1/m_1$.

In terms of orbital separations, we are only interested in close binaries, i.e. binaries that

can interact by mass exchange at some point during their life. Our binary systems therefore have initial orbital separations a between $3\,R_\odot$ and $10^4\,R_\odot$ ($\sim 46\,\mathrm{AU}$). In practice it turns out that only binaries with initial orbital separations less than about $3 \times 10^3\,R_\odot \approx 15\,\mathrm{AU}$ interact. Initially wider binaries are effectively single stars. The distribution function $\chi(\ln P)$ of the initial orbital periods P is given by Sana et al. (2012) for binaries with O-type companions (i.e. $m_1 \geq 15$) and mass ratios $q > 0.1$ and by a flat distribution in $\ln P$ for all other binaries, i.e. $f(P)\,\mathrm{d}P \propto \mathrm{d}P/P$ (Öpik 1924),

$$\chi(\ln P) \propto \begin{cases} (\log P)^{-0.55}, & 0.15 \leq \log P/\mathrm{d} \leq 3.5 \\ \text{const.} & \text{otherwise.} \end{cases} \tag{2.7}$$

The lower boundary of the initial orbital separations, $a_l = 3\,R_\odot$, is increased if a star fills its Roche lobe on the zero age main-sequence (ZAMS) such that stars cannot interact immediately by RLOF.

For our mass function calculations, we evolve a total of $2{,}500{,}000$ binary and $250{,}000$ single stars. The overall mass range of 1–$100\,M_\odot$ is subdivided in 10 equally spaced mass intervals. Each of the 10 mass intervals covers 2500 single stars of different initial masses and $100 \times 50 \times 50$ ($m_1 \times q \times a$) binaries. Masses and orbital separations are distributed equidistantly on a logarithmic grid while the mass ratios are distributed equidistantly on a linear grid.

2.2.3 Binary parameter space

To understand the influence of binary interactions on the PDMF, we need to know quantitatively how much mass is transferred and accreted during binary mass exchange. Given an initial primary mass m_1, we investigate the binary parameter space spanned by the initial secondary mass m_2 ($< m_1$) and initial orbital separation a to calculate the amount of transferred and accreted mass because of RLOF ($\Delta M_{\mathrm{trans}}$ and ΔM_{acc} respectively) *during the MS evolution of the secondary star*. We further compute the mass transfer efficiency,

$$\beta = \frac{\Delta M_{\mathrm{acc}}}{\Delta M_{\mathrm{trans}}}, \tag{2.8}$$

during the different mass transfer Cases A, B and C. ΔM_{acc} and $\Delta M_{\mathrm{trans}}$ are then the accreted and the transferred mass, respectively, during the different mass transfer cases.

In Fig. 2.1 we show the mass transfer efficiency β (Eq. 2.8) in binaries with $10\,M_\odot$ primary stars as a function of initial mass ratio, q_{ini}, and initial orbital separation, a_{ini}. Binaries interact by Case A mass transfer if the initial orbital separation is less than about 20-30 $R_\odot$. They first interact by Case B mass transfer if the initial orbital separation is longer than the boundary for Case A mass transfer and shorter than 800–1000 $R_\odot$. They first interact by Case C mass transfer if the initial orbital separation is longer than 800–1000 $R_\odot$. They do not interact by RLOF at all if the initial orbital separation is longer than about 2000 $R_\odot$. The boundaries depend on the initial mass ratio: if the mass ratio is larger (for a fixed orbital separation), the primary overflows its Roche lobe earlier in its evolution because the Roche lobe is smaller. The boundaries between the different mass transfer cases therefore shift to longer initial orbital separations for larger mass ratios.

There is a small zone/gap above the Case C mass transfer region for large initial mass ratios ($q \gtrsim 0.95$) where stars interact by Case C mass transfer, but only after the secondary has left the MS, hence the gap.
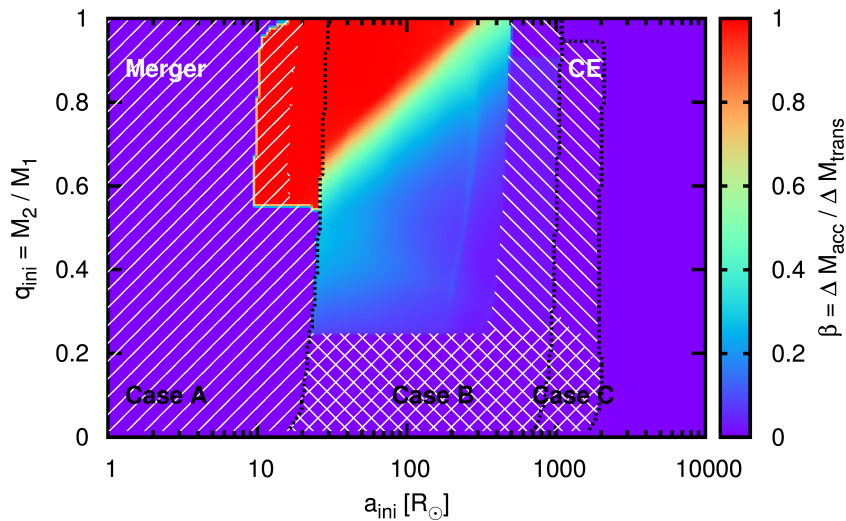
Figure 2.1: Mass transfer efficiency $\beta = \Delta M_{acc}/\Delta M_{trans}$ in binaries with $M_1 = 10\,M_\odot$ primary stars as a function of initial orbital separation a_{ini} and initial mass ratio $q_{ini} = m_2/m_1$. The black, dotted lines indicate the boundaries between the three different mass transfer Cases A, B and C. The white area hatched from bottom-left to top-right shows binaries that result in stellar mergers whereas those hatched from bottom-right to top-left show binaries that go through at least one common envelope phase during their evolution. Binary evolution is followed until the secondary stars leave the MS.

In Fig. 2.1, we also mark those binaries as mergers which start RLOF on the ZAMS (we do not treat these binaries in our simulations). We assume that stars enter a contact phase if their mass ratio at the onset of Case A mass transfer is less than 0.56 (Sec. 2.2.1). Only the products of these Case A mergers are MS stars and only these contribute to our analysis of the PDMF.

There are two more critical mass ratios visible in Fig. 2.1: we assume that stars enter common envelope evolution at the onset of Case B RLOF if the donor star is a Hertzsprung gap star and the mass ratio is below 0.25. For giant-like donor stars, i.e. donor stars with a deep convective envelope (e.g. red supergiants), we use a formula (Eq. 57 in Hurley et al. 2002) to calculate the critical mass ratio. Mass loss from a star with a deep convective envelope leads to an increase of its radius, hence to even more mass transfer and is thus dynamically unstable. The giant-like donor star engulfs its companion and the binary enters common envelope evolution. If all these criteria do not apply for the binary star at the onset of RLOF we use the critical mass ratio $q_c = 0.33$.

The transferred mass ΔM_{trans} from a $10\,M_\odot$ primary star during RLOF is shown in Fig. 2.2. The transferred mass is very similar in all interacting binaries that do not enter a contact phase Case A mass transfer is caused by increasing stellar radii due to nuclear evolution during core hydrogen burning. MS stars with masses larger than $1.25\,M_\odot$ have radiative envelopes in our models. Mass transfer from stars with radiative envelopes is stable, i.e. such stars shrink back into their Roche lobe as a reaction to mass loss. Case A RLOF starts earlier and lasts longer for smaller initial orbital separations, hence the smaller the initial orbital separation the larger the mass lost by the donor, i.e. the transferred mass ΔM_{trans}. During Case B and C mass transfer, RLOF is driven by the expansion of the stellar envelope. Stars stop overfilling their Roche lobes only after losing (nearly) their whole envelope. The envelope mass of the $10\,M_\odot$ donor stars of the Case B binaries which do not enter a CE evolution is always about the same, hence is the total transferred mass in Fig. 2.2.

Figure 2.2: The mass ΔM_{trans} transferred from $10\,\text{M}_\odot$ donor stars by RLOF during the MS evolution of the secondary star as a function of the initial mass ratio and the initial orbital separation. The hatched regions have the same meaning as in Fig. 2.1.

Figure 2.3: As Fig. 2.2 but for the total mass accreted by the secondary star, ΔM_{acc}, during RLOF.

Figure 2.3 shows how much of the mass transferred from the $10\,\mathrm{M}_\odot$ donor stars is accreted by the secondary stars during their MS evolution. The only limit on mass accretion in our 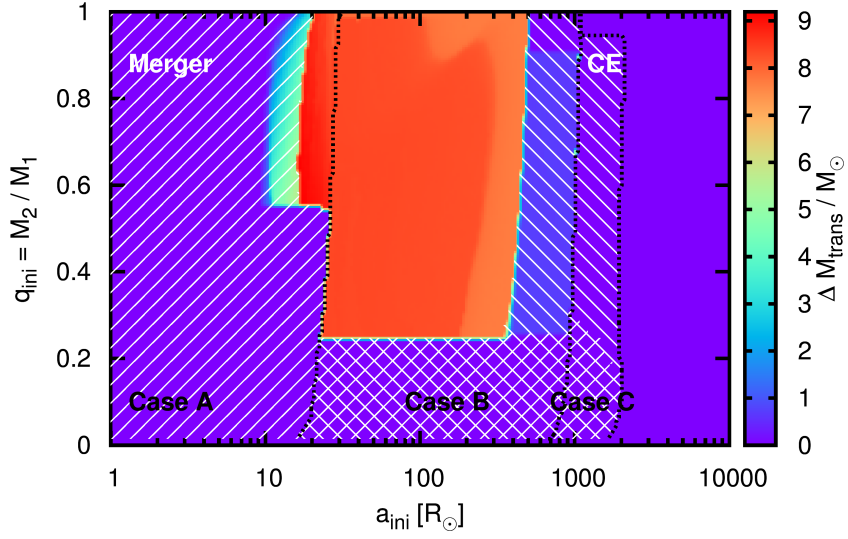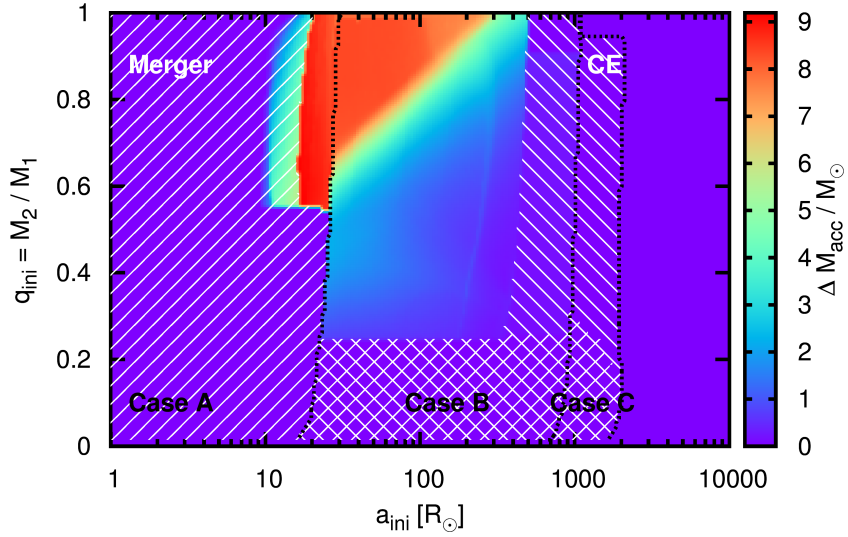models is the thermal timescale of the accretor which ensures that the accretors remain in thermal equilibrium, an implicit assumption when using fitting functions for single star evolution. The thermal (Kelvin-Helmholtz) timescale is given by

$$\tau_{\mathrm{KH}} \approx 10^7 \frac{M/\mathrm{M}_\odot \, M_{\mathrm{env}}/\mathrm{M}_\odot}{R/\mathrm{R}_\odot \, L/\mathrm{L}_\odot} \,\mathrm{yr}, \tag{2.9}$$

where M is the total mass, M_{env} the mass of the envelope ($M_{\mathrm{env}} = M$ for MS stars), R the radius and L the luminosity of the star. Nearly all transferred mass is accreted during Case A mass transfer. Mass transfer during the Hertzsprung gap, i.e. Case B mass transfer, proceeds on the thermal timescale of the primary. At longer initial orbital separations, the thermal timescale of the primary is shorter because the primaries have larger radii when they overfill their Roche lobes (mass and luminosity are nearly constant in the Hertzsprung gap). The thermal timescale of the MS secondary at the same time is inversely proportional to a power of its mass ($\tau_{\mathrm{KH}} \propto M^{-x}, x > 0$). We therefore expect less accretion at longer initial orbital separations (because of shorter thermal timescales of the donor stars and hence faster mass transfer) and for smaller initial secondary masses (because of longer thermal timescales of less massive accretors). This causes the gradient visible in the Case B region of Figs. 2.1 and 2.3.

Combining the results of the transferred and accreted mass during RLOF reveals the mass transfer efficiency as shown in Fig. 2.1. Mass transfer is nearly conservative during Case A, i.e. almost all transferred mass is accreted ($\beta \approx 1$), and becomes non-conservative during Case B and C mass transfer.

Next, we analyse the binary parameter space for different primary masses. Figures 2.17–2.22 in Appendix 2.7.1 contain the mass transfer efficiency, transferred and accreted mass as in Figs. 2.1, 2.2 and 2.3 but for primary masses of 2, 5, 20, 50, 70 and $100\,\mathrm{M}_\odot$. Binaries in which the primary star once filled its Roche lobe are called interacting binaries. From the data of Fig. 2.1, we compute the ratios of the number of binaries that go through a common envelope phase, merge on the MS and transfer mass stably by RLOF to the number of interacting binaries and the ratio of the number of interacting to simulated binaries. We plot these ratios as a function of primary mass in Fig. 2.4 taking into account the initial distribution functions of binaries discussed in Sec. 2.2.2. The overall trend is that the more massive the primary star the larger the fraction of stars that transfer mass stably by RLOF, the larger the fraction of stars that merge on the MS and hence the smaller the fraction of binaries that go through a common envelope phase.

The number of interacting binaries decreases rapidly around $50\,\mathrm{M}_\odot$ because more massive stars cross the Humphreys-Davidson limit (Humphreys & Davidson 1979) after their MS evolution and are subject to strong wind mass loss. The mass loss widens the orbits such that binaries cannot interact by RLOF (cf. Vanbeveren 1991). Consequently, the fraction of MS mergers increases because it is normalized by the number of interacting binaries while the number of Case B binaries that go through a common envelope phase ($q_{\mathrm{ini}} < 0.25$) decreases.

The fraction of interacting binaries shows a kink around $8\,\mathrm{M}_\odot$ because this is the mass above which stars explode as supernovae. Our $7\,\mathrm{M}_\odot$ model reaches a maximum radius that is larger than that of e.g. our $8\,\mathrm{M}_\odot$ model because the latter star explodes before reaching a similarly large radius. The parameter space for interaction is therefore smaller in binaries with $8\,\mathrm{M}_\odot$ primary stars. From thereon, the number of interacting binaries gradually increases
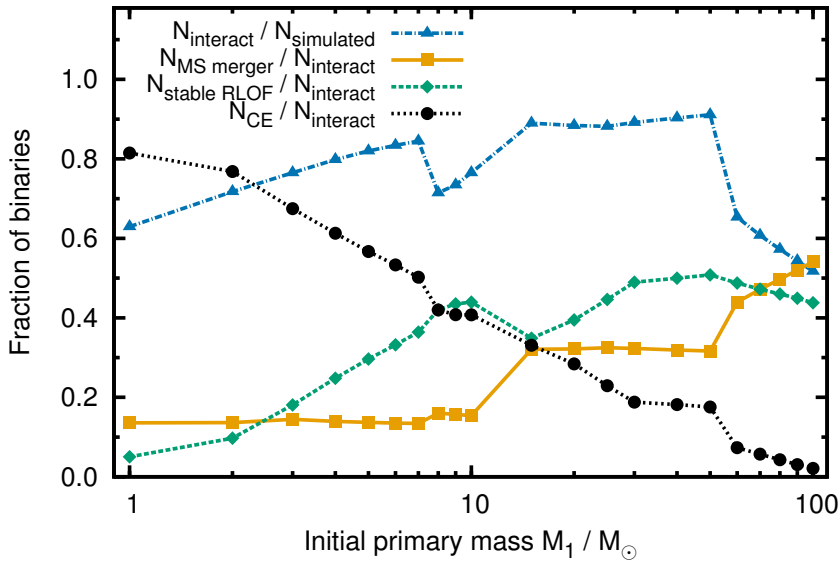
Figure 2.4: Fraction of simulated binaries that interact by RLOF during the MS of the secondary stars and fraction of interacting binaries that merge on the MS, that transfer mass stably by RLOF and that go through a common envelope (CE) phase as a function of the mass of the primary stars. The number of simulated binaries is given by $N_{\text{simulated}}$, the number of interacting binaries by N_{interact}, the number of binaries that merge on the MS by $N_{\text{MS merger}}$, the number of binaries that transfer mass stably by RLOF by $N_{\text{stable RLOF}}$ and the number of binaries that go through a CE phase by N_{CE}. By interacting binaries, we mean that the primary overfills its Roche lobe resulting in mass transfer or a merger.

with primary mass because more massive primary stars reach larger maximum radii. Above $\sim 13\,\text{M}_\odot$, the maximum radius is larger than that of a $7\,\text{M}_\odot$ star and so is the fraction of interacting binaries.

Between 2 and $10\,\text{M}_\odot$ the fraction of binaries that transfer mass stably by RLOF increases while the fraction of systems that go through a common envelope phase decreases. Stars more massive than about $2\,\text{M}_\odot$ expand significantly while crossing the Hertzsprung-Russell diagram and the chance of interaction by Case B mass transfer is therefore larger. Less massive stars are cooler and develop convective envelopes, ascending the giant branch (GB), after little expansion. Mass transfer from such stars is dynamically unstable leading to a common envelope phase. The more massive stars are, the larger the Hertzsprung gap, the larger the number of stars that interact by Case B mass transfer while having a radiative envelope and the fewer the number of binaries that enter a common envelope phase.

Stars with $M \gtrsim 13\,\text{M}_\odot$ ignite helium in the core during the Hertzsprung gap in our models and only slightly climb the giant branch, meaning there is only a limited range of initial orbital separations that leads to stars that interact as giants and thus enter a common envelope phase. Contrarily, the fraction of binaries that transfer mass stably by RLOF plateaus for primary masses greater than $10\,\text{M}_\odot$ because the available range of separations to transfer mass from a star without a fully convective envelope does not change significantly.

Binaries in which the primary star is more massive than about $22\,\text{M}_\odot$ do not experience Case C mass transfer because the primary stars lose their envelopes through strong stellar winds during core helium burning which widens the orbit and prevents the star from further expansion. As a consequence, the star cannot overfill its Roche lobe after core helium burning

and there is no Case C mass transfer.

Binaries with O-type primaries, i.e. with $M_1 \geq 15\,\mathrm{M_\odot}$ are distributed according to the initial orbital period distributions of Sana et al. (2012). This enhances the number of stellar mergers on the MS and the occurrence of Case A mass transfer because there are more binaries with short orbital periods according to the orbital period distribution of Sana et al. (2012) than for a distribution that is flat in $\log P$ as used for less massive stars. The change of the period distribution leads to the abrupt increase in the fraction of MS mergers around $15\,\mathrm{M_\odot}$ and the decrease of the fraction of binaries transferring mass stably by RLOF because the emphasis is now on binaries in the closest orbits which preferentially merge (see Figs. 2.1 and 2.17–2.22).

We discuss uncertainties in our models regarding single and binary star evolution and the initial distribution functions in Appendix 2.7.2.

2.2.4 Construction of mass functions

Constructing the mass function of a population of single stars is straightforward: we bin the masses and count the number of stars per mass bin. In the case of binary stars we construct three different mass functions according to:

1. The primary masses only.

2. The secondary masses only.

3. An *observed* mass reconstructed from the total stellar luminosity.

In the latter case we derive masses from the total luminosity of binaries: we add the luminosities of both components and numerically invert the mass-luminosity (ML) relation given by our fitting formula (Eq. 12 of Hurley et al. 2000). We call mass functions constructed in this way observed mass functions, because it comes closest to mass functions from photometry where luminosities are directly translated into masses and binaries are unresolved. We emphasize again that we only consider MS stars in our analysis.

2.3 Modulation of mass functions by stellar evolution

2.3.1 Single star populations

Two phenomena influence the mass functions of a population of single stars. First, stars have shorter lives the more massive they are. When stars leave the MS, they disappear from our mass functions. Second, massive stars lose mass through stellar winds. This reduces stellar masses and hence changes the mass function. In Fig. 2.5 we show PDMFs of coeval single star populations of different ages. The mass functions are constructed from the theoretically known stellar masses (approach 1 in Sec. 2.2.4). The dashed vertical lines mark the initial mass of stars that have a MS lifetime equal to the age of the population. Over-plotted in black is the initial distribution of stellar masses, i.e. the Salpeter (1955) IMF.

The most massive stars leave the MS first which causes a truncation close to the dashed vertical lines. From here on we call this truncation the turn-off because stars at the truncation of the mass function are located at the turn-off in the Hertzsprung-Russell (HR) diagram of a star cluster. Stars at the turn-off are called 'turn-off stars' and their mass the 'turn-off mass'. Younger than about 10 Myr the turn-off and the dashed lines do not coincide, they are displaced
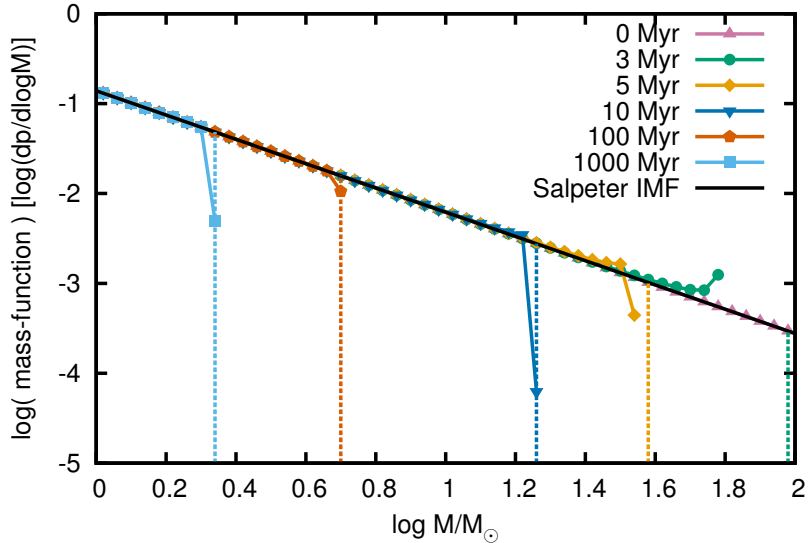
Figure 2.5: Present-day mass functions of coeval single star populations of different ages. Dashed vertical lines correspond to the mass of stars with a MS lifetime equal to the age of the population. The most massive stars have the shortest MS lifetime and hence disappear first. Stellar wind mass loss creates the peaks at the high mass end most prominently seen in the 3.0 Myr old population.

from each other. The displacement is caused by stellar wind mass loss and amounts to $\sim 40\,\mathrm{M_\odot}$ in the 3.0 Myr PDMF for our adopted mass loss recipes.

We use a maximum initial stellar mass of $100\,\mathrm{M_\odot}$. Such stars have MS lifetimes of about 3.0 Myr, so the upper mass boundary plays no role in populations older than 3.0 Myr because all stars with initially masses larger than $100\,\mathrm{M_\odot}$ have left the MS. Our results are influenced by boundary effects at ages younger than 3.0 Myr.

A prominent feature in the PDMF is the accumulation of stars close to the turn-off because of mass loss through stellar winds. The more massive a star the more mass is lost during its MS evolution. Stars with masses close to the turn-off mass are the currently most massive stars in the cluster and will soon leave the MS, so the greatest accumulation of stars in the PDMF is found close to the turn-off. In our calculations, stars initially less massive than $9\,\mathrm{M_\odot}$ at $Z = 0.02$ ($\tau_{\mathrm{MS}} \gtrsim 30\,\mathrm{Myr}$) lose less than 1% of their initial mass via winds during the MS — the accumulation of stars in the PDMF disappears totally and the initial and the present-day turn-off masses are the same (the dashed vertical lines coincide with the turn-off). Note that we do not see a sharp truncation as indicated by the dashed vertical lines because of the finite size of our mass bins.

The magnitude of the wind mass loss peak in the PDMF depends on how many stars are shifted to lower masses and by how much. It therefore depends on the strength of stellar wind mass loss, i.e. also on the metallicity, and the slope of the IMF. In Fig. 2.6 we show this dependence at the high mass end of PDMFs ($\geq 10\,\mathrm{M_\odot}$) on a linear scale where the size of the bump is more apparent: the higher the metallicity, i.e. the stronger the wind mass loss, the bigger the peak. Similarly, the flatter the mass function, i.e. the more high mass stars exist compared to lower mass stars, the bigger the peak. The number of stars in the highest-mass bin of the 3 Myr mass function is increased compared to the IMF by 127% for $\Gamma = -1.35$ and
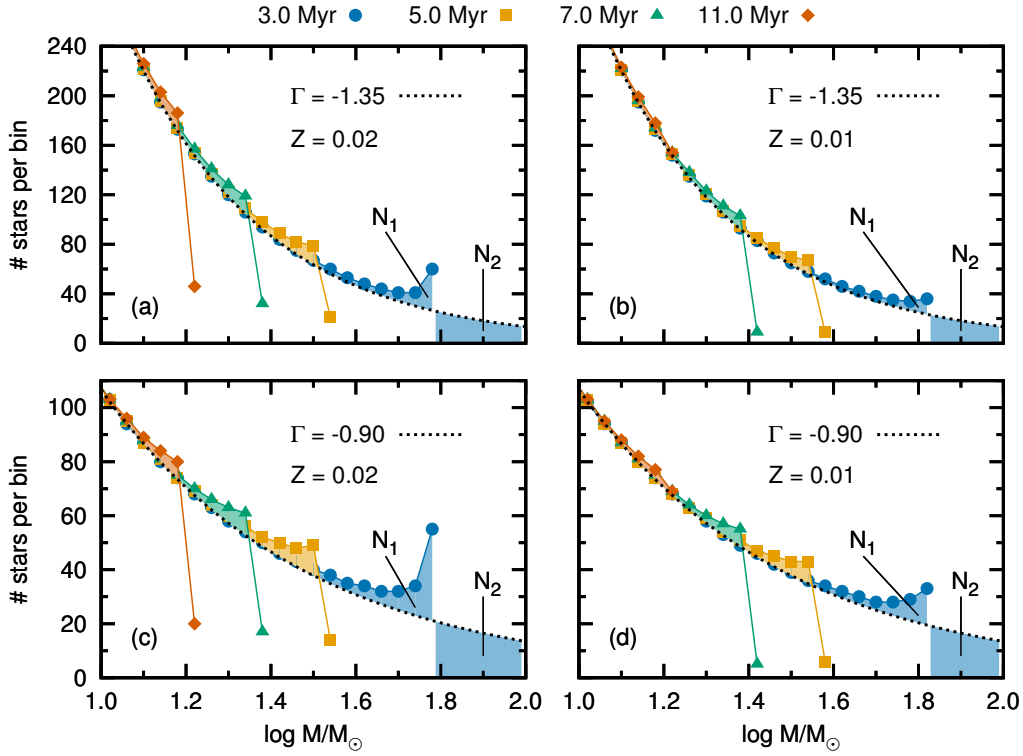
Figure 2.6: High mass end ($\geq 10\,\mathrm{M}_\odot$) of mass functions of coeval stellar populations with IMF slopes Γ and metallicities Z. The panels show (a) a population drawn from a Salpeter IMF $\Gamma = -1.35$ at solar metallicity $Z = 0.02$, (b) as (a) with $Z = 0.01$, (c) as (a) with $\Gamma = -0.9$ and (d) as (c) with $Z = 0.01$. The black dotted line shows the IMF and the filled regions labelled N_1 indicate the accumulation of stars because of stellar wind mass loss at an age of $3\,\mathrm{Myr}$. Because the area labelled N_1 contains those stars that depopulated the mass function for masses beyond the mass function peak, it contains the same number of stars as the area labelled N_2. The wind mass loss peaks are stronger the flatter, i.e. the more positive, the IMF slope and the stronger the wind mass loss (i.e. the higher the metallicity).

by 162% for $\Gamma = -0.9$ at a metallicity $Z = 0.02$ and by about 55% for $\Gamma = -1.35$ and 70% for $\Gamma = -0.9$ at $Z = 0.01$.

The wind mass loss peak allows us to determine the overall mass lost by stars during their main-sequence evolution. In practice, it may be necessary to model luminosity functions rather than mass functions with different mass loss recipes to match observed luminosity functions. Only by doing so can one overcome the inherent problem that masses derived from observed luminosities rely implicitly on the mass loss prescription used to derive the applied mass-luminosity relations.

Figures 2.5 and 2.6 show that the wind mass loss peak is only visible in sufficiently young clusters in which stellar winds are strong. We now investigate the age and metallicity range of stellar populations whose mass functions are likely to show the wind mass loss peak. Let $M_{\mathrm{to,p}}$ be the present-day turn-off mass in the star cluster and N_1 the number of excess stars in the peak compared to the initial mass function which is a power-law with slope Γ (Eq. 2.4). We can then redistribute these stars such that the peak is removed by filling up the IMF from the top end, thereby obtaining the initial mass of the turn-off stars, $M_{\mathrm{to,i}}$. Let ΔM be the mass lost by turn-off stars over their main-sequence evolution, i.e. $\Delta M = M_{\mathrm{to,i}} - M_{\mathrm{to,p}}$. Because the
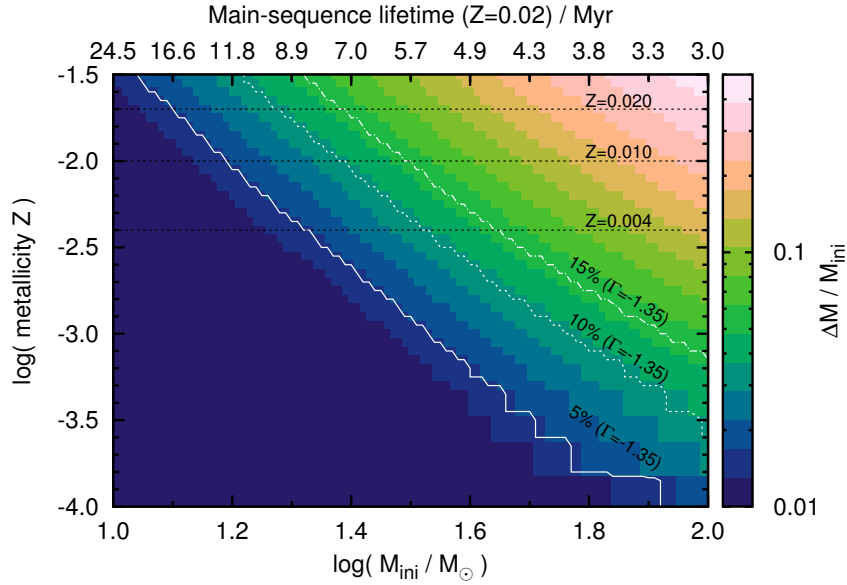
Figure 2.7: Fractional initial mass loss, $\Delta M/M_{\mathrm{ini}}$, of stars during the main-sequence as a function of initial mass and metallicity Z. The solid and dotted lines show the criterion of the visibility of the wind mass loss peak in mass functions from Eq. (2.11) for $N_1/N_{\mathrm{imf}} = 5\%$, 10% and 15%, respectively, and an IMF slope of $\Gamma = -1.35$. According to our criterion, a wind mass loss peak is likely visible in stellar populations to the right of the solid, 10% line (see text for more details).

number of excess stars N_1 equals the number of stars N_2 between $M_{\mathrm{to,p}}$ (Fig. 2.6), we have,

$$
\begin{aligned}
N_1 = N_2 &= \int_{M_{\mathrm{to,p}}}^{M_{\mathrm{to,p}}+\Delta M} \psi(M)\,\mathrm{d}M = N_2 \\
&= \tfrac{A}{\Gamma} M_{\mathrm{to,p}}^{\Gamma} \left[\left(1 + \tfrac{\Delta M}{M_{\mathrm{to,p}}}\right)^{\Gamma} - 1 \right].
\end{aligned}
\tag{2.10}
$$

To judge whether the accumulation of N_1 stars is enough to see a wind mass loss peak, we have to compare N_1 to the number of stars expected from the IMF in a mass range that is slightly less massive than the turn-off, N_{imf}. We define N_{imf} to be the number of stars in the mass range from $fM_{\mathrm{to,p}}$ to $M_{\mathrm{to,p}}$ where $f < 1$. For $f = 0.75$, we require that N_1 has to exceed 10% of N_{imf} to be able to see the wind mass loss peak. The 10% requirement and the value for f are chosen such that a visible wind mass loss peak is predicted in the 7 Myr but not 11 Myr stellar populations at $Z = 0.01$ and $Z = 0.02$ (cf. Fig. 2.6). Analogously to Eq. (2.10), we compute N_{imf} and find that,

$$
\frac{N_1}{N_{\mathrm{imf}}} = \frac{(1 + \Delta M/M_{\mathrm{to,p}})^{\Gamma} - 1}{1 - f^{\Gamma}} > 10\% \text{ for } f = 0.75
\tag{2.11}
$$

in order for the wind mass loss peak to be visible. This criterion translates into a relative wind mass loss of,

$$
\frac{\Delta M}{M_{\mathrm{to,p}}} \geq \left[\frac{N_1}{N_{\mathrm{imf}}} \left(1 - f^{\Gamma}\right) + 1 \right]^{1/\Gamma} - 1.
\tag{2.12}
$$

According to our criterion, the minimum relative mass loss is 3.7% for $\Gamma = -1.35$ and 3.3% for $\Gamma = -0.7$.

In Fig. 2.7, we show how much mass is lost by stars through stellar winds during their main-sequence evolution as a function of initial mass and metallicity. We further indicate the corresponding main-sequence lifetimes for $Z = 0.02$ on the top and plot the criterion from Eq. 2.11 for $N_1/N_{\mathrm{imf}} = 5\%$, 10% and 15%. The mass functions of stellar populations of ages and metallicities to the right of the $N_1/N_{\mathrm{imf}} = 10\%$ line are likely to show the wind mass loss peak. As a rule of thumb, the mass functions of stellar populations younger than about 10 Myr at $Z = 0.02$ are likely to show a visible wind mass loss peak. Note that our criterion is a rather rough estimate and depends on the wind mass loss prescription and its metallicity scaling.

2.3.2 Binary star populations

Two processes additionally influence the mass functions of binary star populations compared to those of single stars. First, stars can merge during their evolution and, second, stars can accrete mass by RLOF. In what follows we discuss three different mass functions to disentangle these effects: we present mass functions of primary stars, of secondary stars and those constructed from the mass-luminosity inversion method (observed mass functions) as discussed in Sec. 2.2.4.

The primary star is initially more massive than the secondary star, so it evolves faster and is the donor star during RLOF. Analogously, the secondary star is the mass gainer. In the top panel of Fig. 2.8 we show the mass functions of primary stars, i.e. stars that have not yet interacted, that have lost mass by mass transfer or that have merged. The mass functions in the middle panel of Fig. 2.8 show secondary stars that have not interacted yet and that have gained mass by RLOF. The observed mass function in the bottom panel of Fig. 2.8 is a combination of all stellar evolutionary effects.

The primary stars are initially distributed according to the Salpeter IMF (Eq. 2.4) and the secondary stars according to

$$
\begin{aligned}
\frac{\mathrm{d}p}{\mathrm{d}\ln m_2} &= \int_{\ln m_2}^{\ln 100} \psi(\ln m_1)\phi(\ln m_2)\, \mathrm{d}\ln m_1 \cdot \underbrace{\int_{\ln a} \chi(\ln a)\, \mathrm{d}\ln a}_{=1} \\
&\approx \frac{A}{\Gamma - 1} m_2 \left(100^{\Gamma-1} - m_2^{\Gamma-1} \right),
\end{aligned}
\tag{2.13}
$$

where $\psi(\ln m_1)$, $\phi(\ln m_2)$ and $\chi(\ln a)$ are the initial distribution functions of the primary and secondary masses and the orbital separations as defined in Sec. 2.2.2 (we assume $q_{\min} \approx 0.0$ in the last step). Compared to the IMF of primary stars, the initial mass distribution of secondary stars is lowered by a factor $(1-\Gamma)^{-1}$ (≈ 0.43). The decline of the secondary initial mass function at the high mass end is caused by the maximum initial mass (cf. the first term on the right-hand side of Eq. 2.13: the maximum initial mass in our calculations is $100\,\mathrm{M}_\odot$). The overall slope is $\Gamma = -1.35$ again because of the flat mass ratio distribution.

In single stars, no star is more massive than the turn-off. Including binary stars it is possible to populate a tail of stars that extends the high mass end of single star PDMFs by about a factor of two in mass.

In the top panel of Fig. 2.8 only stellar mergers populate the PDMF tail (i.e. the PDMF on the right-hand side of the vertical dashed lines). The relative number of mergers in the tail is lower the older the population as expected from our analysis of the binary parameter space in which the fraction of binary stars that merge on the MS increases with the initial mass of the primary star (Fig. 2.4).
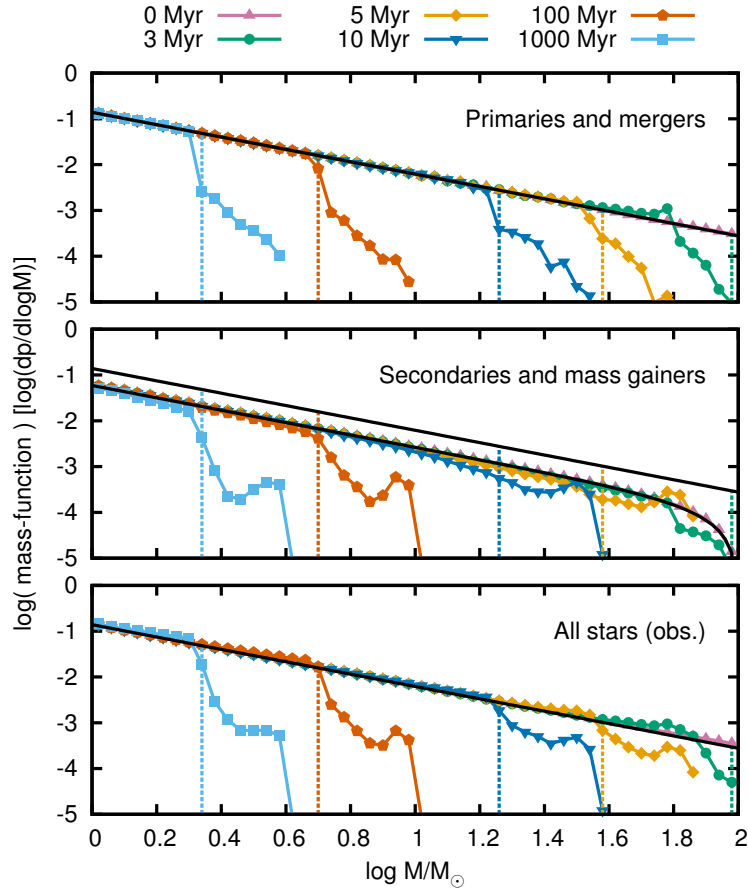
Figure 2.8: Temporal evolution of PDMFs of all primary stars and mergers (top panel), all secondary stars (middle panel) and for observed masses for all stars (bottom panel; see Sec. 2.2.4). By construction, merged stars appear in the PDMFs in the top panel and mass gainers of RLOF in the PDMFs in the middle panel. The vertical dashed lines indicate the mass of stars having a MS lifetime equal to the age of the population, i.e. they indicate the initial mass of the turn-off stars. Contrary to a population made only of single stars, stars more massive than the initial mass of the turn-off stars exist. The black solid lines are the Salpeter IMF and the initial distribution function of the secondary stars (Eq. 2.13) respectively.

The maximum mass of stellar mergers is reached by initially equal-mass binaries in which the final mass is the total mass of the binary minus a fraction of 10% that we assume is lost during a merger (Sec. 2.2.1). This corresponds to a mass increase by a factor of 1.8 or a shift of about 0.26 dex on the logarithmic mass scale. The PDMF at 10 Myr extends slightly further because of the rejuvenation of the merged stars. The mass of the merged star is not increased by more than a factor of 1.8 relative to the primary mass, but fresh hydrogen is mixed into its core. This decreases the fraction of burnt fuel and hence the apparent age of the star. Compared to genuine single stars of comparable mass, i.e. stars which have not interacted, the stellar merger has more available fuel and thus stays longer on the MS. Rejuvenated stars can thus appear to be shifted by more than 0.26 dex because the turn-off mass decreases simultaneously.

The PDMF tails in the middle panel of Fig. 2.8 contain secondary stars that have accreted mass. The PDMFs again extend to slightly larger masses than expected from mass accretion

alone because of rejuvenation. Mass accretion in young stellar populations (ages $\lesssim 10\,\mathrm{Myr}$) forms PDMF tails that even exceed the initial distribution of the secondary stars. At later times, the relative number of stars in the tail is less because the number of interacting binaries that transfer mass stably by RLOF decreases for initially less massive primary stars (Fig. 2.4) as does the overall mass transfer efficiency, β, which is coupled to the thermal timescale of the mass gainers during Case B mass transfer. The thermal timescales of stars become more comparable for larger masses because the mass-luminosity and mass-radius relations are less steep the larger the mass.

In populations younger than $3.0\,\mathrm{Myr}$, the effect of mass accretion on the PDMF is modest because the most massive stars in our models have just left the MS and hence there is no contribution from Case B mass transfer to the PDMF (Case C does not occur for primary masses larger than about $22\,\mathrm{M_\odot}$, see Sec. 2.2.3). The number of interacting binaries drops strongly for primary masses larger than about $50\,\mathrm{M_\odot}$ because of the Humphreys-Davidson limit (Sec. 2.2.3). This is important in stellar populations younger than $\sim 4.3\,\mathrm{Myr}$ which is the MS lifetime of $50\,\mathrm{M_\odot}$ stars in our models.

In the bottom panel of Fig. 2.8 we use the mass-luminosity inversion method (approach 3 in Sec. 2.2.4) to construct the PDMFs. Both, mergers and accretors show up in the PDMF tails. The star with the highest mass in each population is formed by RLOF. However, the difference between the highest mass achieved by stellar mergers and by RLOF is small — at most one bin-width, i.e. $\Delta \log m = 0.04\,\mathrm{dex}$ — and depends on the assumed mass loss in stellar mergers and the mass transfer efficiency. Only at early times ($\lesssim 3.5\,\mathrm{Myr}$) does the star with the highest mass originate in a stellar merger. Unresolved binaries also contribute to the tail of the observed PDMFs but their contribution is small (at most 30% of the tail stars are unresolved binaries in young, $\lesssim 3$–$4\,\mathrm{Myr}$ populations) and greatest for the largest masses because of a flatter mass-luminosity relation of high mass stars compared to lower masses. Unresolved binaries extend the single star mass function by at most $\sim 20\%$ in mass for $1\ldots 2\,\mathrm{M_\odot}$ stars and by at most $\sim 50\%$ in mass for $60\ldots 100\,\mathrm{M_\odot}$ stars (cf. Eq. 2.15 in Sec. 2.3.4).

In Fig. 2.9 we show the PDMF of secondary stars at three different times — 5, 20 and $100\,\mathrm{Myr}$. Case B mass transfer is the dominant contribution after $3\,\mathrm{Myr}$, therefore the mass losing star has left the MS and is no longer included in the PDMFs of the primary stars in the top panel of Fig. 2.8. The Case A mass losers are difficult to find. Nevertheless some of them can be found by comparing the PDMFs of populations of single (Fig. 2.5) and binary stars only (top panel of Fig. 2.8). The mass losers are easiest to spot by the difference in the magnitude of the accumulation of stars because of wind mass loss e.g. in the PDMFs of the $5\,\mathrm{Myr}$ old populations. Populations made only of single stars show a larger accumulation of stars than those made of binary stars, because some donor stars that would appear in the wind mass loss peak lose additional mass during Case A mass transfer. In practice it is very hard to detect the primaries after they have lost mass (de Mink et al. 2014).

Case C mass transfer is typically highly non-conservative in our models (Sec. 2.2.3 and Appendix 2.7.1). The secondary stars of such systems therefore do not gain enough mass to make any significant contribution to the tail.

The stars in the tail of the mass functions are rejuvenated binary products and hence appear younger than the real age of the population — they are blue stragglers. We further characterise these blue straggler stars in Sec. 2.4 in terms of their binary fraction and apparent ages and compare their frequencies to observations.
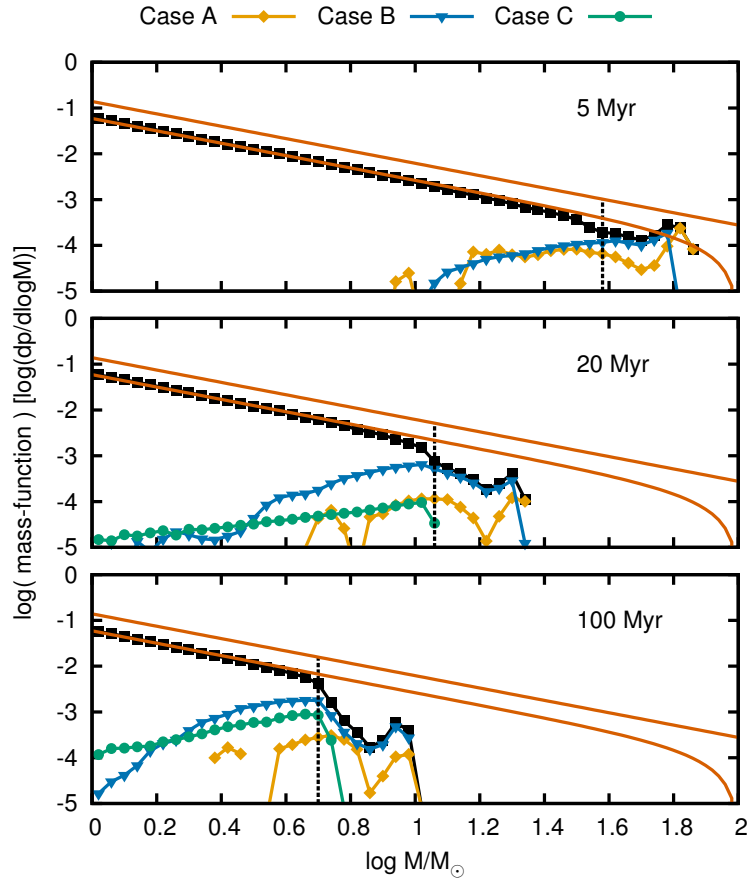
Figure 2.9: Mass functions at 5, 20 and 100 Myr for secondary stars, i.e. mass accretors. The curves show the contributions of the mass transfer Cases A, B and C (as defined in Sec. 2.2.1) to the total PDMF of secondaries (black squares). Case B mass transfer is the dominant contribution to the tail stars for $\gtrsim 3\,\mathrm{Myr}$, hence the mass loser is not a MS star and therefore not present in the PDMFs of primaries in the top panel of Fig. 2.8. This is why the mass gainers are seen clearly in the PDMFs whereas the mass losers are not.

2.3.3 Stellar populations with varying binary fractions

We use the PDMFs of populations of single and binary stars presented in Secs. 2.3.1 and 2.3.2 to build stellar populations composed of a mixture of coeval single and binary stars. Let f_B be the binary fraction at birth, i.e. the number of binary systems divided by the number of total stellar systems ($f_\mathrm{B} = N_\mathrm{B}/[N_\mathrm{S} + N_\mathrm{B}]$ with N_B the number of binary systems and N_S the number of single stars). The considered binaries have initial orbital separations shorter than $10^4\,\mathrm{R_\odot}$ — initially wider binaries are treated as single stars in our models (Sec. 2.2.2). The mass function of a population with this binary fraction is then,

$$\frac{\mathrm{d}p}{\mathrm{d}\log m} = (1 - f_\mathrm{B}) \cdot \left(\frac{\mathrm{d}p}{\mathrm{d}\log m}\right)_\mathrm{s} + f_\mathrm{B} \cdot \left(\frac{\mathrm{d}p}{\mathrm{d}\log m}\right)_\mathrm{b}. \tag{2.14}$$

Here $(\mathrm{d}p/\mathrm{d}\log m)_\mathrm{s}$ is the mass function of single stars only and correspondingly $(\mathrm{d}p/\mathrm{d}\log m)_\mathrm{b}$ is the mass function of binary stars only. In Fig. 2.10 we show the observed mass functions of stellar populations with a primordial binary fraction of $f_\mathrm{B} = 0.5$ (i.e. two out of three stars
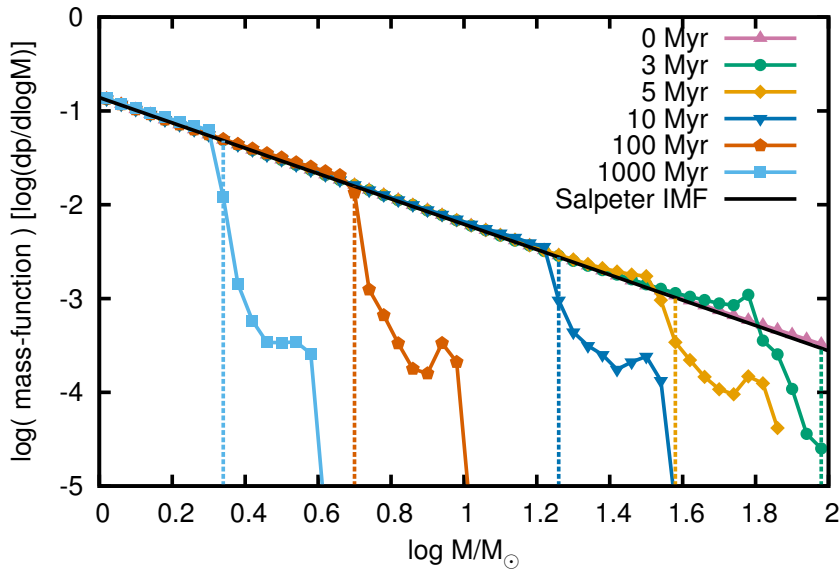
Figure 2.10: As the bottom panel of Fig. 2.8, but for a population of stars with a primordial binary fraction of $f_B = 0.5$. As discussed in Sec. 2.3.3 the number of stars in the binary tails are halved compared to a pure binary star population.

initially born in binaries). In comparison to Fig. 2.8, the number of stars in the binary tail in the PDMFs (Sec. 2.3.2) is attenuated. The tail of the mass functions of stellar populations with a binary fraction of 50% is decreased by 0.3 dex, i.e. by a factor of two, compared to those with a binary fraction of 100%.

2.3.4 Quantification of evolutionary effects on the PDMF

The stellar wind mass-loss peak at the high mass end flattens the mass function. We quantify the flattening by computing the PDMF slopes as a function of stellar mass. We fit straight lines piecewise to three mass bins at a time by a Levenberg-Marquardt method (Levenberg 1944; Marquardt 1963) and show the slopes β of the *single star* PDMFs in Fig. 2.11. The errors are statistical 1σ deviations from the best fit. The more massive a star the more mass is lost by stellar winds, hence the accumulation and resulting flattening of the PDMF is strongest in the 3 Myr population. The slope at the high mass end of the mass function of young stellar populations ($\lesssim 10$ Myr) is much shallower than the Salpeter IMF, $\Gamma = -1.35$. We find extremes of the PDMF slope of $\beta \approx -0.45 \pm 0.20$ at the highest masses around $50 \, M_\odot$ ($\log M/M_\odot \approx 1.7$ dex) in the 3 Myr population. The flattening is still significant for 10 Myr populations at masses more than $10 \, M_\odot$ for which the slope flattens to values of up to $\beta \approx -0.95 \pm 0.09$. In other words, not accounting for wind mass loss when determining the slope of the IMF for the most massive stars may lead to IMF slopes that are biased by up to 1 dex.

We further quantify the wind mass loss peak and the binary tail by dividing the PDMFs of populations consisting purely of single stars, purely of binary stars and of a mixture of single and binary stars by the initial distribution functions (Eqs. 2.4 and 2.13) in order to determine the relative importance of the evolutionary effects compared to the initial distribution of stellar systems. First, we construct PDMFs from the theoretically known stellar masses and not using the mass-luminosity inversion method and show the ratio of PDMF to IMF in Fig. 2.12. This
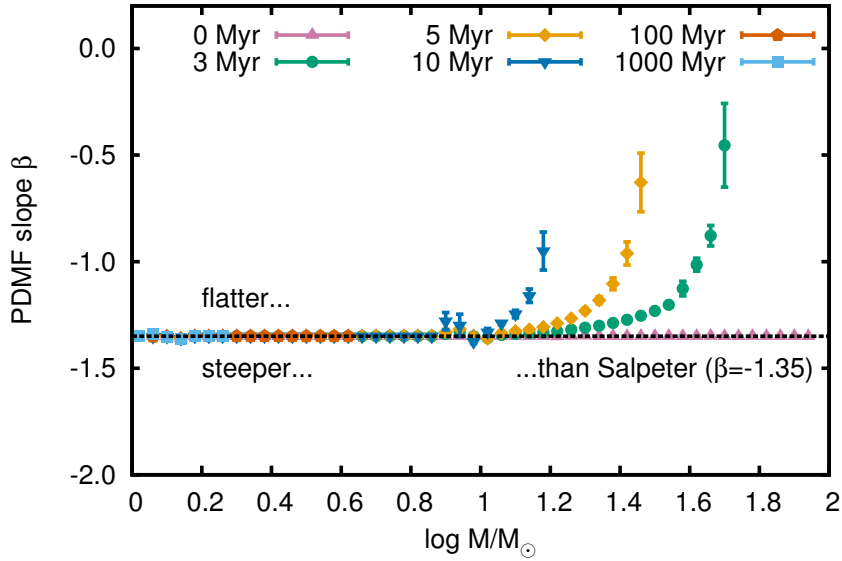
Figure 2.11: Slopes of the PDMF of single stars (Sec. 2.3.1) as a function of logarithmic mass. Stellar wind mass loss flattens the high mass end of the PDMFs.

enables us to distinguish between the effects of single and binary star physics and of unresolved binaries on the PDMF. Again, the truncations of the PDMFs are due to finite stellar lifetimes.

The PDMF of the 5 Myr single star population reaches a level of more than 120% of the IMF because of an accumulation of stars caused by wind mass loss (blue solid line close to the turn-off mass of $\log m \approx 1.5\,\mathrm{dex}$). The wind mass loss peak becomes weaker with age until it completely disappears in stellar populations older than 30 Myr (at a metallicity of $Z = 0.02$ with a Salpeter IMF; see also Sec. 2.3.1).

Stellar mergers and mass transfer by RLOF shift stars towards higher masses. The number of stars that are slightly less massive than the turn-off stars is therefore less than the initial number of stars, i.e. PDMF/IMF < 1 (with no wind mass loss). The tail of the 5 Myr binary population reaches an average level of more than 30% of the initial distribution function, i.e. on average about one third of the IMF in a mass range from about $40\,\mathrm{M_\odot}$ ($\log m \approx 1.6\,\mathrm{dex}$) to $80\,\mathrm{M_\odot}$ ($\log m \approx 1.9\,\mathrm{dex}$) is re-populated by binary evolution. This level gradually decreases the older the population and the smaller the binary fraction.

Being unable to resolve binaries shifts the observed mass function to larger masses (Fig. 2.13). This is well known (Sagar & Richtler 1991; Kroupa et al. 1993; Maíz Apellániz 2008; Weidner et al. 2009) and is evident from the initial mass distribution of pure binary star populations (0 Myr binary population in Fig. 2.13). In a single star population there is no difference between the observed initial mass function and the Salpeter IMF. With unresolved binaries, the PDMF exceeds the IMF and the ratio of PDMF to IMF increases with larger binary fractions. In stellar populations with $f_{\mathrm{B}} = 0.5$ there are $5 - 10\%$ more stellar systems than expected from the Salpeter IMF and up to $\sim 20\%$ more for pure binary populations ($f_{\mathrm{B}} = 1$). The increase is mass dependent: it is greater for larger masses and is understood from the mass-luminosity relation, which can be approximated as $L = L_0 M^x$. In unresolved binaries with equal masses
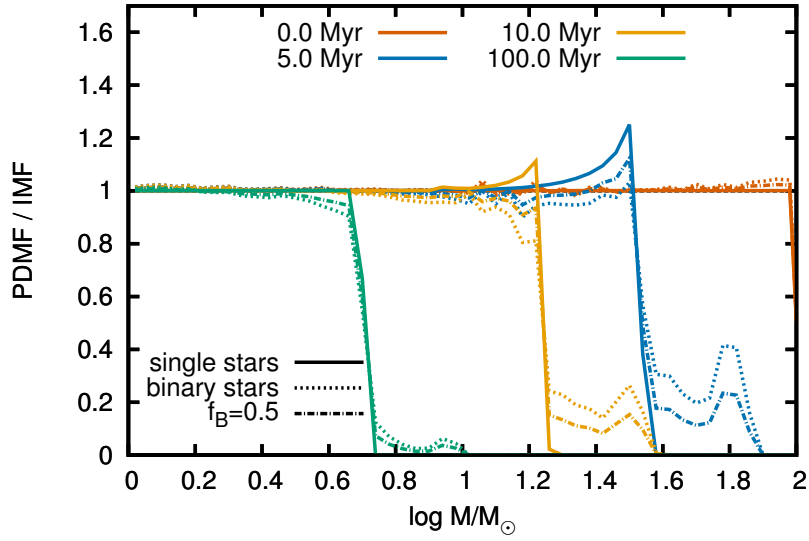
Figure 2.12: Ratio of the PDMFs to IMFs for different ages and primordial binary fractions. The PDMFs are constructed from the known stellar masses (approaches 1 and 2 in Sec. 2.2.4).
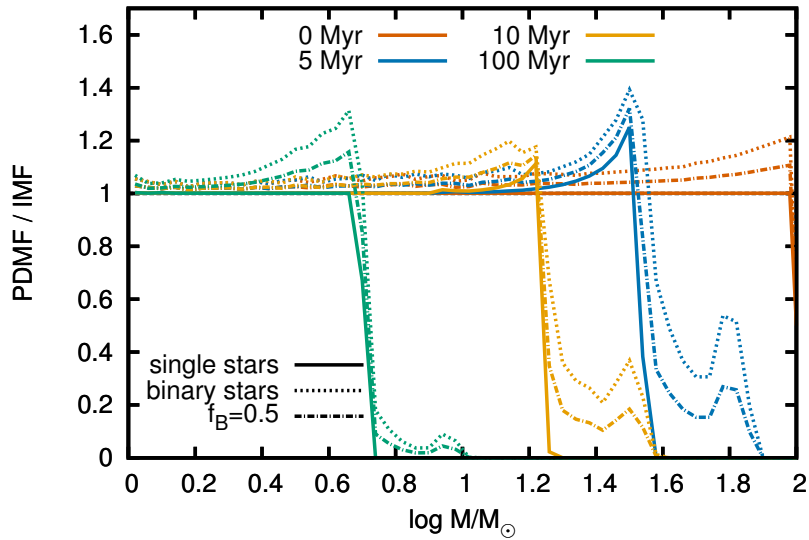
Figure 2.13: As Fig. 2.12 but constructed using the mass-luminosity inversion method (approach 3 in Sec. 2.2.4).

M the observed mass M_{obs} is

$$M_{\mathrm{obs}} = \left(\frac{L_1 + L_1}{L_0}\right)^{1/x} = 2^{1/x}M, \tag{2.15}$$

i.e. larger than M by a factor of $2^{1/x}$. Low mass stars have a larger exponent x than high mass stars, hence the larger the mass M the larger the factor by which the observed mass is increased (e.g. $L \propto M^{4.5}$ for $1 \leq M/\mathrm{M}_\odot \leq 2$ and $L \propto M^{1.8}$ for $60 \leq M/\mathrm{M}_\odot \leq 100$ zero age main sequence stars, Tout et al. 1996). This translates into an increase of the mass function by a factor of

$$\frac{\psi(\ln M)}{\psi(\ln M_{\mathrm{obs}})} = 2^{-\Gamma/x} = 1.23\ldots1.68, \tag{2.16}$$

where Γ is the IMF slope. Unresolved binaries flatten the PDMF most strongly at the largest stellar masses (under the assumption that Γ is constant in the considered mass range). We discuss the effect of unresolved binaries on mass functions with respect to previous work in more detail in Appendix 2.7.3.

Figure 2.13 shows that unresolved binaries flatten the PDMF at masses less than the turn-off mass instead of steepening the PDMF as was the case for resolved binaries. The wind mass-loss peaks in the PDMF reach a level of up to $\sim 140\%$ of the IMF. The tail of the $5\,\mathrm{Myr}$ binary population is re-populated by on average $\gtrsim 40\%$ and with maximum levels of about 55% of the IMF. The number of stars in the binary tail is halved in populations with a binary fraction of $f_{\mathrm{B}} = 0.5$.

We have shown above that stellar wind mass loss, binary products and unresolved binaries re-shape the high mass end of mass functions which may complicate IMF determinations. To avoid biased IMF slope determinations in young as well as old clusters, we suggest to either exclude those parts of the mass function that are expected to be affected by stellar winds, binary products and/or unresolved binaries or to correct for these effects. As evident from Fig. 2.13, this concerns roughly the mass ranges from 0.5–0.6 to twice the turn-off mass in our models (about $\pm 0.3\,\mathrm{dex}$ around the turn-off).

2.4 Blue straggler stars

The stars in the tail of mass functions are mainly rejuvenated binary products — they are classical blue straggler stars. We define a blue straggler as a star whose mass is larger than that of the turn-off stars. This definition does not include all blue stragglers because there are also rejuvenated binary products that are less massive than the turn-off. In the following sections we characterise the blue straggler stars in the binary tail and make predictions about their frequencies, binary fractions and ages as a function of cluster age and compare to observations to test our predictions and to finally improve our understanding of binary evolution.

Because our stellar evolution code cannot evolve stars more massive than $100\,\mathrm{M}_\odot$ (Sec. 2.2.1), boundary effects for ages $\lesssim 3\,\mathrm{Myr}$ are expected. This age range is indicated by hatched regions in Figs. 2.14, 2.15 and 2.16.

2.4.1 Expected and observed blue straggler star frequencies

Blue straggler stars and their frequencies have been investigated in the past using population synthesis calculations including binary stars (e.g. Collier & Jenkins 1984; Pols & Marinus 1994;

van Bever & Vanbeveren 1998; Hurley et al. 2001, 2005; Chen & Han 2009; Chatterjee et al. 2013). Qualitatively, population synthesis calculations show that binary star evolution forms stars that appear as blue stragglers in colour magnitude diagrams through binary mass transfer and mergers. Quantitatively however, the picture is more complicated. Some models predict blue straggler frequencies in agreement with observations (e.g. Collier & Jenkins 1984; Pols & Marinus 1994; Hurley et al. 2001, 2005; Chatterjee et al. 2013) while others disagree (e.g. Chen & Han 2009; Geller et al. 2013). This problem is not yet fully resolved.

Ahumada & Lapasset (2007) present a catalogue of blue stragglers in Galactic open star clusters of various ages. They count the number of blue straggler stars and the number of stars down to two magnitudes below the turn-off based on colour-magnitude diagrams. This is a complicated task because of observational uncertainties such as field contamination. In addition, the turn-off and age of the cluster are uncertain, in particular for the younger cluster where only a few stars define the turn-off.

In our models, the number of blue stragglers, N_{bss}, is given by the number of stars more massive than the turn-off mass. The number of stars two magnitudes below the turn-off, N_2, is computed from the number of stars with luminosities in the range $10^{-5/4} L_{\mathrm{to}}$ to L_{to}, where L_{to} is the turn-off luminosity (the factor $10^{-5/4}$ corresponds to two magnitudes).

Sills et al. (2013) show that the number of blue straggler stars selected from their position in an observed HR diagram following the prescription of Leigh et al. (2011) can be less by a factor of about two than the number of blue stragglers selected from models based on stellar masses. The reason for the difference is that the criteria of Leigh et al. (2011) that are used to identify blue stragglers observationally in an HR diagram of a modelled star cluster do not cover all blue stragglers produced in that model (cf. Fig. 1 of Sills et al. 2013). Ahumada & Lapasset (2007) identify blue stragglers differently in HR diagrams. They count stars as blue stragglers that lie between the ZAMS and an isochrone appropriate for the cluster. It is therefore likely that the number of observationally and theoretically identified blue stragglers do not differ by a factor of two in our case — we expect the difference to be smaller but can not rule out systematic differences. Sills et al. (2013) further show that there is a strong correlation between the number of observationally and theoretically identified blue stragglers such that the relative number of blue straggler stars as a function of cluster age may be compared directly.

From the catalogue of Ahumada & Lapasset (2007), we put the number of blue straggler stars, N_{bss}, and stars down to two magnitudes below the turn-off, N_2, in age bins of size 0.25 dex and plot the ratio N_{bss}/N_2 as a function of cluster age in Fig. 2.14. Additionally, we show the individual datapoints for every cluster and our model predictions. In some clusters, no blue straggler star is found. These clusters are not visible on the logarithmic scale used in Fig. 2.14 but do contribute to the binned data.

In our models, the ratio N_{bss}/N_2 decreases in older populations. Binary evolution is more efficient in producing blue stragglers in high mass, young binaries than in low mass, old binaries. This is because the number of binaries that produce blue straggler stars by MS mergers and by stable mass transfer, i.e. the number of binaries that do *not* go through a common envelope phase, is larger in high mass than in low mass binaries (cf. Figs. 2.4 and 2.17–2.22). The peak in the predicted ratio N_{bss}/N_2 around 10 Myr ($\log \tau_{\mathrm{cl}}/\mathrm{yr} = 7$) is due to a change in the distribution functions of the initial orbital periods from Öpik's law to the results of Sana et al. (2012) for O-star binaries (Sec. 2.2.2). The orbital period distribution of Sana et al. (2012) favours tight over wide binaries more than Öpik's law does and thus binaries that form massive blue straggler stars.

A similar decreasing blue straggler ratio N_{bss}/N_2 in older clusters is predicted from binary
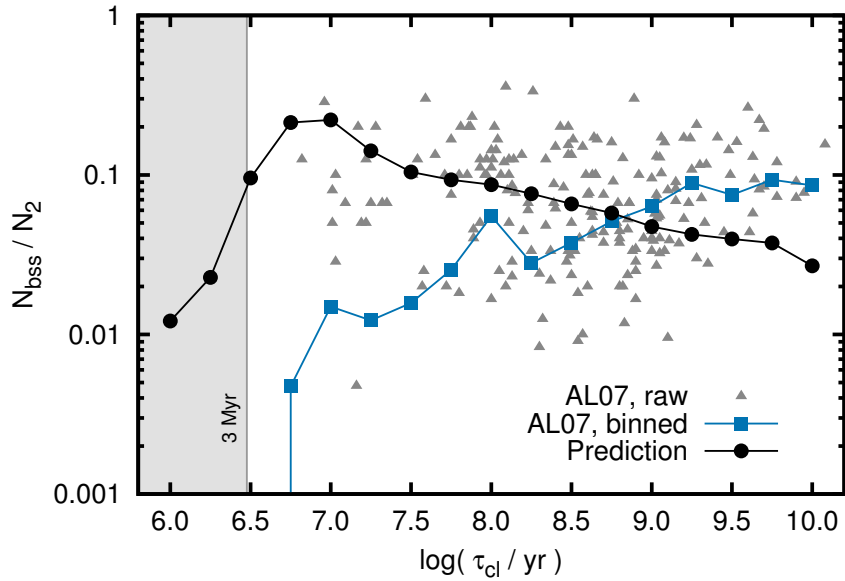
Figure 2.14: Ratio of the number of blue straggler stars, N_{bss}, to the number of stars two magnitudes below the turn-off, N_2, as a function of cluster age, τ_{cl}. The raw observational data for each Galactic open cluster of the blue straggler catalogue of Ahumada & Lapasset (2007), AL07, is given by the grey triangles, while the same data binned by cluster age is given by blue squares. Note that no blue straggler is found in 66% of the clusters younger than 500 Myr. These clusters are not on the logarithmic scale but cause the decreasing blue straggler frequency of the binned observational data with younger cluster ages. Our model predictions are overlayed in black dots. The grey regions indicate ages for which boundary effects play a role.

evolution calculations by Chen & Han (2009) but our ratios are larger by factors of 3–5. Chen & Han notice a similar difference (of a factor of at most two) between their predicted blue straggler frequencies and those computed with the population synthesis code of Hurley et al. (2002). Chen & Han find that the difference is related to how they treat binaries in counting the number of stars two magnitudes below the turn-off. We count each binary as one stellar system because binaries are unresolved in the colour-magnitude diagrams from which the observed blue straggler frequencies are deduced. We notice another difference that might explain the discrepancy: we use a maximum initial orbital separation of $10^4 \, R_\odot$ while Chen & Han (2009) use $5.75 \times 10^6 \, R_\odot$. Hence, our models contain more interacting binaries (cf. Fig. 2.4) that can form blue straggler stars. In other words, our effective binary fraction is larger.

The observations indicate an opposite trend to our models: the ratio N_{bss}/N_2 increases with cluster age. There are complications that render a direct comparison between the observed and our predicted ratio N_{bss}/N_2 difficult. There exist two classes of star clusters in the catalogue of Ahumada & Lapasset (2007): clusters with and without blue straggler stars. The bi-modality is mainly found in clusters younger than about 500 Myr. There is no blue straggler star in 3% of their star clusters older than 500 Myr, in 38% of star clusters with ages between 100 Myr and 500 Myr and in 80% of star clusters younger than 100 Myr. This bi-modality is not understood but causes the observed decreasing blue straggler frequency with younger cluster ages.

Stochastic sampling (Schneider et al. 2014b and Appendix 2.7.4), i.e. lower number statistics in young clusters compared to older clusters because of the IMF, cannot explain this bi-modality. Stochastic sampling is expected to increase the scatter between the blue straggler frequencies of

clusters of similar ages but not to create a bi-modal distribution. However, stochastic sampling may possibly complicate the accurate determination of the turn-off.

Supernova kicks (e.g. Lai 2001) might be part of the solution to this discrepancy. The binary companion of a blue straggler star that formed by RLOF, i.e. the former mass donor, will explode if it is massive enough to undergo core collapse. The supernova can break up the binary such that the blue straggler leaves the cluster as a runaway star, thereby reducing the number of blue stragglers observed in the cluster. Some clusters might lose all their blue stragglers in this way, giving rise to the observed bi-modality. The observed bi-modality is found in star clusters younger than $500\,\mathrm{Myr}$. However, supernova explosions occur only in young star clusters ($\lesssim 40$–$50\,\mathrm{Myr}$) with massive stars ($\gtrsim 7$–$8\,\mathrm{M}_\odot$). Supernova kicks can therefore explain only part of the discrepancy.

The primordial binary fraction in our models is 100%. A smaller binary fraction linearly decreases the number of blue stragglers and hence the ratio N_{bss}/N_2. Our predictions are therefore likely upper limits, implying that our models underpredict the observed blue straggler frequencies in $\gtrsim 100\,\mathrm{Myr}$ star clusters and that additional channels for the formation of blue stragglers are required. Geller & Mathieu (2011) find carbon-oxygen white dwarfs as companions to blue stragglers in NGC 188. The white dwarf mass and period distributions appear to be consistent with a Case C RLOF formation scenario in which an asymptotic giant branch star transfers mass to a MS star. In our models, RLOF from giants typically leads to common envelope evolution and thus not to the formation of blue stragglers. However, Chen & Han (2008) show that Case B and C mass transfer from giants to MS stars can form blue stragglers. Dynamical cluster evolution also produces blue stragglers in stellar collisions (e.g. Geller et al. 2013) and is expected to be more efficient the higher the density of the star cluster (e.g. Chatterjee et al. 2013). Another form of mass transfer, wind Roche lobe overflow from asymptotic giant branch stars, might be efficient enough to also form blue straggler stars (e.g. Mohamed & Podsiadlowski 2007; Abate et al. 2013). All three contributions, the Case B and C formation scenarios, mergers due to collisions and wind RLOF, are missing in our predictions and might potentially help explaining the too low BSS predictions in $\gtrsim 100\,\mathrm{Myr}$ star clusters (see also Geller et al. 2013).

2.4.2 Binary fraction of blue straggler stars

A further testable prediction from our models is the binary fraction among blue straggler stars. The blue stragglers that form from stable mass transfer by RLOF can potentially be observed as binary stars whereas those that form from stellar mergers are observed as single stars. It is, however, difficult to observationally find the companions of blue stragglers that formed by stable mass transfer because the companions can be much fainter than the blue straggler (or even be a compact object) and the binary orbits are often wide such that most searches for radial velocity variations in blue stragglers cannot detect them (e.g. Collier & Jenkins 1984; Pols & Marinus 1994). The blue straggler binary might even be disrupted if the companion star explodes. In general, post-interaction binaries can often not be identified as such from radial velocity variations and mostly appear to be single stars (de Mink et al. 2014).

In our models, the binary fraction of blue straggler stars is independent of the primordial binary fraction in star clusters because only the sub-sample of primordial binaries can produce blue stragglers. The binary fraction among blue straggler stars is thus purely determined through binary evolution.

In Fig. 2.15 we show the binary fraction f_{B} of blue straggler and hence tail stars in our PDMFs
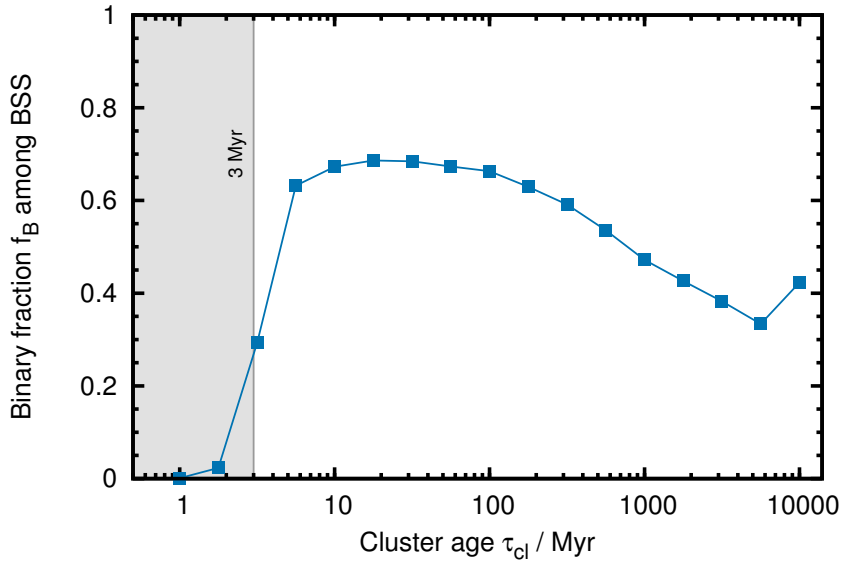
Figure 2.15: Binary fraction among blue straggler stars as a function of cluster age, τ_{cl}, corresponding to stars in the tail of our PDMFs. The given binary fractions are upper limits because we neglect supernova kicks that may disrupt binaries. The grey regions indicate ages for which boundary effects play a role.

as a function of cluster age. In our simulations we assume that all binaries with a mass ratio less than 0.56 merge at the onset of Roche lobe overflow during Case A mass transfer (Sec. 2.2.1), i.e. mass transfer from a MS star. Because of the assumed flat mass ratio distribution, at least 56% of all Case A binaries merge and are thus observed as single stars ($f_B \leq 44\%$). Our analysis of the binary parameter space (Figs. 2.17–2.22) reveals that more than 56% of all binaries merge during Case A mass transfer because even binaries with a mass ratio greater than 0.56 come into contact if they are initially in close orbits (e.g. Wellstein et al. 2001). In binaries younger than 2 Myr, only the primary stars of very short orbit binaries overfill their Roche lobes. Most of them, regardless of the mass ratio, merge, leading to binary fractions $\leq 10\%$. Later, the binary fraction increases with time because also binaries in initially wider orbits interact, producing blue straggler stars by stable Case A and B mass transfer without merging, i.e. leaving behind a blue straggler in a binary.

Case A mass transfer predominantly forms blue stragglers by merging in more than 56% of all Case A binaries in our simulations. Contrarily, Case B mass transfer purely creates blue straggler star binaries (neglecting binary disruption by supernova explosions). The binary fraction in Fig. 2.15 therefore reaches a maximum of ~ 60–70% and stays at this level after all Case B binaries have enough time to interact to contribute blue straggler binaries.

In our models, Case B mass transfer in binaries with primary stars more massive than $5\,M_\odot$ leads to fewer common envelope phases and consequently more blue stragglers than in binaries with less massive primary stars (cf. Case B regions of binaries with $2\,M_\odot$ and $5\,M_\odot$ primary stars in Figs. 2.17 and 2.18, respectively). The binary fraction of blue straggler stars therefore decreases in populations older than the lifetime of $5\,M_\odot$ stars, i.e. older than ~ 100 Myr, and is given by the fraction of stars that merge during Case A (and early Case B) mass transfer.

Our blue straggler star binary fractions are upper limits because we neglect supernova kicks that might disrupt binaries and because the companions might be hard to detect observationally. We exclude supernova kicks because they introduce a random process that can only be fully
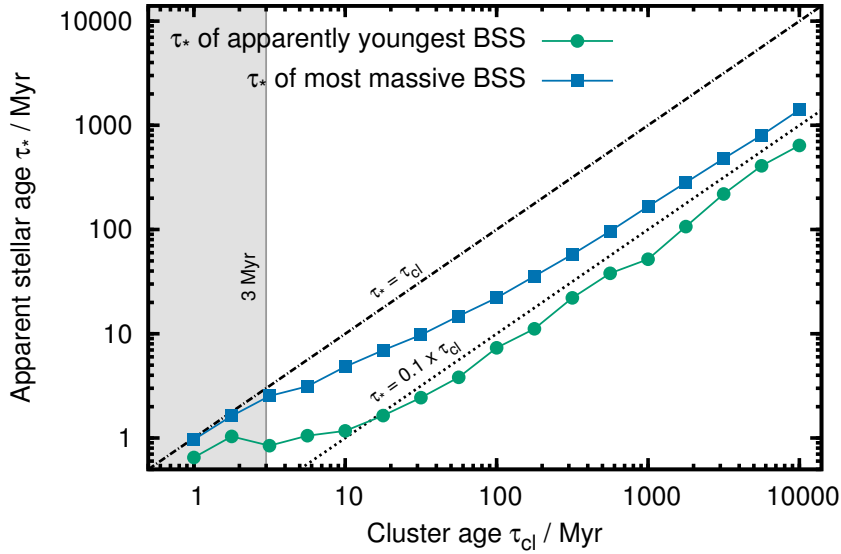
Figure 2.16: Apparent stellar age, τ_*, of the most massive and the apparently youngest blue straggler star as a function of cluster age, τ_{cl}. The grey regions indicate ages for which boundary effects play a role.

taken into account by many repeated calculations which is impractical in our approach.

2.4.3 Apparent ages of blue straggler stars

Mass gainers and mergers appear to be younger than other cluster members because they are rejuvenated by mass accretion (Sec. 2.2.1). The age of a cluster is given by the main-sequence lifetime of the turn-off stars, $\tau_{MS}(M_{to}) \propto M_{to}^{1-x}$, where x is the exponent of the mass-luminosity relation, $L \propto M^x$. The most massive blue straggler stars have a mass of about twice the mass of the turn-off stars in our models. Their apparent age is thus a factor $\tau_{MS}(2M_{to})/\tau_{MS}(M_{to}) = 2^{1-x}$ smaller than their true age if we neglect mixing of fresh fuel into convective cores which makes stars look even younger than the analytic approximation given here. The mass-luminosity relation of MS stars is flatter, i.e. has a smaller exponent x, at high masses. The exponent approaches $x = 1$ in stars close to the Eddington limit and is as large as $x = 4$–5 in low mass stars ($\sim$ 1–2 $M_\odot$). The most massive blue straggler with exponent $x = 4$, i.e. a blue straggler of lower mass in older clusters, appears to be rejuvenated by a factor $1/8$ (the cluster appears 8 times as old as the blue straggler). Contrarily, the most massive blue straggler with an exponent $x = 2$, i.e. a blue straggler of higher mass in younger clusters, appears to be rejuvenated by only a factor of $1/2$ (the cluster appears twice as old as the blue straggler).

In Fig. 2.16 we show the apparent stellar age, τ_*, of the most massive and of the apparently youngest blue straggler star in our simulations as a function of cluster age, τ_{cl}. The above mentioned trend for the most massive blue straggler is recovered, i.e. the most massive blue straggler in young star clusters appears to be less rejuvenated than in old ones: in a 10 Myr star cluster, the most massive blue straggler appears to be younger than the cluster by a factor of 0.48 while this factor is smaller, only 0.17, at 1 Gyr.

The most massive blue straggler is not the one that appears youngest (Fig. 2.16). The apparently youngest blue straggler forms from accretion onto a relatively unevolved star which

then becomes a blue straggler. In our models, the apparently youngest blue straggler is about 40% more massive than the turn-off and forms from late Case A/early Case B mass transfer in a binary with a mass ratio 0.5–0.6. The mass ratio ensures that the secondary star is relatively unevolved. Mass accretion then brings the secondary mass above the mass of the turn-off, forming a blue straggler close to the ZAMS, i.e. apparently very young — the apparent age is of the order of 7% of the cluster age (cf. Fig. 2.16).

The apparent age of the most massive blue straggler depends on how massive blue stragglers can get through mergers and stable RLOF, and on how much fresh fuel is mixed into convective cores during these processes. The apparent age of the most massive blue straggler is younger the more massive the star gets and the more mixing occurs. The apparent age of the seemingly youngest blue straggler depends on the choice of the critical mass ratios, q_{crit}, and the mass transfer efficiency because these parameters determine how small the initial mass ratio can be in order to accrete enough mass to form a blue straggler star. The smaller the mass ratio, the less evolved is the progenitor of the blue straggler and hence the younger the blue straggler appears. Note that the mass ratio can also not be too small: there has to be enough transferred mass such that the secondary mass can exceed the turn-off mass.

2.5 Determination of star cluster ages

As shown in Sec. 2.4.3, a stellar population can be ten times older than some of its most massive stars appear to be. Such rejuvenated stars can bias the age determination of stellar populations because it is not always clear whether a star was influenced by binary mass transfer in the past or not. Especially in young clusters with OB stars, the most luminous and hence most massive stars are often investigated in detail because they are easiest to observe. Their ages are then sometimes interpreted as the cluster age although the most massive stars are likely rejuvenated binary products.

To avoid potential biases and confusion of stars with rejuvenated binary products such as stellar mergers, stars at least half the mass of the most massive cluster members should be used to determine ages of stellar populations. This rule of thumb is implicitly taken into account when dismissing blue stragglers from fitting the turn-off of well-populated star clusters in colour magnitude or HR diagrams.

The turn-off may be blurred by binary products and it is sometimes, especially in young star clusters, challenging to determine its location. In such cases, the mass function may provide a promising alternative because possibly rejuvenated binary products can be identified by the binary tail and the age of the stellar population can be directly determined by reading-off the turn-off mass.

First, we consider single star mass functions to clarify the general approach to determine cluster ages from mass functions. Single star mass functions are truncated at the present-day turn off mass, $M_{\mathrm{to,p}}$, because of finite stellar lifetimes. The present-day and initial mass of the turn off stars in old stellar populations are the same because stars have negligible stellar winds. The age of old populations therefore follows directly from the main-sequence age of stars with an initial mass of that of the turn-off. In young stellar populations, stars lose mass by stellar winds and a peak forms in the mass function. The present-day mass of the turn off stars that is read-off from the truncation of the mass function is no longer equal to their initial mass because of stellar winds. However, without further modeling or the need of stellar models, we can correct for wind mass loss by redistributing the number of excess stars in the wind mass loss

peak, N_1, such that the mass function is filled up to the initial mass of the turn off stars, $M_{to,i}$ (cf. Fig. 2.6 and Sec. 2.3.1). Rewriting the mass lost by stellar winds on the main-sequence, $\Delta M = M_{to,i} - M_{to,p}$, in Eq. (2.10), we have for the number of excess stars in the wind mass loss peak,

$$N_1 = \frac{A}{\Gamma} \left(M_{to,i}^{\Gamma} - M_{to,p}^{\Gamma} \right) , \tag{2.17}$$

from which we find the initial mass of the turn-off stars,

$$M_{to,i} = \left(\frac{N_1 \Gamma}{A} + M_{to,p}^{\Gamma} \right)^{1/\Gamma} , \tag{2.18}$$

in the cluster. The age of the star cluster follows from the main-sequence lifetime of the turn off stars with initial mass $M_{to,i}$.

The mass function of binary stars allows us to determine the age of the stellar population in a similar way. The difference is that the binary star mass functions are not truncated at the turn-off mass but rather at about twice this mass. In practice the mass function may be truncated at less than twice the turn-off mass because of stochastic sampling. Consequently, another indicator of the turn-off mass than the truncation of the mass function is required to determine the age of the stellar population. We use the onset of the binary tail for that purpose. In old stellar populations, the onset of the binary tail, i.e. the turn-off mass, is indicated by a steep decrease in the number of stars. In young stellar populations, the number of stars in our models do not change that strongly at the onset of the binary tail. In such cases, we propose the use of the wind mass loss peak to indicate the onset of the binary tail and hence to determine the turn-off mass and the age of the stellar population. The number of excess stars in the peak can be influenced by unresolved binaries and binary evolution (Sec. 2.3.2). The correction for stellar wind mass loss to derive the initial mass of the turn off stars may therefore not be possible without the use of stellar models that provide the mapping of masses at the end of the main-sequence to initial masses.

The advantage of this over other methods to determine stellar ages is that it is not biased by apparently younger, rejuvenated binary products. Instead, the proposed method identifies and explicitly uses rejuvenated binary products to determine the turn-off mass and hence to derive the cluster age.

This new method is used by Schneider et al. (2014b) to determine the ages of the young Arches and Quintuplet star clusters in the Galactic centre. The mass functions of Arches and Quintuplet show a wind mass loss peak from which it is possible to identify the binary tail and derive an unambiguous age. The age from the wind mass loss peak results in older cluster ages than previously derived for these clusters from the most luminous stars. The most luminous stars belong to the binary tail of the mass function and are thus likely rejuvenated binary products.

2.6 Conclusions

We use a rapid binary evolution code to investigate how single and binary star evolution shape present day mass functions (PDMFs) with time. To that end, we set up coeval populations of single and binary stars, follow their evolution in time and construct mass functions at ages ranging from Myr up to Gyr. Our code incorporates all the relevant single and binary star physics that directly alters stellar masses — wind mass loss, mass transfer in binaries by Roche

lobe overflow (RLOF) and by winds, stellar mergers and rejuvenation of stars.

Finite stellar lifetimes truncate the mass functions and wind mass loss results in an accumulation of stars in the PDMF creating a peak at the high mass end. The magnitude of the peak depends on the strength of stellar winds, i.e. on stellar mass and metallicity, and the slope of the IMF: the flatter the IMF the stronger the peak. The peak can thus be used to constrain stellar wind mass loss. We investigate the age and mass ranges of stellar populations for which we expect a wind mass loss peak in their mass functions. Typically, the peak is present in stellar populations younger than about 10 Myr at $Z = 0.02$ corresponding to stars initially more massive than about 18 M$_\odot$ (Figs. 2.6 and 2.7). Less massive stars have too weak stellar winds. The peak flattens the PDMF slopes at the high mass end by up to 60% in 5 Myr old stellar populations with a Salpeter IMF (IMF slope $\Gamma = -1.35$; Fig. 2.11).

Binary interaction, i.e. mass transfer and stellar mergers, reshape the PDMF at the high mass end, forming a tail which extends the PDMF of single stars by a factor of two in mass. The PDMF tail consists of rejuvenated binary products that are not expected to exist from single star evolution and are better known as blue stragglers. Binary interactions are more efficient in producing the binary tail at high masses (Sec. 2.2.3). The number of rejuvenated binary products in young star clusters (~ 5 Myr) reaches more than 30% of the initial number of stars in the mass range corresponding to the tail (Figs. 2.12 and 2.13). Binary interactions are therefore efficient in repopulating the high mass end of PDMFs even in star clusters that are only a couple of million years old.

Unresolved binaries flatten the slope of the PDMF. The slope is flattened by about 0.1 in our zero-age populations, which is in agreement with previous work on unresolved multiple systems. Altogether, stellar winds, mass exchange in binary systems and unresolved binaries reshape the high mass end of mass functions within ± 0.3 dex of the turn-off mass and can therefore bias IMF determinations.

We compare our predicted blue straggler frequencies to those from the blue straggler catalogue of Galactic open star clusters (Ahumada & Lapasset 2007). Our models predict a decreasing blue straggler frequencies with increasing cluster age — in contrast to the observations. The observed blue straggler frequency drops with younger ages because there are no blue stragglers identified in two-thirds of the open clusters younger than 500 Myr but only in 3% of clusters older than that. Our models predict about the right amount of blue stragglers in young clusters ($\lesssim 100$ Myr) but too few in older clusters. Additional blue straggler formation channels, such as mergers resulting from stellar collisions and wind Roche-lobe overflow from AGB stars, are likely required to explain the observed frequency of blue stragglers in older clusters. Also, the treatment of Case B and C mass transfer may need revision in our models to allow for the formation of blue stragglers from RLOF of giants to main-sequence stars.

The binary fraction among the blue straggler stars in the tail of our PDMFs varies between 40% and 70%, depending on cluster age. It is largest in young (~ 10 Myr) and smallest in old stellar populations (~ 5000 Myr). Our binary fractions are upper limits because we neglect supernova kicks that may disrupt binaries.

The most massive blue stragglers in the binary tail have apparent ages that are younger by factors of 0.17–0.48 than the real cluster age, i.e. cluster ages inferred from the most massive stars would be too young by factors of 2–6. Some of the less massive blue stragglers may show apparent ages that are even younger by a factor of ten. Cluster ages derived from the most luminous stars should therefore be treated with caution because of a likely confusion with rejuvenated binary products. If in doubt, and to avoid potential confusion, cluster ages should not be based on the most luminous cluster members. Instead, we propose the use of mass

functions to identify rejuvenated binary products and to derive cluster ages. This is possible because the turn-off mass and hence the cluster age can be directly determined from mass functions.

In old stellar populations, the turn-off mass is best indicated by a steep decrease of the number of stars at the onset of the binary tail. In younger populations, this decrease of the number of stars is less and the wind mass loss peak may be used instead to determine the turn-off mass. Stellar mass functions and especially the wind mass loss peak constitute a new and unambiguous clock to age-date star clusters. This technique is applied by Schneider et al. (2014b) to the Arches and Quintuplet star clusters to determine unambiguous cluster ages by identifying likely binary products and thereby resolved the apparent age discrepancies among the most luminous members in both clusters.

The binary products in the tail of young PDMFs have potentially far-reaching consequences. So far, they have mostly been neglected when computing the feedback from stellar populations. However, the stars in the tail are the most massive stars in a stellar population and can therefore contribute significantly to the ionising radiation, the mechanical feedback from stellar winds and supernovae explosions and to the chemical enrichment. In the youngest star clusters, binary products might even become so massive that they explode as pair-instability supernovae, thereby contributing significantly to the metal production in the Universe (Heger & Woosley 2002; Gal-Yam et al. 2009; Langer 2012).

2.7 Supplementary material

2.7.1 Binary parameter space continued

In Sec. 2.2.3 we describe how much mass is transferred and accreted in our binary models with $10\,M_\odot$ primary stars to understand quantitatively how binary evolution shapes the high mass end of PDMFs. Here, we continue this description by providing figures equivalent to Figs. 2.1, 2.2 and 2.3 but for primary masses of 2, 5, 20, 50, 70 and $100\,M_\odot$ (Figs. 2.18–2.22, respectively). These analyses enable us to fully understand the quantitative results presented in this paper. The top panels (a) contain the mass transfer efficiency β as defined in Eq. (2.8), the middle panels (b) the mass transferred from the primary to the secondary stars during stable RLOF and the bottom panels (c) the mass accreted by the secondary stars during stable RLOF.
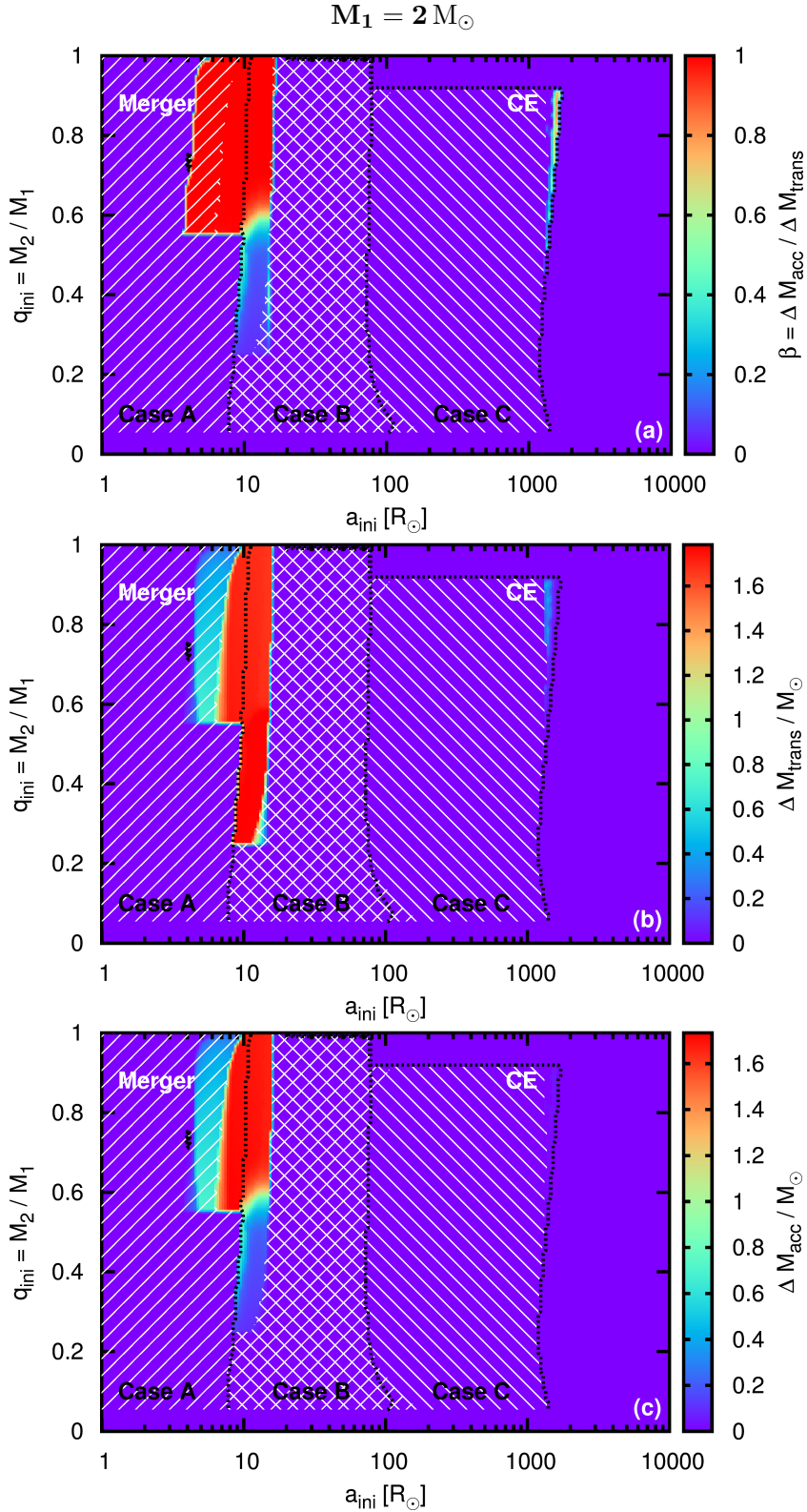
Figure 2.17: Mass transfer efficiency β (top panel a), transferred mass from primary to secondary during stable RLOF (middle panel b) and mass accreted by secondary star during stable RLOF (bottom panel c) as functions of the initial mass ratio q_{ini} (i.e. initial secondary mass) and initial orbital separation a_{ini} for $2\,M_\odot$ primary stars. The shaded regions have the same meaning as in Fig. 2.1 and indicate binaries which merge and/or go through a common envelope phase.

$$\mathbf{M_1 = 5\,M_\odot}$$
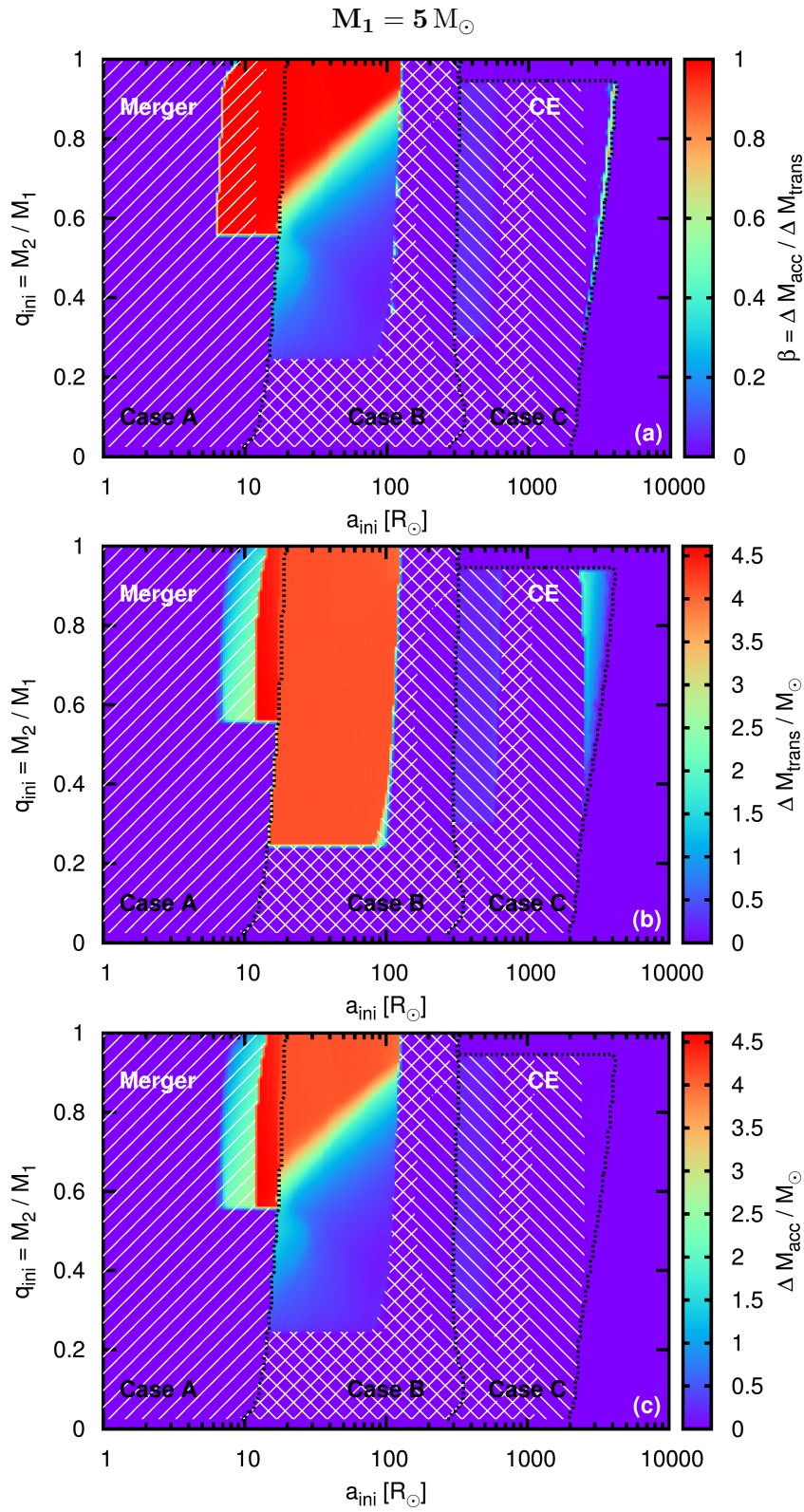
Figure 2.18: As Fig. 2.17 but for $5\,\mathrm{M}_\odot$ primary stars.
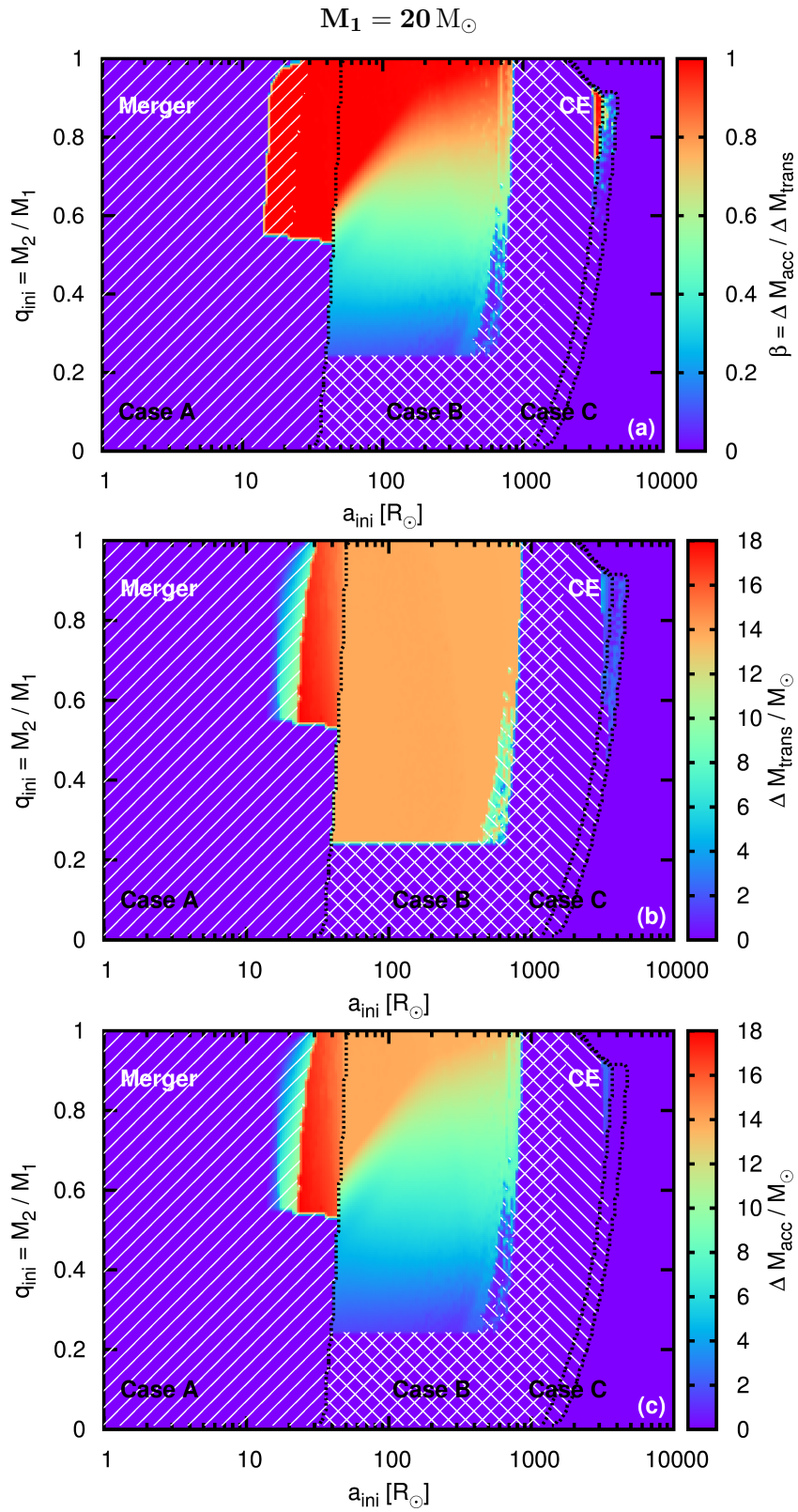
Figure 2.19: As Fig. 2.17 but for $20\,\mathrm{M_\odot}$ primary stars.

$$\mathbf{M_1 = 50\,M_\odot}$$
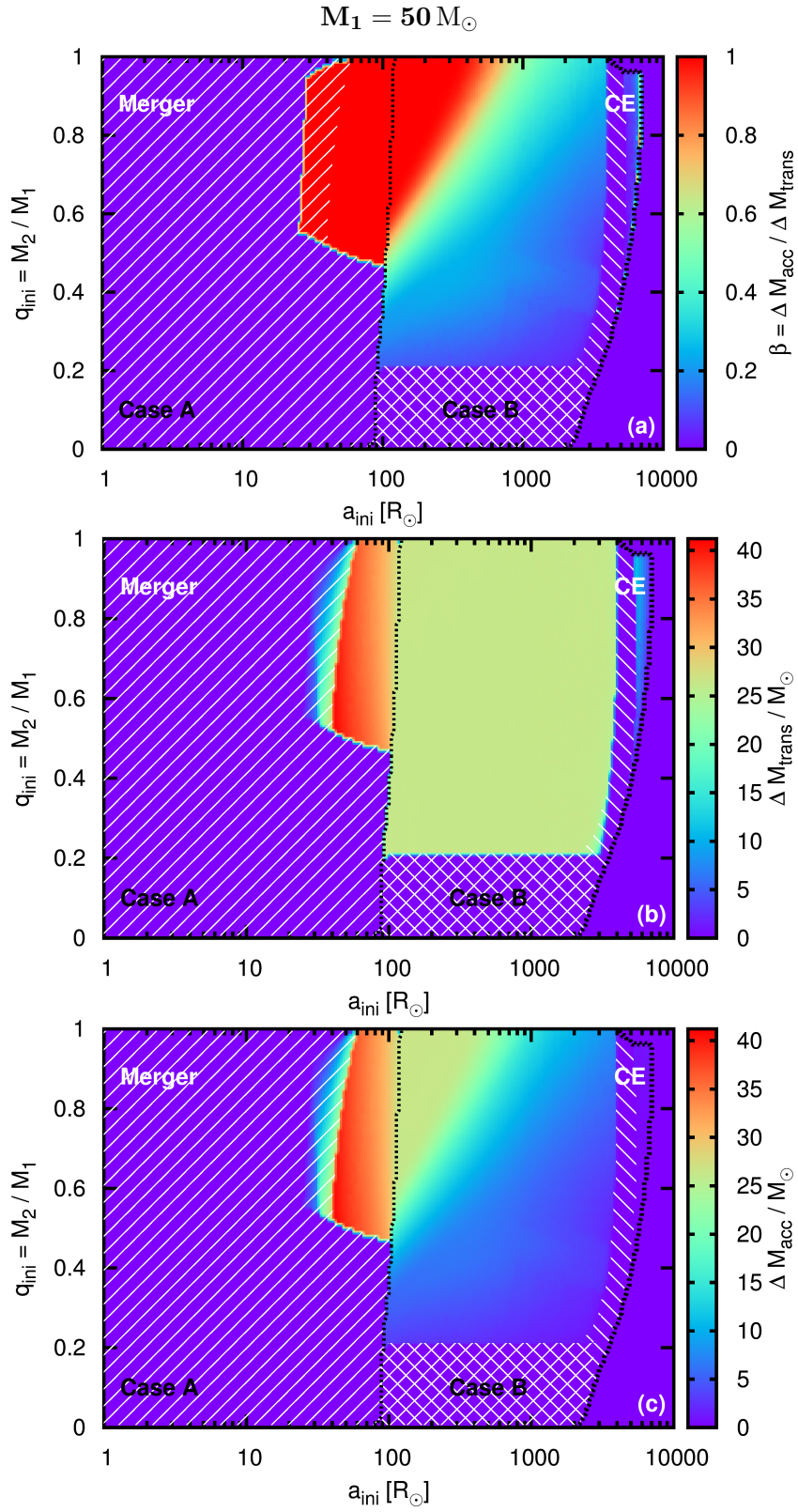
Figure 2.20: As Fig. 2.17 but for 50 M$_\odot$ primary stars.
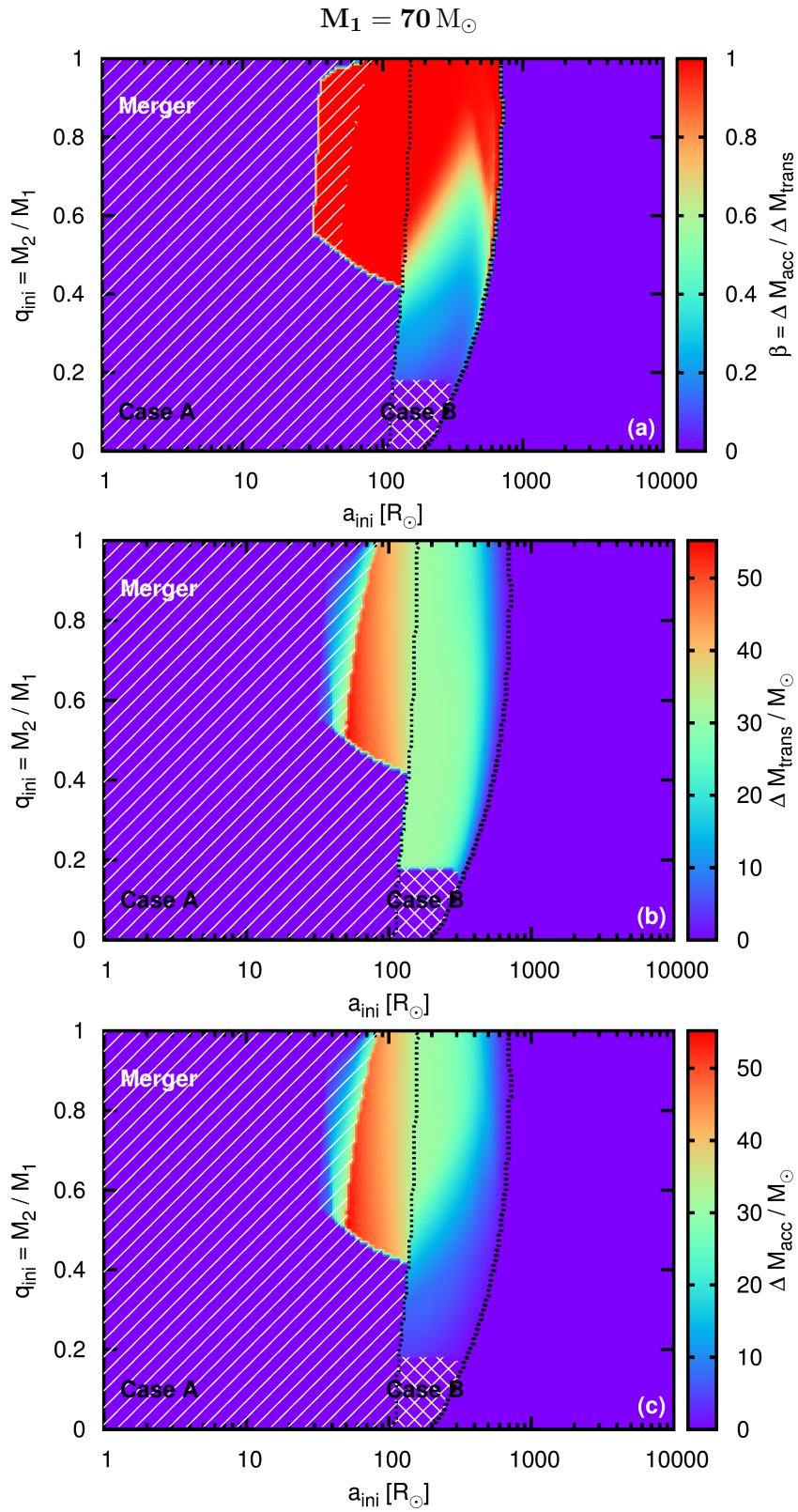
Figure 2.21: As Fig. 2.17 but for $70\,M_\odot$ primary stars.
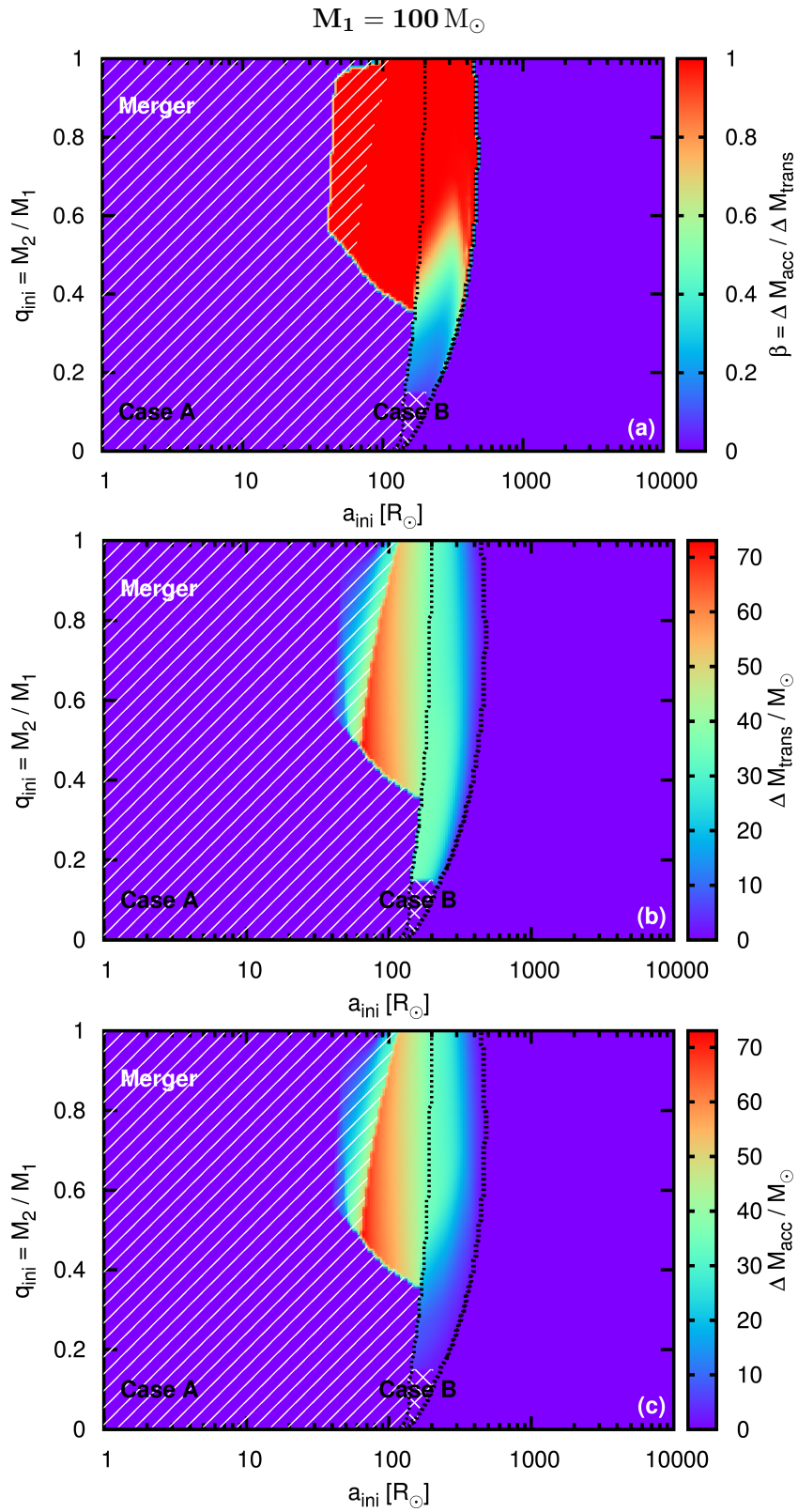
Figure 2.22: As Fig. 2.17 but for $100\,\mathrm{M}_\odot$ primary stars.

2.7.2 Uncertainties in the models

2.7.2.1 Single star evolution

Stars more massive than $10\,M_\odot$ accumulate in a peak at the high mass end of PDMFs because of stellar wind mass loss (Sec. 2.3.1). The magnitude of the accumulation depends on the IMF slope Γ and on the strength of stellar winds, i.e. on the wind mass loss prescription and the metallicity. Our wind mass loss prescription for MS stars (Nieuwenhuijzen & de Jager 1990; Kudritzki et al. 1989) tends to slightly underestimate stellar wind mass loss compared to Vink et al. (2000, 2001). We compare our initial and end-of-MS stellar masses to the latest non-rotating stellar models of Brott et al. (2011a) and Ekström et al. (2012) and find that the turn-off masses agree within 1–3% for stars less massive than about $50\,M_\odot$ and that we overestimate the turn-off masses by up to 20% for more massive stars. This deviation is primarily because of the Wolf-Rayet wind mass loss rates used in Brott et al. (2011a) and Ekström et al. (2012) for massive MS stars which we only apply for post-MS stars. Increasing the wind mass loss for stars $\geq 50\,M_\odot$ to match the turn-off masses of the latest detailed stellar models results into stronger peaks at the high mass end of PDMF younger than about 4.3 Myr. Older populations are not affected.

The wind mass loss peak flattens PDMFs (Sec. 2.3.4). Whether this effect needs to be taken into account when deriving the IMF from observations depends on how mass functions are constructed from a measured sample of stars. If, on the one hand, measured stellar luminosities are converted to masses by means of a suitable mass luminosity relation, the flattening of the PDMF by wind mass loss needs to be taken into account. If, on the other hand, the observed stars are compared individually to stellar evolution tracks to find their initial masses, this effect does not need to be corrected for because stellar tracks usually include wind mass loss. Alternatively, the mass function slope can be determined omitting the high mass end and therefore the wind mass loss peak.

2.7.2.2 Uncertain binary physics

In this section we discuss changes in the treatment of binary interactions and their importance for the PDMFs. Besides mass, angular momentum is transferred during RLOF. Packet (1981) found that a uniformly rotating star needs to accrete only 5 to 10% of its initial mass through a disc to reach a critical (Keplerian) velocity at the equator such that the outermost layers are no longer bound to the star (see also Petrovic et al. 2005). This point of view is debated and there are several arguments regarding accretion and decretion disks which might be able to dissipate angular momentum such that stars stay always below critical rotation and thus can accrete much more mass (Lin & Pringle 1976; Popham & Narayan 1991; Krtička et al. 2011). If a star is spun up to over-critical rotation it probably sheds as much mass as is needed to rotate below critical. Mass is lost from the system and takes away angular momentum from the star. In the case of RLOF this means that not all transferred mass is accreted, mass transfer is non-conservative and typically only a few percent of the transferred mass is accreted (Langer 2012). Low mass transfer efficiencies reduce the PDMF binary tail. For stellar mergers we assume that 10% of the system mass is lost and takes away the excess angular momentum. This is likely rather an upper limit because detailed collision simulations of massive MS stars show that $< 10\%$ is lost even in equal-mass merger events (Glebbeek et al. 2013).

Detailed binary models find mass transfer efficiencies of about 100% for Case A and of the order of 40–100% for early Case B mass transfer (Wellstein et al. 2001). Also, tides in short

period binaries and magnetic fields in combination with mass loss (e.g. by a stellar wind), i.e. magnetic braking, are efficient in dissipating angular momentum such that stars do not reach critical rotation during RLOF. Magnetic fields seem to be even generated by strong shear because of mass accretion (see e.g. Plaskett's star, Grunhut et al. 2013) and stellar mergers (Tout et al. 2008; Ferrario et al. 2009; Langer 2012).

It is mentioned by Hurley et al. (2002) that the critical mass ratio $q_{\mathrm{crit}} = m_2/m_1 = 0.25$ that determines whether stars come into contact during thermal timescale mass transfer, e.g. when the primary star is a Hertzsprung gap star, is rather approximate. Case B mass transfer can lead to a contact phase for extreme mass ratios because the mass transfer timescale becomes faster than the thermal timescale of the accretor (e.g. Ulrich & Burger 1976; Kippenhahn & Meyer-Hofmeister 1977; Neo et al. 1977; Pols & Marinus 1994; Wellstein et al. 2001). We implement a similar criterion with the consequence that nearly all binary systems undergoing Case B mass transfer go through a contact phase in which both stars merge or eject their common envelopes. Merging stars results in a post-MS object and hence a reduction of MS secondary stars. Ejecting envelopes terminates any mass transfer such that the initial secondary stars cannot accrete any matter — in other words the mass transfer efficiency is 0% for most Case B binaries. The resulting changes to our PDMFs are small, because we already limit mass accretion to the thermal timescale of the accretors.

The initial distribution functions of secondary masses (or mass ratios) and orbital periods are also important for our results. We assume an initially flat mass ratio distribution, i.e. all mass ratios are equally probable. Small initial mass ratios often lead to contact phases (see the discussion of the binary parameter space in Sec. 2.2.3). A distribution function of initial mass ratios which favours equal mass binaries enhances the effect of mass transfer and reduces the effect of MS coalescence. Also the Case B contribution, which is the dominant mass transfer channel at later times (Fig. 2.9), is increased because the Case B mass transfer efficiency is higher for larger mass ratios. If the initial orbital separation distribution favours small initial orbital separations compared to Öpik's law, Case A and B mass transfer (including stellar mergers) occur more frequently which increases the magnitude of the tail of the PDMFs.

Different IMF slopes Γ enhance or reduce the importance of binary physics. Binary evolution usually increases the mass of stars: let this increase be given by a multiplicative factor α, i.e. the increased mass is αM. If we increase all stellar masses M by the same factor α, we enhance the mass function at the increased mass αM by the factor,

$$\frac{\psi(\ln M)}{\psi(\ln \alpha M)} = \alpha^{-\Gamma}. \tag{2.19}$$

The steeper the slope of the IMF, i.e. the more negative Γ, the bigger the effect of any mass gain. Also the flattening of the PDMF because of unresolved binaries is more important for steeper IMF slopes and less important for flatter IMF slopes (Sec. 2.3.4). This trend is opposite if mass is lost e.g. by stellar winds: then, a flatter IMF enhances and a steeper one reduces the accumulation of stars.

2.7.3 Unresolved binary stars

Binaries in photometric studies are usually unresolved which leads to an overestimation of their masses (see Eq. 2.15). A mass function, even at zero age, thus looks different compared to the IMF. We find changes in the slope of the mass function of the order of $\Delta\beta \approx 0.1$ towards flattened mass functions for zero age populations. The flattening because of unresolved binaries

is more important for larger masses because of the mass dependence of the power law index of the mass luminosity relation (Sec. 2.3.4). The problem of unresolved binaries is well known (Sagar & Richtler 1991; Kroupa et al. 1993; Maíz Apellániz 2008; Weidner et al. 2009). To compare with their results it is important to know how they distributed stars in binaries (see e.g. the review by Bastian et al. 2010).

Sagar & Richtler (1991), for example, do not use a flat mass ratio distribution, but they draw both binary components randomly from one IMF. For an initial IMF slope of $\Gamma = -1.5$ (our initial IMF slope is Salpeter, i.e. $\Gamma = -1.35$) and a binary fraction of 50% they derive a PDMF slope of $\beta = -1.16$; for a binary fraction of 100% they arrive at $\beta = -1.10$. These changes occur according to their analysis in a mass range of 2–14 $M_\odot$ and are larger than we find. The major difference between their calculation and ours is the assumed distribution function of stars in binaries (mass ratios and IMF slope).

Maíz Apellániz (2008) not only investigates unresolved binary stars but also higher order multiples and chance superpositions in dense clusters. Taking only the effect of binary stars into account they conclude "that for most cases the existence of unresolved binaries has only a small effect on the massive-star IMF slope" of the order of $|\Delta\beta| \approx 0.2$. They use the same mass ratio distribution as in our analysis but slightly different IMF slopes.

Weidner et al. (2009) investigate the effect of unresolved binaries and higher order multiples for different pairing methods. None of their pairing methods correspond to our flat mass ratio distribution. A steepening of the observed PDMF by $\Delta\beta = 0.1$ is reported. Their PDMF is steeper because they take a certain number of stars given by their IMF and pair them randomly into binaries (their RP method). The probability of finding a massive star grouped with another massive star is therefore less than to find it grouped with a lower mass companion, hence estimated system masses do not change significantly for massive stars. At lower masses it is opposite: relatively more binaries with stars of similar masses are found and the companions lead to higher system mass estimates. In total this leads to a steepening of the PDMF.

All in all it seems that unresolved binaries have limited influence on the PDMF of zero age populations. Pairing stars which are randomly sampled from an IMF steepens the mass function, whereas a flat mass ratio distribution flattens the mass function as is shown in our analysis. Observations of massive, i.e. O-type binaries favour a flat mass ratio distribution (Sana et al. 2012), so the high mass end of PDMFs of young stellar populations with O-type stars is expected to be flattened if binaries are unresolved.

2.7.4 Stochastic sampling

The statement that the most massive stars are likely blue stragglers has to be treated with caution, because it is only valid in "rich" (i.e. massive) clusters where there are enough stars to sample the binary parameter space well — this problem is known as stochastic sampling. Binary evolution e.g. re-populates the 5 Myr PDMF on average by more than 40% of the IMF above 40 $M_\odot$ ($\log m \approx 1.6$). If there is initially only one star in this mass range, we expect about 0.4 stars to be re-populated by binary evolution — if there are initially ten stars (if the cluster is a factor of ten more massive), we expect to find about 4 binary products. So if the cluster is not massive enough, there might be no blue straggler star at a certain age. It will also take some time until binary star evolution produces the first blue straggler stars. This again depends on the cluster richness and on how binaries are distributed: the shorter the initial period, the earlier the binary interaction. When the initially most massive stars in a cluster evolve towards the end of core hydrogen burning we know that blue stragglers can be produced

by MS mergers and Case A mass transfer. So the whole contribution of MS mergers and Case A mass transfer products of binaries with initial $100 \, \mathrm{M_\odot}$ primary stars to the blue straggler star population is expected to be present after about $3 \, \mathrm{Myr}$. Blue stragglers can be even present at younger ages — this is just a matter of stochastic sampling which is investigated in more detail in Schneider et al. (2014b).

Ages of young star clusters, massive blue stragglers and the upper mass limit of stars: Analysing age-dependent stellar mass functions

F.R.N. Schneider, R.G. Izzard, S.E. de Mink, N. Langer, A. Stolte, A. de Koter,
V.V. Gvaramadze, B. Hußmann, A. Liermann and H. Sana

Abstract   Massive stars rapidly change their masses through strong stellar winds and mass transfer in binary systems. The latter aspect is important for populations of massive stars as more than 70% of all O stars are expected to interact with a binary companion during their lifetime. We show that such mass changes leave characteristic signatures in stellar mass functions of young star clusters that can be used to infer their ages and to identify products of binary evolution. We model the observed present-day mass functions of the young Galactic Arches and Quintuplet star clusters using our rapid binary evolution code. We find that the shaping of the mass function by stellar wind mass loss allows us to determine the cluster ages as $3.5 \pm 0.7\,\mathrm{Myr}$ and $4.8 \pm 1.1\,\mathrm{Myr}$, respectively. Exploiting the effects of binary mass exchange on the cluster mass function, we find that the most massive stars in both clusters are rejuvenated products of binary mass transfer, i.e. the massive counterpart of classical blue straggler stars. This resolves the problem of an apparent age spread among the most luminous stars exceeding the expected duration of star formation in these clusters. We perform Monte Carlo simulations to probe stochastic sampling, which support the idea of the most massive stars being rejuvenated binary products. We find that the most massive star is expected to be a binary product after $1.0 \pm 0.7\,\mathrm{Myr}$ in Arches and after $1.7 \pm 1.0\,\mathrm{Myr}$ in Quintuplet. Today, the most massive 9 ± 3 stars in Arches and 8 ± 3 in Quintuplet are expected to be such objects. Our findings have strong implications for the stellar upper mass limit and solve the discrepancy between the claimed $150\,\mathrm{M_\odot}$ limit and observations of four stars with initial masses of 165–$320\,\mathrm{M_\odot}$ in R136 and of supernova 2007bi, which is thought to be a pair-instability supernova from an initial $250\,\mathrm{M_\odot}$ star. Using the stellar population of R136, we revise the upper mass limit to values in the range 200–$500\,\mathrm{M_\odot}$.

3.1 Introduction

Massive stars play a key role in our universe. They drive the chemical evolution of galaxies by synthesising most of the heavy elements. Their strong stellar winds, radiation feedback, powerful supernova explosions and long gamma ray bursts shape the interstellar medium. They are thought to have played an essential role in reionising the universe after the dark ages and are visible up to large distances.

Unfortunately, our understanding of the formation and evolution of the most massive stars in the local universe is incomplete (Langer 2012). Recently, it was established that most of the massive stars in the Milky Way are actually part of a binary star system and that more than 70% of them will exchange mass with a companion during their life (Sana et al. 2012). Our understanding of these stars is further hampered by two major controversies. The first one, the cluster age problem, concerns the ages of the youngest star clusters. Emerging star clusters are expected to form stars in a time span shorter than the lifetime of their most massive members (Elmegreen 2000; Kudryavtseva et al. 2012). In contrast, the most luminous stars in two of the richest young clusters in our Galaxy, the Arches and Quintuplet clusters, show an apparently large age range. Their hydrogen- and nitrogen-rich Wolf–Rayet (WNh) stars appear significantly younger than most of their less luminous O stars (Martins et al. 2008; Liermann et al. 2012). Similar age discrepancies are observed in other young stellar systems (Massey 2003), such as the Cyg OB2 association (Herrero et al. 1999; Gvaramadze & Bomans 2008a; Negueruela et al. 2008) and the star clusters Pismis 24 (Gvaramadze et al. 2011) and NGC 6611 (Hillenbrand et al. 1993; Gvaramadze & Bomans 2008b).

The second controversy, the maximum stellar mass problem, concerns the stellar upper mass limit. Such an upper mass limit is theoretically motivated by the Eddington limit which may prevent stellar mass growth by accretion above a certain mass (Larson & Starrfield 1971). Observationally, an upper mass limit of about $150\,\mathrm{M_\odot}$ is derived from the individual stellar mass distributions of the Arches and the R136 clusters (Weidner & Kroupa 2004; Figer 2005; Koen 2006) and from a broader analysis of young stellar clusters (Oey & Clarke 2005). This result is questioned by a recent analysis of very massive stars in the core of R136, in which stars with initial masses of up to about $320\,\mathrm{M_\odot}$ are found (Crowther et al. 2010). Furthermore, recently detected ultraluminous supernovae in the local universe are interpreted as explosions of very massive stars (Langer et al. 2007); for example, SN 2007bi is well explained by a pair-instability supernova from an initially $250\,\mathrm{M_\odot}$ star (Gal-Yam et al. 2009; Langer 2009).

Here we show that both controversies can be resolved by considering a time-dependent stellar mass function in young star clusters that accounts for stellar wind mass loss and binary mass exchange. We perform detailed population synthesis calculations of massive single and binary stars that include all relevant physical processes affecting the stellar masses and compare them to observed present-day mass functions of the Arches and Quintuplet clusters. Our methods and the observations of the mass functions of the Arches and Quintuplet clusters are described in Sec. 3.2. We analyse the Arches and Quintuplet clusters in Sec. 3.3 to derive cluster ages and identify possible binary products by fitting our models to the observed mass functions. Stochastic sampling effects are investigated in Sec. 3.4 and the implications of our findings for the upper mass limit are explored in Sec. 3.5. We discuss our results in Sec. 3.6 and give final conclusions in Sec. 3.7.

3.2 Methods and observational data

We analyse the Arches and Quintuplet clusters in two steps. First, we model their observed stellar mass functions to determine, e.g., the initial mass function (IMF) slopes and the cluster ages. We set up a dense grid of single and binary stars, assign each stellar system in the grid a probability of existence given the initial distribution functions (see Sec. 3.2.2) and evolve the stars in time using our rapid binary evolution code described (see Sec. 3.2.1). Present-day mass functions are then constructed from the individual stellar masses at predefined ages. This ensures that all the relevant physics such as stellar wind mass loss and binary mass exchange, which directly affects stellar masses, is factored in our mass functions.

Second, we investigate stochastic sampling effects to compute, e.g., the probability that the most massive stars in the Arches and Quintuplet clusters are binary products. To that end, we randomly draw single and binary stars from initial distribution functions until the initial cluster masses are reached and, again, evolve the drawn stellar systems with our rapid binary evolution code. The setup of these Monte Carlo experiments is described in detail in Sec. 3.2.3.

The initial distribution functions used in the above-mentioned steps are summarised in Sec. 3.2.2 and an overview of the observations of the Arches and Quintuplet clusters to which we compare our models is given in Sec. 3.2.4. We bin mass functions in a nonstandard way to compare them to observations; the binning procedure is described in Sec. 3.2.5.

3.2.1 Rapid binary evolution code

The details of our population synthesis code are described in Schneider et al. (subm.) and de Mink et al. (2013). Here we briefly summarise the most important methods and assumptions that are used to derive our results.

We use a binary population code (Izzard et al. 2004, 2006, 2009) to evolve single and binary stars and follow the evolution of the stellar masses and of other stellar properties as a function of time. Our code is based on a rapid binary evolution code (Hurley et al. 2002) that uses analytic functions (Hurley et al. 2000) fitted to stellar evolutionary models with convective core overshooting (Pols et al. 1998) to model the evolution of single stars across the whole Hertzsprung–Russell diagram. We use a metallicity of $Z = 0.02$.

Stellar wind mass loss (Nieuwenhuijzen & de Jager 1990) is applied to all stars with luminosities larger than $4000\,L_\odot$ (Hurley et al. 2000). The mass accretion rate during mass transfer is limited to the thermal rate of the accreting star (Wellstein et al. 2001). Binaries enter a contact phase and merge if the mass ratio of accretor to donor is smaller than a critical value at the onset of Roche lobe overflow (de Mink et al. 2013). When two main-sequence stars merge, we assume that 10% of the total mass is lost and that 10% of the envelope mass is mixed with the convective core (de Mink et al. 2013).

Photometric observations of star clusters cannot resolve individual binary components. In order to compare our models to observations we assume that binaries are unresolved in our models and determine masses from the combined luminosity of both binary components utilising our mass–luminosity relation. Hence, unresolved, preinteraction binaries contribute to our mass functions.

We concentrate on main sequence (MS) stars because stars typically spend about 90% of their lifetime in this evolutionary phase; moreover, our sample stars used for comparison are observationally colour selected to remove post-MS objects. If a binary is composed of a post-MS and a MS star, we take only the MS component into account.

3.2.2 Initial distribution functions for stellar masses and orbital periods

We assume that primary stars in binaries and single stars have masses M_1 distributed according to a power-law IMF with slope Γ,

$$\xi(M_1) = \frac{\mathrm{d}N}{\mathrm{d}M_1} \quad = \quad A \, M_1^{\Gamma-1} \,, \tag{3.1}$$

in the mass range 1–100 $\mathrm{M}_\odot$ (where A is a normalisation constant). Secondary star masses M_2 are taken from a flat mass-ratio distribution; that is, all mass ratios $q = M_2/M_1 \leq 1$ are equally probable (Sana et al. 2012). The initial orbital periods for binaries with at least one O star, i.e. a primary star with $M_1 \gtrsim 15\,\mathrm{M}_\odot$, mass ratio $q \geq 0.1$ and a period $0.15 \leq \log(P/\mathrm{days}) \leq 3.5$ are taken from the distribution of stars in Galactic open clusters (Sana et al. 2012). The initial periods of all other binaries follow a flat distribution in the logarithm of the orbital period (Öpik 1924). Orbital periods are chosen such that all interacting binaries are taken into account; that is, the maximum initial orbital separation is $10^4\,\mathrm{R}_\odot$ ($\approx 50\,\mathrm{AU}$). Binaries with wider orbits would be effectively single stars.

3.2.3 Monte Carlo experiments

To address stochastic sampling, we perform Monte Carlo simulations of star clusters and investigate the probability that the most massive star in a star cluster is a product of binary evolution as a function of cluster mass, age, binary fraction and IMF slope.

We assume that all stars are coeval and that every star cluster forms from a finite supply of mass, with stellar masses stochastically sampled from initial distribution functions. While single stars are sampled from the IMF, binary stars are chosen from a larger parameter space of primary and secondary masses and orbital periods. This larger parameter space is better sampled in clusters of higher mass.

We draw single and binary stars for a given binary fraction from the initial distribution functions of primary mass, secondary mass and orbital period until a given initial cluster mass, M_{cl}, is reached. Here we consider only stars with masses in the range of 1–100 $\mathrm{M}_\odot$. The true cluster masses are therefore larger if stars below $1\,\mathrm{M}_\odot$ are added. Including these stars according to a Kroupa IMF (Kroupa 2001) increases the true cluster mass by 20% and 89% for high-mass ($\geq 1\,\mathrm{M}_\odot$) IMF slopes of $\Gamma = -0.70$ and $\Gamma = -1.35$, respectively.

After the stellar content of a cluster is drawn, we evolve the stars in time to analyse whether the most massive stars at a given cluster age result from close binary interaction. Repeating this experiment 1000 times provides the probability that the most massive cluster star formed from binary interactions, how long it takes, on average, until the most massive star is a product of binary evolution $\langle\tau_{\mathrm{B}}\rangle$ and how many stars have, on average, a mass larger than that of the most massive cluster star (M_{S}) which did not accrete from a companion, $\langle N(M > M_{\mathrm{S}})\rangle$. The most massive star that did not accrete from a companion can be a genuine single star or a star in a binary where binary mass transfer has not yet happened. From here on we refer to this star as "the most massive genuine single star". We evolve and distribute stars as described in Secs. 3.2.1 and 3.2.2.

To compare our Monte Carlo simulations with observations of the Arches and Quintuplet clusters, we need to know the corresponding cluster masses M_{cl} in our Monte Carlo experiments. We use IMF slopes of $\Gamma = -0.7$ as later determined in Sec. 3.3.1 for both clusters. The observations used for comparison (Stolte et al. 2005; Hußmann et al. 2012) are complete for

masses $> 10\,\mathrm{M_\odot}$, corresponding to 234 and 134 stellar systems in the Arches and Quintuplet and integrated masses of stars more massive than $10\,\mathrm{M_\odot}$ of 7200 and $3100\,\mathrm{M_\odot}$, respectively.

Our best-fitting Monte Carlo models of the central regions of the Arches and Quintuplet with primordial binary fractions of 100% and 60% have 225 ± 10 stellar systems with an integrated (initial) mass of $(7993 \pm 361)\,\mathrm{M_\odot}$ and 136 ± 10 stellar systems with an integrated initial mass of $(3240 \pm 244)\,\mathrm{M_\odot}$, respectively. These models correspond to initial cluster masses of $M_{\mathrm{cl}} \approx 1.5 \times 10^4\,\mathrm{M_\odot}$ and $M_{\mathrm{cl}} \approx 0.9 \times 10^4\,\mathrm{M_\odot}$, respectively, in stars with $1 \leq M/\mathrm{M_\odot} \leq 100$.

We assume that binaries are resolved in our Monte Carlo calculations, contrary to when we model mass functions in order to compare to observed mass functions. This is because we make theoretical predictions and are thus interested in individual masses of all stars whether or not they are in a binary.

3.2.4 Observations

The observed present-day mass functions of the Arches and Quintuplet clusters were obtained from NAOS/CONICA (NACO) photometry at the Very Large Telescope. The Arches cluster was observed in 2002 over a field of view (FOV) of $27''$. The centre of the Quintuplet cluster was imaged with NACO over a FOV of $40''$ in 2003 and 2008, which allowed the construction of a membership source list from proper motions. Both data sets were obtained in the H ($\lambda_c = 1.66\,\mu\mathrm{m}$) and K_s ($\lambda_c = 2.18\,\mu\mathrm{m}$) passbands. The colour information is used to remove likely blue foreground interlopers, red clump and giant stars towards the Galactic Center line of sight. Details can be found in Stolte et al. (2005) for the Arches cluster and in Hußmann et al. (2012) for the Quintuplet cluster.

In the case of the Arches cluster, the known radial variation of the extinction is removed prior to individual mass determination (Stolte et al. 2002) by employing the extinction law of Rieke & Lebofsky (1985). Masses are then derived from the K_s magnitudes of each star by comparison with a 2 Myr Geneva isochrone (Lejeune & Schaerer 2001). In the case of Quintuplet, the better photometric performance allowed all sources to be individually dereddened to a 4 Myr Padova MS isochrone (Marigo et al. 2008, and references therein) using the recently updated near-infrared extinction law toward the Galactic Center line of sight (Nishiyama et al. 2009). As detailed in Hußmann et al. (2012), isochrone ages of 3 and 5 Myr do not significantly alter the shape and slope of the constructed mass function. All mass determinations are based on solar metallicity evolution models.

With the aim to minimise any residual field contamination, only the central $r < 10''$, or 0.4 pc, of the Arches and $r < 12.5''$, or 0.5 pc, of the Quintuplet (at an assumed distance of 8.0 kpc to the Galactic Center; Ghez et al. 2008) were selected to construct the mass functions. For the Arches cluster, this radial selection corresponds approximately to the half-mass radius, which implies that the mass projected into this annulus is of the order of $\sim 10^4\,\mathrm{M_\odot}$ (see Espinoza et al. 2009; Clarkson et al. 2012; Habibi et al. 2013). In the Quintuplet cluster, the total mass is estimated to be $6000\,\mathrm{M_\odot}$ within the considered 0.5 pc radius (Hußmann et al. 2012). The mass functions in the central regions of Arches and Quintuplet have slopes that are flatter than the usual Salpeter slopes, most likely because of mass segregation (Harfst et al. 2010; Habibi et al. 2013).

The most massive stars in the Arches and Quintuplet clusters are hydrogen- and nitrogen-rich WNh stars. As reliable masses cannot be derived for these WR stars from photometry alone and as several of the WRs in Quintuplet suffered from saturation effects, the most massive stars are excluded from the mass functions. This affects six WNhs stars with uncertain masses in

Arches and three (plus seven post-MS, carbon-rich WR stars) in Quintuplet. These WNh stars are expected to contribute to the high-mass tail of the Arches and Quintuplet mass functions.

3.2.5 Binning procedure of mass functions

Following Stolte et al. (2005), we employ a binning procedure that renders the observed mass functions independent of the starting point of the bins. We shift the starting point by one-tenth of the bin size and create mass functions for each of these starting points. We use a fixed bin size of 0.2 dex to ensure that the number of stars in each bin is not too small and does not introduce a fitting bias (Maíz Apellániz & Úbeda 2005). Each of these 10 mass functions with different starting points is shown when we compare our mass functions to observations.

This procedure results in lowered number counts in the highest-mass bins because only the most massive stars will fall into these bins as seen in the power-law mass function (black dotted lines in Fig. 3.2) where a kink is visible around $\log M/M_\odot \approx 1.85$ (left panel) and $\log M/M_\odot \approx 1.45$ (right panel; see the convolution of a truncated horizontal line with a box function with the width of the bins). This kink is caused by the binning procedure. Importantly, the observations, our models and the power-law mass functions in Figs. 3.2 and 3.8 are binned identically to render the mass functions comparable.

3.3 Analyses of the Arches and Quintuplet clusters

For a meaningful comparison of the modelled to the observed mass functions, the star cluster and the observations thereof need to fulfil certain criteria. They should be (1) between $\sim 2\,\text{Myr}$ and $\sim 10\,\text{Myr}$ in age such that the wind mass loss peak in the mass function is present (see below and Schneider et al. subm.), (2) massive enough such that the mass function samples the largest masses and (3) homogeneously analysed, with a complete present-day mass function above $\sim 10\,M_\odot$. Both the Arches and Quintuplet clusters fulfil all criteria and are therefore chosen for our analysis.

Other possible star clusters, which can be analysed in principle, are the Galactic Center cluster, NGC 3603 YC, Westerlund 1 and R136 in the Large Magellanic Cloud. Trumpler 14 and Trumpler 16 in the Galactic Carina nebula are not massive enough and rather are OB star associations with stars of different ages. For Westerlund 1 (Lim et al. 2013) and NGC 3603 YC (Pang et al. 2013), present-day mass functions were recently derived. A brief inspection of these results shows that both clusters may be suitable for an analysis as performed here for the Arches and Quintuplet clusters. We will investigate this further in the near future. Possibly, NGC 3603 YC is too young such that its mass function is not yet altered enough by stellar evolution to apply our analysis.

3.3.1 The Arches and Quintuplet mass functions

The initially most massive stars in a cluster end their life first. This depopulates the high-mass end of the stellar mass function. Before that, however, massive stars lose a significant fraction of their initial mass because of strong stellar winds; for example, our $100\,M_\odot$ star at solar metallicity loses about $40\,M_\odot$ during core hydrogen burning. Stellar wind mass loss shifts the top of the mass function toward lower masses and a peak accumulates near its high-mass end (Figs. 3.1a and 3.1b). The location of the peak depends strongly on the cluster age and provides a clock to age-date a star cluster.
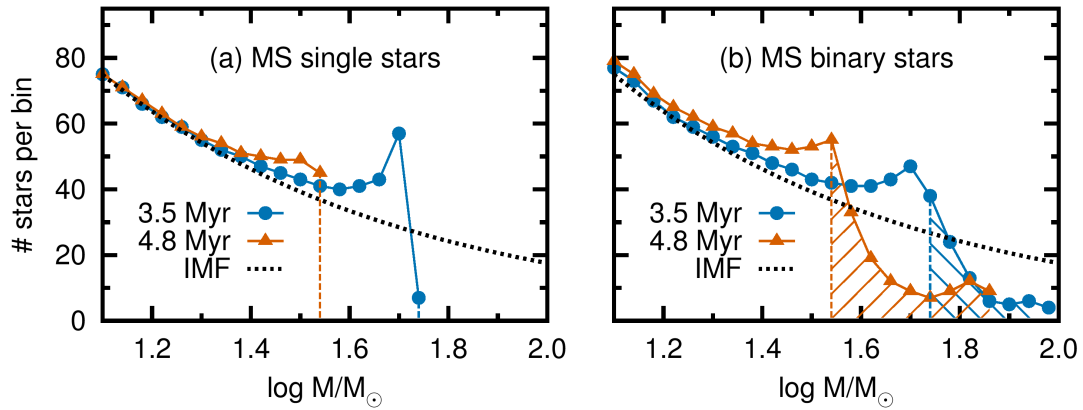
Figure 3.1: Stellar mass functions, i.e. number of stars per logarithmic stellar mass bin, predicted by our population synthesis models for MS (a) single and (b) binary stars. Circles and triangles show the mass function at 3.5 and 4.8 Myr, respectively. The black dotted line shows the adopted initial mass function ($\Gamma = -0.7$). The peaks in the mass functions caused by stellar wind mass loss are apparent in both plots at about $32\,\mathrm{M_\odot}$ ($\log M/\mathrm{M_\odot} \approx 1.5$) and $50\,\mathrm{M_\odot}$ ($\log M/\mathrm{M_\odot} \approx 1.7$) respectively. The tail of stars affected by binary evolution in (b) is highlighted by the hatched regions. The tail extends to about twice the maximum mass expected from single star evolution, which is indicated by the vertical dashed lines.

Stars in close binary systems exchange mass with their companion either by mass transfer or in a stellar merger. A fraction of stars gain mass, producing a tail at the high mass end of the mass function (hatched regions in Fig. 3.1b) that extends beyond the most massive single stars (Fig. 3.1a) by up to a factor of about 2. The mass gainers appear younger than genuine single stars because their convectively mixed stellar core grows upon mass accretion and mixes fresh fuel into their centre, thereby turning their clock backward (van Bever & Vanbeveren 1998). Furthermore, the most massive gainers reach masses that, when interpreted as single stars, have lifetimes that are shorter than the cluster age — they are the massive counterpart of classical blue straggler stars (Schneider et al. subm.).

The mass functions of the cores of the Arches ($r \lesssim 0.4\,\mathrm{pc}$) and Quintuplet ($r \lesssim 0.5\,\mathrm{pc}$) clusters (Stolte et al. 2005; Hußmann et al. 2012) reveal both the stellar wind mass loss peak and the tail because of binary mass exchange. Compared to a power law, we find that the Arches and Quintuplet mass functions are overpopulated in the ranges 32 to $50\,\mathrm{M_\odot}$ ($\log M/\mathrm{M_\odot} = 1.5$–$1.7$) and 20 to $32\,\mathrm{M_\odot}$ ($\log M/\mathrm{M_\odot} = 1.3$–$1.5$), respectively (Fig. 3.2).

These peaks are well reproduced by our models (Figs. 3.1 and 3.2). We can thus determine the cluster age because among the stars in the peak are the initially most massive stars that are (a) still on but about to leave the main sequence and (b) unaffected by binary interactions (we refer to them as turn-off stars in analogy to their position close to the turn-off in a Hertzsprung–Russell diagram). The majority of stars in the peak are turn-off stars but there are small contributions from unresolved and postinteraction binaries (see Schneider et al. subm.). A correction for wind mass loss then reveals the initial mass of the turn-off stars and hence the age of the cluster.

We can correct for wind mass loss by redistributing the number of excess stars in the peak N such that the mass function is homogeneously filled for masses larger than those of the peak stars up to a maximum mass, the initial mass of the turn-off stars $M_{\mathrm{to,i}}$. The number of excess
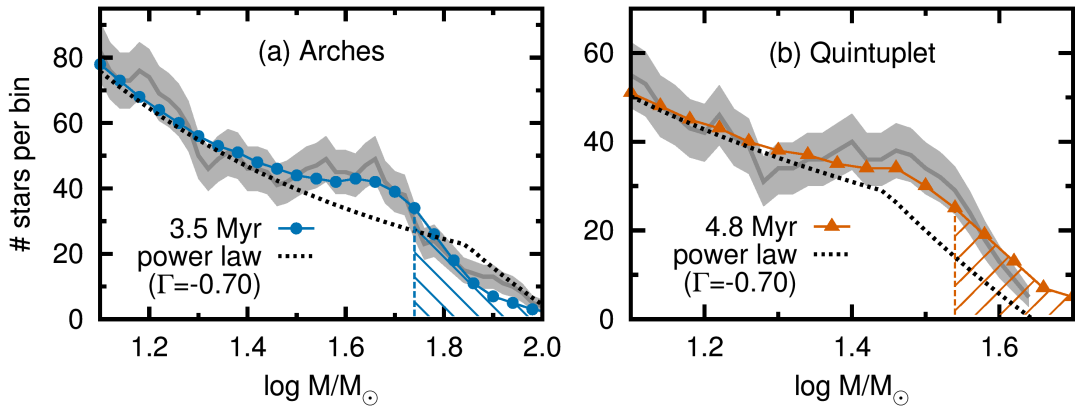
Figure 3.2: Observed stellar mass functions for a bin size of 0.2 dex of (a) the Arches cluster (Stolte et al. 2005) compared to our 3.5 Myr binary population model from Fig. 3.1b (primordial binary fraction 100%) and (b) the Quintuplet cluster (Hußmann et al. 2012) compared to our 4.8 Myr model (primordial binary fraction 60%). The peak and tail of the mass functions are well reproduced by our models. Gray shaded regions around the observed mass functions give Poisson uncertainties and show that the observed peaks deviate by 1σ–2σ from the power-law mass functions. We plot simple power-law mass functions as dotted lines, binned in the same way as the observations and our models (Sec. 3.2.5). The kinks in the power-law mass functions result from our binning procedure.

stars is then

$$N = \int_{M_{\mathrm{to,p}}}^{M_{\mathrm{to,i}}} \xi(M)\,\mathrm{d}M \tag{3.2}$$

where $M_{\mathrm{to,p}}$ is the present-day mass of the turn-off stars, which can be directly read-off from the higher-mass end of the peak, and $\xi(M)$ the initial mass function as defined in Eq. (3.1). The initial mass of the turn-off stars $M_{\mathrm{to,i}}$ and hence the cluster age follows from integrating Eq. (3.2),

$$M_{\mathrm{to,i}} = \left(\frac{N\Gamma}{A} + M_{\mathrm{to,p}}^{\Gamma} \right)^{1/\Gamma}. \tag{3.3}$$

The normalisations, A, of the mass functions to be filled up with the excess stars, N, (dotted, power-law functions in Fig. 3.2) are $A = 964$ and $A = 639$ for Arches and Quintuplet, respectively, with slopes of $\Gamma = -0.7$ in both cases (see discussion below for why the mass functions are so flat). It is difficult to read off the exact value of $M_{\mathrm{to,p}}$ from the observed mass functions because of the binning. However, from binning our modelled mass functions in the same way as the observations, we know that $M_{\mathrm{to,p}}$ corresponds to the mass shortly after the peak reached its local maximum (see the vertical dashed lines in Figs. 3.1 and 3.2). Depending on the exact value of $M_{\mathrm{to,p}}$, $\log M_{\mathrm{to,p}}/\mathrm{M}_\odot = 1.70$–$1.74$ in Arches and $\log M_{\mathrm{to,p}}/\mathrm{M}_\odot = 1.50$–$1.54$ in Quintuplet, we find 12–14 and 7–10 excess stars in the peaks of the Arches and Quintuplet mass functions, respectively. These numbers of excess stars result in turn-off masses $M_{\mathrm{to,i}}$ of 62–72 $\mathrm{M}_\odot$ and 36–43 $\mathrm{M}_\odot$ and hence ages of 3.8–3.5 Myr and 5.2–4.7 Myr for the Arches and Quintuplet clusters, respectively. These are only first, rough age estimates that will be refined below and their ranges stem from the uncertainty in reading off $M_{\mathrm{to,p}}$ from the observed mass functions.

From the difference between the initial and present-day masses of the turn-off stars in Arches and Quintuplet, we can directly measure the amount of mass lost by these stars through stellar

winds. The turn-off stars in Arches lost about 12–$17\,\mathrm{M_\odot}$ and the turn-off stars in Quintuplet lost about 4–$8\,\mathrm{M_\odot}$ during their MS evolution. This is a new method to measure stellar wind mass loss that does not require measurements of stellar wind mass loss rates and can therefore be used to constrain these.

More accurately, we determine the ages of the Arches and Quintuplet clusters by fitting our population synthesis models (Sec. 3.2) to the observed mass functions. First, we fit power-law functions to the observed mass functions in mass regimes in which they are observationally complete and not influenced by stellar wind mass loss ($10 \lesssim M/\mathrm{M_\odot} \lesssim 32$ and $10 \lesssim M/\mathrm{M_\odot} \lesssim 20$, respectively). Binary effects are also negligible because stars with such masses are essentially unevolved at the present cluster ages. This fit gives the normalisation and a first estimate of the slope of the mass function. We then vary the mass function slope, the cluster age and the primordial binary fraction in our models simultaneously such that the least squares deviation from the observations is minimised. Our best-fit models are shown in Fig. 3.2 together with the observed mass functions.

We find slopes of $\Gamma = -0.7$, ages of $3.5 \pm 0.7\,\mathrm{Myr}$ and $4.8 \pm 1.1\,\mathrm{Myr}$ and primordial binary fractions of 100% and 60% for the Arches and Quintuplet clusters, respectively. The binary fractions are less robust and may be the same within uncertainties because we do not take the uncertain masses of the WNh stars into account. While our mass function fits contribute to the age uncertainties by only $\pm 0.3\,\mathrm{Myr}$, its major part, $\pm 0.6\,\mathrm{Myr}$ and $\pm 1.1\,\mathrm{Myr}$ for Arches and Quintuplet, respectively, is due to observational uncertainties in stellar masses of $\pm 30\%$ (Sec. 3.6).

Massive stars tend to sink toward the cluster cores because of dynamical friction (mass segregation), thereby flattening the mass function of stars in the core. The derived mass function slopes of $\Gamma = -0.7$ are flatter than the typical Salpeter slope of $\Gamma = -1.35$ (Salpeter 1955) because we investigate only the mass-segregated central regions of both clusters (see Habibi et al. 2013, as well as Sec. 3.6.3), i.e. a subsample of stars biased toward larger masses.

In our models (Fig. 3.1), the tail of the Arches mass function contains about 30% unresolved, preinteraction binaries with $\log M/\mathrm{M_\odot} \geq 1.76$ ($M \approx 58\,\mathrm{M_\odot}$) and about 20% with $\log M/\mathrm{M_\odot} \geq 1.80$ ($M \approx 63\,\mathrm{M_\odot}$). For Quintuplet, the fraction of unresolved, pre-interaction binaries is about 20% with $\log M/\mathrm{M_\odot} \geq 1.56$ ($M \approx 36\,\mathrm{M_\odot}$) and about 10% with $\log M/\mathrm{M_\odot} \geq 1.60$ ($M \approx 40\,\mathrm{M_\odot}$). The binary fraction among the rejuvenated binary products in the tails is about 55% in our Arches model and 70% in our Quintuplet model, where the remaining stars are single-star binary products, i.e. merger stars.

3.3.2 The ages of Arches and Quintuplet

Previously estimated ages for the Arches and Quintuplet clusters lie in the range 2–$4.5\,\mathrm{Myr}$ (Blum et al. 2001; Figer et al. 2002; Martins et al. 2008) and 2–$5\,\mathrm{Myr}$ (Figer et al. 1999; Liermann et al. 2010, 2012), respectively. Within these ranges, the age discrepancy between the most luminous cluster members, the WN and the less luminous O stars, accounts for about $1\,\mathrm{Myr}$ and $1.5\,\mathrm{Myr}$, respectively (Martins et al. 2008; Liermann et al. 2012), which is eliminated by our method. Our ages of $3.5 \pm 0.7\,\mathrm{Myr}$ and $4.8 \pm 1.1\,\mathrm{Myr}$ for the Arches and Quintuplet clusters, respectively, agree with the ages derived from the O stars and dismiss the proposed younger ages from the brightest stars as a result of neglecting binary interactions. The most famous member of the Quintuplet cluster, the Pistol star, is such an example because it appears to be younger than $2.1\,\mathrm{Myr}$ assuming single-star evolution (Figer et al. 1998).

3.4 Stochastic sampling of binary populations

The initial mass of the primary star, the mass ratio and the orbital period of a binary system determine when mass transfer starts, with more massive and/or closer binaries interacting earlier. Stochastic effects caused by the limited stellar mass budget prevent the formation of all possible binaries in a stellar cluster, i.e. binaries with all possible combinations of primary mass, mass ratio and orbital period. The likelihood that a binary in a given cluster interacts, e.g., after 2 Myr and that the binary product becomes then the most massive star depends thus on the number of binary stars in that cluster and hence on the total cluster mass. Using Monte Carlo simulations, we investigate the influence of stochastic sampling and binary evolution on the most massive stars in young star clusters (see Sec. 3.2.3).

The Galactic star cluster NGC 3603YC contains NGC 3603-A1, a binary star with component masses $(116 \pm 31)\,M_\odot$ and $(89 \pm 16)\,M_\odot$ in a 3.77 d orbit (Schnurr et al. 2008). An initially $120 + 90\,M_\odot$ binary in a 3.77 d orbit starts mass transfer ~ 1.4 Myr after its birth according to the nonrotating models of Ekström et al. (2012). This is the time needed for the $120\,M_\odot$ primary star to fill its Roche lobe as a result of stellar evolutionary expansion. This time provides an upper age estimate for NGC 3603 YC. After mass transfer, the secondary star will be the most massive star in the cluster. Were NGC 3603-A1 in a closer orbit, it could already be a binary product today.

To find the probability that the most massive star in a cluster of a given age is a binary product, we investigate how many close binaries are massive enough to become the most massive star by mass transfer. Were the cluster a perfect representation of the initial stellar distribution functions, we could use these functions to derive the probability directly. However, the finite cluster mass and hence sampling density must be considered for comparison with real clusters. Returning to the example of NGC 3603 YC, if the cluster had larger total mass, its binary parameter space would be better sampled and its most massive star might already be a binary interaction product. For perfect sampling, i.e. infinite cluster mass, the time until a binary product is the most massive star tends toward zero.

The idea that the most massive star in a star cluster may be a binary product resulted from the first discovery of blue straggler stars (Sandage 1953). It was proposed that blue stragglers might stem from binary mass transfer and/or stellar collisions (McCrea 1964; Hills & Day 1976). Stellar population synthesis computations including binary stars then showed that this is indeed possible (e.g. Collier & Jenkins 1984; Pols & Marinus 1994; van Bever & Vanbeveren 1998; Hurley et al. 2001; Chen & Han 2009). Here, we show, using the binary distribution functions of Sana et al. (2012), that the formation of blue stragglers by binary interactions prevails up to the youngest and most massive clusters and we quantify it for the Arches and Quintuplet clusters.

In Fig. 3.3, we show the average time $\langle \tau_{\rm B} \rangle$ after which the most massive star in a star cluster is a product of binary evolution as a function of the cluster mass $M_{\rm cl}$ for two different primordial binary fractions $f_{\rm B}$. The error bars are 1σ standard deviations of 1000 Monte Carlo realisations. The slope of the mass function is $\Gamma = -0.7$, appropriate for the mass-segregated central regions of both Arches and Quintuplet. The more massive a star cluster is, i.e. the more stars that populate the multidimensional binary parameter space, the shorter this average time is because the probability for systems that interact early in their evolution is increased. For less massive clusters $\langle \tau_{\rm B} \rangle$ increases and the statistical uncertainty grows. For example, if $M_{\rm cl} = 10^3\,M_\odot$, there are only about 16 ± 3 binaries in which at least one star has a mass above $10\,M_\odot$ (for $\Gamma = -0.7$ and $f_{\rm B} = 100\%$). The same reasoning holds for different binary fractions: the higher
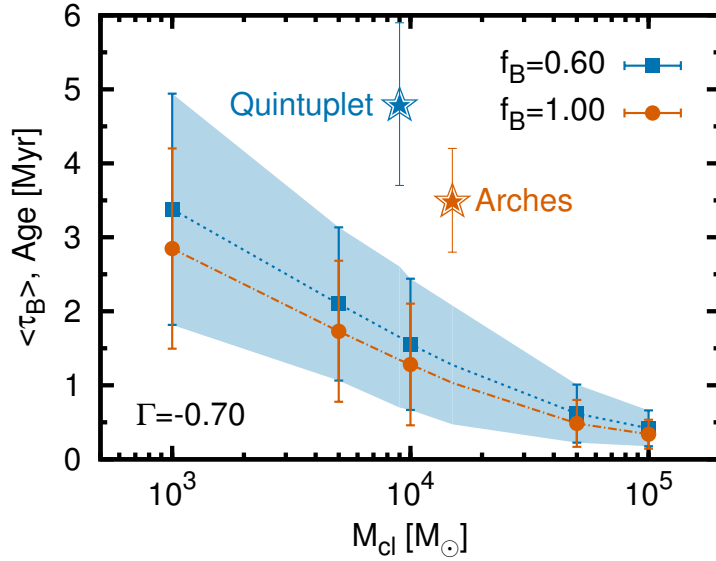
Figure 3.3: Average time $\langle \tau_B \rangle$ until the most massive star in a star cluster is a product of close binary evolution as a function of cluster mass for two primordial binary fractions, f_B, and a mass function slope $\Gamma = -0.7$. For steeper, Salpeter-like mass functions see Fig. 3.4. The error bars are the standard deviation of 1000 realisations of each cluster. The star symbols indicate the age and *central* cluster mass of Arches and Quintuplet as derived in this work.

the binary fraction is, the more binaries there are and hence the shorter the average time is until the most massive star results from binary interactions.

With a Salpeter mass function ($\Gamma = -1.35$, Salpeter 1955) the average time until the most massive star is a binary product increases compared to $\Gamma = -0.7$ (Fig. 3.4) because fewer massive binaries interact to form the most massive star. Assume a 4 Myr old star cluster has a mass function slope of $\Gamma = -1.35$, a total mass in stars above $1\,M_\odot$ of $M_{cl} = 10^4\,M_\odot$ (i.e. a true cluster mass of $1.9 \times 10^4\,M_\odot$ if stars below $1\,M_\odot$ follow a Kroupa IMF; see Sec. 3.2.3) and a primordial binary fraction of $f_B = 60\%$. From Fig. 3.4, we can then read off after which time the most massive star is expected to be a binary product, namely after 2.5 ± 1.1 Myr.

The central regions of the Arches and Quintuplet clusters have masses of $M_{cl} = 1.5 \times 10^4\,M_\odot$ and $0.9 \times 10^4\,M_\odot$ in stars more massive than $1\,M_\odot$ (Sec. 3.2.3) and ages of 3.5 ± 0.7 and 4.8 ± 1.1 Myr (Sec. 3.3.1), respectively. From Fig. 3.3, we expect that the most massive star is a binary product after 1.0 ± 0.7 Myr in the Arches cluster and after 1.7 ± 1.0 Myr in the Quintuplet cluster.

In Fig. 3.5 we show the probability that the most massive star is a binary product and the average number of stars that are more massive than the most massive genuine single star as a function of cluster age for different cluster masses and two different binary fractions. The IMF slope is $\Gamma = -0.7$. The corresponding probabilities and average numbers for a Salpeter ($\Gamma = -1.35$) mass function are shown in Fig. 3.6. Again, the error bars are 1σ standard deviations from 1000 Monte Carlo experiments. Returning to the above-mentioned example star cluster ($M_{cl} = 10^4\,M_\odot$): from Fig. 3.6, we find that the most massive star is a binary product with a probability of 88% and that the most massive 2.1 ± 1.4 stars are expected to be binary products for the exemplary cluster age of 4 Myr.

Given the ages of the Arches and Quintuplet clusters, we find a probability of $> 99.9\%$ that
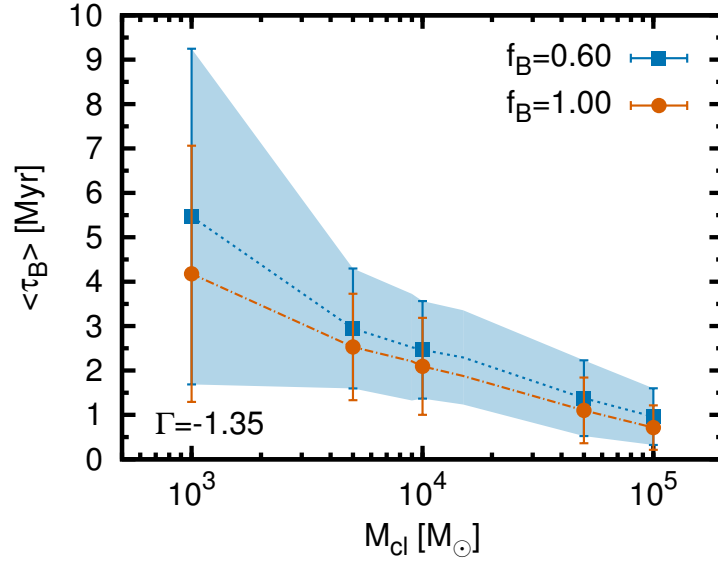
Figure 3.4: As Fig. 3.3, but for a steeper mass function with a Salpeter slope of $\Gamma = -1.35$. The binary parameter space spanned by the initial mass ratios and initial orbital separations for massive primary stars is now less populated, resulting in increased average times until the most massive star is a binary product. Similarly, the standard deviations increase.
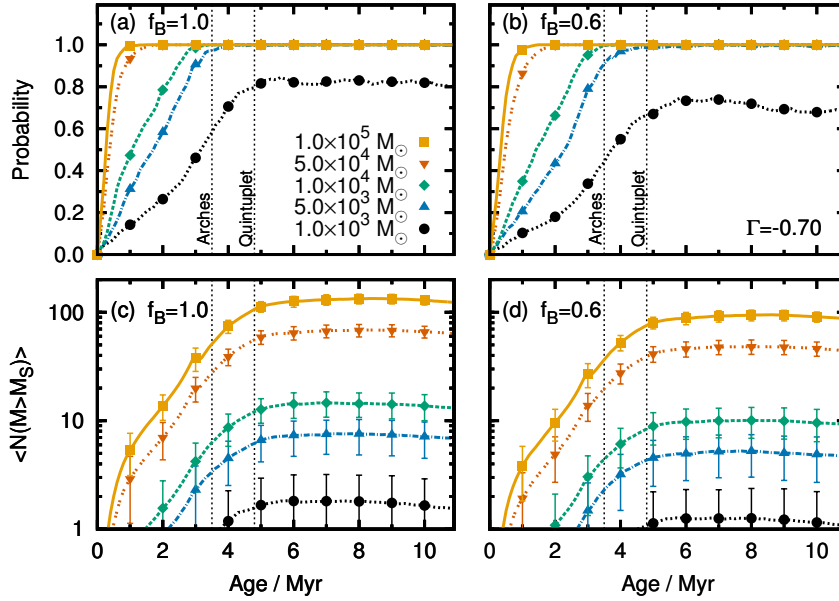
Figure 3.5: (a, b) Probability that the most massive star in a young star cluster is a product of binary evolution and (c, d) average number of stars more massive than the most massive genuine single star $\langle N(M > M_{\rm S}) \rangle$ as a function of age for several cluster masses $M_{\rm cl}$. The left panels have a binary fraction of 100% whereas the right panels have a binary fraction of 60%. The symbols represent different cluster masses $M_{\rm cl}$ and the error bars correspond to the 1σ standard deviation of 1000 realisations per cluster mass. The vertical dashed lines indicate the ages of the Arches and the Quintuplet clusters. The adopted IMF slope is $\Gamma = -0.7$.
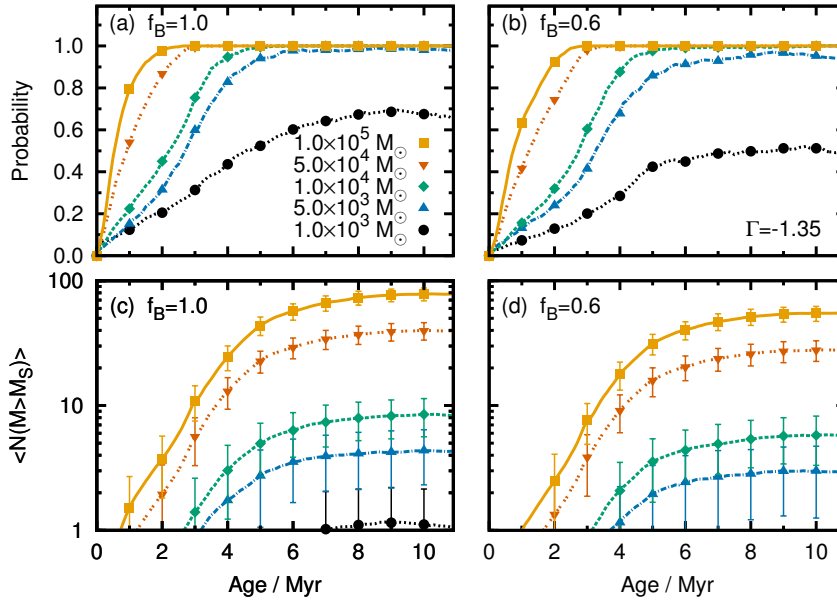
Figure 3.6: As Fig. 3.5, but with a Salpeter mass function, i.e. slope of $\Gamma = -1.35$. The relative fraction of massive stars in each cluster is reduced compared to $\Gamma = -0.7$.

the most massive star in each cluster is a binary product, with the most massive 9.2 ± 3.0 and 7.5 ± 2.8 stars being products of binary evolution in Arches and Quintuplet, respectively. This is compatible with the number of WNh stars in the cores of Arches and Quintuplet, which are the most luminous and hence most massive stars in these clusters, implying they are massive blue stragglers.

3.5 The stellar upper mass limit

Data from two star clusters provide the current evidence for the existence of an upper stellar mass limit around $150 \, M_\odot$: the Arches cluster in the Galactic Center (Figer 2005) and the R136 cluster in the Large Magellanic Cloud (Weidner & Kroupa 2004; Oey & Clarke 2005; Koen 2006). However, according to our analysis an upper mass limit cannot be derived from the Arches cluster because (1) it is too old, hence the most massive stars already exploded, and (2) its present-day high-mass star population is dominated by binary products. The situation might be different in the R136 cluster: current age estimates lie in the range 1–4 Myr (Hunter et al. 1995; Massey & Hunter 1998; de Koter et al. 1998; Andersen et al. 2009; Crowther et al. 2010). In the following we assume that the cluster is young enough such that even the most massive stars have not yet evolved off the main sequence, to explore what we can learn from R136 about a possible stellar upper mass limit.

Four stars in R136 with initial masses of 165–$320 \, M_\odot$ appear to exceed the currently discussed upper mass limit of $150 \, M_\odot$ (Crowther et al. 2010). Either these stars were born with masses exceeding $150 \, M_\odot$ or gained mass from other stars, e.g. by binary interactions (this work) or dynamically induced stellar mergers (Portegies Zwart et al. 1999; Banerjee et al. 2012b).

From our Monte Carlo simulations (Sec. 3.4), we cannot judge with high enough confidence whether the most massive star in R136 is expected to be a binary product or not because of

the uncertain age of R136. R136 has an IMF with approximately a Salpeter slope $\Gamma = -1.35$ (Massey & Hunter 1998) and its cluster mass is $5\text{–}10 \times 10^4 \, \text{M}_\odot$ (Hunter et al. 1995; Andersen et al. 2009; Hénault-Brunet et al. 2012). From our Monte Carlo simulations of star clusters with binary fractions of 60% and cluster masses M_cl of $5 \times 10^4 \, \text{M}_\odot$ and $10^5 \, \text{M}_\odot$ (Fig. 3.6), we find that the most massive star is expected to be a binary product after $1 \, \text{Myr}$ with probabilities of 42% and 63%, respectively. The probabilities increase to 74% and 92%, respectively, for a cluster age of $2 \, \text{Myr}$ and are larger than 98% for an age of $3 \, \text{Myr}$. So if the cluster is older than about $2 \, \text{Myr}$, the most massive star is likely a binary product (note that our calculations are for a metallicity of $Z = 0.02$, whereas the R136 cluster in the Large Magellanic Cloud has a lower metallicity — so the above numbers will slightly change for the appropriate metallicity but are good enough for this estimate). Because it is not clear whether the most massive star in R136 is a binary product or not, we explore both possibilities.

With Monte Carlo simulations, we investigate the likelihood of finding the observed 280–$320 \, \text{M}_\odot$ stars (Crowther et al. 2010) in R136. We randomly sample R136-like star clusters for different adopted stellar upper mass limits M_up using the observed IMF slope (Massey & Hunter 1998) of $\Gamma = -1.35$, a binary fraction of 70% and the fact that R136 contains about 650 stellar systems more massive than $10 \, \text{M}_\odot$ (Hunter et al. 1997). We then compute the average number of stars that are initially more massive than a given mass M, $\langle N_{\geq M} \rangle$, and the probability that at least one star is more massive than M, $P_{\geq M}$, by repeating each experiment 1000 times (the quoted errors are 1σ standard deviations). The average numbers and probabilities for the case that binary interactions did not yet take place are summarised in Table 3.1. For the case where binary interactions already took place, we assume that all massive binaries with initial periods $P_\text{i} \leq 5 \, \text{days}$ interact by mass transfer (which happens within $2\text{–}3 \, \text{Myr}$) and that the postinteraction mass is 90% of the total binary mass. The corresponding average numbers and probabilities for this case can be found in Table 3.2. In both Tables. 3.1 and 3.2, we also give the results for less massive clusters with 100 and 350 stellar systems initially exceeding $10 \, \text{M}_\odot$.

Through binary mergers, stars of up to $300 \, \text{M}_\odot$ can be produced if the star formation process stops at an upper mass of $150 \, \text{M}_\odot$. However, this scenario requires equal-mass O-type binaries, which are rare (Sana et al. 2012, 2013). We find that with an upper mass of $150 \, \text{M}_\odot$, the probability of forming stars in excess of $275 \, \text{M}_\odot$ in R136 is zero[1]. With an upper mass limit of $175 \, \text{M}_\odot$, the probability of forming at least one star of mass $M \geq 275 \, \text{M}_\odot$ increases to 7.0%, and for an upper mass limit of $\sim 200 \, \text{M}_\odot$, the probability of forming at least one star exceeding $275 \, \text{M}_\odot$ and $300 \, \text{M}_\odot$ is 22.8% and 10.6%, respectively. Thus, $200 \, \text{M}_\odot$ provides a lower limit on the maximum stellar birth mass.

It is also unlikely that the upper mass limit exceeds $350 \, \text{M}_\odot$ because then the probability of forming one star above $350 \, \text{M}_\odot$ by binary mass transfer increases to 50.5% but such massive stars are not observed. We conclude that an upper mass limit in the range of about $200\text{–}350 \, \text{M}_\odot$ is needed to explain the most massive stars in R136 by binary evolution.

Dynamically induced stellar coalescence was proposed as a mechanism to produce the very massive stars in R136 (Portegies Zwart et al. 1999; Banerjee et al. 2012b). However, *N*-body simulations of dynamically induced stellar coalescence typically only produce one to two stars, in one case up to four, exceeding $200 \, \text{M}_\odot$ for R136 when adopting an upper mass limit of $150 \, \text{M}_\odot$ (Banerjee et al. 2012b), i.e. fewer than observed in R136. Furthermore, the rate of dynamically induced mergers in these simulations should be viewed as an upper limit only. Observational

---

[1] Given our assumptions, the maximum achievable postinteraction mass is 90% of the total system mass, i.e. $270 \, \text{M}_\odot$ for $M_\text{up} = 150 \, \text{M}_\odot$

results indeed favour a larger half-mass radius (Hunter et al. 1995; Hénault-Brunet et al. 2012), hence a lower density compared to the simulation assumptions. Similarly, adopting the recent measurements of the orbital distributions of massive binaries (Sana et al. 2012, 2013) further decreases the number of possible dynamical mergers that can overcome the $150\,M_\odot$ limit by a factor of 3.5 to 4.0. It appears thus unlikely that dynamically induced stellar coalescence is sufficiently efficient to explain the origin of the very massive stars in R136 if the upper mass limit is $150\,M_\odot$.

As mentioned above, it is also possible that the four massive stars in R136 were born with their deduced initial masses and did not gain mass by other means. This provides then an upper limit on the maximum stellar birth mass. The most massive star found in R136 has an initial mass of $320^{+100}_{-40}\,M_\odot$ (Crowther et al. 2010) — hence, the upper mass limit has to be at least of this order, i.e. $\gtrsim 280\,M_\odot$. This initially $320\,M_\odot$ star allows us to exclude an upper mass limit of $M_{\rm up} = 10^4\,M_\odot$ with 96% confidence because we expect to find 3.2 ± 1.8 stars that initially exceed $500\,M_\odot$ in this case, although no such star is observed. However, it becomes more difficult to exclude an upper mass limit of $500\,M_\odot$ or less because the probability of finding *no* star that initially exceeds $350\,M_\odot$ $(1 - P_{\geq 350})$ is about 13%; in other words, no star would initially exceed $350\,M_\odot$ in about every tenth R136-like star cluster for an upper mass limit of $500\,M_\odot$. The probability increases further to 39% for an upper mass limit of $400\,M_\odot$. We conclude that stochastic sampling effects are important even in the richest massive star clusters in the Local Group.

Altogether, we find that current data do not exclude an upper mass limit as high as 400–$500\,M_\odot$ if binary interactions are neglected. However, the most massive star in R136 is a binary product with a probability of $\gtrsim 40$–60%. Including effects of close binary evolution, an initial stellar upper mass limit of at least $200\,M_\odot$ is required to explain the observed stars with apparent initial masses of about $300\,M_\odot$. The upper mass limit is thus in the range 200–$500\,M_\odot$, thereby solving the maximum mass problem.

3.6 Uncertainties

There are several sources of uncertainty that affect theoretical and observed mass functions and hence e.g. our cluster ages derived from them. It is important to understand the uncertainties to estimate their influence on our conclusions and the derived quantities. The conclusion that binary effects shape the upper end of the stellar mass function remains unaffected. In Sec. 3.6.1, we discuss modelling uncertainties because of the fitting procedure, stellar wind mass loss, binary star evolution and rotation. Observational uncertainties such as the influence of different reddening laws on derived stellar masses of stars in the Galactic Center are discussed in Sec. 3.6.2. We discuss the influence of dynamical interactions on stellar mass functions in Sec. 3.6.3. Star formation histories that are different from single starbursts are considered in Sec. 3.6.4 to investigate whether such scenarios are also consistent with the observed age spread among the most massive stars and the resulting stellar mass functions.

3.6.1 Modelling uncertainties

3.6.1.1 Fitting uncertainties

Stars in the wind mass loss peak of the mass function will very soon leave the main sequence. The mass of these turn-off stars is a sensitive function of cluster age especially for massive

stars, which radiate close to the Eddington limit. Massive stars have lifetimes that depend only weakly on mass and hence a small change in age corresponds to a large change in mass. We cannot reproduce the observed mass functions of Arches and Quintuplet if we change the age of our models in Fig. 3.2 by more than 0.2–0.3 Myr. We therefore adopt 0.3 Myr as the age uncertainty associated with our fitting.

The initial binary fraction is best constrained by the number of stars in the mass function tail because it consists only of either postinteraction or preinteraction, unresolved binaries. In contrast, the wind mass loss peak changes little with the binary fraction. Our observational sample is limited by the exclusion of WNh stars in both Arches and Quintuplet because no reliable masses of the WNh stars could be determined (see Sec. 3.2.4. We thus cannot determine the primordial binary fractions accurately, especially because the tail of the Quintuplet mass function is not very pronounced. Increasing the age of our Quintuplet model by 0.1 Myr allows for 100% binaries while maintaining a satisfactory, albeit slightly inferior to the best, fit to the mass function. Both clusters are thus consistent with having the same primordial binary fraction.

3.6.1.2 Stellar wind mass loss

Our wind mass loss prescription (Nieuwenhuijzen & de Jager 1990) slightly underestimates stellar winds compared to the latest predictions (Vink et al. 2000, 2001). Compared to the most recent stellar evolution models of Ekström et al. (2012), which use the prescriptions of Vink et al. (2000, 2001), we find that our turn-off masses agree to within $2 - 3\%$ for initial masses $\lesssim 50 \, M_\odot$, while in more massive stars our turn-off mass is up to 15% larger, mainly because of the applied Wolf–Rayet wind mass loss rates in Ekström et al. (2012).

The widths of the bins in our model mass functions are 0.04 dex; that is masses differ by about 10% from bin to bin. The observed mass functions have bin sizes of 0.2 dex; that is masses are different by 59% from bin to bin. Wind mass loss prescriptions that lead to stellar masses at the end of the MS that differ by only a few percent result in indistinguishable mass functions — our mass functions and conclusions are therefore essentially independent of whether the empirical wind mass loss prescription of Nieuwenhuijzen & de Jager (1990) or the theoretical prescription of Vink et al. (2000, 2001) is used.

Augmenting our wind loss rate by 70%, we find that an initially $85 \, M_\odot$ star has a turn-off mass of about $49 \, M_\odot$ which matches the recent stellar models by Ekström et al. (2012) (compared to $\sim 58 \, M_\odot$ in our standard model). With the enhanced wind mass loss rate, the Arches wind mass loss peak corresponds to an initially $\sim 85 \, M_\odot$ star with a main sequence lifetime of 3.3 Myr, compared to $70 \, M_\odot$ and 3.5 Myr, respectively, in our standard model. The Quintuplet wind mass loss peak comes from initially $\sim 40 \, M_\odot$ stars for which the uncertainty in wind mass loss is $< 3\%$. Our Quintuplet age estimate is thus robust with respect to the wind mass loss rate uncertainty.

3.6.1.3 Binary star evolution

Our understanding of binary star evolution in general is subject to uncertainties. Uncertainties that directly influence the shape of the mass function tails are discussed in Schneider et al. (subm.). A further, more quantitative discussion of uncertainties in binary star evolution is found in de Mink et al. (2013) and de Mink et al. (2014). Here, we restrict ourselves to MS stars, i.e. to mergers of two MS stars and mass transfer onto MS stars. Mergers that involve a

post-MS star form a post-MS object and are thus not considered here.

We assume that two MS stars merge if the mass ratio of the accretor to donor star is less than 0.56. This threshold is calibrated against the detailed binary models of de Mink et al. (2007) and is of limited relevance to our results: if a binary does not merge but instead transfers mass (or vice versa), the accretor becomes massive because the mass transfer efficiency of MS stars is high (e.g. Wellstein et al. 2001; Langer 2012). In either case, the mass gainer will be a massive star (de Mink et al. 2013). The expected binary fraction of stars in the tail of the mass functions however changes: a lower critical mass ratio leads to fewer MS mergers and hence to a higher binary fraction and vice versa.

The amount of rejuvenation of MS mergers is determined by the amount of mixing of fresh fuel into the core of the merger product and determines by how much the lifetime of the merger product is prolonged. The more rejuvenation there is, the longer the remaining MS lifetime is and the more mergers are expected to be found. We assume that a fraction of 10% of the envelope is mixed into the core, resulting into fairly short remaining MS lifetimes of the merger products compared to the assumption of complete mixing used in the original Hurley et al. (2002) code. Recent simulations of massive mergers seem to support the mild mixing as used in our work (Glebbeek et al. 2013, and references therein).

The mass transfer efficiency is important for our results. The more the transferred mass is accreted during RLOF, the larger the final mass of the accreting star is. The maximum reachable mass of any accretor is given by the total mass of the binary (i.e. at most twice the mass of the donor star) and the larger the overall mass transfer efficiency, the more binary products exceed the most massive genuine single star. In our models, we limit the mass accretion rate to the thermal timescale of the accretor, which results in higher mass transfer efficiencies the larger the mass ratio is and the closer the binary is (see Schneider et al. subm.). This idea is motivated by detailed binary evolution models (e.g. Ulrich & Burger 1976; Kippenhahn & Meyer-Hofmeister 1977; Neo et al. 1977; Pols & Marinus 1994; Wellstein et al. 2001).

The initial distributions of primary masses, mass ratios and orbital separations determine the relative fraction of stars that will merge, transfer mass etc. It turns out that the distribution of orbital separations influences the incidence of binary products most (de Mink et al. 2013, 2014) because initially close binaries transfer mass, on average, more efficiently than wider binaries. A distribution of initial orbital separations that favours close binaries therefore leads to, on average, more massive binary products than distribution functions that favour initially wider binaries.

A more quantitative assessment of the above-quoted uncertainties in binary evolution and initial binary distribution functions reveals that a population of MS stars with luminosities $L > 10^4 \, \mathrm{L_\odot}$ (i.e. O and B stars) contains about $30^{+10}_{-15}\%$ binary products if continuous star formation is assumed (de Mink et al. 2014). All in all, depending on the exact assumptions regarding binary evolution, there will be more or fewer stars in the tail of the mass function. However, the peak–tail structure never disappears unless it is assumed that neither MS mergers nor RLOF are able to increase stellar masses which is unphysical.

3.6.1.4 Stellar rotation

Mixing induced by stellar rotation increases the fuel available to a star and increases its lifetime. The amount of mixing grows with increasing mass, increasing rotation rate and decreasing metallicity and may contribute to the observed age spreads and mass function tails in Arches and Quintuplet. The models of Brott et al. (2011a) show that the MS lifetime of a $60 \, \mathrm{M_\odot}$

star lengthens by $0.2\,\mathrm{Myr}$ and $0.6\,\mathrm{Myr}$ for initial rotational velocities of 300 and $500\,\mathrm{km\,s^{-1}}$, respectively. Assuming that the present-day distribution of rotational velocities of Galactic O and B stars approximately represents the initial distribution, no more than 10% and less than 1% of stars would have initial rotation rates exceeding 300 and $500\,\mathrm{km\,s^{-1}}$, respectively, and are thus expected to be influenced significantly by rotational mixing (see Table 2 in de Mink et al. 2013, and references therein). This is small compared to the 40% of all O stars that undergo strong binary interaction during their main sequence evolution (Sana et al. 2012). The present-day distribution of rotational velocities is probably altered e.g. by binary star evolution such that some of the fast rotators are expected to have gained their fast rotation by binary interactions (de Mink et al. 2013, but see also Ramírez-Agudelo et al. 2013). In this respect, the expected fraction of genuine Galactic single stars that are significantly affected by rotational mixing is even smaller than the above-quoted fractions. The effect of rotation is thus only of limited relevance to our results compared to binary star interactions.

3.6.2 Observational uncertainties

There are two steps involved in determining stellar masses from photometric observations that contribute to the uncertainties of the derived individual stellar masses. The first step involves the conversion of the observed apparent magnitudes (fluxes) to absolute magnitudes and luminosities, respectively, taking, among other things, the distance and extinction into account. The second step involves the conversion of luminosities to stellar masses. This step relies upon mass–luminosity relations that depend on (in general a priori unknown) stellar ages and the applied stellar models. In this section, we estimate the uncertainty on individual stellar masses introduced by these two steps for stars in Arches and Quintuplet. Once we know the uncertainties, we can apply them to the turn-off masses derived from the wind mass loss peak in the mass function to find the corresponding uncertainty in cluster age.

In the top panel of Fig. 3.7 we show main sequence mass–luminosity relations of Milky Way stars of different ages as used in our code (based on Hurley et al. 2000). Not knowing the exact age of a star, but only a probable age range (here 2.0–$3.5\,\mathrm{Myr}$), introduces an uncertainty ΔM on the derived individual stellar masses (cf. lower panel in Fig. 3.7). The more evolved and the more massive a star is, the larger the uncertainty is. If we additionally include the uncertainty in the luminosity (here $\pm 0.2\,\mathrm{dex}$; see below) the uncertainty in the stellar mass grows to $\Delta M'$. The uncertainty in luminosity is the dominant contribution here.

The uncertainties presented in Fig. 3.7 are tailored to stars in the Arches cluster where stellar masses have been derived by Stolte et al. (2005) using a $2\,\mathrm{Myr}$ isochrone (mass–luminosity relation) whereas our analysis reveals an age of about $3.5\,\mathrm{Myr}$ — hence the 2.0–$3.5\,\mathrm{Myr}$ age range for the mass–luminosity relations. Deriving individual stellar masses using two different extinction laws, Habibi et al. (2013) find that stellar masses can deviate by up to 30% when either a Nishiyama et al. (2009) extinction law or the traditional Rieke & Lebofsky (1985) law toward the Galactic Center are used. As the appropriate extinction law toward the Galactic Center line of sight is still a matter of debate, we adopt uncertainties of $\pm 0.2\,\mathrm{dex}$ on luminosities to be in line with the work of Habibi et al. (2013). The situation is similar in Quintuplet: we find slightly smaller uncertainties on derived stellar masses than given in Fig. 3.7 for uncertainties of $\pm 0.2\,\mathrm{dex}$ on luminosities and an age range of 4–$5\,\mathrm{Myr}$. To be conservative, we adopt an uncertainty of $\pm 30\%$ (i.e. $\Delta M'/M = 60\%$) for individual stellar masses in both clusters, which agrees with the diversity of mass estimates in the literature for stars in Arches.

Habibi et al. (2013) find stellar masses that are up to 30% less than those of our analysis for
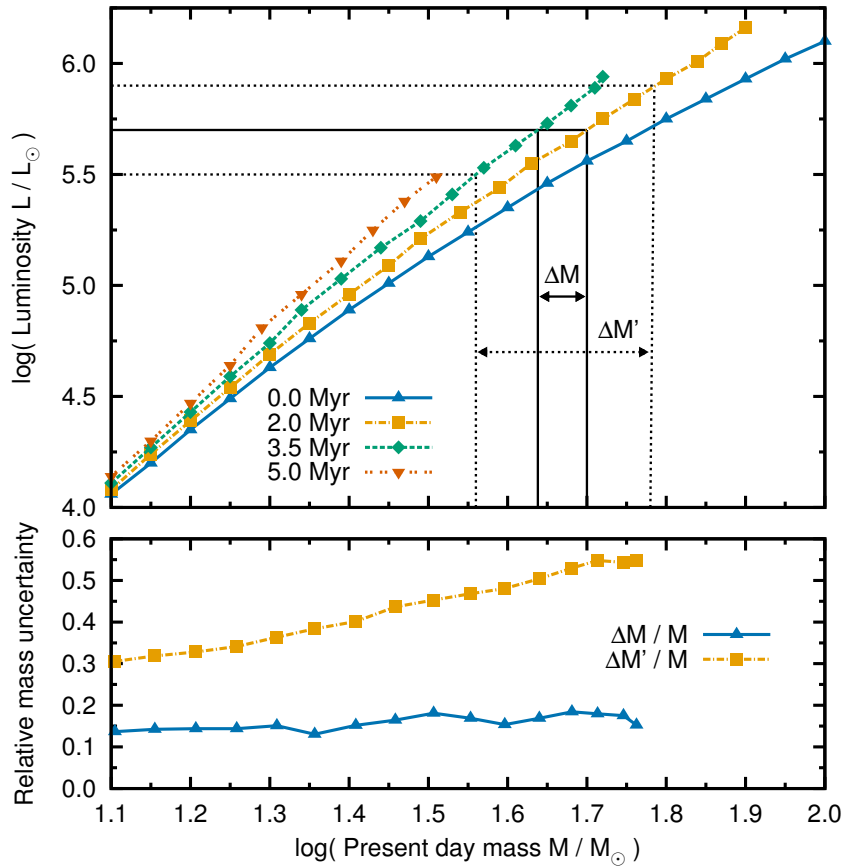
Figure 3.7: Uncertainties on derived individual stellar masses introduced by unknown a priori stellar ages, $\Delta M/M$, and by the combined effect of unknown stellar ages and uncertain luminosities, $\Delta M'/M$. The top panel illustrates how we estimate these uncertainties for a star with luminosity $\log L/\mathrm{L}_\odot = 5.7 \pm 0.2$ using the main-sequence mass–luminosity relations of different ages from our code (Hurley et al. 2000). The bottom panel shows the uncertainties as a function of mass.

a Nishiyama et al. (2009) extinction law. An independent study of the Arches present-day mass function (Kim et al. 2006) shows a similar peak–tail structure at the high-mass end using a different extinction law and the derived masses are comparable to those of our analysis (Stolte et al. 2005). Masses in excess of $150\,\mathrm{M}_\odot$ — i.e. larger than our masses — have been suggested for the most luminous stars in the Arches cluster by Crowther et al. (2010). Hence, an uncertainty of $\pm 30\%$ applied to our adopted stellar masses covers the complete range of suggested masses for stars in Arches.

The overall structure of the mass functions of Arches and Quintuplet — a stellar wind peak and binary tail — is robust to the mentioned uncertainties. We also find the peak–tail structure in the mass function of Habibi et al. (2013) and in mass functions constructed from the photometric data of Stolte et al. (2005) and Hußmann et al. (2012), respectively, using isochrones of different ages. The whole mass functions shift in mass, but the relative structure stays the same. The reason is that different extinction laws or isochrones systematically influence all stars in a similar way and do not introduce differential effects.

Applying $\pm 30\%$ uncertainties on stellar masses leads to turn-off masses of the Arches and Quintuplet of about $70 \pm 21\,\mathrm{M}_\odot$ and $40 \pm 12\,\mathrm{M}_\odot$, with associated age uncertainties of ± 0.6 and

$\pm 1.1\,$Myr, respectively.

3.6.3 Dynamical interactions in star clusters

The observed present-day mass functions are influenced by dynamical cluster evolution (Harfst et al. 2010, and references therein). Flat mass function slopes of the order of $\Gamma = -0.7$, compared to a Salpeter IMF slope of $\Gamma = -1.35$, are likely a consequence of mass segregation in which massive stars sink toward the cluster center For the Arches cluster, Habibi et al. (2013) show that a dynamical model with a standard Salpeter IMF explains the steepening of the IMF slope toward larger distances from the cluster center. While the conclusion is more elusive for the dispersed Quintuplet population, the similarity of the mass function slopes in the inner regions of both clusters and the older age of Quintuplet suggest that similar processes have shaped the present-day mass function of this cluster as well.

We further investigate whether dynamical interactions in star clusters can also cause the peak in the observed mass functions. Mass segregation flattens the high-mass end of the mass function without producing a peak (Portegies Zwart et al. 2007) while dynamical ejection of stars works on all stars with an ejection efficiency monotonically increasing with mass (Fujii & Portegies Zwart 2011; Perets & Šubr 2012; Banerjee et al. 2012a) as confirmed by the observed Galactic fraction of runaway O stars which is larger than that of runaway B stars (Gies & Bolton 1986; Stone 1991). Such a smoothly increasing ejection efficiency does not create a peak in the mass function but can give rise to a tail that is, however, not seen in the mass functions of *N*-body simulations of the Arches cluster (Portegies Zwart et al. 2007; Harfst et al. 2010).

3.6.4 Star formation histories

Star formation is not an instantaneous process but lasts a finite amount of time. Observations show that there is an empirical relationship between the duration of star formation and the crossing time of star clusters (Elmegreen 2000). For example, in Westerlund 1 and NGC 3603YC the age difference among stars less massive than about $11.5\,M_\odot$ and $6.5\,M_\odot$ shows that they were formed within at most 0.4 and 0.1 Myr (Kudryavtseva et al. 2012), respectively, which compares well to the cluster crossing times of 0.3 Myr (Brandner et al. 2008) and 0.1 Myr (Pang et al. 2010).

The core of the Arches cluster has a radius of about 0.23 pc (Figer et al. 2002) and a velocity dispersion of $5.7\,\mathrm{km\,s^{-1}}$ (Clarkson et al. 2012) at a distance of 8.0 kpc corresponding to a crossing time, and hence a duration of star formation, of about 0.04 Myr. A similar estimate for the Quintuplet cluster is more uncertain because the core radius and especially the velocity dispersion are not well known. If we assume that the observed central region of Quintuplet with a radius of about 0.5 pc (Hußmann et al. 2012) corresponds to the core radius and that the velocity dispersion is about $17\,\mathrm{km\,s^{-1}}$ (Liermann et al. 2009), the crossing time is 0.03 Myr. The mass functions produced by such short periods of star formation are indistinguishable from an instantaneous starburst. The apparent age spread among the most luminous stars in Arches and Quintuplet is about 1–1.5 Myr (Martins et al. 2008; Liermann et al. 2012) and hence much larger than the estimated star formation periods.

In the Sec. 3.8.1 we investigate whether a star formation history that is different from a single starburst can also explain the observed peak–tail structure in the mass functions of Arches and Quintuplet. We find that this is possible with e.g. a two-stage starburst but the age spread among the most massive stars would then be inconsistent with observations.

3.7 Conclusions

Massive stars rapidly change their mass, thereby altering the stellar mass function. Stellar wind mass loss reduces stellar masses such that stars accumulate near the high-mass end of present-day mass functions, creating a bump whose position reveals the mass of the turn-off stars and hence the age of young star clusters (Schneider et al. subm.). Binary stars are frequent and important for massive star evolution because of binary mass exchange (Sana et al. 2012): mass transfer and stellar mergers increase stellar masses and create a tail of rejuvenated binary products at the high-mass end of mass functions (Schneider et al. subm.). We model the observed mass functions of the young Arches and Quintuplet star clusters (Stolte et al. 2005; Hußmann et al. 2012) using a rapid binary evolution code (Hurley et al. 2002; Izzard et al. 2004, 2006, 2009) to identify these two features and to address two pressing controversies:

1. *The cluster age problem.* The most massive stars in Arches and Quintuplet, the WNh stars, appear to be younger than the less massive O stars (Martins et al. 2008; Liermann et al. 2012). This is not expected from star cluster formation (Elmegreen 2000; Kudryavtseva et al. 2012) but is well known in older clusters under the blue straggler phenomenon.

2. *The maximum mass problem.* A stellar upper mass limit of $150\,\mathrm{M}_\odot$ is observationally determined (Weidner & Kroupa 2004; Figer 2005; Oey & Clarke 2005; Koen 2006). In contrast, SN 2007bi is thought to be a pair-instability supernova from an initially $250\,\mathrm{M}_\odot$ star (Gal-Yam et al. 2009; Langer 2009) and four stars greatly exceeding this limit are found in the R136 cluster in the Large Magellanic Cloud (Crowther et al. 2010).

We identify the peak and tail in the observed mass functions of the Arches and Quintuplet clusters. By fitting our models to the observations, we determine the ages of Arches and Quintuplet to be $3.5 \pm 0.7\,\mathrm{Myr}$ and $4.8 \pm 1.1\,\mathrm{Myr}$, respectively. This solves the age problem because the most massive stars in Arches and Quintuplet are rejuvenated products of binary mass transfer and the ages derived from these stars are therefore significantly underestimated. While our age error bars are still large, mostly because of uncertain absolute magnitudes, our method removes the ambiguity in the age determination. For the age determination of older star clusters, blue stragglers are eminently disregarded when isochrones are fitted to the turn-off in Hertzsprung–Russell diagrams. Our analysis shows that for young star clusters, where the higher fraction of interacting binaries produces even more blue stragglers, they obviously need to be disregarded as well in order to derive the correct cluster age.

Even without modelling the observed mass functions, the ages and also the mass lost by the turn-off stars during their main-sequence evolution can be determined from the mass function alone. Refilling the mass function above the present-day mass of the turn-off stars with the number of excess stars in the wind mass loss peak gives the initial mass of the turn-off stars and hence the cluster age. The derived ages agree with the more accurate ages from detailed modelling of the observed mass functions. According to this new method, the turn-off stars lost 12–$17\,\mathrm{M}_\odot$ of their initial 62–$72\,\mathrm{M}_\odot$ in Arches and 4–$8\,\mathrm{M}_\odot$ of their initial 36–$47\,\mathrm{M}_\odot$ in Quintuplet. This is the first direct measurement of stellar wind mass loss that does not rely on derivations of stellar wind mass loss rates.

Monte Carlo experiments to investigate the effects of stochastic sampling show that the most massive star in the Arches and Quintuplet clusters is expected to be a rejuvenated product of binary mass transfer after $1.0 \pm 0.7\,\mathrm{Myr}$ and $1.7 \pm 1.0\,\mathrm{Myr}$, respectively. At their present age,

the probability that the most massive star in Arches and Quintuplet is a product of binary mass exchange is $> 99.9\%$ and the most massive 9.2 ± 3.0 and 7.5 ± 2.8 stars in Arches and Quintuplet, respectively, are expected to be such rejuvenated binary products.

Our findings have implications for the maximum mass problem. The Arches cluster is older than previously thought and its most massive stars are most likely binary products. The mass function is thus truncated by finite stellar lifetimes and not by an upper mass limit. To constrain a potential stellar upper mass limit, we consider the massive cluster R136 in the Large Magellanic Cloud which is thought to be so young that its initially most massive stars are still alive today. We find that the most massive star is a binary product with a probability of $> 40\%$, depending on the exact, albeit uncertain cluster age (Sec. 3.5). Assuming binaries already interacted, a stellar upper mass limit of at least $200\,\mathrm{M_\odot}$ is needed to form the observed 165–$320\,\mathrm{M_\odot}$ stars in R136. It can also not exceed $350\,\mathrm{M_\odot}$ because then the probability of forming stars above e.g. $350\,\mathrm{M_\odot}$ becomes larger than about 50% — but such stars are not observed. Assuming that no binary interactions changed the masses of the very massive stars in R136, a stellar upper mass limit of up to 400–$500\,\mathrm{M_\odot}$ cannot be fully excluded because of stochastic sampling even in this rich star cluster. The upper mass limit is thus likely in the range 200–$500\,\mathrm{M_\odot}$, thereby solving the maximum mass problem.

We conclude that the most massive stars in the universe may be the rejuvenated products of binary mass transfer. Because of their extreme mass and luminosity, radiation feedback from these stars is crucial to observable properties of young stellar populations, to the state of the interstellar medium around young stellar clusters and even to the reionization of the universe after the big bang. Our results have strong implications for understanding star-forming regions nearby and at high redshift as observationally derived fundamental properties like initial mass functions are based on the assumption that the brightest stars are single and less massive than $150\,\mathrm{M_\odot}$. These very massive stars are thought to die as pair-instability supernovae and produce huge, so far unaccounted for contributions to the chemical enrichment of nearby and distant galaxies (Langer 2012) and their final explosions may be observable throughout the universe. Understanding the most massive stars in young nearby star clusters is an essential step toward investigating these exciting phenomena that shape our cosmos.

3.8 Supplementary material

Table 3.1: Results of our Monte Carlo simulations to determine the stellar upper mass limit without binary interactions. Given are the average number of stars $\langle N_{\geq M} \rangle$ initially more massive than M and the probability $P_{\geq M}$ that at least one star is initially more massive than M for stochastically sampled star clusters as a function of the stellar upper mass limit, M_{up}, and the number of stars, N_{10}, more massive than $10\,M_\odot$. The corresponding total cluster masses, M_{cl}, extrapolated with a Kroupa IMF (Kroupa 2001) down to $0.08\,M_\odot$ are also provided. All stars are assumed to be effectively single, i.e. that no binary interactions took place.

$M_{up}/M_\odot$	$M/M_\odot$	$N_{10} = 100$ $M_{cl} \approx 2 \times 10^4\,M_\odot$		$N_{10} = 350$ $M_{cl} \approx 7 \times 10^4\,M_\odot$		$N_{10} = 650$ $M_{cl} \approx 10^5\,M_\odot$	
		$\langle N_{\geq M} \rangle$	$P_{\geq M}$	$\langle N_{\geq M} \rangle$	$P_{\geq M}$	$\langle N_{\geq M} \rangle$	$P_{\geq M}$
10000	150	2.6 ± 1.6	92.0%	9.0 ± 3.0	99.9%	16.9 ± 4.1	$> 99.9\%$
	200	1.7 ± 1.3	81.8%	6.1 ± 2.5	99.8%	11.3 ± 3.3	$> 99.9\%$
	250	1.3 ± 1.1	71.5%	4.5 ± 2.1	98.2%	8.3 ± 2.9	$> 99.9\%$
	300	1.0 ± 1.0	63.4%	3.4 ± 1.8	96.8%	6.5 ± 2.6	99.9%
	350	0.8 ± 0.9	55.1%	2.8 ± 1.6	94.1%	5.2 ± 2.3	99.6%
	400	0.7 ± 0.8	48.5%	2.3 ± 1.5	90.6%	4.4 ± 2.1	99.2%
	450	0.6 ± 0.7	43.0%	2.0 ± 1.4	86.1%	3.7 ± 1.9	98.1%
	500	0.5 ± 0.7	38.5%	1.7 ± 1.3	81.4%	3.2 ± 1.8	96.3%
1000	150	2.5 ± 1.5	92.5%	8.3 ± 2.8	$> 99.9\%$	15.4 ± 3.9	$> 99.9\%$
	200	1.6 ± 1.2	81.3%	5.4 ± 2.3	99.5%	10.0 ± 3.2	$> 99.9\%$
	250	1.1 ± 1.0	69.1%	3.8 ± 2.0	97.5%	7.0 ± 2.7	99.9%
	300	0.8 ± 0.9	58.0%	2.8 ± 1.7	93.2%	5.2 ± 2.3	99.3%
	350	0.6 ± 0.7	48.4%	2.1 ± 1.4	87.8%	4.0 ± 2.1	97.3%
	400	0.5 ± 0.7	40.0%	1.6 ± 1.2	80.3%	3.1 ± 1.8	94.4%
	450	0.4 ± 0.6	32.8%	1.3 ± 1.1	72.6%	2.5 ± 1.6	91.2%
	500	0.3 ± 0.5	27.4%	1.0 ± 1.0	65.0%	2.0 ± 1.4	86.4%
500	150	2.2 ± 1.5	88.5%	7.3 ± 2.6	$> 99.9\%$	13.3 ± 3.5	$> 99.9\%$
	200	1.3 ± 1.2	73.0%	4.4 ± 2.1	98.5%	8.0 ± 2.7	$> 99.9\%$
	250	0.9 ± 0.9	57.4%	2.8 ± 1.7	94.5%	5.1 ± 2.2	99.5%
	300	0.5 ± 0.7	42.5%	1.9 ± 1.3	84.8%	3.3 ± 1.8	96.3%
	350	0.3 ± 0.6	28.7%	1.1 ± 1.0	68.1%	2.0 ± 1.4	87.3%
	400	0.2 ± 0.4	18.0%	0.7 ± 0.8	48.9%	1.1 ± 1.0	68.7%
	450	0.1 ± 0.3	7.9%	0.3 ± 0.5	24.6%	0.5 ± 0.7	39.0%
	500	0.0 ± 0.0	0.0%	0.0 ± 0.0	0.0%	0.0 ± 0.0	0.0%
400	150	1.9 ± 1.4	84.2%	6.7 ± 2.5	99.9%	12.6 ± 3.5	$> 99.9\%$
	200	1.0 ± 1.0	64.9%	3.7 ± 1.9	97.8%	7.1 ± 2.7	$> 99.9\%$
	250	0.6 ± 0.8	43.1%	2.2 ± 1.4	88.6%	4.1 ± 2.1	97.5%
	300	0.3 ± 0.6	26.5%	1.1 ± 1.0	69.2%	2.2 ± 1.5	89.9%
	350	0.1 ± 0.3	11.4%	0.5 ± 0.7	36.3%	0.9 ± 1.0	60.6%
	400	0.0 ± 0.0	0.0%	0.0 ± 0.0	0.0%	0.0 ± 0.0	0.0%

Table 3.1: continued

$M_{\rm up}/\rm M_\odot$	$M/\rm M_\odot$	$N_{10} = 100$ $M_{\rm cl} \approx 2 \times 10^4\,\rm M_\odot$		$N_{10} = 350$ $M_{\rm cl} \approx 7 \times 10^4\,\rm M_\odot$		$N_{10} = 650$ $M_{\rm cl} \approx 10^5\,\rm M_\odot$	
		$\langle N_{\geq M}\rangle$	$P_{\geq M}$	$\langle N_{\geq M}\rangle$	$P_{\geq M}$	$\langle N_{\geq M}\rangle$	$P_{\geq M}$
300	150	1.7 ± 1.3	81.5%	5.6 ± 2.3	99.7%	10.4 ± 3.2	$> 99.9\%$
	200	0.8 ± 0.9	53.8%	2.6 ± 1.6	93.1%	4.9 ± 2.2	99.1%
	250	0.3 ± 0.6	26.2%	1.0 ± 1.0	61.4%	1.8 ± 1.3	84.9%
	300	0.0 ± 0.0	0.0%	0.0 ± 0.0	0.0%	0.0 ± 0.0	0.0%
200	150	0.9 ± 0.9	56.7%	3.0 ± 1.7	95.9%	5.7 ± 2.4	99.8%
	200	0.0 ± 0.0	0.0%	0.0 ± 0.0	0.0%	0.0 ± 0.0	0.0%

Table 3.2: Results of our Monte Carlo simulations to determine the stellar upper mass limit with binary interactions. As in Table 3.1 but now it is assumed that binary interactions took place in all massive binaries with initial orbital periods shorter than 5 d such that higher masses than the stellar upper mass limit can be achieved because of binary mass transfer. Stars with masses smaller than the upper mass limit are either (effectively) single stars or again products of binary mass exchange in binaries with initial orbital periods shorter than 5 d.

$M_{\rm up}/\rm M_\odot$	$M/\rm M_\odot$	$N_{10} = 100$ $M_{\rm cl} \approx 2 \times 10^4\,\rm M_\odot$		$N_{10} = 350$ $M_{\rm cl} \approx 7 \times 10^4\,\rm M_\odot$		$N_{10} = 650$ $M_{\rm cl} \approx 10^5\,\rm M_\odot$	
		$\langle N_{\geq M}\rangle$	$P_{\geq M}$	$\langle N_{\geq M}\rangle$	$P_{\geq M}$	$\langle N_{\geq M}\rangle$	$P_{\geq M}$
400	150	2.2 ± 1.5	87.7%	7.6 ± 2.8	99.9%	14.2 ± 3.6	$> 99.9\%$
	200	1.3 ± 1.1	70.9%	4.4 ± 2.2	98.4%	8.1 ± 2.8	$> 99.9\%$
	250	0.8 ± 0.9	51.4%	2.6 ± 1.6	92.9%	4.8 ± 2.2	99.3%
	300	0.5 ± 0.7	36.1%	1.5 ± 1.2	79.1%	2.8 ± 1.7	93.3%
	350	0.2 ± 0.5	20.8%	0.8 ± 0.9	56.2%	1.5 ± 1.2	75.2%
	400	0.1 ± 0.3	7.1%	0.3 ± 0.5	24.6%	0.5 ± 0.7	39.8%
	450	0.0 ± 0.2	4.7%	0.2 ± 0.5	18.5%	0.3 ± 0.6	26.2%
	500	0.0 ± 0.2	2.7%	0.1 ± 0.3	11.5%	0.2 ± 0.4	16.3%
	550	0.0 ± 0.1	1.6%	0.1 ± 0.3	6.2%	0.1 ± 0.3	9.4%
	600	0.0 ± 0.1	0.7%	0.0 ± 0.2	2.9%	0.0 ± 0.2	4.3%
	650	0.0 ± 0.1	0.3%	0.0 ± 0.1	0.8%	0.0 ± 0.1	1.5%
	700	0.0 ± 0.0	0.1%	0.0 ± 0.0	0.2%	0.0 ± 0.0	0.1%
	750	0.0 ± 0.0	0.0%	0.0 ± 0.0	0.0%	0.0 ± 0.0	0.0%
	800	0.0 ± 0.0	0.0%	0.0 ± 0.0	0.0%	0.0 ± 0.0	0.0%

Table 3.2: continued

$M_{up}/M_\odot$	$M/M_\odot$	$N_{10} = 100$ $M_{cl} \approx 2 \times 10^4\,M_\odot$		$N_{10} = 350$ $M_{cl} \approx 7 \times 10^4\,M_\odot$		$N_{10} = 650$ $M_{cl} \approx 10^5\,M_\odot$	
		$\langle N_{\geq M}\rangle$	$P_{\geq M}$	$\langle N_{\geq M}\rangle$	$P_{\geq M}$	$\langle N_{\geq M}\rangle$	$P_{\geq M}$
350	150	2.1 ± 1.4	87.0%	7.2 ± 2.6	$> 99.9\%$	13.6 ± 3.6	$> 99.9\%$
	200	1.1 ± 1.1	68.4%	3.9 ± 1.9	98.2%	7.6 ± 2.6	99.9%
	250	0.6 ± 0.8	46.9%	2.1 ± 1.4	88.2%	4.2 ± 2.0	98.8%
	300	0.3 ± 0.5	24.4%	1.1 ± 1.0	66.1%	2.1 ± 1.5	88.0%
	350	0.1 ± 0.3	8.3%	0.3 ± 0.6	28.2%	0.7 ± 0.8	50.5%
	400	0.0 ± 0.2	4.2%	0.2 ± 0.4	16.4%	0.4 ± 0.6	33.0%
	450	0.0 ± 0.1	2.1%	0.1 ± 0.3	8.3%	0.2 ± 0.5	20.7%
	500	0.0 ± 0.1	1.1%	0.0 ± 0.2	3.2%	0.1 ± 0.3	10.4%
	550	0.0 ± 0.1	0.3%	0.0 ± 0.1	1.6%	0.0 ± 0.2	2.9%
	600	0.0 ± 0.0	0.0%	0.0 ± 0.0	0.0%	0.0 ± 0.0	0.0%
	650	0.0 ± 0.0	0.0%	0.0 ± 0.0	0.0%	0.0 ± 0.0	0.0%
	700	0.0 ± 0.0	0.0%	0.0 ± 0.0	0.0%	0.0 ± 0.0	0.0%
300	150	1.9 ± 1.4	86.5%	6.5 ± 2.5	$> 99.9\%$	12.3 ± 3.5	$> 99.9\%$
	200	1.0 ± 0.9	63.8%	3.3 ± 1.7	97.5%	6.1 ± 2.5	99.8%
	250	0.5 ± 0.7	38.4%	1.5 ± 1.2	79.1%	2.8 ± 1.7	93.0%
	300	0.1 ± 0.4	12.7%	0.4 ± 0.6	33.7%	0.7 ± 0.8	51.5%
	350	0.1 ± 0.3	7.7%	0.2 ± 0.5	19.1%	0.4 ± 0.6	30.4%
	400	0.0 ± 0.2	3.7%	0.1 ± 0.3	10.1%	0.2 ± 0.4	15.4%
	450	0.0 ± 0.1	1.5%	0.0 ± 0.2	3.3%	0.1 ± 0.2	5.5%
	500	0.0 ± 0.1	0.4%	0.0 ± 0.1	0.7%	0.0 ± 0.1	0.8%
	550	0.0 ± 0.0	0.0%	0.0 ± 0.0	0.0%	0.0 ± 0.0	0.0%
	600	0.0 ± 0.0	0.0%	0.0 ± 0.0	0.0%	0.0 ± 0.0	0.0%
250	150	1.6 ± 1.3	78.2%	5.5 ± 2.5	99.8%	10.6 ± 3.3	$> 99.9\%$
	200	0.7 ± 0.8	47.2%	2.4 ± 1.6	89.8%	4.4 ± 2.1	98.5%
	250	0.1 ± 0.4	12.7%	0.5 ± 0.7	39.6%	1.0 ± 1.0	61.6%
	300	0.1 ± 0.2	4.8%	0.2 ± 0.5	20.5%	0.4 ± 0.7	36.1%
	350	0.0 ± 0.1	1.6%	0.1 ± 0.3	7.9%	0.2 ± 0.4	15.4%
	400	0.0 ± 0.1	0.3%	0.0 ± 0.1	1.7%	0.0 ± 0.2	2.8%
	450	0.0 ± 0.0	0.0%	0.0 ± 0.0	0.0%	0.0 ± 0.0	0.0%
	500	0.0 ± 0.0	0.0%	0.0 ± 0.0	0.0%	0.0 ± 0.0	0.0%
200	150	1.2 ± 1.1	69.2%	4.1 ± 2.0	98.4%	7.5 ± 2.8	$> 99.9\%$
	200	0.2 ± 0.4	20.1%	0.8 ± 0.9	52.9%	1.4 ± 1.1	76.3%
	250	0.1 ± 0.3	8.0%	0.3 ± 0.5	23.7%	0.5 ± 0.7	38.5%
	300	0.0 ± 0.1	1.8%	0.1 ± 0.3	6.7%	0.1 ± 0.4	10.6%
	350	0.0 ± 0.0	0.1%	0.0 ± 0.0	0.2%	0.0 ± 0.0	0.2%
	400	0.0 ± 0.0	0.0%	0.0 ± 0.0	0.0%	0.0 ± 0.0	0.0%
150	150	0.3 ± 0.5	23.6%	1.1 ± 1.0	66.7%	2.0 ± 1.4	87.8%
	200	0.1 ± 0.3	7.2%	0.3 ± 0.5	24.9%	0.5 ± 0.7	39.6%
	250	0.0 ± 0.1	0.6%	0.0 ± 0.1	1.7%	0.0 ± 0.2	3.5%
	300	0.0 ± 0.0	0.0%	0.0 ± 0.0	0.0%	0.0 ± 0.0	0.0%

Table 3.3: Star formation (SF) scenarios used to compute the mass functions that are compared to observations in Fig. 3.8. Given are the primordial binary fraction f_B for each model as well as the least-square deviation χ^2_{tot} in the total mass range ($1.1 \leq \log M/M_\odot \leq 2.0$) and χ^2_{peak} in a mass region around the wind-mass-loss peak ($1.4 \leq \log M/M_\odot \leq 1.8$ for Arches and $1.3 \leq \log M/M_\odot \leq 1.6$ for Quintuplet). The best fit models are A2, A4, Q2 and Q4.

SF model	t_1/Myr	t_2/Myr	f_B	χ^2_{tot}	χ^2_{peak}	Description
A1	—	—	—	1.19	1.59	power law mass function truncated at the most massive observed star; power law index $\Gamma = -0.7$
A2	3.5	—	100%	0.57	0.36	single starburst at t_1
A3	3.2	3.3	0%	1.85	0.31	constant SF between t_1 and t_2
A4	0.7	3.3	0%	0.49	0.69	two starbursts at t_1 and t_2
Q1	—	—	—	2.11	4.23	power law mass function truncated at the most massive observed star; power law index $\Gamma = -0.7$
Q2	4.8	—	60%	0.56	0.36	single starburst at t_1
Q3	4.8	—	0%	0.70	0.97	single starburst at t_1
Q4	4.5	4.7	0%	0.43	0.46	constant SF between t_1 and t_2

3.8.1 Star formation histories cont.

Here we investigate changes in the mass function due to a star formation scenario that deviates from a true starburst in order to understand whether the observed mass functions of Arches and Quintuplet can be reproduced without binaries. We analyse two scenarios: (1) a period of prolonged but constant star formation rate and (2) two instantaneous starbursts separated in time. The latter scenario represents not only a two stage starburst within one cluster but also two merged star clusters where stars in each cluster are coeval. This situation most probably applies to the massive star cluster R136 in the Large Magellanic Cloud, which is thought to be a double cluster in the process of merging (Sabbi et al. 2012). We compute mass functions for star formation scenarios 1 and 2 (which include single, true starbursts) and search for parameter values that minimise the least squares deviation, of the modelled ($y_{model,i}$) from the observed ($y_{obs,i}$) mass functions of the Arches and Quintuplet clusters assuming Poisson uncertainties, i.e. $\sigma^2_{obs,i} = y_{obs,i}$,

$$\chi^2 = \frac{1}{N} \sum_{i=1}^{N} \frac{(y_{model,i} - y_{obs,i})^2}{\sigma^2_{obs,i}}, \tag{3.4}$$

where N is the number of mass bins. Exemplary star formation scenarios are described in Table 3.3 and the resulting mass functions are compared to observations in Fig. 3.8. Among these examples are those star formation scenarios that lead to the best fits (models A2, A4, Q2 and Q4).

From Table 3.3 and the top panels of Fig. 3.8 it is evident that simple power-law mass functions (models A1 and Q1) fit the observed mass functions of Arches and Quintuplet much worse than the best single-starburst models including binary stars (A2 and Q2). Particularly the mass region around the wind mass loss peak is not fitted well by models A1 and Q1 (see
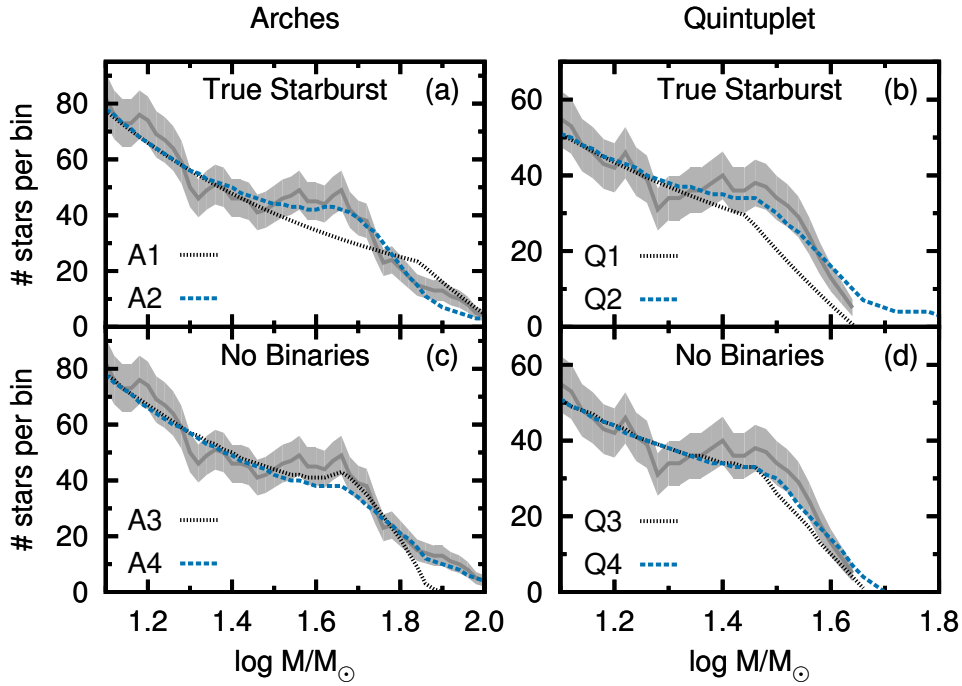
Figure 3.8: Modelled mass functions using different star formation scenarios compared to observations of the (a, c) Arches and (b, d) Quintuplet clusters. In the top panels, we compare the observations to our best-fitting starburst models including binary stars and to simple power-law mass functions truncated at the observed maximum mass. In the bottom panels, we show mass functions composed only of single stars with more complex star formation scenarios. The individual star formation models A1–A4 and Q1–Q4 are explained in Table 3.3 together with their least squares deviation χ^2 (see Eq. 3.4). All modelled mass functions are binned in the same way as the observations (see Sec. 3.2.5).

χ^2_{peak} in Table 3.3). The mass functions of the Arches and Quintuplet clusters do not follow simple power laws.

In the bottom panels of Fig. 3.8, we also present models of the observed mass functions of the Arches and Quintuplet clusters *without* binary stars. We do not find satisfactory models that fit peak and tail simultaneously with a single starburst without binaries. Model A3, for example, fits the peak due to mass loss well ($\chi^2_{\mathrm{peak}} = 0.31$) but fails to explain the high-mass end of the observed mass function ($\chi^2_{\mathrm{tot}} = 1.85$).

We can improve this situation by adding a younger stellar population that fits the tail. Such a scenario is given by model A4, which fits the peak and the total mass function. However, this two-component model has an age spread of 2.6 Myr which is more than twice as large as the observed age discrepancy of about 1 Myr in the Arches cluster (Martins et al. 2008) and much larger than the expected star formation duration.

A two-component solution is not needed to model the observed mass function of the Quintuplet cluster because the tail of the mass function is not very pronounced. Consequently our models Q3 and Q4 predict no or a too small age spread — contrary to the observations.

The age spread of 0.2 Myr of model Q4 might be compatible with the above-estimated star formation duration given the quite uncertain core radius and velocity dispersion of Quintuplet. The single-starburst model, Q3, is shown to illustrate the difference between the mass functions with (Q2) and without (Q3) binaries. The tail of the mass function is, however, underestimated

in the observed mass function in Fig. 3.8 because no self-consistent mass determination for the three WNh stars in the core of Quintuplet is available (Hußmann et al. 2012). If the tail were visible, we could, of course, model it by an additional younger population as is in Arches.

In summary, we conclude that we can reproduce the mass functions of Arches and Quintuplet without binaries but with freedom in the star formation history. However, the best-fit star formation parameters (e.g. the age spread of 2.6 Myr) are inconsistent with other observables. Our single-starburst models which include binaries are thus the only models that fulfil all observational constraints. These models are also consistent with a star formation duration of the order of the crossing time of the cluster.

BONNSAI: a Bayesian tool for comparing stars with stellar evolution models

F.R.N. Schneider, N. Langer, A. de Koter, I. Brott, R.G. Izzard and H.H.B. Lau

Abstract   Powerful telescopes equipped with multi-fibre or integral field spectrographs combined with detailed models of stellar atmospheres and automated fitting techniques allow for the analysis of large number of stars. These datasets contain a wealth of information that require new analysis techniques to bridge the gap between observations and stellar evolution models. To that end, we develop Bonnsai[1] (BONN Stellar Astrophysics Interface), a Bayesian statistical method, that is capable of comparing all available observables simultaneously to stellar models while taking observed uncertainties and prior knowledge such as initial mass functions and distributions of stellar rotational velocities into account. Bonnsai can be used to (1) determine probability distributions of fundamental stellar parameters such as initial masses and stellar ages from complex datasets, (2) predict stellar parameters that were not yet observationally determined and (3) test stellar models to further advance our understanding of stellar evolution. An important aspect of Bonnsai is that it singles out stars that cannot be reproduced by stellar models through χ^2 hypothesis tests and posterior predictive checks. Bonnsai can be used with any set of stellar models and currently supports massive main-sequence single star models of Milky Way and Large and Small Magellanic Cloud composition. We apply our new method to mock stars to demonstrate its functionality and capabilities. In a first application, we use Bonnsai to test the stellar models of Brott et al. (2011a) by comparing the stellar ages inferred for the primary and secondary stars of eclipsing Milky Way binaries of which the components range in mass between 4.5 and $28\,M_\odot$. Ages are determined from dynamical masses and radii that are known to better than 3%. We show that the stellar models must include rotation because stellar radii can be increased by several percent via centrifugal forces. We find that the average age difference between the primary and secondary stars of the binaries is $0.9 \pm 2.3\,\mathrm{Myr}$ (95% CI), i.e. that the stellar models reproduce the Milky Way binaries well. The predicted effective temperatures are in agreement for observed effective temperatures for stars cooler than $25,000\,\mathrm{K}$. In hotter stars, i.e. stars earlier than B1–2V and more massive than about

---

[1] Bonnsai is available through a web-interface at http://www.astro.uni-bonn.de/stars/bonnsai.

$10\,\mathrm{M_\odot}$, we find that the observed effective temperatures are on average hotter by $1.1 \pm 0.3\,\mathrm{kK}$ (95% CI) than predicted by the stellar models. The hotter temperatures consequently result in bolometric luminosities that are larger by $0.06 \pm 0.02\,\mathrm{dex}$ (95% CI) than those predicted by the models.

4.1 Introduction

Stars are the building blocks of galaxies and hence the Universe. Our knowledge of their evolution is deduced from detailed comparisons of observations to theoretical models. The interface, where observations meet theory, is often provided by the Hertzsprung-Russell (HR) diagram and its relative, the colour-magnitude diagram. In an HR diagram, two surface properties of stars, the effective temperature and the luminosity, are compared to stellar evolutionary models to, e.g., determine fundamental stellar parameters like initial mass and age that are both inaccessible by observations alone and of utmost importance to modern astrophysics.

With the advent of large spectroscopic surveys[2] such as the Gaia-ESO survey (Gilmore et al. 2012), SEGUE/SDSS (Yanny et al. 2009), GOSSS (Maíz Apellániz et al. 2011, 2013), RAVE (Steinmetz et al. 2006), OWN (Barbá et al. 2010), IACOB (Simón-Díaz et al. 2011a; Simón-Díaz & Herrero 2014), the VLT FLAMES Survey of Massive Stars (Evans et al. 2005, 2006) and the VLT-FLAMES Tarantula Survey (Evans et al. 2011), much more is known about stars than just their positions in the HR diagram: surface abundances, surface gravities, surface rotational velocities and more. Such a wealth of information not only allows the determination of fundamental stellar parameters with high precision but also to thoroughly test and thus advance our understanding of stellar evolution. However, bridging the gap between such manifold observations and stellar models requires more sophisticated analysis techniques than simply comparing stars to models in the HR diagram because the comparison needs to be performed in a multidimensional space.

Bayesian inference is widely applied in determining cosmological parameters and offers a promising framework to infer stellar parameters from observations. Steps into this direction have been taken by Pont & Eyer (2004) and Jørgensen & Lindegren (2005) to infer stellar ages and masses from colour-magnitude diagrams. Since then, Bayesian modelling has been used by several authors to infer a wide range of stellar parameters from spectroscopy, photometry, astrometry, spectropolarimetry and also asteroseismology (e.g. da Silva et al. 2006; Takeda et al. 2007; Shkedy et al. 2007; Burnett & Binney 2010; Casagrande et al. 2011; Gruberbauer et al. 2012; Petit & Wade 2012; Bazot et al. 2012; Serenelli et al. 2013; Schönrich & Bergemann 2014). Bayesian inference is further used to derive properties of stellar ensembles such as cluster ages, mass functions and star formation histories (e.g. von Hippel et al. 2006; De Gennaro et al. 2009; van Dyk et al. 2009; Weisz et al. 2013; Walmswell et al. 2013; Dib 2014). The big advantage of a Bayesian approach is the knowledge of full probability distribution functions of stellar parameters that take observational uncertainties and prior knowledge into account.

Incorporating prior knowledge may be essential because the determination of stellar parameters can otherwise be biased (e.g. Pont & Eyer 2004). For example, the evolution of stars speeds up with time such that stars spend different amounts of time in various evolutionary

---

[2] Sloan Digital Sky Survey (SDSS), Sloan Extension for Galactic Understanding and Exploration (SEGUE/SDSS), Galactic O Star Spectroscopic Survey (GOSSS), RAdial Velocity Experiment (RAVE), Spectroscopic Survey of Galactic O and WN stars (OWN), Instituto de Astrofísica de Canarias OB star survey (IACOB)

Table 4.1: Initial mass ranges M_{ini}, age ranges and initial rotational velocity ranges v_{ini} of the Bonn Milky Way (MW), Large Magellanic Cloud (LMC) and Small Magellanic Cloud (SMC) stellar models (Brott et al. 2011a; Köhler et al. 2014). The models contain main-sequence single stars. We discuss the metallicities of the models in Sec. 4.4.3.

Stellar models	$M_{ini}/M_\odot$	Age / Myr	$v_{ini}/km\,s^{-1}$
Bonn MW	5–50	0–100	0–600
Bonn LMC	5–500	0–100	0–600
Bonn SMC	5–60	0–100	0–600

phases (this even holds for stars on the main-sequence). This knowledge is typically neglected when determining stellar parameters from the position of stars in an HR diagram and may thus result in biased stellar parameters.

In this paper, we present a method that *simultaneously* takes all available observables, their uncertainties and prior knowledge into account to determine stellar parameters and their full probability density distributions from a set of stellar models. This method further allows us to predict yet unobserved stellar properties like rotation rates or surface abundances. By applying sophisticated goodness-of-fit tests within our Bayesian framework, we are able to securely identify stars that cannot be reproduced by the chosen stellar models which will help to improve our understanding of stellar evolution.

Currently, BONNSAI supports the Bonn stellar models for the Milky Way (MW), Large Magellanic Cloud (LMC) and Small Magellanic Cloud (SMC; Brott et al. 2011a; Köhler et al. 2014) with initial mass and rotational velocity ranges given in Table 4.1. We plan to integrate further stellar model grids in the future and make BONNSAI available through a web-interface[3].

We describe the BONNSAI approach in Sec. 4.2 and apply it to mock stars in Sec. 4.3 to show its functionality and to demonstrate its capabilities. In Sec. 4.4 we apply BONNSAI to high-precision observations of Milky Way binaries to thoroughly test the Milky Way stellar models of Brott et al. (2011a) and conclude in Sec. 4.5.

4.2 Method

Besides the observables, there are two main ingredients in BONNSAI. On the one hand, there is the statistical method and on the other hand there are the stellar models. The statistical method uses the stellar models to derive stellar parameters from a given set of observables. In the following, we describe our statistical method (Secs. 4.2.1–4.2.4 and 4.2.6–4.2.7) and the so far implemented stellar models (Sec. 4.2.5).

4.2.1 Bayes' theorem

Bayes' theorem directly follows from the definition of conditional probabilities. Let $P(M|D)$ be the conditional probability that an event M occurs given that an event D already took place, i.e. $P(M|D) = P(M \cap D)/P(D)$ where $P(M \cap D)$ is the joint probability of both events and

---

[3] http://www.astro.uni-bonn.de/stars/bonnsai

$P(D) \neq 0$ the probability for the occurrence of event D. We then arrive at Bayes' theorem,

$$P(M|D) = \frac{\frac{P(M \cap D)}{P(M)}P(M)}{P(D)} = \frac{P(D|M)P(M)}{P(D)}. \tag{4.1}$$

In the context of Bayesian inference, M is the model parameter, D is the (observed) data and

- $P(M|D)$ is the *posterior* probability function, i.e. the probability of the model parameter given the data,

- $P(D|M)$ is the *likelihood*, i.e. the probability of the data given the model parameter,

- $P(M)$ is the *prior* function, i.e. the probability of the model parameter,

- and $P(D)$ is the *evidence* that serves as a normalisation constant in this context because it does not depend on the model parameter.

The likelihood function per se is *not a* probability distribution of the model parameters that we seek to derive but it describes how likely each value of an observable is given a model. To derive the probability distribution of the model parameters, i.e. the posterior probability distribution, we apply Bayes' theorem. In case of a uniform prior function, $P(M) = \text{const.}$, the likelihood is the posterior probability distribution and Bayesian inference reduces to a maximum likelihood approach.

4.2.2 Bayesian stellar parameter determination

In the case of stellar parameter determination, the data $\mathbf{d}$ are now an n_{obs}-dimensional vector containing the n_{obs} observables like luminosities L, effective temperatures T_{eff}, surface abundances etc.[4] The model parameter $\mathbf{m}$ for rotating single stars is a 4-dimensional vector consisting of the initial mass M_{ini}, the initial rotational velocity at the equator v_{ini}, the initial chemical composition/metallicity Z and the stellar age τ. Further physics that alters the evolution of stars, like magnetic fields or duplicity, may be added to the stellar models and hence to the model parameters if needed. The model parameters uniquely map to the observables; e.g. stellar models predict luminosities, effective temperatures, etc. for given stellar initial conditions and age, $\mathbf{m} = (M_{\mathrm{ini}}, v_{\mathrm{ini}}, Z, \tau) \rightarrow \mathbf{d}(\mathbf{m}) = (L, T_{\mathrm{eff}}, \ldots)$. The reverse mapping is not always unique as evident from Fig. 4.2 where stellar tracks of different stars cross each other in the HRD, i.e. different model parameters, $\mathbf{m}$, can predict the same observables $\mathbf{d}$.

Bayes' theorem in terms of probability *density* functions reads, analogously to Eq. 4.1,

$$p(\mathbf{m}|\mathbf{d}) \propto p(\mathbf{d}|\mathbf{m})p(\mathbf{m}). \tag{4.2}$$

The proportionality constant follows from the normalisation condition,

$$\int_{\mathbf{m}} p(\mathbf{m}|\mathbf{d})\,\mathrm{d}\mathbf{m} = 1, \tag{4.3}$$

where $\mathrm{d}\mathbf{m} = \mathrm{d}M_{\mathrm{ini}}\,\mathrm{d}v_{\mathrm{ini}}\,\mathrm{d}Z\,\mathrm{d}\tau$. To compute $p(\mathbf{m}|\mathbf{d})$ we must define the likelihood and prior functions, which we do in the following two sections.

---

[4] What we call observables are actually not observables but quantities derived from observations, e.g. from modelling of stellar spectra. For clarity we nevertheless use the phrase observables in this paper.

4.2.3 Likelihood function

We assume two-piece Gaussian likelihood functions to compute the posterior probability distribution according to Bayes' theorem, Eq. 4.1. The probability density function of an observed quantity d_i with 1σ uncertainties $+\sigma_{p,i}$ and $-\sigma_{m,i}$ is then,

$$p(d_i|\mathbf{m}) \equiv L_i = \frac{2}{\sqrt{2\pi}(\sigma_{m,i} + \sigma_{p,i})} \exp\left[-\frac{(d_i - d_i(\mathbf{m}))^2}{2\sigma_i^2}\right], \tag{4.4}$$

with

$$\sigma_i = \begin{cases} \sigma_{m,i}, & d_i \leq d_i(\mathbf{m}), \\ \sigma_{p,i}, & d_i > d_i(\mathbf{m}). \end{cases} \tag{4.5}$$

If $\sigma_{m,i} = \sigma_{p,i}$, the likelihood function (Eq. 4.4) reduces to the usual Gaussian distribution function. We assume that all n_{obs} observables are statistically independent, i.e. they are assumed to be uncorrelated. The full likelihood function $p(\mathbf{d}|\mathbf{m})$ needed in Eq. (4.2) is then the product of the individual probability density functions L_i of the observed data d_i given the model parameters $\mathbf{m}$,

$$p(\mathbf{d}|\mathbf{m}) = \prod_{i=1}^{n_{\text{obs}}} L_i\,. \tag{4.6}$$

We further define the usual χ^2,

$$\chi^2 = \sum_{i=1}^{n_{\text{obs}}} \frac{(d_i - d_i(\mathbf{m}))^2}{\sigma_i^2}, \tag{4.7}$$

which is useful later on.

Whenever only lower or upper limits of observables are known, we use a step function as the likelihood instead of the Gaussian function from Eq. 4.4. This means that all values above the lower limit and all values below the upper limit, respectively, are equally probable.

In Eq. 4.6 we assume that the observables are not correlated, which may lead to a loss of information. For example, effective temperatures and surface gravities that are inferred from models of stellar spectra calculated with a stellar atmosphere code are typically correlated. They are correlated in the sense that fitting a spectral line equally well with a hotter effective temperature requires a larger gravity. Such correlations are not accounted for in our current approach because the needed information is usually not published. The correlations are valuable because they contain information to constrain stellar parameters better and may thus result in smaller uncertainties. In principle correlations can readily be incorporated in our approach by including the covariance matrix in the likelihood function.

4.2.4 Prior functions

The prior functions contain our a priori knowledge of the model parameters $\mathbf{m}$ (i.e. M_{ini}, v_{ini}, Z, τ). The prior functions do not include our knowledge of stellar evolution such as how much time stars spend in different evolutionary phases. This knowledge, that essentially is also a priori, enters our approach through the stellar models (Sec. 4.2.5). As for the likelihood function, we assume that the individual model parameters are independent such that the prior function

splits into a product of four individual priors for the four model parameters,

$$p(\mathbf{m}) = \xi(M_{\mathrm{ini}})\,\theta(v_{\mathrm{ini}})\,\psi(Z)\,\zeta(\tau). \tag{4.8}$$

Our a priori knowledge of initial masses, i.e. the initial mass prior $\xi(M_{\mathrm{ini}})$, is given by the initial mass function. The initial mass function is commonly expressed as a power-law function,

$$\xi(M_{\mathrm{ini}}) \propto M_{\mathrm{ini}}^{\gamma}, \tag{4.9}$$

with slope γ. The slope is $\gamma = -2.35$ for a Salpeter initial mass function (Salpeter 1955), meaning that lower initial masses are more probable/frequent than higher. Alternative parameterisations of the initial mass function may be used as well (see e.g. the review by Bastian et al. 2010). A uniform mass function, i.e. $\xi(M_{\mathrm{ini}}) = \mathrm{const.}$, may be used if no initial mass shall be preferred a priorly.

As an initial rotational velocity prior, $\theta(v_{\mathrm{ini}})$, we use observed distributions of stellar rotational velocities such as those found by Hunter et al. (2008a) for O and B-type stars in the Milky Way and Magellanic Clouds. For MW and LMC stars, the observed Hunter et al. (2008a) distributions follow a Gaussian distribution with mean of $100\,\mathrm{km\,s^{-1}}$ and standard deviation $106\,\mathrm{km\,s^{-1}}$ and for SMC stars a Gaussian distribution with mean $175\,\mathrm{km\,s^{-1}}$ and standard deviation $106\,\mathrm{km\,s^{-1}}$. Other observed rotational velocity distributions of OB stars are equally well suited as priors; e.g. the distributions found by Conti & Ebbets (1977), Howarth et al. (1997), Abt et al. (2002), Martayan et al. (2006, 2007), Penny & Gies (2009), Huang et al. (2010), Dufton et al. (2013) or Ramírez-Agudelo et al. (2013). We note that the observed distributions of rotational velocities are not necessarily the initial distributions that are actually required as prior function (see de Mink et al. 2013). A uniform prior, i.e. every initial rotational velocity is a priori equally probable, may be used as well.

The metallicity prior $\psi(Z)$ has yet no influence because the metallicity is not a free model parameter in the currently supported stellar model grids. In principle, any probability distribution such as a uniform or Gaussian distribution is suited to describe a priori knowledge of the metallicity of a star under investigation. The prior can, for example, encompass knowledge of a spread in metallicity of a population of stars (e.g. Bergemann et al. 2014).

The age prior $\zeta(\tau)$ is set by the star formation history of the region to which an observed star belongs. If the observed star is a member of a star cluster that formed in a single starburst, the age prior may be a Gaussian distribution with mean equal to the age of the cluster and width corresponding to the duration of the star formation process. A uniform age prior corresponds to assuming a constant star formation rate in the past such that all ages are a priori equally probable.

It is typically assumed that the inclination of a star with respect to our line-of-sight does not affect observables except for projected rotational velocities, $v \sin i$. This assumption breaks down for rapid rotators because their equators are cooler than their poles as a result of a distortion of the otherwise spherically symmetric shape of a star by the centrifugal force. The inferred effective temperature and luminosity are then a function of the inclination angle of the star towards our line-of-sight The latter effect is beyond the scope of this paper. However, projected rotational velocities are often determined from stellar spectra. Whenever $v \sin i$ measurements are compared to stellar models, we take the equatorial rotational velocities of the models and combine them with any possible orientation of the star in space, i.e. with any possible inclination angle, to derive the $v \sin i$ values. By doing so, we introduce a fifth model parameter, the

inclination angle i, and have to define the appropriate inclination prior, $\phi(i)$. Our assumption that the rotation axes of stars are randomly oriented in space results in inclination angles that are not equally probable. It is, for example, more likely that a star is seen equator-on ($i = 90°$) than pole-on ($i = 0°$) because the solid angle of a unit sphere, $d\Omega \propto \sin i \, di$, of a region around the equator is larger than that of a region around the pole. The inclination prior is then,

$$\phi(i) = \sin i, \tag{4.10}$$

and the full prior in Eq. (4.2) reads

$$p(\mathbf{m}) = \xi(M_{\text{ini}}) \, \theta(v_{\text{ini}}) \, \psi(Z) \, \zeta(\tau) \, \phi(i). \tag{4.11}$$

Note that the functional form of the priors may predict non-zero probabilities for values of the model parameters that are physically meaningless. A Gaussian v_{ini} prior may result in non-zero probabilities for negative rotational velocities and a Gaussian age prior in non-zero probabilities for negative ages. Ideally, the prior functions should be properly truncated and renormalised to allow only for meaningful values of the model parameters. However, we can skip this step because the stellar model grids ensure that we only analyse physically meaningful values of the model parameters and the application of Bayes' theorem as in Eq. (4.2) requires a proper renormalisation anyhow such that we can simply work with priors that are not properly normalised but describe relative differences correctly.

By default, BONNSAI assumes a Salpeter initial mass prior, uniform priors in v_{ini}, Z and age and that stellar rotation axes are randomly oriented in space.

4.2.5 Stellar model grids

Currently, BONNSAI supports the stellar models of Brott et al. (2011a) and Köhler et al. (2014) summarised in Table 4.1. BONNSAI follows a grid-based approach, i.e. we compute the posterior probability distribution by sampling models from a dense, precomputed and interpolated grid. The model grids have a resolution in initial mass of $\Delta M_{\text{ini}} = 0.2 \, M_\odot$, in age of $\Delta \tau = 0.02 \, \text{Myr}$ and in initial rotational velocity of $\Delta v_{\text{ini}} = 10 \, \text{km s}^{-1}$. The model grids Bonn MW, LMC and SMC with their different initial mass coverage contain about 7.5, 20 and 8 million stellar models, respectively. If projected rotational velocities are matched to stellar models, we probe ten inclination angles from $0°$ to $90°$. The model grids are computed by a linear interpolation of the stellar models of Brott et al. (2011a) and Köhler et al. (2014) with the technique described in Brott et al. (2011b).

The stellar model grids contain our (a priori) knowledge of stellar evolution. For example, the density of the stellar models is indicative of the time spent by the models in different evolutionary phases and thus ensures that this knowledge is properly taken into account in our approach.

4.2.6 Goodness-of-fit

A crucial aspect of any fitting procedure is to check the goodness of the fit (e.g. when fitting a straight line to data points that may actually follow an exponential distribution). Typically the χ^2 of the fit is used as the goodness of the fit. Similarly, we have to check whether the stellar models fitted to observations are a good representation of the observations for the determined model parameters $\mathbf{m}$.
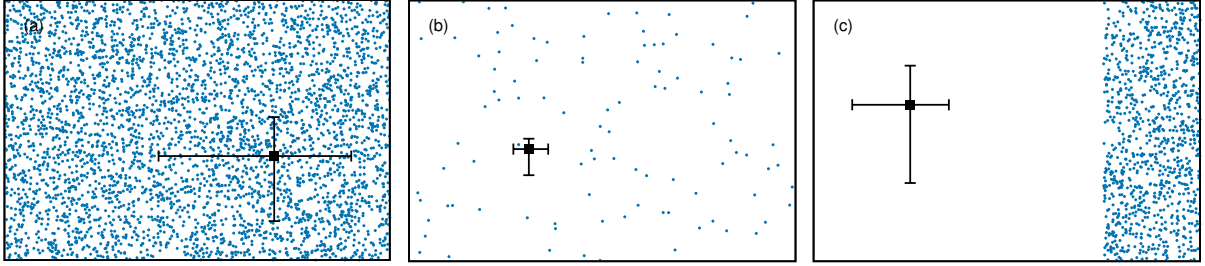
Figure 4.1: Hypothetical model grid coverage of three observations. The resolution of the model grid is high compared to the observed uncertainties in the left panel (a) and the models sample the observation well. The model grid is sparse in the middle panel (b) such that the model density is not enough to resolve the 1σ uncertainties of the observations — reliable model parameters cannot be determined. In the right panel (c), the models are physically unable to match the observations, i.e. the resolution of the model grid is high compared to the observed uncertainties but the models do not probe the observed region of the parameter space.

As an example, consider a star in the HR diagram that lies more than 5σ bluewards of the zero-age main-sequence and is compared to non-rotating, main-sequence single star models. Our Bayesian approach presented so far would return model parameters although the models are actually unable to reach the observed position of the star in the HR diagram.

In general, the stellar models may fail to match an observation because

- the star is not covered by the underlying stellar model grid,

- physics is missing in the stellar models, e.g. magnetic fields, a different treatment of rotation and rotational mixing or duplicity,

- there are problems with the calibrations of e.g. convective core overshooting, the efficiency of rotational mixing or stellar winds,

- there are difficulties with the methods from which observables like the surface gravity are derived (e.g. stellar atmosphere models),

- there are problematic observations like unseen binary companions that lead to misinterpretation of fluxes and spectra.

The goodness of a fit is often checked by eye. Besides a by-eye method, we develop objective and robust tests that allow us to reject the determined model parameters for a given significance level. By default, we use a significance level of $\alpha = 5\%$ in our tests as commonly adopted in statistics.

Within our approach, stellar models might be unable to match observations not only because of the reasons given above but also because of a too low resolution of the model grid. We illustrate these cases in Fig. 4.1. The left panel of Fig. 4.1 contains a hypothetical observation including error bars and a hypothetical coverage of the observed parameter space by a stellar model grid. It is evident that the models densely cover the observation. The resolution of the model grid, i.e. the average distance between adjacent models, is small compared to the observational uncertainties. In the middle panel of Fig. 4.1, the stellar model grid in principle covers the observations but the model grid is sparse compared to the observational uncertainties. In order to determine reliable model parameters, the resolution of the model grid needs to be

increased. Such situations are encountered whenever the observational uncertainties are so accurate that the observations including their error bars fall in between model grid points. In the right panel of Fig. 4.1, the model grid is dense compared to the observational uncertainties but the models are unable to match the observations. The resolution of the model grid could be infinite but the models would still not reproduce the observations. We not only want to identify situations as in Figs. 4.1b and c but also want to be able to distinguish between these situations.

To test whether the resolution of the stellar model grid is sufficient to determine reliable model parameters, we investigate the average spacing of those ten models that are closest to the best-fitting model. We take the nearest neighbours of each of the eleven models and compute the average differences of each observable and the average χ^2 of these pairs. We define as our resolution criterion that the average differences are less than one fifth of the corresponding 1σ uncertainties. This ensures that there are about ten models within 1σ of each observable and that we know how significant the χ^2 of the best fitting model is with respect to the resolution of the stellar model grid.

Once it is ensured that the resolution of the model grid is sufficient, we test whether the stellar models are able to match the observations. One straightforward way to judge the goodness of the estimated parameters is to do a classical χ^2-hypothesis test (Pearson's χ^2-hypothesis test). The χ^2 of the best-fitting model, χ^2_{best}, is compared to the maximum allowable χ^2_{max} for a given significance level α, where the maximum allowable χ^2_{max} is such that the integrated probability of the χ^2-distribution for $\chi^2 \geq \chi^2_{\mathrm{max}}$ is equal to the significance level. This means that there is a probability less than α that $\chi^2_{\mathrm{best}} \geq \chi^2_{\mathrm{max}}$ for the best-fitting stellar model. The χ^2-distribution is defined by the degrees of freedom which, in our case, is given by the number of observables. If some observables are dependent on each other, i.e. if some observables can be derived from others as is the case for surface gravity, mass and radius or luminosity, effective temperature and radius, the χ^2-test gives a too large χ^2_{max}, i.e. the test is performed with an effectively smaller significance level.

The χ^2-test only incorporates the best-fitting stellar model. In a Bayesian analysis there are not only the model parameters of the best-fitting stellar model but the full posterior probability distribution of the model parameters that do not necessarily peak at the best-fitting model parameters. We make use of this by conducting a posterior predictive check. The idea is to compare the predictions of the stellar models for the estimated model parameters to the observations to check whether the predictions are in agreement with the observations. If they are not in agreement, the estimated model parameters and hence the stellar models cannot reproduce/replicate the observations. In Bayesian statistics, the predictions of the models for the observables are called replicated observables, $\mathbf{d}_{\mathrm{rep}}$, and are computed from the full posterior probability distribution, $p(\mathbf{m}|\mathbf{d})$,

$$p(\mathbf{d}_{\mathrm{rep}}|\mathbf{d}) = \int_{\mathbf{m}} p(\mathbf{d}_{\mathrm{rep}}|\mathbf{m})p(\mathbf{m}|\mathbf{d})\,\mathrm{d}\mathbf{m}, \tag{4.12}$$

where $p(\mathbf{d}_{\mathrm{rep}}|\mathbf{d})$ is the probability distribution of the replicated observables (given the original observables) and $p(\mathbf{d}_{\mathrm{rep}}|\mathbf{m})$ is the probability of the replicated parameters $\mathbf{d}_{\mathrm{rep}}$ given a stellar model with parameters $\mathbf{m}$ (i.e. $p(\mathbf{d}_{\mathrm{rep}}|\mathbf{m})$ consists, in our case, of delta-functions). From the likelihood function (Eq. 4.6) and the posterior predictive probability distribution of the replicated observables (Eq. 4.12), we compute the probability distributions $p(\Delta d_i|\mathbf{d})$ of the differences between the replicated and original observables, $\Delta d_i \equiv d_{\mathrm{rep},i} - d_i$. If the stellar models can

reproduce the observations, the differences between replicated and original observables have to be consistent with being zero. We define the differences to be consistent with zero if the integrated probabilities for $\Delta d_i > 0$ and $\Delta d_i < 0$ are both larger than the significance level α for all observables d_i, $i = 1 \ldots n_{\mathrm{obs}}$, i.e.

$$\int_{\Delta d_i < 0} p(\Delta d_i | \mathbf{d}) \, \mathrm{d}d_i \quad \geq \quad \alpha \; \wedge \; \int_{\Delta d_i > 0} p(\Delta d_i | \mathbf{d}) \, \mathrm{d}d_i \geq \alpha, \; \forall i \,. \tag{4.13}$$

In other words, we say that the stellar models cannot reproduce the observations if the probability that the model prediction of any quantity is larger or smaller than the observational value is $\geq 95\%$ ($\geq 1 - \alpha$ with $\alpha = 5\%$).

Besides these automated and objective tests, we check the coverage of the observed parameter space graphically in diagrams similar to the illustrations in Fig. 4.1. We place one dot for each stellar model together with the observables and their uncertainties into two-dimensional projections of the parameter space of the observables. This results in $n_{\mathrm{obs}}(n_{\mathrm{obs}}+1)/2$ projections for n_{obs} observables from which the resolution can be assessed as well as whether the models are able to reproduce the observations (see Fig. 4.6 below for an example).

4.2.7 Our new approach in practice

In practice we perform the following steps:

1. We select all stellar models from a database (model grid) that are within $5\sigma_i$ of all observables. The pre-selection reduces the parameter space of the stellar models ($M_{\mathrm{ini}}, v_{\mathrm{ini}}, Z, \tau, i$) that needs to be scanned and thus accelerates the analysis.

2. We scan the pre-selected model parameter space and compute for each model the posterior probability according to Eq. (4.2). The posterior probability consists of the likelihood from Eq. (4.6) and a weighting factor that gives the probability of finding a stellar model with the given model parameters, $\mathbf{m}$. The weighting factor consists of two contributions: first, it takes into account the prior function from Eq. 4.11 factoring in our a priori knowledge about the probability of finding a particular stellar model and, second, the volume $\Delta V = \Delta M_{\mathrm{ini}} \, \Delta v_{\mathrm{ini}} \, \Delta Z \, \Delta \tau \, \Delta i$ that a particular stellar model covers in the model grid. The latter allows us to use non-equidistant model grids.

3. We renormalise the posterior probabilities such that Eq. (4.3) is fulfilled and create 1D and 2D probability functions/maps for the model parameters $\mathbf{m}$ by marginalisation, i.e. by projecting the posterior probability distribution onto, e.g., the M_{ini} axis or into the $v_{\mathrm{ini}} - M_{\mathrm{ini}}$ plane. Additionally we use Eq. (4.12) to derive probability functions/maps of any stellar parameter to e.g. predict yet unobserved surface nitrogen abundances of the stellar models for the estimated model parameters.

4. The resolution and goodness-of-fit tests are conducted.

5. The 1D probability functions are analysed to compute the mean, median and mode including their 1σ uncertainties.
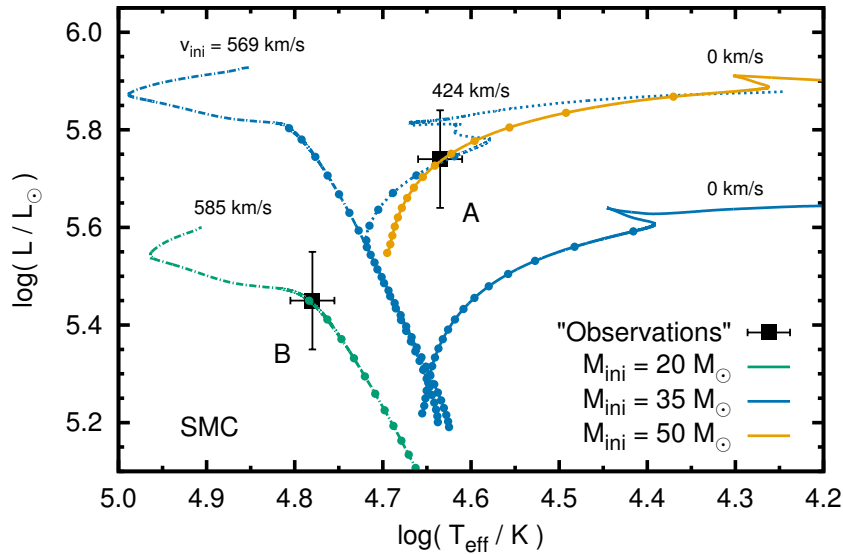
Figure 4.2: Position of the mock stars, Star A and Star B, in the HR diagram compared to rotating and non-rotating stellar evolutionary models of Brott et al. (2011a) of SMC composition. The dots on the stellar tracks are equally spaced by 0.25 Myr.

4.3 Testing Bonnsai with mock stars

In the following sections, we apply Bonnsai to the two SMC mock stars, Star A and Star B, whose position in the HR diagram is shown in Fig. 4.2 together with SMC stellar evolutionary models of Brott et al. (2011a). We analyse Star A in Sec. 4.3.1 and Star B in 4.3.2.

4.3.1 Mock Star A

Mock Star A has an effective temperature of $T_{\mathrm{eff}} = 43200 \pm 2500\,\mathrm{K}$ and a luminosity of $\log L/\mathrm{L}_\odot = 5.74 \pm 0.10$ (Fig. 4.2). Its position in the HR diagram is equally well matched by an initially rapidly ($424\,\mathrm{km\,s^{-1}}$) rotating $35\,\mathrm{M}_\odot$ star and a non-rotating $50\,\mathrm{M}_\odot$ star. The initial rapid rotator starts out evolving chemically homogeneously. Rotationally induced mixing brings helium, synthesized by hydrogen burning in the stellar core, to the surface which in turn reduces the electron scattering opacity. Therefore, it stays more compact, evolves towards hotter effective temperatures and becomes more luminous than its non-rotating counterpart. It is tempting to conclude that both evolutionary scenarios are equally likely because both fit the position of the star in the HR diagram equally well. However, this is a biased view that does not take a priori knowledge of stars and stellar evolution into account — we can actually exclude the rapidly rotating $35\,\mathrm{M}_\odot$ star with more than 95% confidence as we show below.

There are two different sources of a priori knowledge, namely that of (a) the model parameters, i.e. what we know about the initial mass, age, initial rotational velocity and metallicity of the star before analysing it, and (b) stellar evolution. The former enters our approach through the prior functions (Sec. 4.2.4) and the latter through the stellar models used to compute the likelihood (Sec. 4.2.3). From the point of view of the prior functions, $35\,\mathrm{M}_\odot$ models are preferred over $50\,\mathrm{M}_\odot$ because of the IMF, but moderately rotating $50\,\mathrm{M}_\odot$ models over rapidly rotating $35\,\mathrm{M}_\odot$ stars because of observed distributions of stellar rotation rates. From the point of view of stellar models, the $50\,\mathrm{M}_\odot$ track is preferred because the $50\,\mathrm{M}_\odot$ model spends more time at
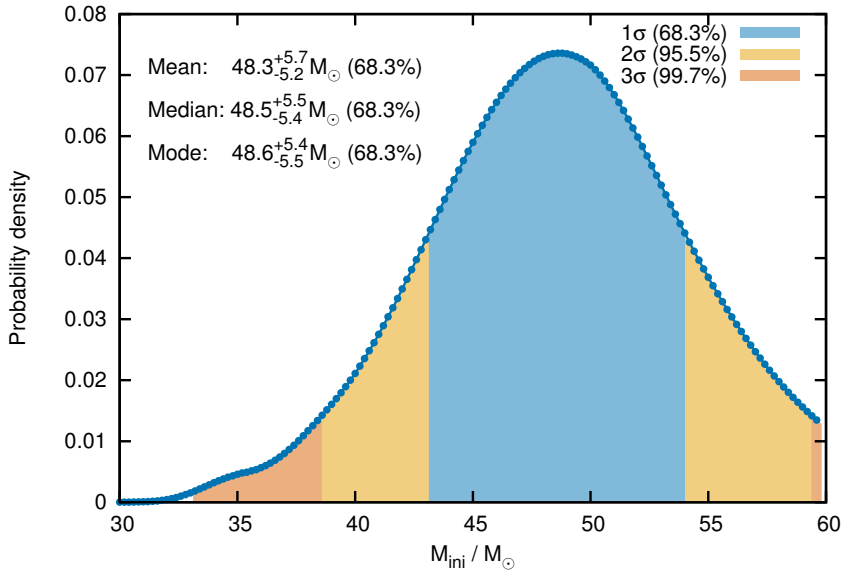
Figure 4.3: Initial mass posterior probability distribution of mock Star A from Fig. 4.2. The shaded regions give the 1σ, 2σ and 3σ confidence regions.

the observed position in the HR diagram than the $35\,\mathrm{M_\odot}$ model that is close to the end of its main-sequence evolution where evolution is more rapid. The $50\,\mathrm{M_\odot}$ models are also preferred because there are many models of that mass with different initial rotational velocities that reach the observed position in the HR diagram while there is only a narrow range of initial rotation rates of $35\,\mathrm{M_\odot}$ models that match the observations.

The a priori knowledge allows us to quantify how likely both models are. Only additional observables that are sensitive to rotation enable us to fully resolve the degenerate situation.

In the following, we match Star A against the SMC models of Brott et al. (2011a), choose a Salpeter mass function as initial mass prior and a uniform age prior. We vary the initial rotational velocity prior and use an additional constraint on the surface helium abundance to show their influence on the posterior probability distributions. The resolution test, the χ^2-hypothesis test and the posterior predictive checks are passed in all cases. We present a summary of our test cases in Table 4.2.

4.3.1.1 Uniform initial rotational velocity prior

At first we apply a uniform v_{ini} prior, i.e. we assume that all initial rotational velocities are a priori equally probable. The resulting posterior probability distribution of the initial mass is shown in Fig. 4.3 as a histogram with a binwidth of $0.2\,\mathrm{M_\odot}$. The mean, median and mode are given with their 1σ uncertainties (the confidence level is indicated in parentheses). The most probable initial mass is $48.6^{+5.4}_{-5.5}\,\mathrm{M_\odot}$, the most probable age is $2.3^{+0.5}_{-0.6}\,\mathrm{Myr}$ and the initial rotational velocity is unconstrained, i.e. its posterior probability distribution is uniform until it steeply drops-off at $v_{\mathrm{ini}} \gtrsim 400\,\mathrm{km\,s^{-1}}$ (left panel in Fig. 4.4). The likelihood of a $35\,\mathrm{M_\odot}$ star is small. It is only within the 3σ uncertainty despite the Salpeter IMF prior that prefers lower initial masses. The reason why the $50\,\mathrm{M_\odot}$ models are favoured over rapidly rotating $35\,\mathrm{M_\odot}$ stars is best seen in the $v_{\mathrm{ini}} - M_{\mathrm{ini}}$ plane of the posterior probability distribution in Fig. 4.4. Only a small subset of $35\,\mathrm{M_\odot}$ fast rotators, those with $v_{\mathrm{ini}} \gtrsim 400\,\mathrm{km\,s^{-1}}$, reach the observed
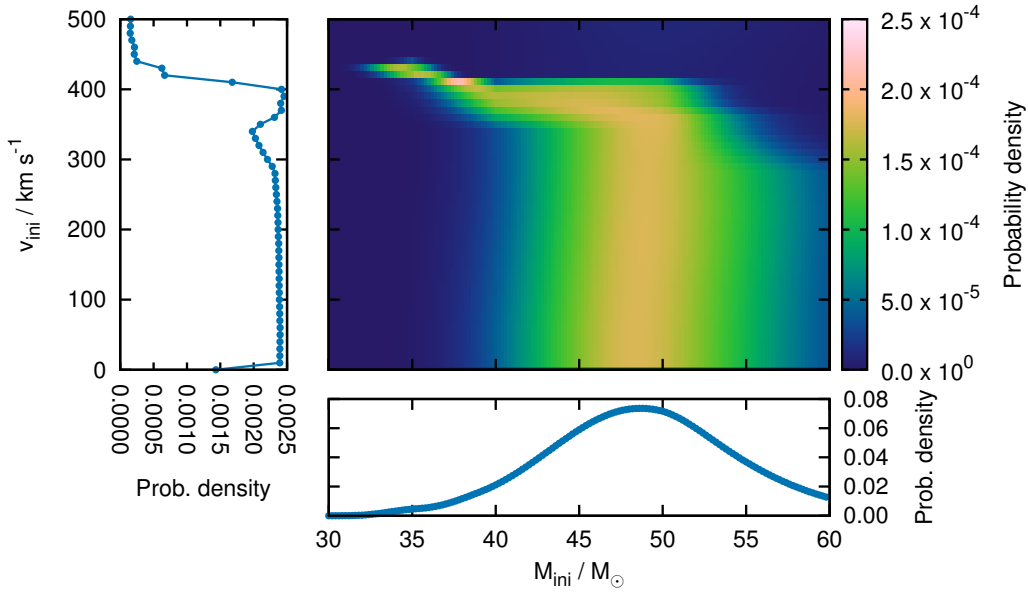
Figure 4.4: Posterior probability map of the $v_{\rm ini} - M_{\rm ini}$ plane (middle panel) adopting a Salpeter initial mass function as $M_{\rm ini}$ prior and a uniform prior for $v_{\rm ini}$. One dimensional posterior probability distributions of initial rotational velocities $v_{\rm ini}$ (left panel) and initial masses $M_{\rm ini}$ (bottom panel) are also given.

position in the HR diagram and thus contribute to the posterior probability distribution of the initial mass in Fig. 4.3. The range of initial rotational velocities of stars around $50\,{\rm M_\odot}$ that contribute to the posterior probability is much larger and has thus a correspondingly larger weight (Fig. 4.4). In conclusion, both the 35 and $50\,{\rm M_\odot}$ models reproduce the position in the HR diagram equally well but it is much more likely that the star is a $50\,{\rm M_\odot}$ star: $35\,{\rm M_\odot}$ models are excluded with a confidence of more than 97.5%.

As evident from this example, the (marginalised) posterior distributions contain a wealth of information that is partly lost when looking only at the summary statistics, e.g. the mode and confidence levels. We therefore encourage all BONNSAI users to first inspect the marginalised posterior probability distributions before making use of the summary statistics.

4.3.1.2 Gaussian initial rotational velocity prior

We now change the initial rotational velocity prior to show its influence on the posterior probability. We use the observationally determined distribution of rotational velocities of SMC early B-type stars from Hunter et al. (2008a) as a prior. This distribution is well approximated by a Gaussian with mean $\langle v_{\rm rot}\rangle = 175\,{\rm km\,s^{-1}}$ and standard deviation $\sigma_{\rm v} = 106\,{\rm km\,s^{-1}}$. The distribution disfavours slow ($\lesssim 100\,{\rm km\,s^{-1}}$) and fast rotators ($\gtrsim 250\,{\rm km\,s^{-1}}$) compared to the uniform $v_{\rm ini}$ prior. This is reflected in the $v_{\rm ini} - M_{\rm ini}$ plane of the posterior probability in Fig. 4.5. Slow and fast rotators are now less likely than before with the uniform $v_{\rm ini}$ prior. The posterior probability function of the initial mass and age are however nearly unaffected: the most likely initial mass is $48.8^{+5.4}_{-5.1}\,{\rm M_\odot}$. Fast-rotating $35\,{\rm M_\odot}$ stars are now even less likely because the chosen prior favours moderate rotators. The most likely initial rotational velocity now is $170^{+99}_{-94}\,{\rm km\,s^{-1}}$, i.e. it follows the $v_{\rm ini}$ prior both in the mean value and the uncertainty because it is otherwise unconstrained in this example (Sec. 4.3.1.1).
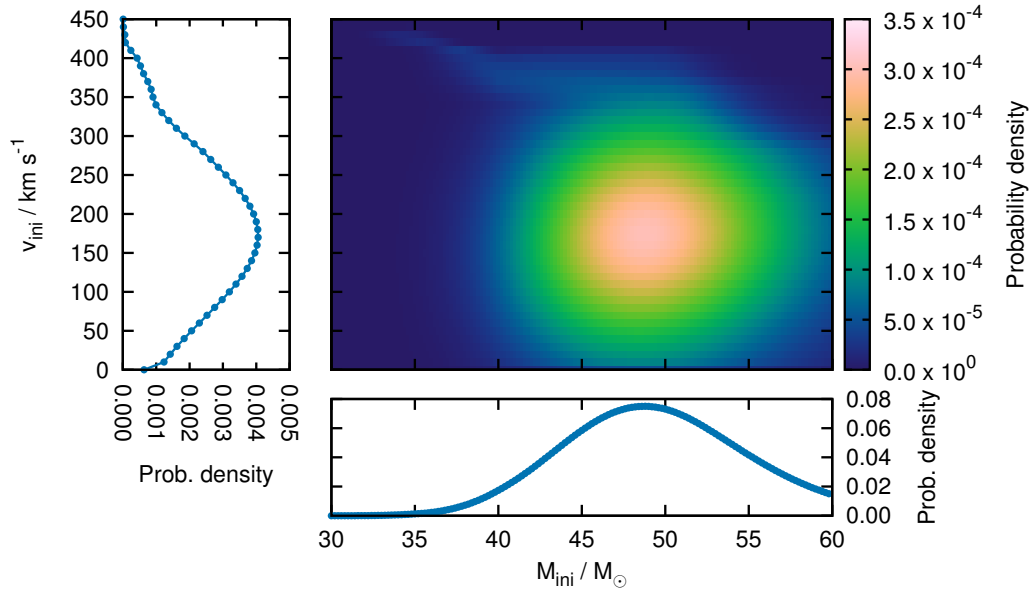
Figure 4.5: As Fig. 4.4 but using as v_{ini} prior the observed distribution of rotational velocities of SMC early B-type stars from Hunter et al. (2008a).

4.3.1.3 Including the surface helium mass fraction

The degeneracy in HR diagrams (Fig. 4.2) that arises from rotational mixing can be removed if observables that are sensitive to rotation are incorporated in the analysis. We use observed surface helium mass fractions, Y, as an additional constraint to demonstrate this (the initial mass fraction of the SMC models of Brott et al. (2011a) is $Y_{ini} = 0.2515$). The surface helium abundance is sensitive to rotation as rotational mixing brings more helium to the surface the faster the star rotates.

A surface helium mass fraction of $Y \leq 0.3$ rules out rapid rotators ($\gtrsim 350\,\mathrm{km\,s^{-1}}$) because their surfaces are enriched in helium to more than 30% in mass. When assuming a uniform v_{ini} prior, the most likely initial mass is $49.2^{+4.7}_{-5.5}\,\mathrm{M_\odot}$, i.e. slightly larger than before because rapid rotators are totally excluded and not only suppressed as in Sec. 4.3.1.2 without the additional surface helium mass fraction constraint and a Gaussian v_{ini} prior.

Contrarily, a surface helium mass fraction of $Y \geq 0.4$ allows only for rapid rotators because stars rotating initially slower than about $350\,\mathrm{km\,s^{-1}}$ do not enrich their surfaces by more than 40% in helium at the observed position in the HR diagram. So even assuming that the initial rotational velocities are distributed according to Hunter et al. (2008a) — a Gaussian distribution that highly suppresses rapid rotators — results in a most likely initial rotational velocity of $400^{+14}_{-15}\,\mathrm{km\,s^{-1}}$. Consequently, the most likely initial mass is lower, namely $39.4^{+5.7}_{-3.2}\,\mathrm{M_\odot}$, and the most likely age is older, namely $3.9^{+0.8}_{-0.7}\,\mathrm{Myr}$.

4.3.2 Mock Star B

Next we consider the mock Star B with a luminosity of $\log L/\mathrm{L_\odot} = 5.45 \pm 0.10$, effective temperature $T_{eff} = 60200 \pm 3500\,\mathrm{K}$ and surface helium mass fraction $Y = 0.25 \pm 0.05$ (Fig. 4.2). Only rapid rotators evolving chemically homogeneously reach the position of Star B in the HR diagram. Main-sequence SMC models of Brott et al. (2011a) at that position in the HR

Table 4.2: Summary of the assumptions, additional constraints and resulting model parameters of our mock Star A (Secs. 4.3.1.1–4.3.1.3).

Add. constraint	$v_{\rm ini}$ prior	$M_{\rm ini}$ ($M_\odot$)	τ (Myr)	$v_{\rm ini}$ (km s^{-1})
–	uniform	$48.6^{+5.4}_{-5.5}$	$2.3^{+0.5}_{-0.6}$	unconstr.
–	Hunter '08	$48.8^{+5.4}_{-5.1}$	$2.3^{+0.4}_{-0.5}$	170^{+99}_{-94}
$Y \leq 0.3$	uniform	$49.2^{+4.7}_{-5.5}$	$2.3^{+0.4}_{-0.5}$	≤ 350
$Y \geq 0.4$	Hunter '08	$39.4^{+5.7}_{-3.2}$	$3.9^{+0.8}_{-0.7}$	400^{+14}_{-15}

diagram are significantly enriched with helium at their surface, $Y = 0.89^{+0.05}_{-0.09}$ ($Y_{\rm ini} = 0.2515$). Contrarily, our mock Star B has the initial helium abundance, thus the stellar models cannot reproduce the star. In the following, we show how such situations are robustly identified within BONNSAI using the goodness-of-fit criteria from Sec. 4.2.6 after ensuring that the resolution of the model grid is sufficiently high.

4.3.2.1 Resolution and χ^2-hypothesis test

In Fig. 4.6 we show the stellar model coverage of the parameter space of the observables. As described in Sec. 4.2.7, stellar models are chosen within 5σ of the observations from the model database, i.e. the luminosities of the stellar models are in the range $\log L/L_\odot = 4.95$–5.95, the effective temperatures in $T_{\rm eff} = 42700$–77700 K and the surface helium mass fractions in $Y = 0.00$–0.50. There are no stellar models in the direct vicinity of the observation because only those stars that are highly enriched with helium at their surface ($Y = 0.89^{+0.05}_{-0.09}$) are found at the observed position in the HR diagram.

Projections like those in Fig. 4.6 can not be readily used as a criterion to accept a BONNSAI solution but should only be used as an analysis tool. The best-fitting stellar model might be far away from the observation (e.g. 5σ) while all projections homogeneously and densely cover the observation. This can happen whenever the stellar models cover the surface of the $n_{\rm obs}$-dimensional parameter space but not the inside. The projections are then homogeneously filled with stellar models but the closest model is still far away from the observation.

In the present case, the automatic resolution test as described in Sec. 4.2.6 confirms the visual impression of Fig. 4.6 that the resolution of the stellar model grid is sufficiently high, i.e. that the observables, including their error bars, do not fall between model grid points. An insufficient resolution as a reason for not finding stellar models close to the observation can be excluded and the results of our analysis do not suffer from resolution problems.

The maximum allowable χ^2 for a significance level $\alpha = 5\%$ and three degrees of freedom is $\chi^2_{\rm max} \approx 7.8$. The χ^2 of the best-fitting stellar model is $\chi^2_{\rm best} \approx 10.2$. We therefore conclude that the stellar models are unable to explain the observables with a confidence of $\geq 95\%$.

4.3.2.2 Posterior predictive check

In a Bayesian analysis we not only test the best fitting model but use the full posterior probability distribution to evaluate the goodness of the fit. From the obtained model parameters, we compute the model predictions, i.e. the probability distributions, of the observables effective temperature, luminosity and surface helium mass fraction, that are called replicated observables. The probability distributions of the replicated observables are then compared to those
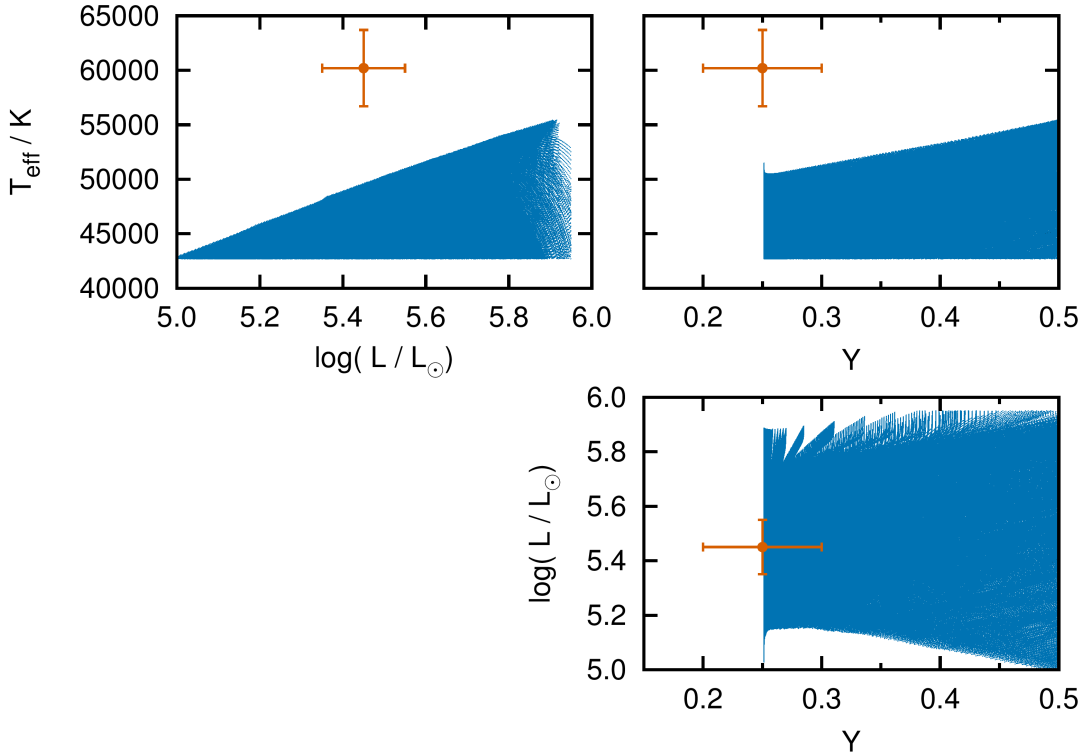
Figure 4.6: Coverage of the projected parameter space of the observables of our mock Star B (Sec. 4.3.2). One dot for each stellar model and the observables including their 1σ uncertainties are plotted.

of the original observations, i.e. to the individual likelihood functions, L_i (Eq. 4.4), to check whether the predictions of the models for the obtained model parameters are in agreement with the observations. To that end, we compute the probability distributions of the differences of replicated and original observables which we show in Fig. 4.7. We find that the effective temperatures deviate by $\Delta T_{\mathrm{eff}} = T_{\mathrm{eff,rep}} - T_{\mathrm{eff,obs}} = -11,920 \pm 3,735\,\mathrm{K}$ such that the replicated effective temperatures are cooler than the observed temperatures in more than 99% of the cases — the stellar models can clearly not reproduce the observations. The replicated luminosities and surface helium mass fractions are in agreement with the observations ($\Delta \log L/\mathrm{L}_\odot = 0.10 \pm 0.13$ and $\Delta Y = -0.01 \pm 0.06$; Fig. 4.7).

4.4 Testing stellar evolution models with eclipsing binaries

In the previous sections we show that our new method provides stellar parameters including robust uncertainties and reliably identifies stars that cannot be reproduced by stellar models when applied to mock data (Sec. 4.3). One of the primary goals of BONNSAI is to test the physics in stellar models by matching the models to observations in a statistically sound way. For that it is necessary to have well determined stellar parameters that — ideally — do not rely on extensive modelling and/or calibrations. Eclipsing, double-lined spectroscopic binaries and interferometric observations of single stars are prime candidates for this purpose.

We use BONNSAI in combination with precise measurements of stellar masses and radii of Milky Way binaries (Torres et al. 2010) to test the Milky Way stellar models of Brott et al.
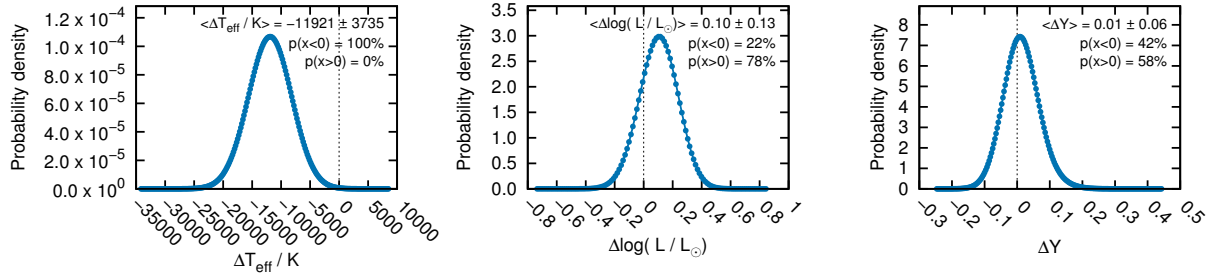
Figure 4.7: Probability distributions of the differences of the replicated and original observables of our mock Star B (left panel: effective temperature; middle panel: luminosity; right panel: surface helium mass fraction). The stellar models predict effective temperatures that are significantly cooler than the observations and are thus not able to reproduce the star.

(2011a). The stellar masses and radii of the Milky Way binary components are determined from observed radial-velocity curves and light curves. We call masses and radii determined in this way dynamical masses and dynamical radii. The surface gravities, $\log g$, follow directly from the measured dynamical masses and radii. Additionally, the stellar bolometric luminosities follow from the Stefan-Boltzmann law if the effective temperatures are known as well. The latter typically rely on multi-band photometry and calibrations, individual spectra or a comparison of the spectral energy distributions obtained by narrow band filters with stellar atmosphere models (spectro-photometry).

The Torres et al. (2010) sample of Milky Way binary stars is an updated extension of the sample of Andersen (1991). All binary stars are analysed homogeneously and dynamical masses and radii are known to better than 3%. We work with a subsample of the Torres et al. (2010) sample, namely with all stars that are within the mass range covered by our Milky Way stellar models. We extend the published stellar models of Brott et al. (2011a) by unpublished ones down to $4\,M_\odot$ to increase our binary sample size by three. We describe our method to test the stellar models in Sec. 4.4.1, explain why stellar rotation needs to be accounted for in Sec. 4.4.2, present the results of our test in Sec. 4.4.3 and compare effective temperatures and bolometric luminosities predicted by the models to the observed values in Sec. 4.4.4.

Table 4.3: Observed stellar parameters of those Milky Way binaries in the sample of Torres et al. (2010) that we use to test BONNSAI and the stellar models of Brott et al. (2011a). Listed are the orbital period P (semi major axis a in parentheses), the dynamical mass $M_{\rm dyn}$ and radius $R_{\rm dyn}$, the projected rotational velocity $v \sin i$, the spectral type SpT, the effective temperature $T_{\rm eff,obs}$, the surface gravity $\log g_{\rm obs}$ and the bolometric luminosity $\log L_{\rm obs}$.

Binary	P (days)		SpT	$M_{\rm dyn}$ (M$_\odot$)	$R_{\rm dyn}$ (R$_\odot$)	$v \sin i$ (km s^{-1})	$T_{\rm eff,obs}$ (K)	$\log g_{\rm obs}$ (cgs)	$\log L_{\rm obs}$ (L$_\odot$)
V3903 Sgr	1.74	A	O7V	27.27±0.55	8.088±0.086	230±23	38,000±1900	4.058±0.016	5.088±0.087
	(21.9 R$_\odot$)	B	O9V	19.01±0.44	6.125±0.060	170±17	34,100±1700	4.143±0.013	4.658±0.088
EM Car	3.41	A	O8V	22.83±0.32	9.350±0.170	150±20	34,000±2000	3.855±0.016	5.021±0.104
	(33.7 R$_\odot$)	B	O8V	21.38±0.33	8.350±0.160	130±15	34,000±2000	3.925±0.016	4.922±0.104
V1034 Sco	2.44	A	O9V	17.21±0.46	7.507±0.081	. . .	33,200±900	3.923±0.008	4.789±0.048
	(22.8 R$_\odot$)	B	B1.5V	9.59±0.27	4.217±0.089	. . .	26,330±900	4.170±0.013	3.885±0.062
V478 Cyg	2.88	A	O9.5V	16.62±0.33	7.426±0.072	. . .	30,479±1000	3.917±0.007	4.631±0.058
	(27.3 R$_\odot$)	B	O9.5V	16.27±0.33	7.426±0.072	. . .	30,549±1000	3.908±0.008	4.635±0.057
AH Cep	1.77	A	B0.5Vn	15.26±0.35	6.346±0.071	185±30	29,900±1000	4.017±0.009	4.461±0.059
	(18.9 R$_\odot$)	B	B0.5Vn	13.44±0.25	5.836±0.085	185±30	28,600±1000	4.034±0.012	4.311±0.062
V578 Mon	2.41	A	B1V	14.50±0.12	5.149±0.091	117±5	30,000±740	4.176±0.015	4.285±0.045
	(22.0 R$_\odot$)	B	B2V	10.26±0.08	4.210±0.100	94±4	26,400±600	4.200±0.021	3.888±0.045
V453 Cyg	3.89	A	B0.4IV	13.82±0.35	8.445±0.068	109±3	27,800±400	3.725±0.006	4.583±0.026
	(30.2 R$_\odot$)	B	B0.7IV	10.64±0.22	5.420±0.068	98±5	26,200±500	3.997±0.010	4.094±0.035
CW Cep	2.73	A	B0.5V	13.05±0.20	5.640±0.120	. . .	28,300±1000	4.050±0.019	4.263±0.064
	(24.0 R$_\odot$)	B	B0.5V	11.91±0.20	5.140±0.120	. . .	27,700±1000	4.092±0.021	4.145±0.067
DW Car	1.33	A	B1V	11.34±0.18	4.561±0.050	182±3	27,900±1000	4.175±0.009	4.054±0.063
	(14.3 R$_\odot$)	B	B1V	10.63±0.20	4.299±0.058	177±3	26,500±1000	4.198±0.011	3.913±0.067
QX Car	4.48	A	B2V	9.25±0.12	4.291±0.091	120±10	23,800±500	4.139±0.018	3.725±0.041
	(29.8 R$_\odot$)	B	B2V	8.46±0.12	4.053±0.091	110±10	22,600±500	4.150±0.019	3.585±0.043
V1388 Ori	2.19	A	B2.5IV-V	7.42±0.16	5.600±0.080	125±10	20,500±500	3.812±0.016	3.697±0.044
	(16.5 R$_\odot$)	B	B3V	5.16±0.06	3.760±0.060	75±15	18,500±500	4.000±0.015	3.172±0.049
V539 Ara	3.17	A	B3V	6.24±0.07	4.516±0.084	75±8	18,100±500	3.924±0.016	3.293±0.051
	(20.5 R$_\odot$)	B	B4V	5.31±0.06	3.428±0.083	48±5	17,100±500	4.093±0.021	2.955±0.055
CV Vel	6.89	A	B2.5V	6.09±0.04	4.089±0.036	19±1	18,100±500	3.999±0.008	3.207±0.049
	(35.0 R$_\odot$)	B	B2.5V	5.98±0.04	3.950±0.036	31±2	17,900±500	4.022±0.008	3.158±0.049

Table 4.3: continued

Binary	P (days)		SpT	$M_{\rm dyn}$ ($M_\odot$)	$R_{\rm dyn}$ ($R_\odot$)	$v\sin i$ (km s^{-1})	$T_{\rm eff,obs}$ (K)	$\log g_{\rm obs}$ (cgs)	$\log L_{\rm obs}$ ($L_\odot$)
AG Per	2.03	A	B3.4V	5.35±0.16	2.995±0.071	94±23	18,200±800	4.213±0.020	2.946±0.079
	(14.7 R$_\odot$)	B	B3.5V	4.89±0.13	2.605±0.070	70±9	17,400±800	4.296±0.023	2.747±0.083
U Oph	1.68	A	B5V	5.27±0.09	3.484±0.021	125±5	16,440±250	4.076±0.004	2.901±0.027
	(12.8 R$_\odot$)	B	B6V	4.74±0.07	3.110±0.034	115±5	15,590±250	4.128±0.009	2.710±0.029
DI Her	10.55	A	B5V	5.17±0.11	2.681±0.046	. . .	17,000±800	4.295±0.015	2.732±0.083
	(43.2 R$_\odot$)	B	B5V	4.52±0.07	2.478±0.046	. . .	15,100±700	4.305±0.015	2.457±0.082
V760 Sco	1.73	A	B4V	4.97±0.09	3.015±0.066	95±10	16,900±500	4.176±0.019	2.823±0.055
	(12.9 R$_\odot$)	B	B4V	4.61±0.07	2.641±0.066	85±10	16,300±500	4.258±0.021	2.645±0.058
MU Cas	9.65	A	B5V	4.66±0.10	4.195±0.058	21±2	14,750±800	3.861±0.012	2.874±0.096
	(40.0 R$_\odot$)	B	B5V	4.58±0.09	3.670±0.057	22±2	15,100±800	3.969±0.013	2.798±0.094

4.4.1 Description of our test

The primary and secondary stars in binaries can be assumed to be coeval. We use this condition to test stellar models by comparing the ages determined individually for the primary and secondary star of each binary. The ages inferred for the primary and secondary star may deviate if the physics and calibrations of the stellar models are not accurate. This or a similar test is often applied to binaries in order to test stellar evolution and investigate convective core overshooting (see e.g. Andersen 1991; Schroder et al. 1997; Pols et al. 1997; Clausen et al. 2010; Torres et al. 2010, 2014, and references therein).

In case of observed dynamical masses and radii, the stellar ages are constrained through the time dependence of stellar radii because the masses of stars in the binary sample of Torres et al. (2010) hardly change with time. However, stellar radii, R, depend not only on age but on a variety of parameters,

$$R = R(M, \tau, v_{\mathrm{rot}}, Z, \alpha_{\mathrm{ML}}, l_{\mathrm{ov}}, \dots),$$

such as — in addition to age τ — mass M, rotational velocity v_{rot}, metallicity Z and the treatment of convection, indicated here by the convective mixing length parameter α_{ML} and the convective core overshooting length l_{ov}. The mixing length parameter, α_{ML}, plays only a minor role in the hot stars considered here. Besides the dynamically measured masses and radii, we use, if available, the observed projected rotational velocities $v \sin i$ to determine stellar ages (Table 4.3). The parameters radius, mass and rotational velocity are fixed within their uncertainties by the observations and the derived stellar ages depend on the remaining parameters. That is, our test probes the chemical composition (metallicity) and the implementation and calibration of rotation and convection in the stellar models. The metallicities are also known to a certain degree because the binary sample consists of Milky Way stars.

Because of the precise observations, we use denser stellar model grids than those available by default in the BONNSAI web-service. With the higher resolution our resolution test, the χ^2-hypothesis test and our posterior predictive check are passed by all stars.

Our test loses significance if the stars in a binary have very similar masses and radii because the ages derived for such similar stars have to be the same no matter which stellar models and calibrations are used. In the following we therefore cite the mass ratios q of secondary to primary star to easily spot binaries with similar stellar components.

We compare the stars in the binaries to stellar evolutionary models of single stars. This assumption is good as long as the past evolution of the stars is not influenced significantly by binary interactions. Past mass transfer episodes are not expected to have occurred in our binary sample because all the stars are on the main-sequence and presently do not fill their Roche lobes. Tidal interactions, however, have influenced the binaries and affect stellar radii in two ways: (1) tides spin stars up or down which consequently changes their radii by rotational mixing and centrifugal forces; (2) tides dissipate energy inside stars, thereby giving rise to an additional energy source that might increase stellar radii. All binary stars in Torres et al. (2010) whose radii are larger than about 25% of the orbital separation are circularised, implying that the stellar rotation periods are synchronised with the orbital periods because synchronisation is expected to precede circularisation. Once the binaries are synchronised and circularised, no torques act on the stars and tides no longer influence the evolution until stellar evolution either changes the spin period of the stars or the orbit by e.g. wind mass loss such that tides are active again. We have to keep this in mind when comparing the observations to single star models that do not take tidal evolution into account.
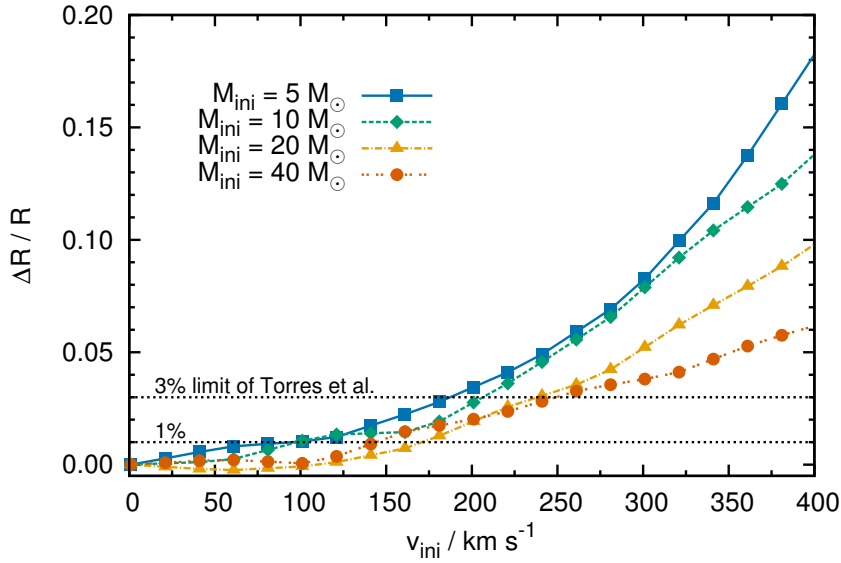
Figure 4.8: Relative radius difference of zero-age, rotating and non-rotating stellar models from Brott et al. (2011a) as a function of initial rotational velocity v_{ini} and initial stellar mass M_{ini}.

4.4.2 The role of rotation in Milky Way binaries

The stars with known rotation rates in our sample have projected rotational velocities $v \sin i$ between 20 and $230\,\mathrm{km\,s^{-1}}$. The associated centrifugal forces lead to larger stellar radii. Within the Roche model, we approximate by how much stellar radii change as a function of rotational velocity. The Roche potential $\psi(r, \vartheta)$ of a star with mass M rotating with frequency $\Omega = 2\pi/P_{\mathrm{s}}$ (P_{s} being the rotation period) is given by

$$\psi(r, \vartheta) = -\frac{Gm_r}{r} - \frac{1}{2}\Omega^2 r^2 \sin\vartheta, \qquad (4.14)$$

where r is the radial distance and ϑ the polar angle, G is the gravitational constant and m_r is the mass within radius r. The Roche potential evaluated at the stellar pole ($r = R_p$, $\vartheta = 0$) and at the stellar equator ($r = R_e$, $\vartheta = \pi/2$) are equal because the stellar surface is on an equipotential. Equating $\psi(R, 0) = \psi(R, \pi/2)$, introducing the break-up or critical rotational frequency $\Omega_{\mathrm{crit}} = \sqrt{GM/R_e^3}$ (i.e. Keplerian frequency at the equator) and $\Gamma = \Omega/\Omega_{\mathrm{crit}}$, we have for the relative difference of the equatorial and polar radius

$$\frac{\Delta R}{R} \equiv \frac{R_e - R_p}{R_p} = \frac{\Gamma^2}{2}. \qquad (4.15)$$

The polar radius R_p is not explicitly affected by rotation and hence it can be viewed as the radius of a star in absence of rotation (centrifugal forces do not act in the direction of the rotation axis). Hence, Eq. 4.15 provides an estimate of the relative increase in equatorial radius of stars rotating with a fraction Γ of critical rotation. The equatorial radius increases by 3% if the star rotates with about 25% of critical rotation.

In Fig. 4.8 we show the increase of the equatorial stellar radii of rotating zero-age main-sequence stars compared to non-rotating stars ($\Delta R/R \equiv [R_{\mathrm{rot}} - R_{\mathrm{non-rot}}]/R_{\mathrm{non-rot}}$) as a function of initial rotational velocity v_{ini} and initial stellar mass M_{ini}. Stars that have masses

$\leq 10\,\mathrm{M}_\odot$ and rotate with about $100\,\mathrm{km\,s^{-1}}$ have radii increased by about 1%. The radii are increased by more than 3% if stars rotate faster than about $200\,\mathrm{km\,s^{-1}}$. Given that dynamical radii in Torres et al. (2010) are all known to better than 3% and often to about 1%, our estimates show that, at such accuracies, rotation has to be considered to accurately test the stellar models.

4.4.3 The ages of primary and secondary stars

We determine stellar parameters of the binary stars from dynamical masses, dynamical radii and projected rotational velocities (Table 4.3). The latter are not available for the binaries V1034 Sco, V478 Cyg, CW Cep and DI Her, so we determine their stellar parameters from their dynamical masses and radii alone. Our determined initial mass, age, initial rotational velocity, effective temperature, surface gravity and luminosity are summarised in Table 4.4 including their (mostly) 1σ uncertainties (see caption of Table 4.4). We also indicate the approximate fractional main-sequence age, τ/τ_MS, of the stars in 5% steps. The main-sequence lifetimes, τ_MS, of the stellar models are determined from the obtained initial mass and initial rotational velocity.

Table 4.4: Evolutionary parameters of the Milky Way binaries from Table 4.3 as determined with BONNSAI. We provide the initial stellar mass M_{ini}, the stellar age τ, the initial rotational velocity v_{ini}, the fractional main-sequence age τ/τ_{MS}, the effective temperature $T_{\mathrm{eff,theo}}$, the surface gravity $\log g_{\mathrm{theo}}$ and the bolometric luminosity $\log L_{\mathrm{theo}}$, including their (mostly) 1σ (68.3%) confidence intervals. Note that the confidence level of the surface gravity of CV Vel A is 71.5%, that of the initial rotational velocity of V1034 Sco B is 76.3% and that of the effective temperatures of CW Cep A and CW Cep B are 81.8% and 87.0%, respectively (because of broad posterior distributions that do not allow us to compute smaller confidence intervals).

Binary		M_{ini} (M$_\odot$)	τ (Myr)	v_{ini} (km s^{-1})	τ/τ_{MS}	$T_{\mathrm{eff,theo}}$ (K)	$\log g_{\mathrm{theo}}$ (cgs)	$\log L_{\mathrm{theo}}$ (L$_\odot$)
V3903 Sgr	A	$27.70^{+0.60}_{-0.62}$	$2.0^{+0.3}_{-0.2}$	$240.0^{+101.8}_{-36.1}$	30%	$37,475^{+402}_{-424}$	$4.08^{+0.02}_{-0.04}$	$5.08^{+0.03}_{-0.04}$
	B	$19.02^{+0.44}_{-0.44}$	$1.9^{+0.4}_{-0.4}$	$180.0^{+116.4}_{-40.4}$	20%	$33,275^{+506}_{-590}$	$4.12^{+0.04}_{-0.03}$	$4.62^{+0.03}_{-0.05}$
EM Car	A	$23.28^{+0.34}_{-0.36}$	$4.3^{+0.2}_{-0.2}$	$160.0^{+85.5}_{-34.6}$	60%	$33,425^{+327}_{-331}$	$3.88^{+0.02}_{-0.05}$	$4.97^{+0.04}_{-0.03}$
	B	$21.66^{+0.35}_{-0.35}$	$4.2^{+0.2}_{-0.2}$	$140.0^{+85.4}_{-37.5}$	55%	$33,375^{+319}_{-386}$	$3.92^{+0.03}_{-0.03}$	$4.88^{+0.04}_{-0.03}$
V1034 Sco	A	$17.30^{+0.49}_{-0.46}$	$5.7^{+0.6}_{-0.5}$	$520.0^{+4.9}_{-350.1}$	45%–60%	$30,375^{+581}_{-611}$	$3.92^{+0.03}_{-0.03}$	$4.62^{+0.05}_{-0.04}$
	B	$9.56^{+0.26}_{-0.28}$	$5.7^{+2.0}_{-2.6}$	$420.0^{+48.9}_{-318.7}$	20%	$24,275^{+536}_{-1003}$	$4.17^{+0.03}_{-0.04}$	$3.73^{+0.06}_{-0.06}$
V478 Cyg	A	$16.70^{+0.36}_{-0.32}$	$6.1^{+0.5}_{-0.5}$	$520.0^{+6.7}_{-346.3}$	45%–60%	$29,875^{+488}_{-522}$	$3.92^{+0.02}_{-0.03}$	$4.58^{+0.06}_{-0.02}$
	B	$16.36^{+0.34}_{-0.34}$	$6.4^{+0.5}_{-0.5}$	$520.0^{+7.5}_{-346.7}$	50%–60%	$29,475^{+518}_{-499}$	$3.92^{+0.02}_{-0.04}$	$4.58^{+0.04}_{-0.04}$
AH Cep	A	$15.28^{+0.37}_{-0.35}$	$5.3^{+0.5}_{-0.4}$	$200.0^{+90.5}_{-52.8}$	45%	$29,475^{+478}_{-447}$	$4.03^{+0.03}_{-0.03}$	$4.42^{+0.05}_{-0.03}$
	B	$13.46^{+0.24}_{-0.26}$	$6.2^{+0.5}_{-0.5}$	$200.0^{+91.5}_{-52.7}$	45%	$27,975^{+386}_{-512}$	$4.03^{+0.03}_{-0.03}$	$4.28^{+0.03}_{-0.05}$
V578 Mon	A	$14.50^{+0.13}_{-0.11}$	$2.3^{+0.6}_{-0.5}$	$120.0^{+87.3}_{-33.9}$	20%	$29,975^{+244}_{-270}$	$4.17^{+0.03}_{-0.03}$	$4.28^{+0.03}_{-0.03}$
	B	$10.26^{+0.09}_{-0.08}$	$4.0^{+1.1}_{-1.1}$	$100.0^{+66.0}_{-34.4}$	20%	$25,475^{+218}_{-208}$	$4.17^{+0.06}_{-0.01}$	$3.83^{+0.03}_{-0.03}$
V453 Cyg	A	$13.84^{+0.37}_{-0.34}$	$10.2^{+0.5}_{-0.6}$	$120.0^{+71.0}_{-37.2}$	80%	$26,025^{+449}_{-492}$	$3.73^{+0.02}_{-0.02}$	$4.47^{+0.03}_{-0.05}$
	B	$10.64^{+0.22}_{-0.22}$	$10.9^{+0.8}_{-0.9}$	$100.0^{+78.5}_{-31.4}$	55%	$24,925^{+368}_{-439}$	$3.98^{+0.05}_{-0.02}$	$4.03^{+0.02}_{-0.06}$
CW Cep	A	$13.06^{+0.21}_{-0.20}$	$6.2^{+0.6}_{-0.7}$	$520.0^{+30.0}_{-327.0}$	35%–40%	$27,825^{+308}_{-1,285}$	$4.08^{+0.01}_{-0.06}$	$4.22^{+0.03}_{-0.07}$
	B	$11.92^{+0.20}_{-0.20}$	$5.9^{+1.1}_{-1.2}$	$520.0^{+30.0}_{-305.0}$	30%–35%	$25,475^{+1,746}_{-373}$	$4.08^{+0.05}_{-0.02}$	$4.08^{+0.03}_{-0.09}$
DW Car	A	$11.34^{+0.17}_{-0.19}$	$3.7^{+0.7}_{-0.8}$	$200.0^{+83.6}_{-47.0}$	20%	$26,475^{+333}_{-465}$	$4.17^{+0.02}_{-0.02}$	$3.98^{+0.02}_{-0.06}$
	B	$10.62^{+0.19}_{-0.21}$	$3.3^{+1.0}_{-1.0}$	$180.0^{+87.5}_{-30.7}$	15%	$25,675^{+396}_{-412}$	$4.17^{+0.05}_{-0.02}$	$3.88^{+0.02}_{-0.06}$
QX Car	A	$9.24^{+0.13}_{-0.11}$	$8.4^{+1.2}_{-1.5}$	$140.0^{+71.8}_{-49.6}$	30%	$23,825^{+293}_{-327}$	$4.12^{+0.04}_{-0.03}$	$3.73^{+0.03}_{-0.04}$
	B	$8.46^{+0.12}_{-0.12}$	$9.6^{+1.6}_{-1.7}$	$120.0^{+75.5}_{-37.5}$	30%	$22,775^{+267}_{-345}$	$4.12^{+0.06}_{-0.01}$	$3.58^{+0.06}_{-0.03}$
V1388 Ori	A	$7.44^{+0.16}_{-0.17}$	$29.4^{+1.9}_{-1.7}$	$140.0^{+95.7}_{-36.0}$	75%	$19,275^{+383}_{-446}$	$3.83^{+0.03}_{-0.04}$	$3.58^{+0.06}_{-0.04}$
	B	$5.16^{+0.07}_{-0.06}$	$51.6^{+3.0}_{-3.3}$	$80.0^{+76.3}_{-33.6}$	60%	$16,475^{+188}_{-249}$	$3.98^{+0.06}_{-0.01}$	$2.98^{+0.03}_{-0.04}$

Table 4.4: continued

Binary		M_{ini} (M$_\odot$)	τ (Myr)	v_{ini} (km s^{-1})	τ/τ_{MS}	$T_{eff,theo}$ (K)	$\log g_{theo}$ (cgs)	$\log L_{theo}$ (L$_\odot$)
V539 Ara	A	$6.26^{+0.06}_{-0.08}$	$38.0^{+1.8}_{-1.8}$	$80.0^{+78.4}_{-33.3}$	65%	$18,125^{+206}_{-256}$	$3.92^{+0.03}_{-0.03}$	$3.27^{+0.05}_{-0.03}$
	B	$5.32^{+0.06}_{-0.06}$	$38.4^{+3.5}_{-3.8}$	$60.0^{+49.2}_{-40.9}$	50%	$17,225^{+177}_{-227}$	$4.08^{+0.05}_{-0.02}$	$2.98^{+0.03}_{-0.04}$
CV Vel	A	$6.10^{+0.04}_{-0.05}$	$36.0^{+1.0}_{-1.2}$	$20.0^{+39.8}_{-18.2}$	60%	$18,275^{+118}_{-119}$	$4.03^{+0.03}_{-0.04}$	$3.23^{+0.02}_{-0.03}$
	B	$5.98^{+0.05}_{-0.03}$	$35.6^{+1.0}_{-1.2}$	$40.0^{+37.9}_{-33.0}$	60%	$18,175^{+121}_{-94}$	$4.03^{+0.02}_{-0.02}$	$3.17^{+0.02}_{-0.02}$
AG Per	A	$5.34^{+0.15}_{-0.17}$	$19.4^{+5.8}_{-5.7}$	$100.0^{+69.9}_{-35.5}$	25%	$17,625^{+396}_{-442}$	$4.22^{+0.03}_{-0.05}$	$2.88^{+0.06}_{-0.04}$
	B	$4.86^{+0.14}_{-0.12}$	$9.6^{+5.7}_{-5.2}$	$80.0^{+45.5}_{-35.8}$	10%	$17,025^{+347}_{-378}$	$4.28^{+0.05}_{-0.02}$	$2.73^{+0.03}_{-0.07}$
U Oph	A	$5.28^{+0.09}_{-0.10}$	$39.8^{+3.7}_{-4.1}$	$140.0^{+82.0}_{-39.0}$	50%	$16,875^{+324}_{-286}$	$4.08^{+0.02}_{-0.02}$	$2.92^{+0.07}_{-0.02}$
	B	$4.74^{+0.07}_{-0.08}$	$43.2^{+4.6}_{-5.0}$	$120.0^{+85.3}_{-31.6}$	40%	$16,025^{+255}_{-281}$	$4.12^{+0.02}_{-0.02}$	$2.77^{+0.02}_{-0.06}$
DI Her	A	$5.14^{+0.12}_{-0.10}$	$6.8^{+3.9}_{-4.2}$	$60.0^{+155.2}_{-45.0}$	10%	$17,575^{+302}_{-375}$	$4.28^{+0.04}_{-0.03}$	$2.77^{+0.05}_{-0.03}$
	B	$4.52^{+0.06}_{-0.07}$	$8.7^{+4.5}_{-5.6}$	$40.0^{+162.2}_{-25.6}$	5%	$16,225^{+243}_{-255}$	$4.33^{+0.02}_{-0.05}$	$2.58^{+0.04}_{-0.03}$
V760 Sco	A	$4.96^{+0.10}_{-0.09}$	$31.1^{+5.1}_{-5.6}$	$100.0^{+72.1}_{-32.1}$	35%	$16,725^{+288}_{-287}$	$4.17^{+0.03}_{-0.03}$	$2.83^{+0.02}_{-0.06}$
	B	$4.60^{+0.08}_{-0.07}$	$19.5^{+6.0}_{-6.4}$	$100.0^{+50.9}_{-40.5}$	15%	$16,225^{+275}_{-204}$	$4.28^{+0.02}_{-0.05}$	$2.62^{+0.05}_{-0.03}$
MU Cas	A	$4.66^{+0.09}_{-0.10}$	$81.2^{+5.3}_{-4.8}$	$20.0^{+45.7}_{-16.9}$	70%	$14,725^{+269}_{-276}$	$3.88^{+0.03}_{-0.04}$	$2.88^{+0.04}_{-0.05}$
	B	$4.58^{+0.08}_{-0.10}$	$73.3^{+5.2}_{-4.7}$	$20.0^{+45.5}_{-16.6}$	60%	$15,075^{+271}_{-244}$	$3.98^{+0.03}_{-0.03}$	$2.77^{+0.06}_{-0.02}$

The ages τ_A and τ_B of the primary and secondary star of binaries from Table 4.4 are plotted against each other in Fig. 4.9. If the stellar models were a perfect representation of the observed stars, the ages of the binary components should agree within their 1σ uncertainties in 68.3%, i.e. in 12–13 of the 18 cases. A first inspection reveals that the ages of the binary components agree well within their uncertainties, except for one $> 6\sigma$ outlier, V1388 Ori. We do not have an explanation for the discrepant ages of V1388 Ori. Perhaps the metallicity of this star differs from solar, which may induce an age difference. Alternatively, the formation history of the system may be peculiar.

Stellar radii grow only slowly in the beginning of a stellar life but more quickly when approaching the end of the main-sequence evolution. For example, a non-rotating $10\,M_\odot$ Milky Way star of Brott et al. (2011a) has increased its radius by about 40% at half of its main-sequence life but by about 230% towards its end. Hence, the accuracy with which ages can be determined from dynamical masses and radii depends strongly on the fractional main-sequence age of stars and becomes better the more evolved a star is. Because of this the age of CV Vel ($\tau/\tau_{MS} \approx 60\%$) is determined to about 3% whereas the age of DI Her ($\tau/\tau_{MS} \approx 5\text{–}10\%$) is only determined to about 50–60%, despite an accuracy of 1–2% in stellar masses and radii in both cases.

We quantify the age differences, $\Delta\tau = \tau_A - \tau_B$, of the primary and secondary stars and evaluate whether the age differences deviate significantly from zero. As noted in Sec. 4.4.1, our test loses significance if both stars in a binary are too similar, therefore we exclude those binaries from our analysis that have mass ratios larger than 0.97. This holds for the binaries V478 Cyg, CV Vel and MU Cas (the largest mass ratio of the remaining binaries, namely that of EM Car and DW Car, is 0.94). We also exclude the outlier V1388 Ori. The mean, relative age difference of the remaining 14 binaries is $\langle\Delta\tau/\delta\Delta\tau\rangle = -0.09 \pm 0.43$ (95% CI), where $\delta\Delta\tau$ are the 1σ uncertainties of the age differences $\Delta\tau$ and the uncertainty ± 0.43 is the 95% confidence interval of the standard error $\sigma/\sqrt{n}$ with $\sigma = 0.82$ being the standard deviation of the relative age differences and $n = 14$ the sample size. Further χ^2- and t-tests confirm, with a confidence level of 95% (p-values of 0.85 and 0.47, respectively), that the age differences are consistent with being zero (mean age difference $\langle\Delta\tau\rangle = 0.9 \pm 2.3\,\mathrm{Myr}$, 95% CI).

Convective core overshooting influences stellar radii most strongly towards the end of the main-sequence evolution and has little influence on unevolved stars. A test with a $5\,M_\odot$ Milky Way star with an overshooting of 0.5 pressure scale heights compared to no overshooting shows that the stellar radii differ by less than 3%–4% for fractional main-sequence ages younger than 30%–40%. The maximum radii reached during the main-sequence evolution at fractional main-sequence ages of 98%–99% differ by 53%, i.e. the model with overshooting has a radius larger by a factor of $1/(1 - 0.53) \approx 2.1$. In the following we assume that stars with fractional main-sequence ages less than 35% can be viewed as being unaffected by convective core overshooting. Hence, by restricting the test to those binaries in which the primary stars have fractional main-sequence ages younger than about 35%, i.e. to the binaries V3903 Sgr, V578 Mon, DW Car, QX Car, AG Per, DI Her and V760 Sco, we mainly probe the combination of metallicity and rotation in our models. The mean, relative age difference of this subsample of binary stars is $\langle\Delta\tau/\delta\Delta\tau\rangle = 0.14 \pm 0.73$ (95% CI) and χ^2- and t-tests confirm, with a 95% confidence level (p-values of 0.54 and 0.30, respectively), that the age differences are consistent with zero (mean age difference $\langle\Delta\tau\rangle = 2.4 \pm 4.2\,\mathrm{Myr}$, 95% CI). We find no significant evidence for a correlation between the inferred age- and observed mass-differences of the binary stars.

Our test with the subsample of binaries that are not expected to be influenced by convective core overshooting shows that the Milky Way stellar models of Brott et al. (2011a), with their
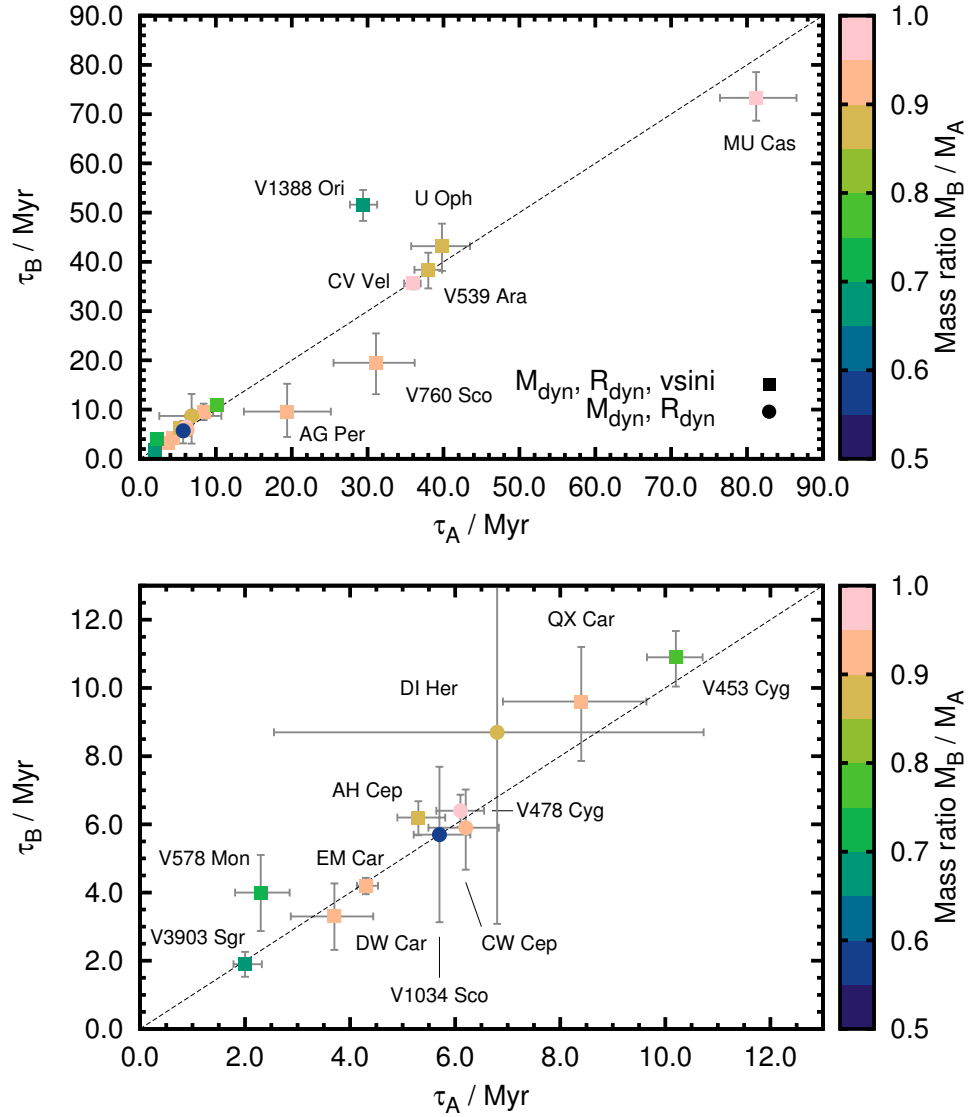
Figure 4.9: Ages of primary (τ_A) and secondary (τ_B) stars determined from dynamical masses, dynamical radii and (if available) projected rotational velocities $v \sin i$. The colour coding indicates the mass ratios of secondary (M_B) to primary (M_A) stars. Squares and filled circles show binaries for which $v \sin i$ measurements are available and are lacking to derive stellar ages, respectively. The bottom panel is a zoom into the age range 0–12.5 Myr of the top panel.

Table 4.5: Iron abundances, total metallicities Z_{Brott} as given in Brott et al. (2011a) and the corresponding metallicities Z_κ of the opacity tables used in the Brott et al. (2011a) models.

	MW	LMC	SMC
$\log(\mathrm{Fe/H}) + 12$	7.40	7.05	6.78
Z_{Brott}	0.0088	0.0047	0.0021
Z_κ	0.0143	0.0065	0.0035

metallicity and calibration of rotation, reproduce the massive $(4.5\text{–}28\,\mathrm{M}_\odot)$ Milky Way binaries in the sample of Torres et al. (2010). This might come as a surprise because the models are computed for a metallicity of $Z = 0.0088$, which is small compared to current estimates of the metallicity of the Sun ($Z_\odot = 0.014\text{–}0.020$; Grevesse & Sauval 1998; Asplund et al. 2009). Though the total metallicity in the models of Brott et al. (2011a) is rather low compared to that of the Sun, the iron abundance is not. The opacities in the models are interpolated linearly in the iron abundances from standard OPAL opacity tables (Iglesias & Rogers 1996). The iron abundance in the Brott et al. (2011a) models is $\log(\mathrm{Fe/H}) + 12 = 7.40$ (Table 4.5) which is close to the iron abundance of $\log(\mathrm{Fe/H}) + 12 \approx 7.50$ in the Sun (e.g. Grevesse & Sauval 1998; Asplund et al. 2009), hence the structures of stars from Brott et al. (2011a) follow those of stars with a solar-like composition.

Rotation increases the stellar radii at a level which is comparable to that of the uncertainties of the radii (Fig. 4.8) and thus must be accounted for when testing stellar models (Sec. 4.4.2). Rotating stars are larger than non-rotating stars and hence reach the observed radii earlier in their evolution. Stellar ages inferred from rotating stellar models are therefore systematically younger than those inferred from non-rotating stellar models. To quantify the systematic age shift, we determine the ages of all 36 stars in our sample using only the non-rotating Milky Way stellar models of Brott et al. (2011a). We find a mean, relative age difference of $\langle (\tau_{\mathrm{rot}} - \tau_{\mathrm{non-rot}}) / \tau_{\mathrm{non-rot}} \rangle = -7.4 \pm 1.2\%$ (95% CI) where the error is again the 95% confidence interval of the standard error. The ages inferred from rotating stellar models are younger than those from non-rotating models for all stars.

4.4.4 Effective temperatures and bolometric luminosities

The effective temperatures of stars in the Milky Way binary sample of Torres et al. (2010) are independent observables. The effective temperatures mainly follow from multi-band photometry, calibrations with respect to spectral types and colours, individual stellar spectra and spectral energy distributions. Once the effective temperatures are known, the bolometric luminosities are derived using the Stefan Boltzmann law and the dynamical radii. Besides determining, e.g., stellar ages, we further compute the posterior probability distributions of the effective temperatures of stars from the measured dynamical masses, radii and projected rotational velocities. We then compare the predictions of the stellar models in terms of effective temperatures and bolometric luminosities to the observations (Fig. 4.10). In the following we exclude V1388 Ori because our stellar models cannot reproduce this binary.

We find that the observed effective temperatures and hence bolometric luminosities of our stars are in agreement with the predictions of the stellar models of Brott et al. (2011a) for observed effective temperatures $T_{\mathrm{eff,obs}} < 25{,}000\,\mathrm{K}$ ($\langle \Delta T_{\mathrm{eff}} \rangle = 133 \pm 188\,\mathrm{K}$, 95% CI;
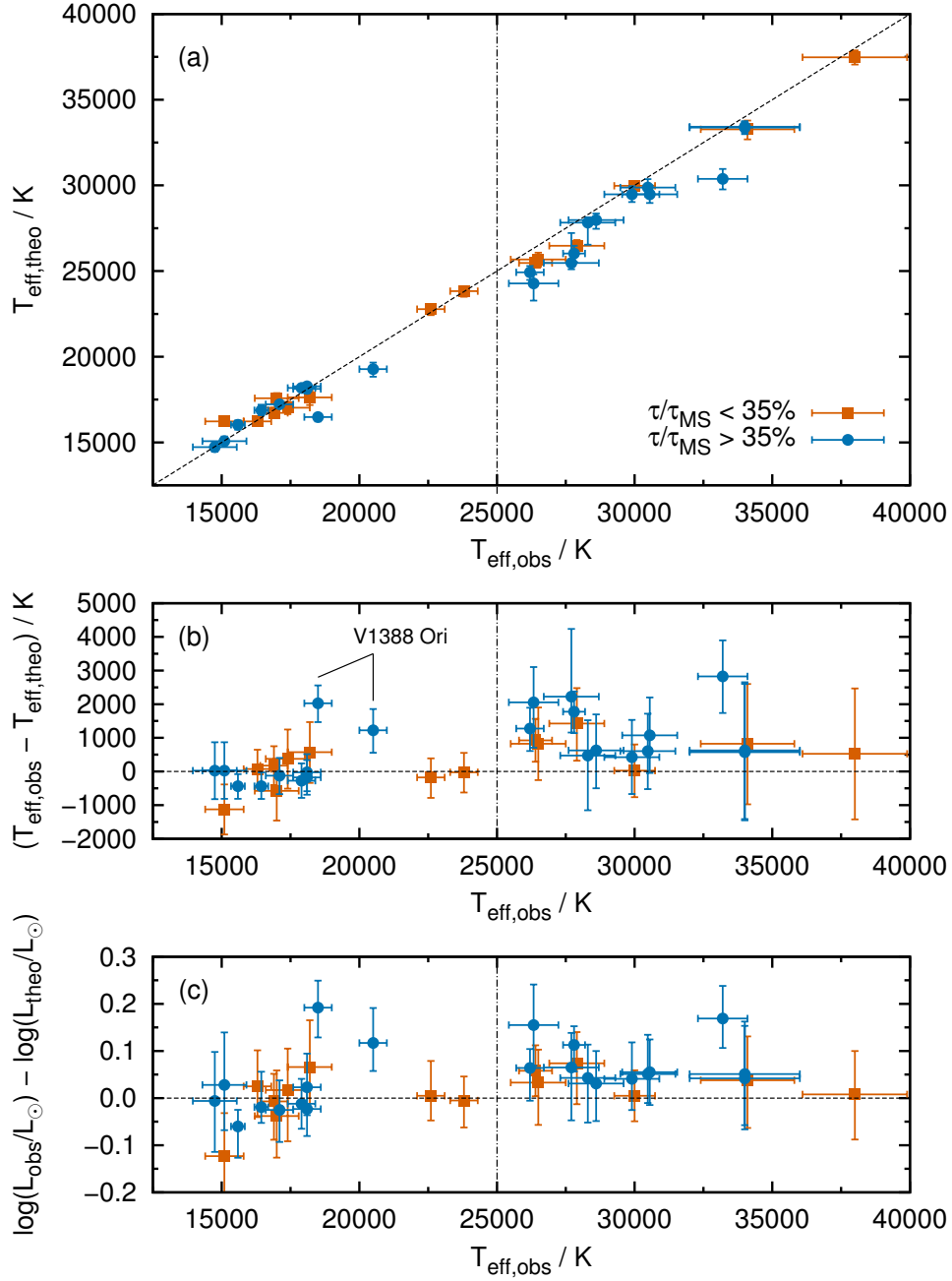
Figure 4.10: Comparison of observed $T_{\mathrm{eff,obs}}$ with predicted effective temperatures $T_{\mathrm{eff,theo}}$ for stars in our Milky Way binary sample and its consequence for stellar luminosities (cf. Tables 4.3 and 4.4). Panel (a) shows a direct comparison of the observed and predicted effective temperatures, panel (b) the differences of these temperatures $\Delta T_{\mathrm{eff}} = T_{\mathrm{eff,obs}} - T_{\mathrm{eff,theo}}$ as a function of observed effective temperature and panel (c) the resulting differences of the observed and predicted bolometric luminosities $\Delta \log L = \log L_{\mathrm{obs}} - \log L_{\mathrm{theo}}$. The squares show stars with fractional main-sequence ages τ/τ_{MS} younger than 35% (models not influenced by core overshooting) while the filled circles represent $\tau/\tau_{\mathrm{MS}} > 35\%$ (models influenced by core overshooting).

$\langle \Delta \log L/\mathrm{L}_\odot \rangle = 0.01 \pm 0.02\,\mathrm{dex}$, 95% CI). However, the observed effective temperatures are on average hotter by $1062 \pm 330\,\mathrm{K}$ (95% CI) and the bolometric luminosities are consequently larger by $0.06 \pm 0.02\,\mathrm{dex}$ (95% CI) for $T_{\mathrm{eff,obs}} > 25,000\,\mathrm{K}$ than predicted by the stellar models.

The convective core overshooting in our models is not responsible for the discrepant effective temperatures for $T_{\mathrm{eff,obs}} > 25,000\,\mathrm{K}$. The average difference between observed and predicted effective temperatures of those stars whose radii are not influenced yet by convective core overshooting (stars with fractional main-sequence ages $\tau/\tau_{\mathrm{MS}} \leq 35\%$) is $-88 \pm 377\,\mathrm{K}$ (95% CI) for $T_{\mathrm{eff,obs}} < 25,000\,\mathrm{K}$ and $758 \pm 371\,\mathrm{K}$ (95% CI) for $T_{\mathrm{eff,obs}} > 25,000\,\mathrm{K}$. The average differences in effective temperatures of stars expected to be influenced by core overshooting ($\tau/\tau_{\mathrm{MS}} > 35\%$) are $183 \pm 496\,\mathrm{K}$ (95% CI) for $T_{\mathrm{eff,obs}} < 25,000\,\mathrm{K}$ and $1213 \pm 461\,\mathrm{K}$ (95% CI) for $T_{\mathrm{eff,obs}} > 25,000\,\mathrm{K}$.

The cause of the discrepant effective temperatures in stars hotter than $25,000\,\mathrm{K}$, i.e. earlier than B1–2V or more massive than about $10\,\mathrm{M}_\odot$, is unknown. We speculate that the discrepancy is partly explained by calibrations becoming less accurate for more massive stars. To understand this, we recall how such calibrations are obtained in practice. In cool stars, fundamental effective temperatures, i.e. that do not rely on any modelling, can be determined from bolometric fluxes F_{bol} that are derived from spectral energy distributions and from interferometric measurements of stellar angular diameters θ ($F_{\mathrm{bol}} = [\theta/2]^2 \sigma T_{\mathrm{eff}}^4$, where σ is the Stefan Boltzmann constant). Such fundamental measurements of effective temperatures are more complicated and practically impossible in hot stars because they radiate a substantial fraction of their light in the ultraviolet (UV) that is difficult to access observationally (most UV space telescopes cannot observe shortward of $90\,\mathrm{nm}$ which is the wavelength at which a black body of $T_{\mathrm{eff}} \approx 32,000\,\mathrm{K}$ radiates most of its energy). Bolometric fluxes of hot stars are therefore difficult to measure directly and stellar atmosphere models are often used to predict the flux in the far UV. Instead of this procedure, model atmosphere computations are applied to infer effective temperatures directly from spectra and to establish the calibrations with spectral types and colours. The derived effective temperatures are therefore dependent on the treatment of, for instance, non-LTE effects, line blanketing, and stellar winds. Compared to these model atmospheres, the boundary conditions of the stellar structure models are relatively simple and this may be a cause of the discrepant effective temperatures.

4.5 Conclusions

With the advent of large stellar surveys on powerful telescopes and advances in analysis techniques of stellar atmospheres more is known about stars than just their position in the Hertzsprung-Russell (HR) diagram — rotation rates, surface gravities and abundances of many stars are derived. Therefore, the comparison of observations to theoretical stellar models to infer essential quantities like initial mass or stellar age and to test stellar models has to be done in a multidimensional space spanned by all available observables. To that end we develop BONNSAI[5], a Bayesian method that allows us to match all available observables simultaneously to stellar models taking the observed uncertainties and prior knowledge like mass functions properly into account. Our method is based on Bayes' theorem from which we determine full (posterior) probability distributions of the stellar parameters such as initial mass and stellar age. The probability distributions are analysed to infer the model parameters including robust uncertainties. BONNSAI securely identifies cases where the observed stars are not reproduced

---

[5] The BONNSAI web-service is available at `http://www.astro.uni-bonn.de/stars/bonnsai`.

by the underlying stellar models through χ^2-hypothesis tests and posterior predictive checks. We test BONNSAI with mock data to demonstrate its functionality and to show its capabilities.

We apply BONNSAI to the massive star subsample ($\geq 4\,M_\odot$) of the Milky Way binaries of Torres et al. (2010). The masses and radii of the binaries are known to better than 3%. For each of the 36 binary components in this sample, we determine the initial masses, ages, fractional main-sequence ages and initial rotational velocities from the observed masses, radii and, if available, projected rotational velocities applying the stellar models of Brott et al. (2011a).We find that the Milky Way stellar models of Brott et al. (2011a) result in stellar ages for 17 binaries that are equal within the uncertainties. There is no statistically significant age difference (95% confidence level). We find that BONNSAI, in combination with the Milky Way stellar models of Brott et al. (2011a), can not fit one binary, V1388 Ori, for which the ages of both stars differ by $> 6\sigma$.

We further compare the effective temperatures predicted by the stellar models to the observed effective temperatures. The predicted effective temperatures agree with the observed within their uncertainties for observed effective temperatures $T_{\mathrm{eff,obs}} \leq 25,000\,\mathrm{K}$. The observed effective temperatures are hotter by $1063 \pm 330\,\mathrm{K}$ (95% CI) than the effective temperatures of the models when $T_{\mathrm{eff,obs}} > 25,000\,\mathrm{K}$. The cause of this discrepancy is unknown but may be connected to the complexities of the atmospheres of hot OB stars. The systematically hotter temperatures result in stars being brighter by $0.06 \pm 0.02\,\mathrm{dex}$ (95% CI) compared to the stellar models.

The BONNSAI approach is flexible and can be easily extended and applied to different fields in stellar astrophysics. In its current form, BONNSAI allows us to compare observed stellar surface properties to models of massive, rotating, main-sequence single stars. Asteroseismology nowadays offers a look into the interiors of stars. By extending the stellar models to asteroseismic observables, BONNSAI could make use of these observables as well to constrain stellar models. Similarly, BONNSAI can be extended to also match pre main-sequence stars, post main-sequence stars, low mass stars, binary stars, stars of varying metallicities etc. to corresponding stellar models. Our statistical approach also enables the calibration of stellar parameters such as convective core overshooting including robust uncertainties and to analyse whole stellar populations to, e.g., unravel initial mass functions and star formation histories in a statistically sound way while properly taking observable uncertainties into account.

The age distribution of massive O and WN stars in 30 Doradus

F.R.N. Schneider, O.H. Ramírez-Agudelo, F. Tramper, J.M. Bestenlehner, S. Simón-Díaz,
C. Sabín-Sanjulían, N. Langer, N. Castro, R.G. Izzard, H. Sana and N.R. Walborn

Abstract The 30 Doradus (30 Dor) nebula in the Large Magellanic Cloud is a unique nearby stellar nursery hosting more than 1000 OB stars and several star clusters. Within the VLT-FLAMES Tarantula Survey (VFTS), the spectra of nearly 200 massive O and WN stars are modelled with state-of-the-art stellar atmosphere codes. We use these data to match the derived observables against stellar models using the Bayesian code BONNSAI to determine fundamental stellar parameters such as initial mass and age. Our aim is to study the recent massive star formation in 30 Dor and the age structure of this prototype starburst. The stars in our sample are mainly field stars and we find no spatially coherent age pattern. Hence the stars either formed continuously in the whole 30 Dor region or in clusters and associations of various ages and then moved to their currently observed positions. To distinguish between these scenarios, we infer age probability distributions of various subsamples of stars in 30 Dor to identify groups of stars by their ages. We find two peaks in the age distributions at about 2.7 and 4.5 Myr that may correspond to two coeval stellar populations. If R136, the central star cluster in 30 Dor, hosts a coeval stellar population that is visible in our age distributions, it must be associated with the ≈ 2.7 Myr old stars because we can limit the R136 cluster age to 1–3 Myr from the high masses and enhanced surface helium mass fractions of some of its WNh stars. The ≈ 4.5 Myr old stars are mainly found outside 1.2 arcmin of R136, suggesting they formed elsewhere, e.g. in NGC 2060, the second most obvious site of recent massive star formation in 30 Dor. The age distribution of stars that do not belong to the potential 2.7 and 4.5 Myr populations reveals three further age groups at $\lesssim 2$, 3.6 and 5.3 Myr. The 3.6 Myr group is found around R136 and may be associated with the north-east clump identified by Sabbi et al. (2012) in this part of 30 Dor while the $\lesssim 2$ and 5.3 Myr groups are rather found at distances larger than 1.2 arcmin from R136. Altogether, the age distribution of our sample stars may be explained by at least four distinct starbursts but continuous star formation cannot be ruled out without proper motion information.

5.1 Introduction

30 Doradus (30 Dor) in the Large Magellanic Cloud (LMC) was once thought to be a single star—the 30th brightest in the constellation of Doradus—until Nicolas Louis de Lacaille realised its nebular structure in 1751[1]. Today we know that 30 Dor is a highly complex nebula and the brightest HII region in the Local Group (Kennicutt 1984) illuminated by the central massive star cluster R136 that contains some of the most massive stars known to date (Crowther et al. 2010; Bestenlehner et al. 2011; Hainich et al. 2014). Several other extreme objects such as the fastest rotating star VFTS-102 (Dufton et al. 2011), the fastest rotating and most energetic young pulsar PSR J0537-6910 (Chen et al. 2006) and the very massive runaway star VFTS-016 (Evans et al. 2010) reside within 30 Dor.

At a distance of about 50 kpc (Pietrzyński et al. 2013), 30 Dor is a unique starburst region which can be used to study massive star evolution, star formation and cluster evolution in great detail. It is a template for distant, unresolved starbursts and can be used to explore their role in galaxies and the overall cosmos. The central cluster R136 is thought to be a young counterpart of relatively low-mass globular clusters (e.g. Kennicutt & Chu 1988; Meylan 1993; O'Connell et al. 1994; Hunter et al. 1995; Andersen et al. 2009; Bosch et al. 2009) and the star formation and stellar populations in this region may be key to understanding the multiple main-sequences and abundance anomalies observed in globular clusters (see e.g. Gratton et al. 2012). It is thus essential to investigate the age structure of giant starburst regions such as 30 Dor.

30 Dor is a complicated region. Its stars range in age up to at least 20–30 Myr (Grebel & Chu 2000; De Marchi et al. 2011). The main constituents of 30 Dor are the star clusters Hodge 301, R136, SL 639 and the NGC 2060 nebula connected to the LH99 stellar association. Besides these clusters and associations, Sabbi et al. (2012) found a second cluster just north-est of R136 that may be in the process of merging with R136. In the bright nebular filaments surrounding R136 to the north and west, several spots with ongoing star formation and embedded O stars are found, likely forming the next generation of stars (e.g. Walborn & Blades 1987; Hyland et al. 1992; Walborn & Blades 1997; Rubio et al. 1998; Brandner et al. 2001; Walborn et al. 2002; Maercker & Burton 2005). Dense, sub-parsec molecular clumps are found in the same region by sub-millimeter and radio observations (Indebetouw et al. 2013; Anderson et al. 2014). Walborn & Blades (1997) further suggest the existence of a loose association of stars around the luminous blue variable R143, about 2.2 arcmin ($\approx$ 32 pc) south/south-east of R136. Star formation in 30 Dor is currently being further explored within the Hubble Tarantula Treasury Project (Sabbi et al. 2013), a panchromatic imaging survey of 30 Dor using the Hubble Space Telescope.

In the Milky Way, Getman et al. (2014a,b) use data from the MYStIX[2] project (Feigelson et al. 2013) to unravel the age structure of 15 massive star forming regions, among them the Orion and Carina nebulae, using X-ray luminosities and near infrared photometry of pre main-sequence stars. They find that unclustered stellar populations are, on average, older than those in sub-clustered populations. Some star forming regions show coherent spatial age gradients indicating that a wave of star formation moved through the molecular cloud whereas no coherent age gradients are found in other regions (Getman et al. 2014b). For example, in the Orion and Flame nebulae (NGC 2024), Getman et al. (2014a) find a core–halo age structure, i.e. stars

---

[1] See e.g. notes on 30 Dor also known as NGC 2070 in the Messier and NGC catalogues
(http://www.messier.obspm.fr/xtra/ngc/n2070.html).

[2] Massive Young Star-Forming Complex Study in Infrared and X-Ray

towards the cluster core are on average younger than those in the outskirts. A similar feature is also suggested to be present in and around R136 (e.g. Selman et al. 1999).

The VLT FLAMES Tarantula Survey (VFTS; Evans et al. 2011) offers the unique possibility to study the age distribution of massive stars in 30 Dor. Within the VFTS, multi-epoch optical spectra of more than 800 OB stars have been taken, of which 342 are classified as O stars (Walborn et al. 2014), six as O2-3.5 If*/WN5-7, called "slash" stars from here on, (Crowther & Walborn 2011) and 17 as Wolf–Rayet (WR) stars (two earlier and 12 later than WN 5 and three WCs; see e.g. Doran et al. 2013, for the whole WR star population in 30 Dor). For a significant fraction of these massive stars (> 200), detailed atmosphere models have been computed (Sabín-Sanjulián et al. 2014; Bestenlehner et al. 2014; Ramírez-Agudelo et al. in prep.). In combination with stellar evolutionary models and sophisticated statistical methods, these datasets allow us to determine fundamental stellar parameters such as initial mass and age for each star and hence to follow the star formation process in 30 Dor during the last few million years.

We describe how we determine age probability distributions of individual and of samples of stars from the observed VFTS spectra using detailed atmosphere modelling and the Bayesian code BONNSAI[3] (Schneider et al. 2014a) in Sec. 5.2. In Sec. 5.3 we discuss the sample of stars analysed in this work in relation to their evolutionary status and distribution in the Hertzsprung–Russell (HR) diagram. We present the age distributions of our sample stars in Sec. 5.4 for all our stars in the 30 Dor field and for those around R136, NGC 2060 and outside these regions. We discuss our results with respect to previous investigations of star formation in 30 Dor, the hypothesis of massive star formation in isolation (Bressert et al. 2012), the 30 Dor runaway population (Sana et al. in prep.) and the influence of possible rejuvenated binary products in Sec. 5.5. Conclusions are drawn in Sec. 5.6.

5.2 Method

There are two major steps involved in determining stellar parameters and their probability distributions. First, stellar effective temperatures and surface gravities, including their uncertainties, are derived from the modelling of observed spectra. Second, the derived parameters are matched against stellar evolutionary models to determine probability distributions and summary statistics of, e.g., stellar masses and ages of individual stars. The individual age probability distributions are then combined to derive those of whole stellar populations. In the following we briefly describe these two major steps (Secs. 5.2.1 and 5.2.2), our sample selection (Sec. 5.2.3) and incompleteness correction (Sec. 5.2.4).

5.2.1 Atmosphere modelling

Within the VFTS, atmospheric modelling of the O dwarfs is mainly carried out by the Tenerife group (Sabín-Sanjulián et al. 2014), the O giants by the Amsterdam group (Ramírez-Agudelo et al. in prep.), and the slash and WN stars by the Armagh group (Bestenlehner et al. 2014). The groups apply different analysis techniques and use different atmosphere codes to model spectra which we briefly discuss in the following sections.

---

[3] The BONNSAI web-service is available at `http://www.astro.uni-bonn.de/stars/bonnsai`.

5.2.1.1 Dwarfs

The stellar parameters of most of the dwarfs and sub-giants in the sample are determined by means of the IACOB-GBAT package (Simón-Díaz et al. 2011b), a χ^2-fitting algorithm based on a large grid of pre-computed FASTWIND (Puls et al. 2005) models, and standard techniques for the hydrogen/helium analysis of O-type stars (see e.g. Herrero et al. 1992; Repolust et al. 2004). Details of the grid and strategy followed for the spectroscopic analysis of the VFTS observations can be found in Sabín-Sanjulián et al. (2014).

The sample considered here also includes a few OIV stars not present in the study of Sabín-Sanjulián et al. (2014) but analysed in the same way as described there. The dwarfs VFTS-404, 455 and 532 are analysed by Bestenlehner et al. (2014) with the techniques described in Sec. 5.2.1.3. The dwarfs VFTS-102, 190 and 406 are runaway stars and are analysed by Sana et al. (in prep.) with the techniques described in Sec. 5.2.1.2.

5.2.1.2 Giants

The stellar parameters of the giants and supergiants in the sample are derived by Ramírez-Agudelo et al. (in prep.) using a genetic algorithm (Mokiem et al. 2005; Tramper et al. in prep.). This method uses the algorithm PIKAIA (Charbonneau 1995) to fit synthetic line profiles generated by the non-LTE atmosphere code FASTWIND to the observed spectrum.

The genetic algorithm uses a selection of hydrogen, He I and He II lines to derive the effective temperature, T_{eff}, the surface gravity, $\log g$, the mass-loss rate, $\dot{M}$, the exponent of the wind acceleration law, β, the surface helium abundance, N_{He}, the microturbulent velocity, v_{tur}, and the projected rotational velocity, $v \sin i$. To calculate the errors on these values, the χ^2 of all models are scaled such that the best fitting model has a reduced χ^2 of one. We accept models that have a χ^2 probability $P(\chi^2, \nu) > 0.05$ with ν the degrees of freedom (Tramper et al. 2011).

We have extensively compared parameters found by both the genetic algorithm and IACOB-GBAT for a representative subsample of stars. The parameters are in good agreement, i.e. there is no bias and the parameters agree within the uncertainties.

The sample of Bestenlehner et al. (2014) contains further O-type giants that are not analysed by Ramírez-Agudelo et al. (in prep.). Unfortunately, Bestenlehner et al. (2014) fix the surface gravity to $\log g = 4.0$ which is likely too large for giants. Their derived effective temperatures and luminosities are therefore probably too high which results in systematically too young ages and too large masses. Thus, we discard these giants from our analysis to avoid spurious contributions to the age distributions. The giants all have $\log L/\mathrm{L}_\odot \gtrsim 5.5$ and would likely have added valuable age constraints.

Bestenlehner et al. (2014) further model the spectrum of Mk 42, an O2 If* supergiant not observed within the VFTS. As for the slash/WN stars (below), the surface gravity does not influence its spectral modelling. The derived stellar parameters are robust despite the fixed surface gravity of $\log g = 4.0$ (see also Sec. 5.2.1.3).

5.2.1.3 Slash and WN stars

The slash and WNh stars require complex non-LTE stellar atmosphere models using the radiative transfer code CMFGEN (Hillier & Miller 1998). Unlike the methods described in Secs. 5.2.1.1 and 5.2.1.2, Bestenlehner et al. (2014) perform a grid analysis using a tailored merit function that mimics a least-square fit method applied on temperature, mass loss and helium abundance diagnostics. The luminosities and reddening parameters are determined by matching B, V

and K_s photometry with model spectral energy distributions reddened with the law of Cardelli et al. (1989) as described in Bestenlehner et al. (2011, 2014). To reduce the computation time a limited number of parameters is varied; for example, $\log g$ is fixed at 4.0 dex. A constant surface gravity hardly influences the results for the slash and WNh stars, but it may lead to higher temperatures and luminosities for the O giants and supergiants and to lower values for the O dwarfs, respectively. In the study of Bestenlehner et al. (2014) a fixed surface gravity is not critical. However, in the current work it may result in younger ages and higher masses for the O giants and supergiants and vice versa for the O dwarfs. Uncertainties and systematic errors are discussed in detail in Bestenlehner et al. (2014). Relevant to our study are the 1σ uncertainties in effective temperature, luminosity and surface helium mass fraction that are determined individually for each star.

5.2.2 BONNSAI

We use BONNSAI[4] (Schneider et al. 2014a), a Bayesian method, to determine the stellar age probability distribution of each star in our sample by simultaneously matching all available observables to stellar models while taking observed uncertainties and prior knowledge, like the initial mass function, properly into account. BONNSAI uses Bayes' theorem,

$$p(\mathbf{m}|\mathbf{d}) \propto p(\mathbf{d}|\mathbf{m})p(\mathbf{m}), \tag{5.1}$$

to determine the posterior probability distribution, $p(\mathbf{m}|\mathbf{d})$, of the model parameters, $\mathbf{m}$, from the likelihood function, $p(\mathbf{d}|\mathbf{m})$, of the observed data, $\mathbf{d}$, given a model, $\mathbf{m}$, and the prior function, $p(\mathbf{m})$. We assume that the observables are independent of each other and that the probability distributions of the values of each observable follow a Gaussian (Schneider et al. 2014a). We match the observables against the rotating, single star models of Brott et al. (2011a) and Köhler et al. (2014). The model parameters $\mathbf{m} = (M_\mathrm{ini}, v_\mathrm{ini}, \tau, i)$ are the initial mass, M_ini, initial rotational velocity, v_ini, stellar age, τ, and inclination towards our line of sight, i. For each model parameter we assign a prior function to specify our knowledge about the model parameter before we incorporate the observations. A priori we assume that initial masses are distributed according to a Salpeter (1955) initial mass function, initial rotational velocities follow the observed distribution of rotational velocities of the VFTS O stars (Ramírez-Agudelo et al. 2013), all ages are equally probable and all rotation axes are randomly oriented in space.

The posterior probability distribution of the stellar age, $p(\tau|\mathbf{d})$, then follows from marginalising $p(\mathbf{m}|\mathbf{d})$ over the model parameters initial mass, M_ini, initial rotational velocity, v_ini, and inclination, i,

$$p(\tau|\mathbf{d}) = \int p(\mathbf{m}|\mathbf{d}) \, \mathrm{d}M_\mathrm{ini} \, \mathrm{d}v_\mathrm{ini} \, \mathrm{d}i. \tag{5.2}$$

For each star j, we obtain a posterior age probability distribution, $p_j(\tau|\mathbf{d})$. Adding the individual $p_j(\tau|\mathbf{d})$ results in the probability distribution of stellar age of (sub-)samples of stars. With this procedure, we can determine the age distribution of subsamples of stars to investigate spatially distinct stellar populations.

Our determined age probability distributions of stellar samples are *not* star formation histories: we can only determine the present-day age distribution. For example, some stars will have already ended their lives and their contribution to the star formation history is thus lacking. In principle it is possible to correct for that but this is not required for our analysis because we

---

[4] The BONNSAI web-service is available at `http://www.astro.uni-bonn.de/stars/bonnsai`.

want to identify distinct stellar populations by age to find out how stars formed in the last few million years.

It should also be noted here that all our ages are only apparent ages derived from the rotating, single star evolutionary models of Brott et al. (2011a) and Köhler et al. (2014). A different set of stellar models may result in different ages and the ages inferred for, e.g., binary products are likely too young because of rejuvenation. In the following we mostly omit "apparent" for simplicity but caution the reader that we can only provide apparent and not necessarily true stellar ages.

Another important aspect of BONNSAI is that it allows us to securely identify stars that cannot be reproduced by the chosen stellar models. To that end, BONNSAI conducts a Pearson's χ^2-hypothesis test to check the goodness-of-fit of the best-fitting model and posterior predictive checks that take the posterior probability distribution into account to test whether the predictions of the stellar models for the determined model parameters are in agreement with the observations. In both tests, we use a significance level of 5%, i.e. if one or both tests fail we are confident at $\geq 95\%$ that the stellar models are unable to reproduce all observables simultaneously within the observed uncertainties.

5.2.3 Sample selection

Walborn et al. (2014) find at least four stars within the aperture of the fibre pointing at VFTS-468. The observed spectrum of VFTS-468 further shows weak He I lines that should not be there given its O2 spectral type and the star is a X-ray source (Walborn et al. 2014). This likely biases the derivation of the observables and thus results in an unreliable age. Similar problems are found for, e.g., VFTS-303 and 621, which are multiples of two and three stars, respectively (Walborn et al. 2014). VFTS-506 shows radial velocity variations (SB1s) and is a X-ray source (Walborn et al. 2014). Its full resolution spectrum shows weak He I lines that should not be there given its ON2 spectral type; the spectrum is therefore likely a composite. Bestenlehner et al. (2014) discard the He I line and find an effective temperature of 47.3 kK from the ratio of the N III, N IV and N V lines. This temperature is cooler by about 7.7 kK than what is found with the analysis techniques for dwarfs described in Sec. 5.2.1.1. Our derived age is therefore unreliable. VFTS-599 shows radial velocity variations (SB1s) and its spectrum is nearly identical to that of VFTS-566 (Walborn et al. 2014). Despite this similarity of the spectra, the effective temperature derived for VFTS-599 is hotter by 13.3 kK than that derived for VFTS-566 (and too hot for an O3 star). Hence, the stellar parameters determined from spectral modelling and also the derived age are unreliable.

To avoid such problems and that spurious ages contaminate the distributions, we select only those O, slash and WN stars from the VFTS sample for which robust observables could be determined. Two criteria must be fulfilled to obtain robust stellar parameters from spectral modelling. First, the spectra must be of high quality and, second, they must not be polluted by possible companions, chance superpositions or nearby bright stars.

To ensure a high quality of the spectra, we follow Walborn et al. (2014) and exclude all VFTS stars with a lower-rated ("BBB") spectral classification from our analysis (e.g. because of a relatively low signal-to-noise ratio and/or severe nebular contamination). To remove stars with a potential composite spectrum, we discard all stars that Walborn et al. (2014) mark as VMn (visual multiple of n components) and SB(l,s,vs), SB1(l,s,vs), SB2 or SB2?, spectroscopic bin-

aries with large (l), small (s) or very small (vs) radial velocity variations[5] (the SB classification is from Sana et al. 2013).

The above mentioned selection criteria do not apply to the slash and WN stars. From the sample of Bestenlehner et al. (2014), we only exclude stars with uncertain stellar parameters, i.e. the WN stars VFTS-147, 402 and 509 (see their Table 6).

Because of the above selection criteria, 79 stars analysed by Sabín-Sanjulián et al. (2014) and Ramírez-Agudelo et al. (in prep.) are excluded from our analysis such that the final sample contains 119 O-type, slash and WN stars. Among the excluded stars may be some with robust stellar parameters. To ensure that we do not remove important information and features in the derived age distributions, we check the contributions of these excluded stars and find that they do not alter our conclusions.

Given that we exclude stars for which visual multiples are found within the aperture of the FLAMES fibres, our sample stars are preferentially located outside crowded regions such as the dense cores of stellar clusters and associations. Furthermore, the VFTS does not cover stars in the core of R136. This implies that our stellar sample is essentially made of field stars and that no potential coeval star forming site can be directly analysed. Hence, most of our sample stars either moved away from clusters (e.g. as runaways), formed in isolation or inside low-mass clusters/associations that have yet not been recognised as such.

By removing binary candidates, we restrict our sample to apparently single stars. As shown by de Mink et al. (2014), a sample of apparently single stars contains more binary products such as mergers than a sample that contains only binary stars. Under the assumption of constant star formation, de Mink et al. (2014) predict that 30% of a sample of main-sequence stars are binary products. These binary products are rejuvenated upon mass transfer (e.g. Schneider et al. 2014b, subm.) and the age distribution of a sample of apparently single stars is hence likely biased towards younger ages. We discuss this issue further in Sec. 5.5.4.

5.2.4 Incompleteness correction

In total, our final stellar sample contains 82 out of the 194 O-type dwarfs, 23 out of the 110 O-type giants and 14 out of the 17 slash/WN stars observed within the VFTS. For another 35 O stars, no luminosity class could be assigned.

Given that the completeness of the three stellar groups (dwarfs, giants and slash/WN) is different, we need to correct for this when determining age distributions. Whenever we select samples of stars, e.g. stars in a certain region of 30 Dor, we compute the completeness factor of the three groups, i.e. the number of stars in our sample divided by the total number of stars in that region, and weight the age distributions of dwarfs, giants and slash/WNs by the inverse of their respective completeness factors. We further weight the O-type dwarfs and giants with the inverse of the completeness factor of O stars with known luminosity class. In all cases the age distributions computed with and without incompleteness correction are very similar—the contribution of the slash/WN stars are slightly lowered while the contribution of the O-type giants is enhanced when correcting for incompleteness.

By correcting the incompleteness in this way, we implicitly assume that the ages of, e.g., the dwarfs *not* analysed are distributed in the same way as the ages of the dwarfs which are analysed. This assumption breaks down if a representative age distribution cannot be derived from the existing stars, e.g. in case of low number statistics.

---

[5] (l) means radial velocity variations $> 20\,\mathrm{km\,s^{-1}}$, (s) 10–20 $\mathrm{km\,s^{-1}}$ and (vs) $< 10\,\mathrm{km\,s^{-1}}$.

The 30 Dor region contains O and WR stars that are not observed within the VFTS. We are not correcting for this bias because the VFTS sample is randomly chosen (except for the exclusion of stars in the innermost core of R136) and a bias correction is therefore unnecessary.

5.3 Our sample of massive VFTS stars

We match as many observed stellar parameters as available to stellar models to obtain the best possible age constraints. In most cases, we match luminosities, $\log L/L_\odot$, effective temperatures, T_{eff}, surface gravities, $\log g$, and projected rotational velocities, $v \sin i$, against the single, rotating main-sequence star models with Large Magellanic Cloud composition of Brott et al. (2011a) and Köhler et al. (2014) using BONNSAI. The stellar models cover a mass range of 5–500 $M_\odot$ and an initial rotational velocity range of about 0–600 km s^{-1}. From the stellar models, we determine posterior probability distributions of the initial mass, M_{ini}, initial rotational velocity, v_{ini}, and age. We further predict the present-day masses, M_{present}, radii, R, surface helium mass fractions, Y, and surface nitrogen abundances, $\log N/H + 12$, of the VFTS stars. All observables including their 1σ uncertainties and summary statistics of the BONNSAI results are given in Table 5.6 for stars included in our analysis.

For five dwarfs, VFTS-014, 483, 554, 582 and 704, there is, as yet, no photometry and hence no luminosity available, meaning we only match T_{eff}, $\log g$ and $v \sin i$ against the stellar models. From the stellar models we predict luminosities including 1σ error bars and provide these values in Table 5.6. The luminosities are used to place the stars in the HR diagram (Fig. 5.1).

Surface gravities cannot be determined for the slash and WN stars from atmospheric modelling (Sec. 5.2.1.3). Also, for some of these stars, no $v \sin i$ measurements are possible or only upper limits can be determined. As opposed to the O dwarfs and giants, surface helium mass fractions are known for all slash and WN stars (Bestenlehner et al. 2014). For the slash and WN stars, we match luminosities, effective temperatures, surface helium mass fraction and, if available, $v \sin i$ constraints against the stellar models. As effective temperatures, we use $T_\star$ provided in Table 5 of Bestenlehner et al. (2014) because their T_{eff} values are defined in the wind and are thus not comparable to the effective temperatures of our stellar models. Bestenlehner et al. (2014) define $T_\star$ close to the hydrostatic surface of the stars which is comparable to what is provided by the stellar models.

In total, two stars with robust stellar parameters, VFTS-190 and 285, and eight of the excluded stars, VFTS-102, 160, 188, 303, 389, 451, 711 and 787, cannot be reproduced by our stellar models. In Appendix 5.7.1 we comment in detail on possible reasons for the discrepancies of VFTS-190, 285 and 102. In summary, these stars rotate too fast to be covered by the applied stellar models. The fast rotation of these stars is likely due to past binary mass transfer such that the found discrepancy is of physical origin.

Stars removed from our sample include seven stars that cannot be explained by our stellar models and for which there is no obvious computational or physical explanation for the discrepancy. These seven stars can likely not be reproduced because of lower quality or composite spectra leading to spurious stellar parameters. Contrarily, there is no such case in the sample of stars that we use to derive age distributions. This substantiates our selection criteria to work only with the highest quality data to ensure robust age distributions.
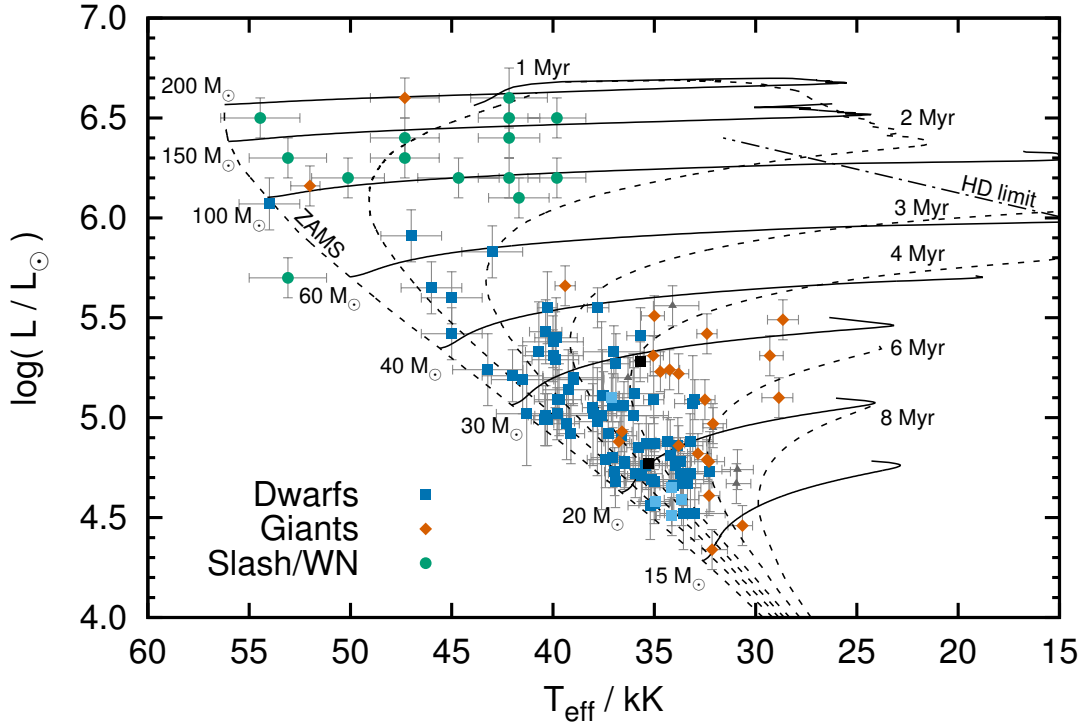
Figure 5.1: Hertzsprung–Russell diagram of the VFTS O, slash and WN stars in 30 Doradus analysed in this paper together with non-rotating stellar evolutionary tracks (solid lines) and isochrones (dashed lines) of Brott et al. (2011a) and Köhler et al. (2014) with Large Magellanic Cloud composition. The Humphreys–Davidson (HD) limit is shown by the dot-dashed line in the top-right. The light blue squares indicate those dwarfs for which we determined luminosities from BONNSAI because no photometry is available. The two dwarfs in black, VFTS-190 and 285, cannot be reproduced by the stellar models.

5.3.1 Hertzsprung–Russell diagram

In Fig. 5.1, we show the position of the VFTS O, slash and WN stars used in this work in the HR diagram together with stellar evolutionary models and isochrones of Brott et al. (2011a) and Köhler et al. (2014). Except for the late O-type giants VFTS-046, 165 and 777 with $T_{\mathrm{eff}} \approx 29\,\mathrm{kK}$, there is no star in our sample with an effective temperature cooler than about $30\,\mathrm{kK}$—consequently, we can only probe the formation of massive stars within the last 6–8 Myr. The HR diagram for $T_{\mathrm{eff}} \lesssim 30\,\mathrm{kK}$ is populated with B stars for which no complete stellar atmosphere modelling is yet accomplished within the VFTS.

There seems to be a dearth of stars with luminosities around $\log L/L_{\odot} = 5.8$. This gap may be populated by O supergiants that we discard in our analysis because of the fixed gravity in the spectral modelling of Bestenlehner et al. (2014) and the correspondingly likely too hot temperatures and too bright luminosities (Sec. 5.2)—these are the stars VFTS-422, 603, 1018 and 1021. Further stars with uncertain stellar parameters in Table 6 of Bestenlehner et al. (2014) that we discard from our analysis and some of the removed stars may help filling this gap.

The coolest and brightest O supergiant not shown in the HR diagram, VFTS-1021, has an effective temperature $T_{\mathrm{eff}} \approx 40\,\mathrm{kK}$ and luminosity $\log L/L_{\odot} \approx 6.3$ (Bestenlehner et al. 2014). Taking also the two brightest B supergiants into account, VFTS-003 and 591 with effective

127

temperatures of about 21 kK and 25 kK and luminosities of $\log L/\mathrm{L}_\odot \approx 6.0$ and $\log L/\mathrm{L}_\odot \approx 6.1$, respectively (McEvoy et al. in prep.), there are no stars in the VFTS sample cooler than about 35 kK and at the same time brighter than $\log L/\mathrm{L}_\odot \approx 6.1$. This is consistent with the Humphreys–Davidson limit (Humphreys & Davidson 1979, 1994) as indicated in Fig. 5.1.

Our stellar models predict stars at effective temperatures cooler than 35 kK and brighter than $\log L/\mathrm{L}_\odot = 6.1$ which is in contradiction with the massive stars in 30 Dor. Initial 100–200 $\mathrm{M}_\odot$ moderately rotating ($\lesssim 100\,\mathrm{km\,s^{-1}}$) models of Köhler et al. (2014) spend about 30–40% of their main-sequence lifetime at effective temperatures cooler than 35 kK and luminosities brighter than $\log L/\mathrm{L}_\odot = 6.1$. Given that there are 16 stars hotter than 35 kK and brighter than $\log L/\mathrm{L}_\odot = 6.1$, our models predict 5–6 stars in a region of the HR diagram where no star is observed. This is a $> 2\sigma$ mismatch assuming Poisson uncertainties and a constant star formation rate in the last 2–3 Myr.

Our stellar models in this region of the HR diagram have inflated envelopes (Köhler et al. 2014). Inflated envelopes are found in all models of Brott et al. (2011a) and Köhler et al. (2014) brighter than $\log L/\mathrm{L}_\odot \approx 6.0$ and already develop in some models brighter than $\log L/\mathrm{L}_\odot \approx 5.5$ (Sanyal et al. in prep.). The inflation occurs because stars approach or even exceed the Eddington limit in their interiors. The inflation may be reduced or may even be removed if either the convective energy transport in the super Eddington outer layers is more efficient or if the inflated envelope cannot build up due to strong mass loss.

The inflated envelopes of stars with $\log L/\mathrm{L}_\odot \approx 6.0$ influence the determined ages. Ages inferred from models with inflated envelopes are younger than those inferred from models without that may reach such large radii only later in their evolution. This may apply to the slash and WN stars and also to some of the luminous giants and dwarfs, i.e. to the most massive and hence the youngest stars ($\lesssim 2\,\mathrm{Myr}$).

Surface helium enrichment is obtained in two ways in our stellar models: first, by the removal of the hydrogen envelope through stellar winds which exposes material processed by nuclear burning in the stellar core and, second, by rotational induced mixing. An initial rotational velocity of faster than $300\,\mathrm{km\,s^{-1}}$ is required in 7–10 of the 14 slash/WN stars, i.e. in more than 50%, to explain the high surface helium mass fractions because the stellar wind in our models is not efficient enough, on its own, to enrich the stellar surfaces to the observed values. According to our models, all these stars evolve chemically homogeneously at the beginning of the main-sequence before losing so much angular momentum through stellar winds that they turn back to a normal redward evolution. We consider such a large fraction of initially fast rotators as implausible given that less than 20% of OB stars rotate that fast (Dufton et al. 2013; Ramírez-Agudelo et al. 2013). Hence, the stellar models may lack physics to fully describe the evolution of stars in the upper part of the HR diagram. Possible solutions are that the stellar wind mass loss in the models of such stars is underestimated and/or that some of them are binary products (as suggested by Schneider et al. 2014b for some of the Arches and Quintuplet WNh stars). A wind enhancement for stars close to the Eddington limit is found by Bestenlehner et al. (2014) and may help to remove the discrepancy between the stellar models and observations in this part of the HR diagram. We discard the possibility that all of them are post main-sequence objects because for each post main-sequence object we should find about nine main-sequence stars. This nicely shows the power of the VFTS that allows us for the first time to observationally constrain, improve and calibrate the physics of such massive star models.

A quantitative comparison of the massive VFTS stars with another set of stellar evolutionary models is difficult because of the scarcity of LMC high mass tracks of various initial rotational

velocities. Yusof et al. (2013) provide non-rotating, initially 150 and 500 $M_\odot$ models of LMC composition but no models in between. Their non-rotating 150 $M_\odot$ model reaches effective temperatures of about 20–25 kK towards the end of core hydrogen burning, similar to the non-rotating models of Köhler et al. (2014). The models presented in Crowther et al. (2010) are also computed with a recent version of the GENEVA evolution code and indicate that non-rotating models of initially 200 and 300 $M_\odot$ reach effective temperatures cooler than 35 kK during core hydrogen burning. We cannot say how cool they get because the end of the core hydrogen burning phase is not shown. We therefore speculate that also the models of Yusof et al. (2013) predict too many too cool and luminous stars ($T_{\rm eff} < 35$ kK and $\log L/L_\odot > 6.1$) that have not been observed within the VFTS. The rotating models of Yusof et al. (2013) ($v_{\rm ini} \approx 400$–470 km s^{-1}) of initially 150, 200 and 300 $M_\odot$ stay hotter than 50 kK during core hydrogen burning and are thus unable to explain most of the luminous ($\log L/L_\odot > 6.0$) VFTS stars. As is the case for the Köhler et al. (2014) models, there seems to be physics lacking in the models to adequately describe the observed, luminous VFTS stars.

Another intriguing object is the WN7h star VFTS-108. Its observables match an initially 35 $M_\odot$ star evolving chemically homogeneously because of an initial rotational velocity of about 500 km s^{-1}. If true, VFTS-108 is viewed at an inclination angle of $\lesssim 24°$ and may be a promising candidate for a long gamma-ray burst. However, VFTS-108 may simply be a post main-sequence star, i.e. a classical WR star (Bestenlehner et al. 2014). If VFTS-108 is a post main-sequence star, the stellar parameters determined with BONNSAI are meaningless. In any case, the age of about 6.3 Myr inferred for VFTS-108 does not influence our overall conclusions.

Five stars, Mk 42, VFTS-682, 695, 1022 and 1025, have luminosities $\log L/L_\odot \gtrsim 6.5$ and likely exceed an initial mass of 150 $M_\odot$. VFTS-1025 is also known as R136c and is part of the group of four stars found by Crowther et al. (2010) that question the tentative stellar upper mass limit of 150 $M_\odot$ (e.g. Weidner & Kroupa 2004; Figer 2005; Oey & Clarke 2005; Koen 2006). As discussed by Schneider et al. (2014b), these stars are either born that massive and hence violate the proposed stellar upper mass limit or they gained mass, e.g., by mass transfer or merging in binary systems and became that massive during their evolution (see also Banerjee et al. 2012b).

5.4 The ages of the massive VFTS stars

5.4.1 The whole 30 Dor region

In Fig. 5.2, we show the positions of the stars in our sample in 30 Dor. Their ages are colour coded and the positions of all VFTS O stars, early type WR/WC stars and the LBV R143 are shown as well. Most of the O stars in 30 Dor are close to the central cluster R136, circled in red, and the NGC 2060 region, circled in blue. The energetic 16 ms X-ray pulsar PSR J0537-6910 and its supernovae remnant N157B reside in the centre of the NGC 2060 region (Chen et al. 2006). Hodge 301, a 20 ± 5 Myr old star cluster (Grebel & Chu 2000) hosting three red giants and VFTS B stars, lies about 3 arcmin (≈ 44 pc) north-west of R136, and the star cluster SL 639, hosting B stars but no red giants, about 7.5 arcmin (≈ 110 pc) south-east of R136.

The age distribution of all our sample stars is computed as described in Sec. 5.2.2 and depicted in Fig. 5.3. The $\pm 1\sigma$ estimate displays the standard deviation in each bin of the age distribution computed with a bootstrapping method. The $\pm 1\sigma$ errors are correlated because of the normalisation of the probability distributions, e.g. because increasing the probability in one age range of the age distribution means decreasing it in another. The shown errors are
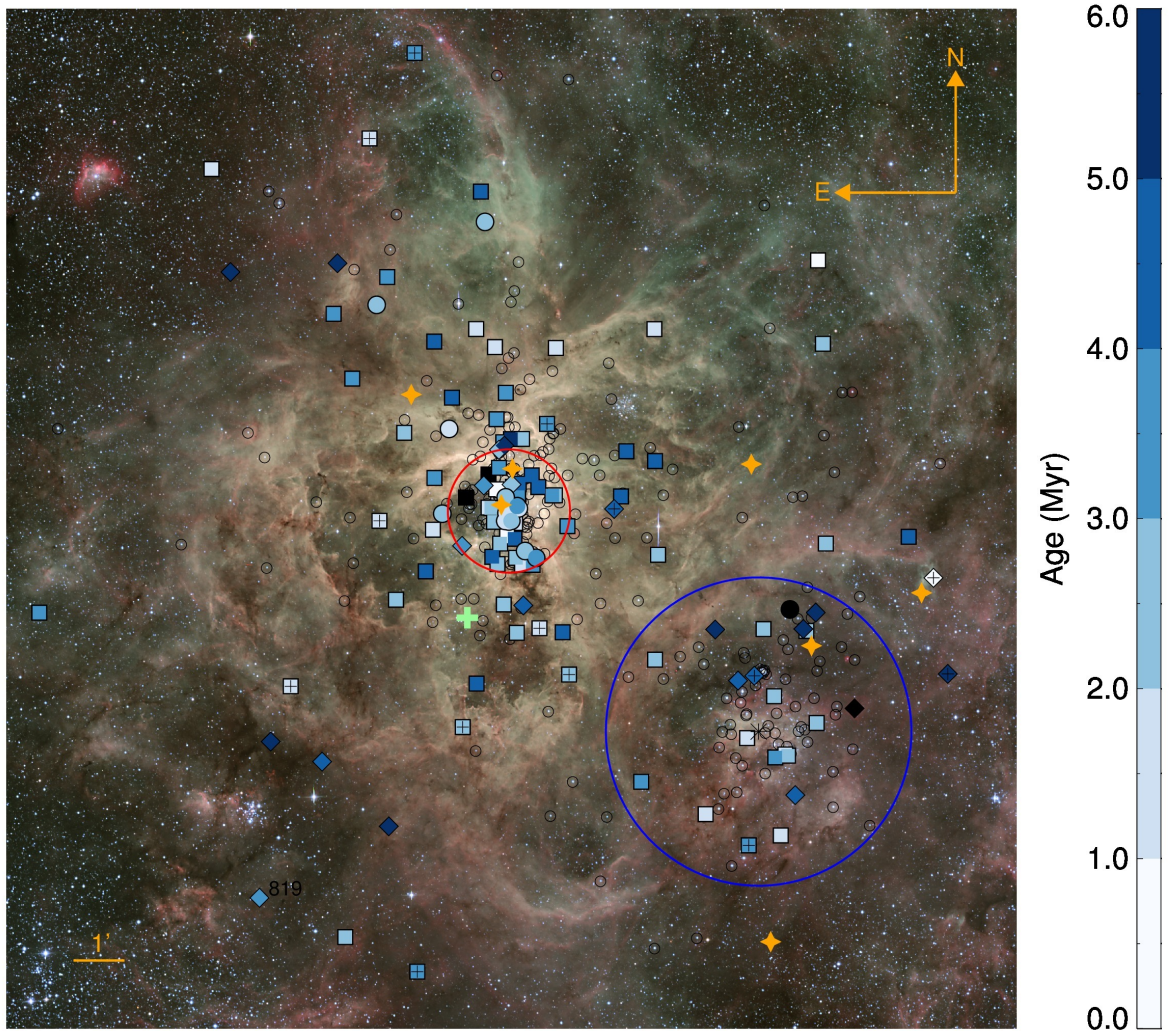
Figure 5.2: Age map of the massive VFTS stars in our sample. As in Fig. 5.1, squares are dwarfs, diamonds are giants and circles are slash/WN stars. The open, small circles show the positions of the other VFTS O stars, the orange star symbols the position of early type WR/WC stars taken from Doran et al. (2013) and the green plus sign the position of the LBV R143 (Parker et al. 1993). The runaway stars in our sample identified by Sana et al. (in prep.) are indicated by plus signs and the position of the pulsar PSR J0537-6910 by a black asterisk. Stars mentioned in the text are marked with their VFTS number or other names. The red and blue circles show regions of 1.2 arcmin or 17.5 pc around R136 and 3 arcmin or 43.6 pc around NGC 2060 (the pulsar), respectively, assuming a distance of 50 kpc to the LMC (Pietrzyński et al. 2013). The stars in black are apparently older than 6 Myr. The background image of 30 Dor is an optical (B, V, O III and Hα) composite taken with the Wide Field Imager (WFI) at the MPG/ESO 2.2-m telescope on La Silla under programme ID 076.C-0888, processed and released by the ESO VOS/ADP group.
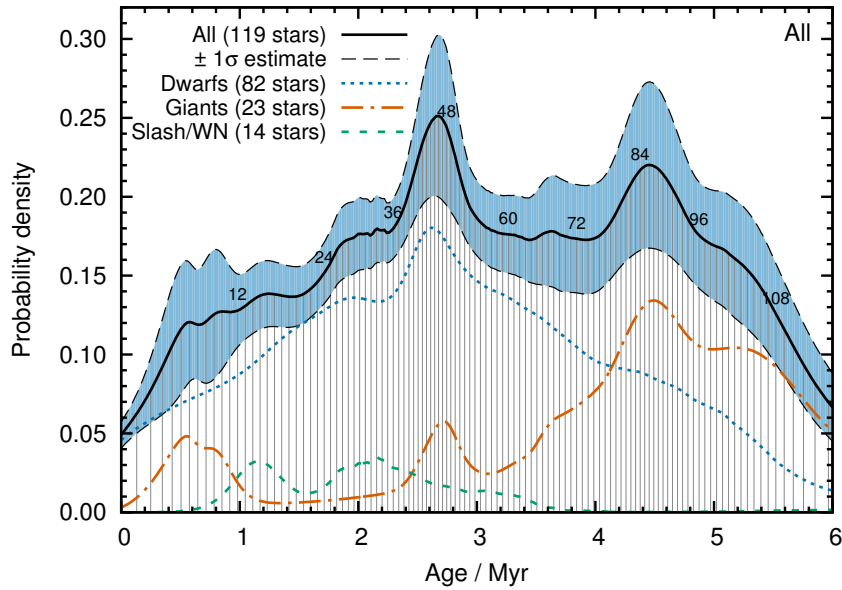
Figure 5.3: Probability density distribution of the apparent ages of all the stars in our sample. The contributions of the dwarfs, giants and slash/WN stars are shown separately. There is one vertical line for each star in the sample and cumulative number counts are given every 12th star, i.e. about every 10%, on top of the corresponding vertical line to give a feeling for the number statistics. The blue shaded area is a bootstrapped $\pm 1\sigma$ estimate of the age distribution.

therefore only thought to indicate the potential scatter of the age distribution to judge which peaks and wiggles are likely real and which are likely noise.

The age map already shows that 30 Dor, and also the central region around R136, is complex with stars of different ages spread over the place (Fig. 5.2). This picture is reflected in the age distribution of the sample stars (Fig. 5.3). Our sample stars all formed during the last 6 Myr but in unknown places. An over-abundance of apparently 2.7 Myr and 4.5 Myr-old massive stars indicates enhanced star formation during these times. These two ages either correspond to spatially localised star formation in, e.g., star clusters or stellar associations, or to a spatially non-localised, coincident enhanced star formation in the whole 30 Dor region.

The age distribution decreases for ages younger than about 2.0 Myr. Given the dearth of stars in the HR diagram around a luminosity of $\log L/L_\odot \approx 5.8$ (Fig. 5.1; see also the discussion in Sec. 5.3.1), we may expect that there are more stars younger than about 3.0 Myr than currently included in the age distribution. This young part of the age distribution may therefore be altered if these luminous, missing stars are considered.

The bootstrapped 1σ error estimates indicate that the first peak in the age distribution at 2.7 Myr is significant at about a 1σ level. The second peak mentioned above at 4.5 Myr falls inside the 1σ bootstrap error estimate and is therefore not significant at a 1σ or higher level. However, we will see in Sec. 5.4.4 that this peak corresponds to a well defined and significant peak in the age distribution of stars that are located 1.2 arcmin away from R136 and 3.0 arcmin away from NGC 2060. All other wiggles in the age distribution of all stars in our sample (Fig. 5.3) are not significant.

In the following, we investigate the ages of our sample stars in spatially localised regions, namely around R136, NGC 2060 and outside these regions to further disentangle and understand
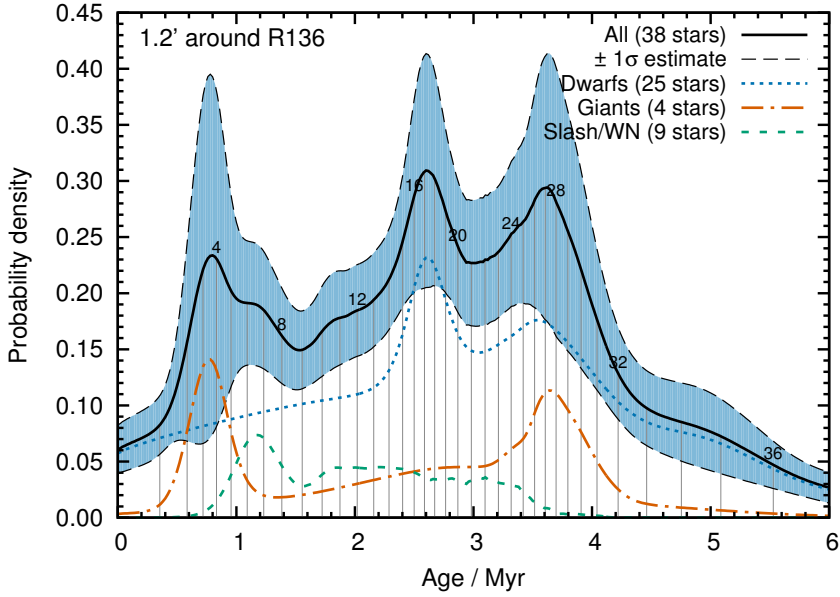
Figure 5.4: As Fig. 5.3 but for stars within 1.2 arcmin ($\approx 17.5\,\mathrm{pc}$) of R136.

the age distribution in Fig. 5.3 and its two peaks.

5.4.2 The R136 region

Within the VFTS, the core of the R136 star cluster was not observed with FLAMES because of crowding. It was partially observed with UVES and is subject to follow up observations with STIS aboard Hubble (PI, P. Crowther). Consequently, our stellar sample lacks stars belonging to R136 and it is therefore not clear how well our age distributions capture its age.

In Fig. 5.4 we show the apparent age distribution of our sample stars within 1.2 arcmin ($\approx 17.5\,\mathrm{pc}$) of R136. More than 80% of the stars (about 31 out of 38) appear to be younger than 4 Myr. The age distribution suggests three characteristic ages of about 0.8, 2.6 and 3.6 Myr. However, given the bootstrapped 1σ uncertainty estimates, the peak around 0.8 Myr is not significant on its own and the latter two at 2.6 and 3.6 Myr may actually correspond to only one broad peak at about 3.0 Myr. The error estimates at different ages are correlated because of the normalisation of the probability distribution and it is therefore not straightforward to say whether there are two peaks at 2.6 and 3.6 Myr or just one at about 3.0 Myr. We discuss this further in Sec. 5.4.6.

The stars belonging to the 0.8 Myr peak in the age distribution consist of those slash/WN stars that are not enriched with helium on their surface by more than 40% in mass and the giant Mk 42. The ages of these and other luminous stars are more uncertain than indicated in the age distribution for the following reasons:

- As explained in Sec. 5.3.1, the stellar models for $\log L/\mathrm{L}_\odot \gtrsim 6.0$ have significantly inflated envelopes which may result in too young ages for these stars.

- The most luminous stars in any cluster have a high probability of being a binary product (Schneider et al. 2014b), meaning that their real age may be older than that inferred here.
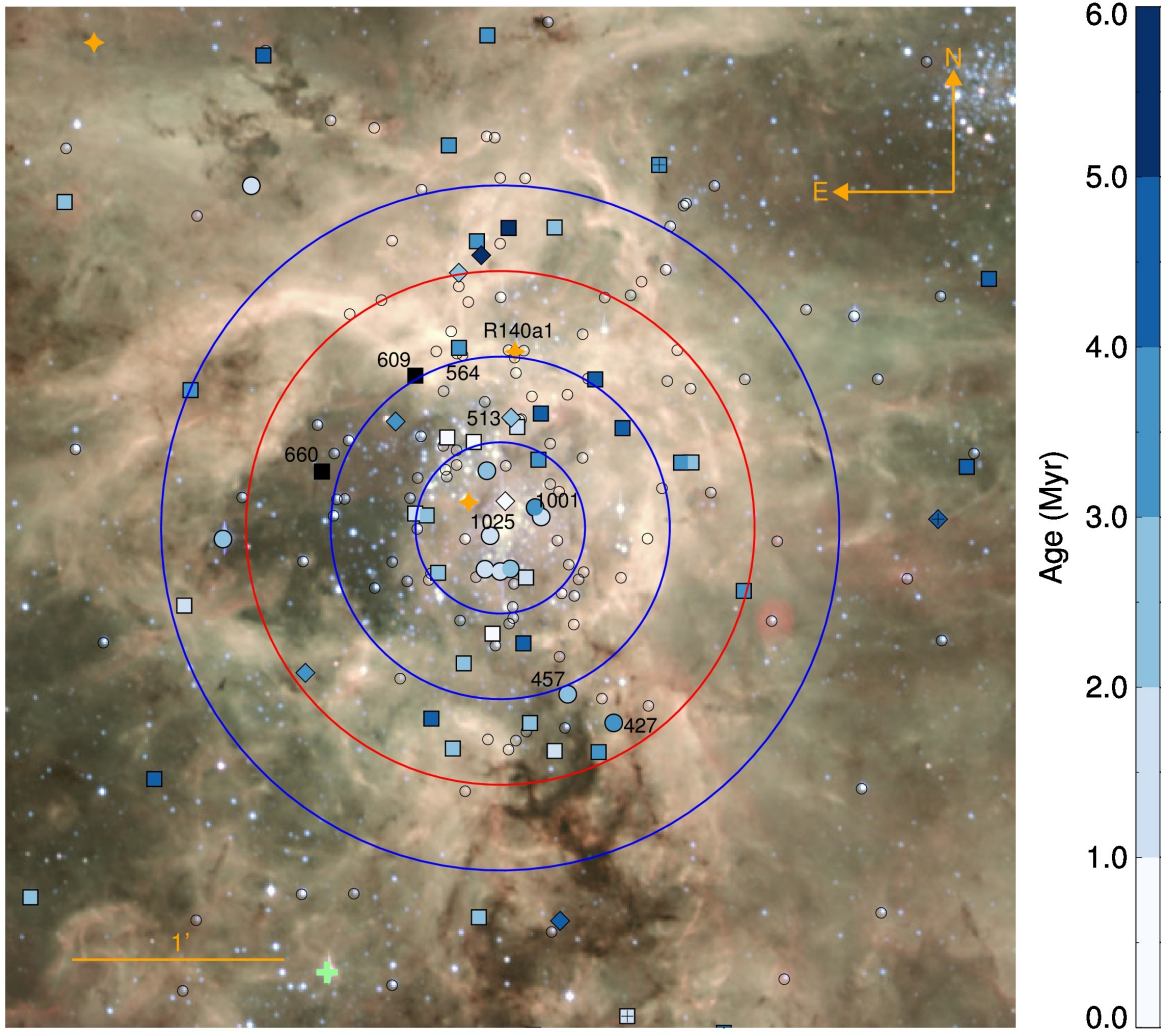
Figure 5.5: As Fig. 5.2 but zoomed in to the R136 region. The four circles around R136 have radii of 0.4 (5.8), 0.8 (11.6), 1.2 (17.5) and 1.6 arcmin (23.3 pc) and the age distributions of stars within these circles are shown in Fig. 5.6.

The slash/WN stars that are more enriched in helium by more than 40% are, according to the models, quite old (up to 3.5 Myr) because they would have first evolved chemically homogeneously before reaching their currently observed surface helium enrichment and position in the HR diagram. As noted in Sec. 5.3.1 the stellar models may require a stronger mass loss that would reduce the inferred ages of these slash/WN stars. If this is so, the age distribution of the slash and WN stars in Fig. 5.4 may be narrower than we predict.

In any case, if these luminous stars are genuinely single, they cannot be older than 2–3 Myr because of their high masses and correspondingly short lifetimes. These very luminous and hence massive stars are concentrated towards R136. Eight of nine stars more luminous than $\log L/\mathrm{L}_\odot = 6.0$ are found within 0.4 arcmin (≈ 5.8 pc) of R136 showing that the most massive stars around R136 are clustered in the innermost region.

To further disentangle the contributions of different stars to the age distribution in Fig. 5.4, we investigate the spatial location and age distributions of stars within circles of radii of 0.4 (5.8),

0.8 (11.6), 1.2 (17.5) and 1.6 arcmin (23.3 pc) around R136 in Figs. 5.5 and 5.6, respectively. When drawing conclusions from the age map and the age distributions, we have to bear in mind that we see the projection of a complex 3D stellar distribution.

We do not correct the age distributions in Fig. 5.6 for incompleteness because of low number statistics, especially within the innermost region. We distinguish between age distributions that include and that discard stars above $\log L/\mathrm{L}_\odot = 6.0$ to study the influence of potentially biased age estimates because of physics lacking in the stellar models (Sec. 5.3.1). Figure 5.6e, in comparison to Fig. 5.4, shows how our incompleteness correction alters the age distribution. Without the incompleteness correction, the slash and WN stars contribute more, primarily increasing the first peak at about 1 Myr, while the giants' contribution at 3.6 Myr lowers.

Most of the stars in our sample surrounding R136 may have not formed where they are observed currently and given our sample selection we are biased towards field stars (Sec. 5.2.3). This complicates the interpretation of the star formation process around R136. However, the age map in Fig. 5.5 and the age distributions in Fig. 5.6 show that the apparently youngest stars (< 2 Myr) are located closer to the R136 star cluster while older stars are preferentially found in the outskirts. In the following we go through the R136 region in more detail and relate individual and groups of stars to the various features seen in the age distributions.

The innermost 0.4 arcmin contains most of the very luminous and hence most massive stars ($\log L/\mathrm{L}_\odot > 6.0$, $M_{\mathrm{ini}} \gtrsim 90\,\mathrm{M}_\odot$). It cannot be proven whether all of these massive stars belong to R136 but it seems to be a reasonable assumption that such massive stars are born in such a nearby massive star cluster. The situation is less clear for the four dwarfs in this region and their inferred ages may not be representative of the true R136 cluster age.

The ages inferred for the most massive stars ($\log L/\mathrm{L}_\odot > 6.0$) may be biased because of physics missing in the stellar models (see Sec. 5.3.1) or past binary mass exchange. The observed surface helium mass fractions of these stars may serve as lower limits for the true R136 cluster age. The surface helium mass fractions inferred by Bestenlehner et al. (2014) for the WN6(h) star VFTS-1001 and WN5h star VFTS-1025 (also known as R136c) are 0.85 ± 0.05 and 0.70 ± 0.05, respectively. Given the observed luminosity of about $\log L/\mathrm{L}_\odot \approx 6.2$ and effective temperature of about $T_{\mathrm{eff}} \approx 42.2$ kK of VFTS-1001, it falls on an initially $100\,\mathrm{M}_\odot$ stellar track. Such stars have main-sequence lifetimes of about 2.6 Myr, meaning VFTS-1001 must be older than 1.9 Myr with 84% confidence and 1.7 Myr with 98% confidence[6]. VFTS-1025 with an observed luminosity of about $\log L/\mathrm{L}_\odot \approx 6.6$ and effective temperature of about $T_{\mathrm{eff}} \approx 42.2$ kK is close to an initially $200\,\mathrm{M}_\odot$ track that has a main-sequence lifetime of about 2.1 Myr. Hence, VFTS-1025 is older than 1.1 Myr with 84% confidence and older than 1.0 Myr with 98% confidence.

Within a radius of 0.8 arcmin are all stars of the north-east clump (Sabbi et al. 2012) and several stars in the dusty arc-like structure that surrounds R136. The age distributions are similar to those within 0.4 Myr with the exception of the addition of some older stars that give rise to the little features in the age distributions (c) and (d) in Fig. 5.6 at ages > 3 Myr. As mentioned previously, we cannot say where our sample stars formed and it is therefore not feasible to provide an age estimate of the north-east clump from individual or small groups of

---

[6] The lower age limits are derived by assuming that the helium core mass fraction, Y_{core}, is the same as that observed at the surface and that the core helium mass fraction scales linearly with age, i.e. $t/\tau_{\mathrm{MS}} = (Y_{\mathrm{core}} - Y_{\mathrm{ini}})/(1 - Y_{\mathrm{ini}})$ with t being the age of the star, $Y_{\mathrm{ini}} \approx 0.26$ the initial helium mass fraction and τ_{MS} the main-sequence lifetime. The confidence levels are derived from the uncertainties of the observed surface helium mass fraction. The lower age limits become larger if the star was initially rotating faster, prolonging the main-sequence, or if the star is a binary product in which case it was likely rejuvenated.
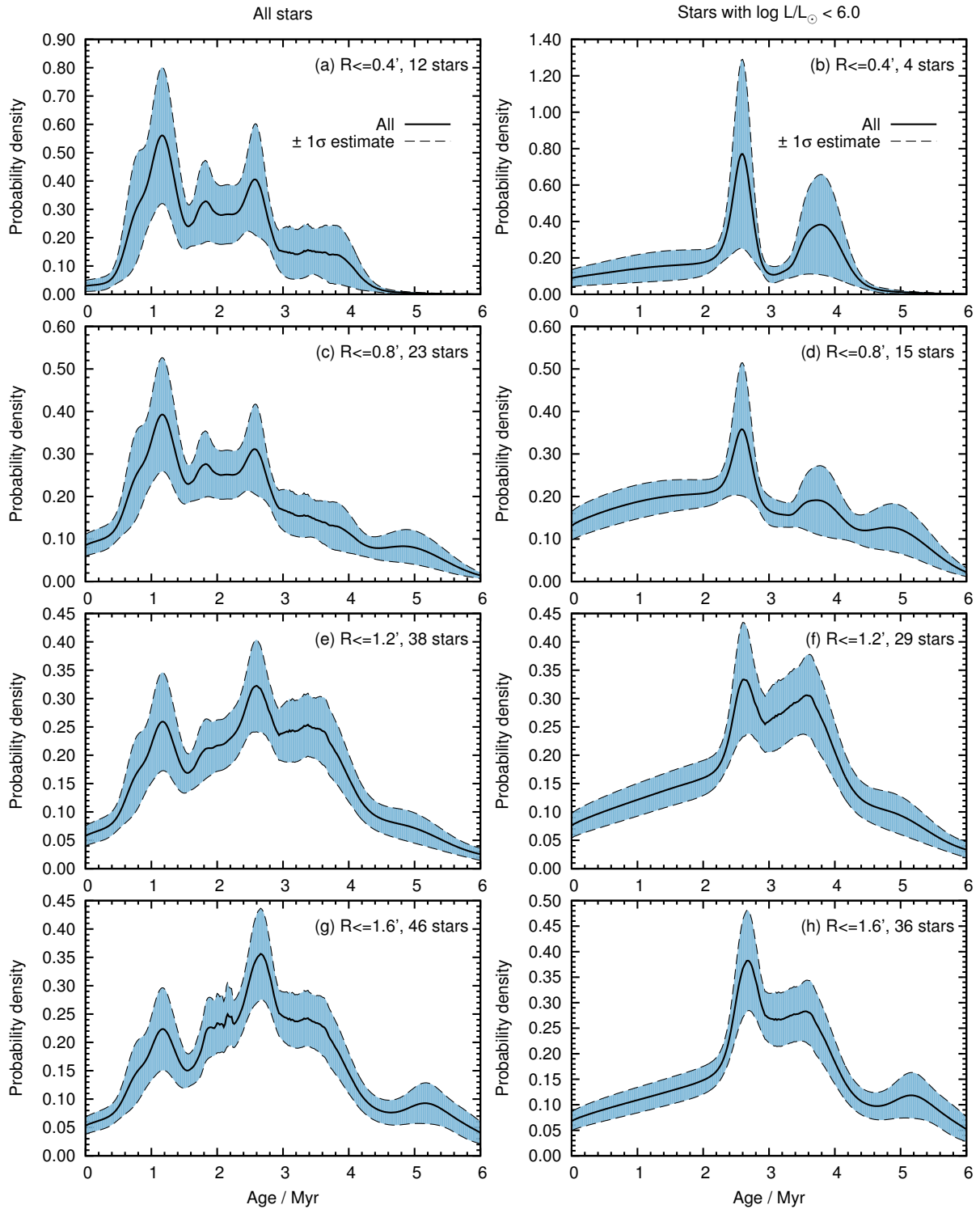
Figure 5.6: Age distributions of stars around R136 within circles of radii of 0.4 (5.8), 0.8 (11.6), 1.2 (17.5) and 1.6 arcmin (23.3 pc; see Fig. 5.5). The age distributions on the left side are for all stars in our sample and those on the right side only for stars less luminous than $\log L/L_\odot = 6.0$ to remove stars with possibly biased ages because of physics lacking in the stellar models (Sec. 5.3.1). The age distributions are not incompleteness corrected because of the low number statistics within the innermost region.

stars.

The north-east clump extends up to the dusty shells north of R136 and to the brightest X-ray source in 30 Dor, the multiple star system containing the WC4 star R140a1. Another three O stars surround the R140 star system and together they may form an association of stars. Three to five O stars are found close to the position of the $3.0^{+0.5}_{-0.6}$ Myr star VFTS-564 and may form another small association just as five O stars that cluster around the position of the $2.8^{+0.6}_{-0.9}$ Myr giant VFTS-513. All together this may suggest that R136 is surrounded by further stellar associations along the dusty shell to its north/north-west.

Increasing the radius to 1.2 arcmin adds stars that primarily fall in the age range 2–4 Myr, thereby explaining the (potential) double peak in the age distributions (e) and (f) in Fig. 5.6. Six out of eleven stars are found about 1 arcmin south of R136 and contain the WN8(h) star VFTS-427 and the O3.5 If*/WN7 star VFTS-457. The WN8(h) star has a surface helium mass fraction of 0.93 ± 0.05 that is hard to reproduce with our stellar models given the observed position in the HR diagram—our stellar models predict a surface helium mass fraction of 0.84 ± 0.04. From its high helium surface mass fraction we conclude that the star is either close to the end of the main sequence or already burning helium in the core. The high surface helium mass fractions further indicates that VFTS-427 is older than 2.2 Myr with 84% confidence given that its position in HR diagram corresponds to that of an initially moderate rotator of about $100 \, M_\odot$ (see also above discussion on the age of VFTS-1001 and 1025).

Within 1.2 arcmin are also the two dwarfs VFTS-609 and 660 with ages of $6.5^{+1.1}_{-1.0}$ Myr and $6.3^{+2.1}_{-2.4}$ Myr, respectively. The latter star, located about 0.9 arcmin east/north-east of R136, is a rapid rotator with an observed projected rotational velocity $v \sin i \approx 520 \, \mathrm{km \, s^{-1}}$. According to our stellar models, the star is not massive enough to mix helium synthesised in its core to the surface and hence is predicted to show nitrogen but no helium surface enrichment. Its very fast rotation makes VFTS-660 a promising candidate for a binary product in which case its inferred age is unreliable. The origin of the other old dwarf, VFTS-609, remains unclear.

Increasing the radius further to 1.6 arcmin includes a group of stars about 1.4 arcmin north of R136 that add a little bump to the age distributions (g) and (h) in Fig. 5.6 at about 5.2 Myr. The rest of the age distribution is very similar to those within 1.2 arcmin.

5.4.3 The NGC 2060 region

The second most obvious site of star formation is the NGC 2060 region. We show an age map of that region in Fig. 5.7 and the age distribution of stars within 3 arcmin (≈ 43.6 pc) of the 16 ms pulsar PSR J0537-6910 in Fig. 5.8. The age distribution shows two broad features at about 2.3 and 4.8 Myr. According to the bootstrapped 1σ uncertainty estimates, the other wiggles and peaks in the age distribution are insignificant.

The number of stars in our sample in this region is rather low so it is challenging to understand the star formation process around NGC 2060 in detail. Overall the stars are less luminous than those around R136—the two most luminous stars of our sample in that region are the dwarf VFTS-216 with $\log L/L_\odot \approx 5.8$ and the WN7h star VFTS-108 with $\log L/L_\odot \approx 5.7$. Hence, our sample stars around NGC 2060 are less massive, initially up to about $60 \, M_\odot$, and on average older than the stars around R136.

Besides the pulsar PSR J0537-6910 and the rapidly rotating runaway star VFTS-102, that may be physically linked to each other (Dufton et al. 2011), the region in Fig. 5.7 contains several interesting stars and stellar populations such as the WN7h star VFTS-108 about 2.5 arcmin north/north-west of the pulsar PSR J0537-6910 (see discussion on its evolutionary state in
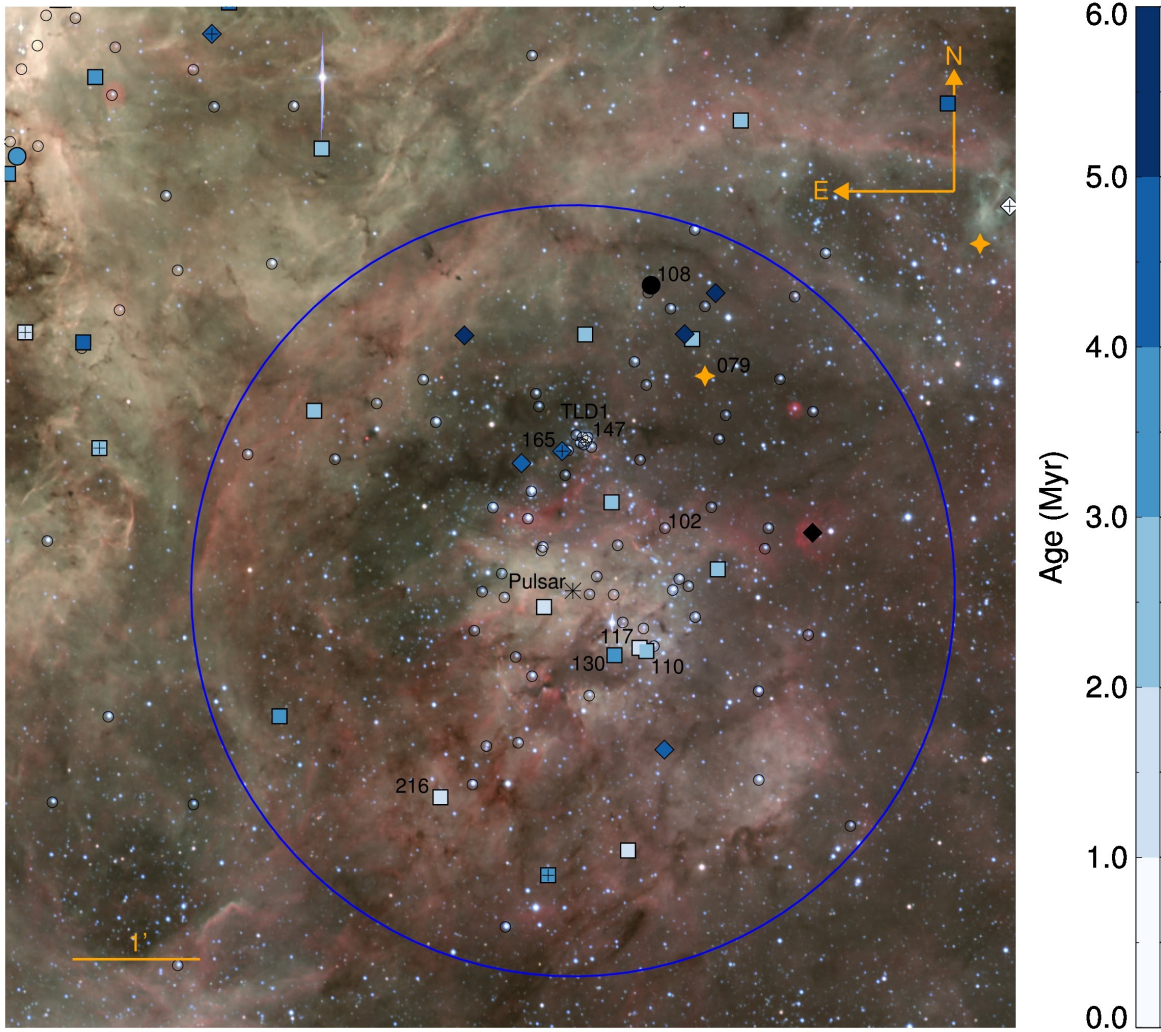
Figure 5.7: As Fig. 5.2 but zoomed in to NGC 2060. The age distribution of the stars is shown in Fig. 5.8. The position of the pulsar PSR J0537-6910 is indicated by an asterisk and is the centre of the blue circle.

Sec. 5.3.1). In the north-west part of the region is the WN4b/WCE star VFTS-079 (Br 70a) indicated by the yellow star symbol. About 1.1 arcmin south-east of VFTS-079 and 1.2 arcmin north of the pulsar PSR J0537-6910 lies the stellar association TLD1 that hosts several OB stars and the WN6(h) star VFTS-147 (Testor et al. 1988; Bica et al. 1999, 2008). The $4.7^{+0.4}_{-0.4}$ Myr old giant VFTS-165 just east of this association is identified by Sana et al. (in prep.) as a runaway star, so its age may not be representative of the association. Within the TLD1 association are the O dwarf VFTS-154 and the O giants VFTS-141, 151 and 153. The giants have BBB spectral classifications and VFTS-151 and 153 are visual multiples of at least five and three stars, respectively (Walborn et al. 2014). Their inferred ages are therefore highly uncertain and we are unable to provide a robust age for this association.

About 0.6 arcmin south-west from the pulsar PSR J0537-6910 are the three dwarfs VFTS-110, 117 and 130 with ages of $2.7^{+0.3}_{-0.3}$ Myr, $1.3^{+0.7}_{-1.0}$ Myr and $3.4^{+0.7}_{-1.0}$ Myr, respectively. Some of them may belong to a group of stars in this part of NGC 2060 given their spatial coincidence
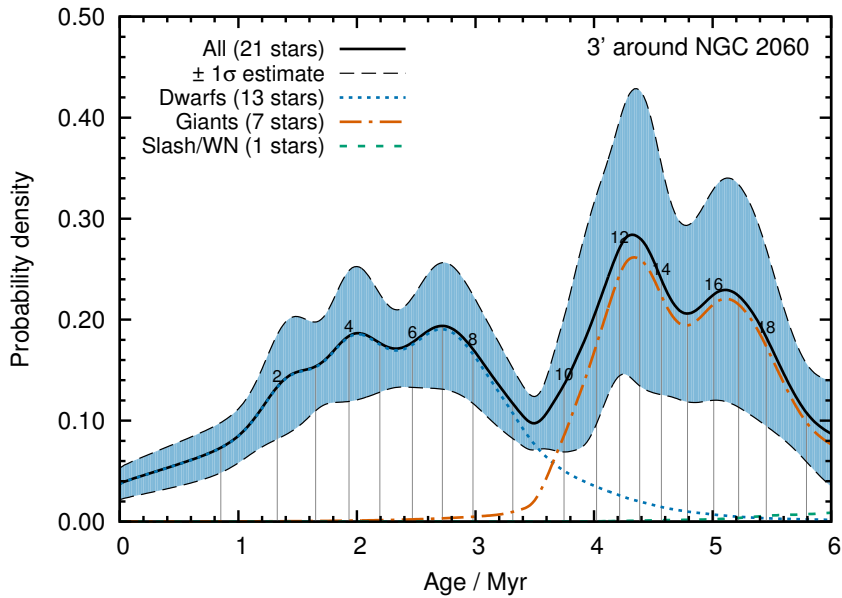
Figure 5.8: As Fig. 5.3 but for stars within 3.0 arcmin of NGC 2060.

with a small cluster like association of stars seen in the optical image of NGC 2060 at that location.

5.4.4 Stars outside R136 and NGC 2060

About half of our sample stars are within 1.2 arcmin of R136 and 3 arcmin of NGC 2060 (59 out of 119 stars) while another 60 stars surround these two regions. We show the age distribution of these 60 stars in Fig. 5.9. The age distribution has two remarkable features: peaks at about 2.7 and 4.5 Myr. The first peak is not significant at a 1σ or higher level but the second is. Both features are also present in the age distributions of the R136 and NGC 2060 regions (Figs. 5.4, 5.6 and 5.8). The age distribution of stars in the vicinity of R136 shows no peak at 4.5 Myr but a single or even double peak at 2.7 Myr (Fig. 5.4). The opposite is true for stars in the NGC 2060 region: a clear peak at about 4.5 Myr is visible in their age distribution while a younger peak of 2.7 Myr is not that prominent (Fig. 5.8). These findings may suggest that the stars in our sample of about 2.7 Myr formed primarily close to (or even in) R136 while an older group of about 4.5 Myr stars primarily formed in the NGC 2060 region. This may be the case for 27 stars that have ages consistent with 2.4–2.9 Myr within 1σ and for 22 stars with ages that are within 1σ in the age range 4.2–4.8 Myr. However, only future proper motion measurements will confirm or disprove this scenario by tracing back the formation sites of these stars.

5.4.5 The age of the central R136 cluster

Previous age estimates of the R136 cluster range from less than 1–2 Myr up to 4 Myr depending on which stars are analysed (e.g. Hunter et al. 1995; Brandl et al. 1996; de Koter et al. 1997; Massey & Hunter 1998; Selman et al. 1999; Andersen et al. 2009; Crowther et al. 2010; Sabbi et al. 2012). Ages derived from the most massive stars are the youngest while average ages for a larger sample of stars tend to be older. These findings are in agreement with our results showing that stars projected onto the central region of R136 have apparent ages up to 4 Myr (Fig. 5.4
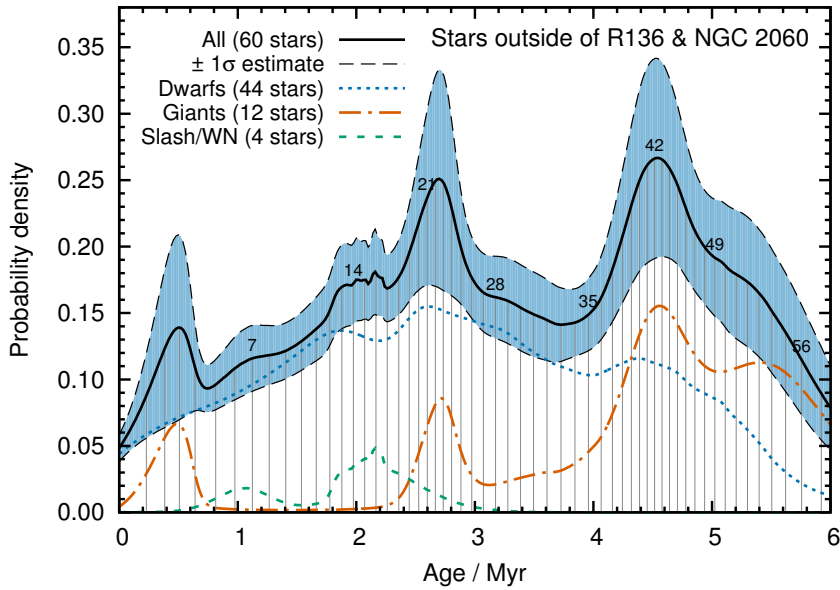
Figure 5.9: As Fig. 5.3 but for stars outside of R136 (> 1.2 arcmin) and NGC 2060 (> 3.0 arcmin), i.e. outside the red and blue circles in Fig. 5.2.

and Sec. 5.4.2). With the data at hand we cannot give a definite age for the R136 cluster because our sample stars are mostly outside of the R136 core and their cluster membership is not yet established. However, there are three different constraints that may serve as hints to the real age of the central cluster.

The central region hosts stars whose initial masses greatly exceed $100 \, M_\odot$ and even reach $200 \, M_\odot$ (Fig. 5.1). Crowther et al. (2010) finds stars in the innermost core of R136 that may have been initially as massive as $300 \, M_\odot$. The derived ages of these stars are uncertain given the uncertainties in the physics of stellar models at such high masses and a large fraction of them may even be rejuvenated binary products (Sec. 5.4.2 and Schneider et al. 2014b). However given that such massive stars live only for 2–3 Myr, we can set an upper age limit on the R136 cluster age of about 3 Myr.

A lower age limit may be derived from the observed surface helium mass fractions of the massive WNh stars in our sample that are spatially concentrated towards R136. In Sec. 5.4.2 we discuss that the WN6(h) star VFTS-1001 and the WN5h star VFTS-1025 must be older than 1.7 Myr and 1.0 Myr, respectively, in order to produce the large amount of helium observed in their spectra. This restricts the potential R136 cluster age to the range 1.0–3.0 Myr. If future observations can show that VFTS-1001 is a member of R136, the potential age range narrows to 1.7–3.0 Myr.

The third hint comes from the two characteristic ages of about 2.7 and 4.5 Myr found in the age distributions of our sample stars. The strongest recent star formation took place in R136 and if R136 formed a coeval stellar population that is also represented in our sample of stars, the R136 cluster age would be linked to the strongest and youngest age signal, i.e. to the peak found around 2.4–2.9 Myr in our age distributions. This feature stands out in the age distribution of our sample stars in the whole 30 Dor region (Fig. 5.3) as well as in the R136 region (Fig. 5.4) and outside of R136 and NGC 2060 (Fig. 5.9). A cluster age of about 2.7 Myr is consistent with the 1.0–3.0 Myr estimate derived from the most massive stars near
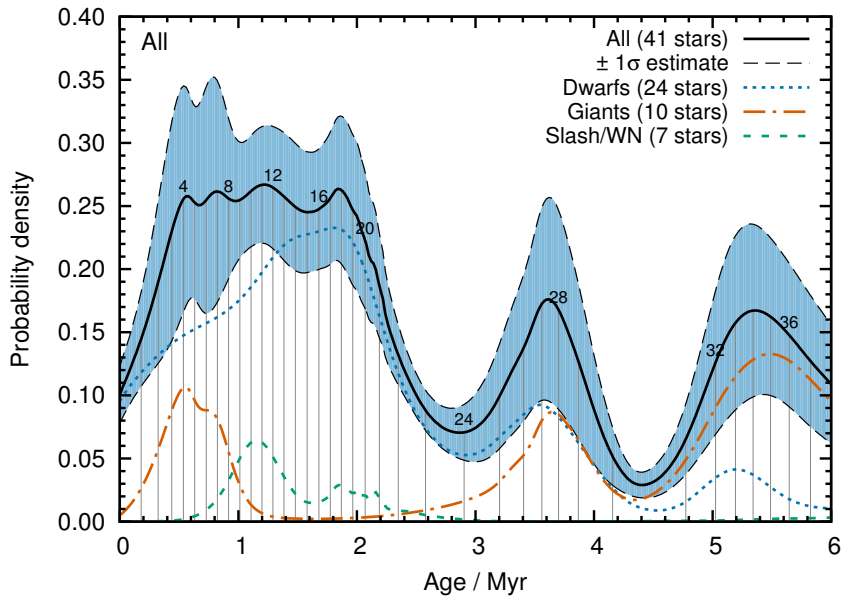
Figure 5.10: As Fig. 5.3 but stars that have ages within 1σ of 2.4–2.9 Myr and 4.2–4.8 Myr have been removed.

the core of R136. We note however that these constraints are rather indirect and that only future observations and detailed modelling of stars in the core of R136 will settle the discussion on the true R136 cluster age.

5.4.6 The overall star formation process

As stressed earlier, our stellar sample consists mostly of field stars that may have formed far away from where they are currently observed. They may originate from dissolving clusters or associations, have formed in apparent isolation or have been kicked out of clusters as runaway stars. To discriminate between these origins, i.e. between continuous star formation over the whole 30 Dor field and star formation in discrete, spatially localised regions, we try to identify groups of stars that may have formed together and are now spread over 30 Dor by their inferred ages.

All the age distributions discussed so far (Figs. 5.3, 5.4, 5.6, 5.8 and 5.9) indicate the existence of a stellar population in the age range 2.4–2.9 Myr that we suggest formed in the R136 star cluster (Sec. 5.4.5). The other stellar population identified by its age consists of stars with apparent ages in the range 4.2–4.8 Myr. This population cannot be found in the R136 region (Fig. 5.4) but rather in the NGC 2060 region (Fig. 5.8) and the outskirts of R136 and NGC 2060 (Fig. 5.9). Of our 119 sample stars, 53 (45%) have an age that is consistent within 1σ in the range 2.4–2.9 Myr (Table 5.1), 35 (29%) have an age that is consistent with the age range 4.2–4.8 Myr (Table 5.2) and 41 (35%) have ages that are *not* consistent with either of the two age ranges (Table 5.3). Note that some stars have so large age uncertainties that they may belong to both age ranges.

If we remove stars that apparently do not belong to either of the two age ranges within their 1σ uncertainties from the age distribution in Fig. 5.3, we obtain that shown in Fig. 5.10. This age distribution suggests the existence of three further stellar groups: stars that are younger

Table 5.1: Sample stars that have an age within 1σ of 2.4–2.9 Myr (53 out of 119 stars, i.e. 45%).

VFTS No.	Age (Myr)	VFTS No.	Age (Myr)	VFTS No.	Age (Myr)
065	$2.4^{+0.9}_{-1.4}$	470	$2.8^{+0.3}_{-0.6}$	617	$2.1^{+0.4}_{-0.3}$
067	$2.0^{+1.3}_{-1.6}$	483	$4.3^{+0.8}_{-1.7}$	620	$3.3^{+1.3}_{-1.6}$
074	$2.1^{+1.2}_{-1.7}$	488	$2.5^{+0.2}_{-0.2}$	627	$4.2^{+0.8}_{-1.3}$
089	$2.5^{+0.4}_{-0.8}$	491	$2.6^{+0.2}_{-0.2}$	663	$2.5^{+1.3}_{-1.7}$
110	$2.7^{+0.3}_{-0.3}$	505	$1.8^{+1.1}_{-1.2}$	704	$4.2^{+1.1}_{-2.1}$
130	$3.4^{+0.7}_{-1.0}$	513	$2.8^{+0.6}_{-0.9}$	706	$3.5^{+1.5}_{-0.9}$
132	$2.3^{+0.9}_{-1.2}$	537	$3.3^{+0.5}_{-0.5}$	724	$3.6^{+1.4}_{-2.6}$
149	$2.9^{+1.3}_{-1.9}$	542	$2.2^{+0.3}_{-0.4}$	737	$2.1^{+0.7}_{-1.0}$
168	$3.0^{+0.5}_{-0.7}$	549	$2.2^{+0.6}_{-1.1}$	746	$2.8^{+0.4}_{-0.4}$
249	$2.7^{+0.9}_{-1.3}$	550	$3.3^{+0.5}_{-0.4}$	751	$3.8^{+1.1}_{-2.0}$
250	$3.0^{+0.9}_{-1.4}$	560	$2.6^{+1.5}_{-1.9}$	755	$1.8^{+1.7}_{-0.8}$
266	$3.0^{+0.3}_{-0.6}$	564	$3.0^{+0.5}_{-0.6}$	758	$2.2^{+0.4}_{-0.2}$
356	$2.6^{+0.6}_{-0.9}$	566	$2.7^{+0.1}_{-0.2}$	770	$3.2^{+0.9}_{-1.6}$
369	$4.4^{+1.2}_{-1.8}$	577	$2.1^{+0.5}_{-0.7}$	775	$2.3^{+1.2}_{-1.5}$
382	$3.0^{+0.4}_{-0.4}$	581	$3.0^{+0.4}_{-0.3}$	778	$3.9^{+1.1}_{-1.9}$
406	$3.3^{+1.6}_{-0.4}$	592	$2.5^{+1.2}_{-1.6}$	1001	$3.3^{+0.1}_{-0.5}$
427	$3.1^{+0.3}_{-0.3}$	601	$2.6^{+0.2}_{-0.2}$	1017	$2.2^{+0.4}_{-0.4}$
457	$2.4^{+0.2}_{-0.4}$	611	$1.9^{+0.9}_{-1.2}$		

Table 5.2: Sample stars that have an age within 1σ of 4.2–4.8 Myr (35 out of 119 stars, i.e. 29%).

VFTS No.	Age (Myr)	VFTS No.	Age (Myr)	VFTS No.	Age (Myr)
012	$5.3^{+0.4}_{-0.6}$	406	$3.3^{+1.6}_{-0.4}$	679	$4.7^{+0.9}_{-1.7}$
021	$5.0^{+0.5}_{-0.6}$	419	$4.9^{+0.6}_{-0.5}$	704	$4.2^{+1.1}_{-2.1}$
091	$5.1^{+0.5}_{-0.5}$	435	$3.9^{+0.6}_{-0.6}$	706	$3.5^{+1.5}_{-0.9}$
103	$4.4^{+0.2}_{-0.2}$	436	$4.6^{+0.8}_{-0.8}$	717	$4.4^{+0.3}_{-0.2}$
165	$4.7^{+0.4}_{-0.4}$	466	$4.5^{+0.2}_{-0.2}$	722	$3.9^{+2.0}_{-0.8}$
185	$4.0^{+0.3}_{-0.3}$	483	$4.3^{+0.8}_{-1.7}$	724	$3.6^{+1.4}_{-2.6}$
210	$5.1^{+0.7}_{-0.9}$	498	$5.0^{+0.7}_{-0.9}$	751	$3.8^{+1.1}_{-2.0}$
251	$4.7^{+0.5}_{-0.8}$	597	$4.0^{+0.5}_{-0.6}$	778	$3.9^{+1.1}_{-1.9}$
280	$4.7^{+0.3}_{-0.3}$	620	$3.3^{+1.3}_{-1.6}$	782	$4.6^{+0.3}_{-0.3}$
290	$4.7^{+0.5}_{-0.6}$	627	$4.2^{+0.8}_{-1.3}$	807	$5.0^{+0.7}_{-0.5}$
306	$4.3^{+0.3}_{-0.3}$	639	$4.1^{+0.7}_{-1.1}$	892	$3.8^{+0.5}_{-0.7}$
369	$4.4^{+1.2}_{-1.8}$	660	$6.3^{+2.1}_{-2.4}$		

Table 5.3: Sample stars that have an age that is *not* consistent within 1σ to be in the ranges 2.4–2.8 Myr and 4.2–4.8 Myr (41 out of 119 stars, i.e. 35%).

VFTS No.	Age (Myr)	VFTS No.	Age (Myr)	VFTS No.	Age (Myr)
016	$0.5^{+0.1}_{-0.2}$	472	$1.5^{+0.6}_{-0.9}$	682	$1.1^{+0.2}_{-0.3}$
046	$6.2^{+0.5}_{-0.5}$	482	$1.3^{+0.2}_{-0.2}$	695	$2.2^{+0.1}_{-0.3}$
072	$0.4^{+1.9}_{-0.4}$	484	$3.8^{+0.3}_{-0.3}$	710	$1.1^{+1.1}_{-1.0}$
076	$5.3^{+0.3}_{-0.3}$	493	$1.5^{+0.9}_{-1.0}$	753	$5.6^{+0.6}_{-0.7}$
108	$6.3^{+1.2}_{-0.9}$	517	$5.2^{+0.3}_{-0.3}$	761	$1.2^{+0.6}_{-0.8}$
117	$1.3^{+0.7}_{-1.0}$	536	$0.9^{+0.7}_{-0.8}$	777	$5.2^{+0.5}_{-0.4}$
123	$1.4^{+0.6}_{-0.9}$	545	$1.1^{+0.2}_{-0.2}$	797	$1.9^{+0.3}_{-0.3}$
169	$1.4^{+0.3}_{-0.3}$	546	$5.7^{+0.4}_{-0.4}$	819	$3.5^{+0.4}_{-0.6}$
216	$2.0^{+0.3}_{-0.2}$	554	$0.4^{+1.7}_{-0.4}$	843	$5.9^{+0.7}_{-1.0}$
252	$1.1^{+0.8}_{-0.8}$	582	$0.4^{+1.5}_{-0.4}$	849	$1.5^{+0.6}_{-0.9}$
361	$3.5^{+0.3}_{-0.5}$	586	$1.5^{+0.4}_{-0.6}$	1022	$1.2^{+0.2}_{-0.2}$
380	$1.7^{+0.7}_{-0.9}$	609	$6.5^{+1.1}_{-1.0}$	1025	$1.8^{+0.4}_{-0.2}$
392	$3.4^{+0.3}_{-0.3}$	638	$1.0^{+0.9}_{-0.8}$	MK42	$0.8^{+0.2}_{-0.2}$
418	$1.4^{+0.6}_{-0.9}$	664	$3.7^{+0.3}_{-0.2}$		

than about 2 Myr, one group that is about 3.6 Myr old and one that is about 5.3 Myr old. The $\lesssim 2$ Myr stars are mainly composed of dwarfs that are primarily located outside the R136 region while four of the six apparently young (< 3 Myr) slash and WN stars and one of the two young ($\lesssim 1$ Myr) giants are found within 1.2 arcmin of R136. Consequently, most of these apparently young stars are found outside 1.2 arcmin of R136. Contrarily, the potential 3.6 Myr stellar population is, except for VFTS-819 (Fig. 5.2), solely found within 1.2 arcmin of R136. Together with the 2.7 Myr old stars, this population makes up the potential double peak in the age distribution of stars around R136 (Fig. 5.4). Assuming the 2.7 Myr stars belong to R136, the 3.6 Myr stars would have to belong to another, distinct stellar population in the R136 region. The north-east clump suggested by Sabbi et al. (2012) to be in the process of merging with R136 may be a good candidate for the origin of this population if these stars indeed formed together in one place. Stars of about 5.3 Myr are only present outside 1.2 arcmin of R136 but are found within 3 arcmin of NGC 2060. Their origin remains obscure and it is not clear whether they formed together in a spatially localised region of 30 Dor or not.

Overall the following picture may emerge: 30 Dor contains a 2.7 Myr population that is possibly linked to R136 and a 4.5 Myr population that may have formed within the NGC 2060 region. Stars younger than 2 Myr could be rejuvenated binary products that belong to the 2.7 Myr population, i.e. possibly to R136, and stars that formed recently in 30 Dor such as those found in the dense knots in the filamentary structure to the north and north-west of R136. In this picture, the age distribution of stars around R136 shows a double peak instead of one broad peak, where the 2.7 Myr component belongs to stars from R136 and the 3.6 Myr component makes up a distinct stellar population that may correspond to stars from the north-east clump found by Sabbi et al. (2012). The origin of the remaining stars, i.e. those with apparent ages of about 5.3 Myr, remains obscure. There are several possible formation sites but we have no evidence that clearly points to one of them. However, we note that continuous formation of our sample stars in relative isolation over the whole 30 Dor field cannot be ruled

out with the current data.

5.5 Discussion

5.5.1 The ages of our sample stars in context of previous investigations

30 Dor is a complex starburst region and so far most attention has been devoted to the central ionising cluster R136. The oldest stars in 30 Dor are 20–30 Myr old (Grebel & Chu 2000; De Marchi et al. 2011) whereas the youngest stars are still embedded in dense molecular clumps, primarily found to the north and west of R136 (e.g. Walborn & Blades 1987; Hyland et al. 1992; Walborn & Blades 1997; Rubio et al. 1998; Brandner et al. 2001; Walborn et al. 2002; Maercker & Burton 2005). Just a couple of million years ago, the star formation rate reached its maximum when giving birth to R136 and the stars in NGC 2060. Besides the clearly visible clusters Hodge 301, NGC 2060, R136 and SL 639, further distinct groups and associations of stars are thought to have formed together:

- the stars in knots 1–3 (Walborn & Blades 1997),

- the stars surrounding the LBV R143 (Walborn & Blades 1997),

- the stars in field 15 of Brandner et al. (2001),

- the stars in the north field of Walborn et al. (2002), right at the edge of the filament between R136 and Hodge 301

- and the stars in the north-east clump that may be even merging with R136 (Sabbi et al. 2012).

Using ALMA and the Australia Telescope Compact Array, respectively, Indebetouw et al. (2013) and Anderson et al. (2014) find molecular clumps in the filamentary structure north of R136, i.e. in the region of knots 1 and 2, that seem to be gravitationally unstable and are likely to collapse to form the next generation of stars.

De Marchi et al. (2011) investigate the spatial distribution of pre main-sequence stars around R136. They find that pre main-sequence stars younger than 4 Myr primarily cluster around R136 and towards its north whereas those older than about 12 Myr are rather found east/south-east of R136. These two groups overlap in the outskirts of R136, indicative of the 3D structure of the 30 Dor nebula.

From photometry of stars near R136, Brandl et al. (1996) and Selman et al. (1999) determine stellar age distributions similar to ours in Sec. 5.4.2. They also find three distinct peaks albeit at slightly different ages suggesting that the region around R136 consists not only of one stellar population but rather of several. Selman et al. (1999) find that the youngest stars are concentrated towards the core of R136, in agreement with our findings. Similar core–halo age gradients are found in other star forming regions, e.g. in the Orion nebula, the Flame nebula (NGC 2024) and W40 (Getman et al. 2014a,b) and seem to be a ubiquitous feature of star formation that can have several origins as discussed by Getman et al. (2014a) but is not yet understood.

Table 5.4: Candidates for massive stars formed in isolation from Bressert et al. (2012) including our age estimates and distances to R136, d_{R136}, and NGC 2060, d_{NGC2060}.

VFTS No.	Age (Myr)	d_{R136}/arcmin	d_{NGC2060}/arcmin
089	$2.5^{+0.4}_{-0.8}$	6.3	2.2
123	$1.4^{+0.6}_{-0.9}$	8.3	2.1
216	$2.0^{+0.3}_{-0.2}$	7.0	1.9
382	$3.0^{+0.4}_{-0.4}$	1.0	6.1
392	$3.4^{+0.3}_{-0.3}$	0.9	6.1
470	$2.8^{+0.3}_{-0.6}$	1.4	7.3
488	$2.5^{+0.2}_{-0.2}$	2.4	5.1
537	$3.3^{+0.5}_{-0.5}$	2.3	8.3
577	$2.1^{+0.5}_{-0.7}$	1.1	6.1
581	$3.0^{+0.4}_{-0.3}$	1.8	8.0
682	$1.1^{+0.2}_{-0.3}$	2.0	8.5
706	$3.5^{+1.5}_{-0.9}$	1.6	8.1
849	$1.5^{+0.6}_{-0.9}$	8.9	15.3

5.5.2 Massive star formation in isolation

Bressert et al. (2012) propose that 16 O stars in 30 Dor formed in apparent isolation. In this work we determine the apparent ages of 13 of these stars. Although only future proper motion measurements in combination with our age estimates will be able to establish a formation scenario, it is instructive to check whether the ages of the 13 candidates alone already give a hint towards potential birth places within 30 Dor. In Table 5.4, we compile a list of the 13 candidates including our inferred ages and the distances to R136 and NGC 2060. Eight of the 13 candidates, VFTS-089, 382, 470, 488, 537, 577, 581 and 706, have ages consistent with 2.4–2.9 Myr to within 1σ. VFTS-706 may instead belong to the 4.2–4.8 Myr age group. Its fast projected rotational velocity, $v \sin i \approx 380\,\mathrm{km\,s^{-1}}$, may point to a past binary mass transfer phase, hence these eight stars could originate from the R136 region rather than have formed in apparent isolation. The ages of the remaining five candidates do not allow an association with the two prominent peaks at about 2.7 Myr and 4.5 Myr in the age distributions of our sample stars (Figs. 5.3 and 5.9). VFTS-392 could belong to the potential 3.6 Myr population discussed in Sec. 5.4.6. This would leave VFTS-123, 216, 682 and 849 as candidates that may have formed in isolation. All of them are apparently younger than about 2 Myr.

5.5.3 Runaway stars

Sana et al. (in prep.) identify runaway candidates from radial velocity measurements and conclude that most of the runaways were formed in a supernova explosion that disrupted the binary progenitor system. In this scenario, many of the runaways experienced a past mass transfer phase that not only spun the stars up but that also rejuvenated them. Rejuvenation makes stars look younger than they really are and may be visible in the age distribution of the identified runaway stars in comparison to that of all stars.

In Fig. 5.11 we show the age distribution of the runaway stars and list them in Table 5.5 including their radial velocities relative to the 30 Dor mean, δv_{rad}, their projected rotational
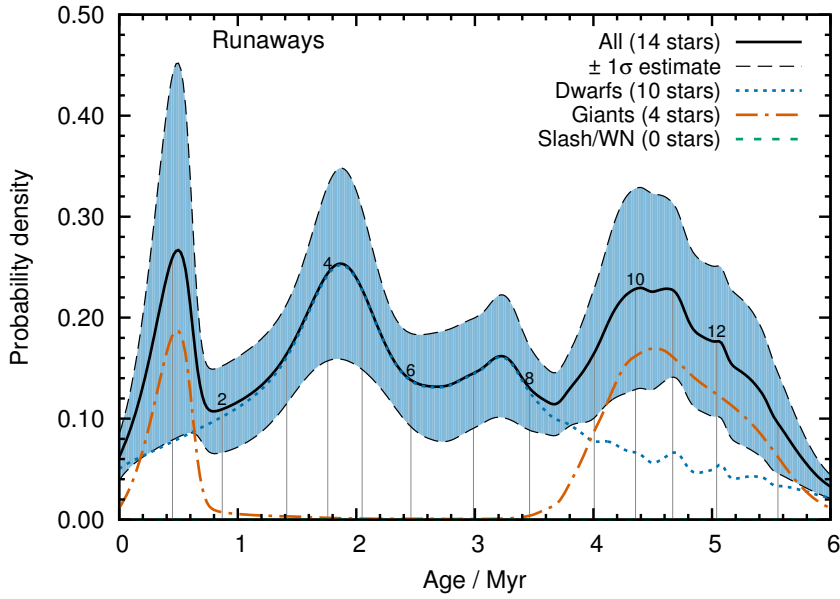
Figure 5.11: As Fig. 5.3 but for the runaway stars in our sample identified by Sana et al. (in prep.). The runaway stars in our sample are marked by additional plus signs in Figs. 5.2, 5.5 and 5.7.

velocities, $v \sin i$, their inferred ages and initial masses, M_{ini}. Of the 24 runaway stars identified by Sana et al. (in prep.), one is a known binary for which no atmospheric modelling is available, seven have been removed from our sample mainly because of their BBB spectral classification and two cannot be reproduced by the stellar models because the stars are rotating too fast (Sec. 5.3). The age distribution shows three interesting features—peaks at about 0.5, 1.9 and 4.5 Myr.

The 0.5 Myr peak is due to VFTS-016, a runaway with a bow shock that is thought to have been ejected from R136 (Evans et al. 2010). Its position in the HR diagram (Fig. 5.1) is very close to the zero-age main-sequence and its age of $0.5^{+0.1}_{-0.2}$ Myr is significantly younger than any stellar population found in this work. Hence, from its apparent age we conclude that VFTS-016 is a rejuvenated binary product. However, its large relative radial velocity of $\delta v_{\mathrm{rad}} = 78.3 \, \mathrm{km \, s^{-1}}$ rather points towards a star that has been dynamically ejected from R136 (Sana et al. in prep.). We therefore propose that VFTS-016 is a binary product that either accreted mass or merged with a companion prior to its dynamical ejection from R136 or it was ejected as a binary and merged later on. Such an object is expected to rotate rapidly. Its relatively low $v \sin i$ of about $94 \, \mathrm{km \, s^{-1}}$ may therefore be due to an unfavourable inclination angle or the generation of a magnetic field because of past mass accretion or merging that spun the star down (magnetic braking). Evans et al. (2010) find that the surface nitrogen mass fraction of VFTS-016 is enhanced by a factor of five and Bestenlehner et al. (2014) report a partial surface nitrogen enhancement though note that the stellar surface is not strongly enriched with nitrogen. This may be in favour of a binary merger origin (e.g. Glebbeek et al. 2013) but is not yet conclusive.

The 1.9 Myr peak is intriguing. Either the peak contains stars that were dynamically ejected from R136 and hence is indicative of the true cluster age of R136 or it contains stars that belong to the 2.7 Myr population found around R136 and were rejuvenated by binary mass transfer before being ejected by the supernova explosion of their companion. The peak is mainly formed by the stars VFTS-755 and 797. If these runaways are rejuvenated binary products, we expect

Table 5.5: Runaway candidates from Sana et al. (in prep.), their radial velocities relative to the mean of the 30 Dor population, $\delta v_{\rm rad}$, projected rotational velocities, $v \sin i$, inferred ages and initial mass, $M_{\rm ini}$.

VFTS No.	$\delta v_{\rm rad}$ $\rm km\,s^{-1}$	$v \sin i$ $\rm km\,s^{-1}$	Age Myr	$M_{\rm ini}$ $\rm M_\odot$
012	48.6	306	$5.3^{+0.4}_{-0.6}$	$19.0^{+1.0}_{-1.0}$
016	78.3	94	$0.5^{+0.1}_{-0.2}$	$100.0^{+13.9}_{-10.6}$
102	56.2	610	$\ldots$	$\ldots$
165	61.6	75	$4.7^{+0.4}_{-0.4}$	$31.2^{+3.6}_{-3.0}$
168	36.6	39	$3.0^{+0.5}_{-0.7}$	$23.6^{+1.2}_{-1.2}$
190	45.0	444	$\ldots$	$\ldots$
285	38.6	622	$\ldots$	$\ldots$
306	33.4	71	$4.3^{+0.3}_{-0.3}$	$31.4^{+3.3}_{-2.7}$
356	70.3	211	$2.6^{+0.6}_{-0.9}$	$28.2^{+3.2}_{-2.9}$
406	35.7	356	$3.3^{+1.6}_{-0.4}$	$38.6^{+3.3}_{-7.3}$
418	30.6	133	$1.4^{+0.6}_{-0.9}$	$34.2^{+4.6}_{-3.9}$
661	26.4	$\ldots$	$\ldots$	$\ldots$
663	37.2	90	$2.5^{+1.3}_{-1.7}$	$20.6^{+2.0}_{-1.6}$
722	38.8	404	$3.9^{+2.0}_{-0.8}$	$23.6^{+2.0}_{-2.5}$
724	28.6	369	$3.6^{+1.4}_{-2.6}$	$22.0^{+5.2}_{-4.0}$
755	33.7	286	$1.8^{+1.7}_{-0.8}$	$51.6^{+4.8}_{-11.9}$
761	98.8	111	$1.2^{+0.6}_{-0.8}$	$28.0^{+1.6}_{-1.6}$
797	29.2	138	$1.9^{+0.3}_{-0.3}$	$49.0^{+7.5}_{-6.3}$

them to rotate rapidly. If they were dynamically ejected from R136, they may show relative radial velocities of $\delta v_{\rm rad} > 60\,{\rm km\,s^{-1}}$ (Sana et al. in prep.). Both stars have $\delta v_{\rm rad} < 60\,{\rm km\,s^{-1}}$ but VFTS-755 rotates with a projected rotational velocity of $v \sin i \approx 285\,{\rm km\,s^{-1}}$, suggestive of being a rejuvenated binary product. Unfortunately, its age is not constrained well enough to give a definite answer to its origin.

The 4.5 Myr peak in Fig. 5.11 is produced by VFTS-165 and 306. Their projected rotational velocities suggest that they are not binary products and the relative radial velocity of $61.6\,{\rm km\,s^{-1}}$ of VFTS-165 points towards a dynamical ejection (Sana et al. in prep.), explaining why this peak is not shifted towards younger (rejuvenated) ages compared to the corresponding peak of 4.5 Myr in the age distribution of stars in the surroundings of R136 and NGC 2060 (Fig. 5.9).

5.5.4 Binary products

Sana et al. (2013) show that close binaries are frequent among the O stars in 30 Dor and that more than 50% of them will exchange mass with a binary companion during their life. From observations, post mass-transfer binaries are hard to distinguish from genuinely single stars such that a sample of apparent single O stars may contain more binary products than a sample of binary stars. This is because stars detected as binaries from radial velocity measurements are mostly pre-interaction binary stars (de Mink et al. 2014). The stellar sample used in this work is chosen to exclude potential composite spectra, i.e. binaries, but is still expected to contain a significant fraction of binary products. Within a coeval stellar population, binary products are

preferentially found among the most massive stars because these stars evolve fastest (Schneider et al. subm.). The O stars in our sample are younger than about 6 Myr which corresponds to the main-sequence lifetime of a moderately rotating, initially $27 \, M_\odot$ star (Brott et al. 2011a). We therefore expect to find an increasing fraction of binary products in our sample stars from an initial mass of about $27 \, M_\odot$ and greater.

When analysing binary products with single star models, the inferred ages are younger than the real stellar ages because of rejuvenation (e.g. Schneider et al. 2014b, subm.). We already suggest that the 2 Myr group among the runaways (Sec. 5.5.3) and the $\lesssim 2$ Myr stars from Sec. 5.4.6 may be such rejuvenated binary products. In Sec. 5.4.5 we conclude that the central R136 cluster must be older than 1.7 Myr if VFTS-1001 is a genuine cluster member. Given that we do not find any spatially localised population that is younger than that in R136, a significant fraction of stars that are apparently younger than 1.7 Myr may be rejuvenated binary products. Within 1σ, the dwarf VFTS-536, the giants VFTS-016 and Mk42 and the slash/WN stars VFTS-482, 545, 682 and 1022 are younger than 1.7 Myr and thus are potential binary products. Given that the ages of stars in the upper part of the HR diagram are not robust (Sec. 5.3.1), further binary product candidates are VFTS-072, 617 and 1017 because of their proximity to the zero age main-sequence in the HR diagram (Fig. 5.1).

VFTS-682 sticks out not just because of its young age but also because it is found in apparent isolation (Bestenlehner et al. 2011). VFTS-682 either formed in isolation, hence it is young, or it is a binary product.

Identifying further binary products older than about 2.0–2.5 Myr purely from inferred ages is difficult because of the broad age distribution of all stars and the overlap with older stellar populations (Fig. 5.3). Unusually rapid rotation, surface nitrogen or helium enrichment, and/or the clear association of apparently young stars to older stellar populations may be further indicators of binary products. For the latter, the membership probability of stars needs to be assessed which likely requires full 3D stellar velocity information.

5.6 Conclusions

The atmospheric parameters of 198 massive O, slash and WN stars observed and modelled within the VLT FLAMES Tarantula Survey (VFTS; Evans et al. 2011) have been matched against the rotating, main-sequence star models of Large Magellanic Cloud composition of Brott et al. (2011a) and Köhler et al. (2014) to derive stellar ages and other parameters such as initial mass. All inferred ages, and also all other parameters, have to be considered as apparent ages because we expect that our sample of stars contains a non-negligible fraction of rejuvenated binary products for which we infer too young ages. We derive stellar age probability distributions for each star using the Bayesian tool BONNSAI[7] (Schneider et al. 2014a) and combine them to construct age distributions of the massive VFTS stars to analyse their formation process in 30 Dor. Out of the 198 stars, 79 are removed from further analysis because their spectra are of lower quality and/or are potential composites because of chance superpositions and duplicity that may result in biased atmospheric parameters when modelled with the methods of Sabín-Sanjulián et al. (2014) and Ramírez-Agudelo et al. (in prep.). The stars of our sample are mainly located outside of known clusters and associations—a fact that is important to take into account when interpreting the derived age distributions.

---

[7] The BONNSAI web-service is available at `http://www.astro.uni-bonn.de/stars/bonnsai`.

The spatial distribution of our sample stars shows no obviously coherent age pattern. Massive O stars of various ages are spread over the whole 30 Dor region. Given that our sample contains mainly field stars, this means that our sample stars either formed continuously over the whole 30 Dor field or in distinct clusters and/or associations from which they have been released to reach their currently observed positions. A mixture of both formation scenarios is also possible.

The age distribution of the 119 sample stars shows two prominent peaks at ages of about 2.7 and 4.5 Myr. The first group of stars is found in the whole 30 Dor region whereas the latter is mainly found outside 1.2 arcmin ($\approx$ 17.5 pc) of R136. Stars inside 1.2 arcmin of R136 are mostly younger than 4 Myr, with stars being on average younger the closer they are to R136.

The R136 cluster age cannot be determined straightforwardly because our sample stars do not cover the innermost region of R136. However, from the high masses and consequently short lifetimes of the massive WNh stars in R136 and the observed high surface helium mass fractions of VFTS-1001 and 1025, we estimate that they, and R136 (if it consists of coeval stars), are 1–3 Myr old. If VFTS-1001 is a genuine cluster member, R136 has an age of at least 1.7 Myr.

If stars in R136 are coeval and produce a peak in our age distribution, the only possible peak associated with that is at 2.7 Myr. If this is the case, the age distribution of stars within 1.2 arcmin of R136 shows a double and not a single peak that, besides the 2.7 Myr stars, contains a distinct group of 3.6 Myr stars. These stars might be associated with the north-east clump found by Sabbi et al. (2012).

If also the group of 4.5 Myr stars belong to one stellar population—they may originate from NGC 2060, the second most obvious site of recent star formation after R136—, our age distributions reveal at least two further groups of $\lesssim$ 2 and 5.3 Myr stars, whose formation sites remain unknown. In that picture, most of our sample stars would have formed in at least four distinct clusters or associations and moved to their currently observed positions. Future proper motion measurements in combination with our ages will help to trace back the formation sites of stars and to settle the question to which extent stars formed continuously in the whole 30 Dor region and to which extent in star clusters and associations.

5.7 Supplementary material

5.7.1 Discrepant stars

Two of our sample stars, VFTS-190 and 285, and one of the excluded stars, VFTS-102, cannot be reproduced by the stellar models because the fast rotation rates of these stars are not covered by the stellar models. In the following we discuss these stars in more detail to point out that this discrepancy is likely of physical nature and not just a problem of the stellar models.

VFTS-190 is a runaway star and a fast rotator with $v \sin i \approx 450 \, \mathrm{km \, s^{-1}}$. The observables place it in a sparsely populated region of our model parameter space because of its fast rotation. The resolution test and the posterior predictive checks conducted by BONNSAI fail because the stellar models are initially not rotating fast enough to model this star. It may be that this star was spun-up by mass transfer in a binary. This hypothesis is supported by its runaway nature and fast rotation. Mass transfer from a former companion

spun the star up and the supernova explosion ejected the star, releasing it as a runaway (Sana et al. in prep.).

VFTS-**285** is also a runaway and with a $v \sin i$ of about $600 \, \mathrm{km \, s^{-1}}$ one of the fastest spinning stars ever observed. As for VFTS-190, the resolution test and the posterior predictive checks fail. The stellar models of Brott et al. (2011a) and Köhler et al. (2014) are computed for $v_{\mathrm{ini}} \leq 600 \, \mathrm{km \, s^{-1}}$ and it is therefore impossible to reproduce this star. However, given its runaway nature and extreme rotation, the star may be a binary product that was spun up by mass transfer from a former companion or in a merger (de Mink et al. 2013; Sana et al. in prep.).

VFTS-**102** is yet another extremely fast-rotating runaway star ($v \sin i \approx 600 \, \mathrm{km \, s^{-1}}$) and Dufton et al. (2011) propose that it was spun up by mass transfer from the progenitor of the pulsar PSR J0537-6910. As with VFTS-190 and 285, our resolution test and the posterior predictive check fail because of a lack of stellar models with initial rotational velocities $\gtrsim 500$–$600 \, \mathrm{km \, s^{-1}}$.

Table 5.6: Derived observables, bolometric luminosity $\log L/lsun$, effective temperature T_{eff}, surface gravity $\log g$, projected rotational velocity $v\sin i$ and surface helium mass fraction Y_{obs}, from spectral fitting and stellar parameters, initial mass M_{ini}, initial rotational velocity v_{ini}, age, present-day mass M_{present}, radius R, surface helium mass fraction Y and surface nitrogen abundance $\log \mathrm{N/H} + 12$, determined from the stellar models of Brott et al. (2011a) and Köhler et al. (2014) using BONNSAI. The spectral types, SpT, are from Walborn et al. (2014) and the provided uncertainties are 1σ confidence levels if not stated otherwise.

VFTS No.	SpT	$\log L/L_\odot$	T_{eff} (K)	$\log g$ (cgs)	$v\sin i$ (km s^{-1})	Y_{obs}	M_{ini} (M$_\odot$)	v_{ini} (km s^{-1})	Age (Myr)	M_{present} (M$_\odot$)	R (R$_\odot$)	Y	$\log \mathrm{N/H} + 12$ (dex)
MK42	O2 If*	$6.60^{+0.10}_{-0.10}$	47315^{+1700}_{-1700}	−	< 200	$0.33^{+0.05}_{-0.05}$	$184.8^{+37.4}_{-30.3}$	120^{+85}_{-52}	$0.8^{+0.2}_{-0.2}$	$173.4^{+35.8}_{-29.1}$	$28.5^{+4.2}_{-3.9}$	...*	$8.22^{+0.26}_{-0.57}$ (68%) (2)
012	O9.5 IIIn	$4.79^{+0.10}_{-0.10}$	32400^{+612}_{-500}	$3.93^{+0.10}_{-0.11}$	306^{+31}_{-31}	−	$19.0^{+1.0}_{-1.0}$	310^{+48}_{-44}	$5.3^{+0.4}_{-0.6}$	$18.8^{+1.0}_{-0.9}$	$7.6^{+0.7}_{-0.8}$	...*	$7.70^{+0.21}_{-0.15}$ (68%) (1)
016	O2 III-If*	$6.16^{+0.10}_{-0.10}$	52000^{+944}_{-500}	$4.07^{+0.10}_{-0.10}$	104^{+30}_{-30}	−	$100.0^{+13.9}_{-10.6}$	110^{+57}_{-40}	$0.5^{+0.1}_{-0.2}$	$97.2^{+14.4}_{-9.0}$	$14.3^{+1.4}_{-1.4}$	...*	$6.89^{+0.44}_{-0.02}$ (68%) (1)
021	O9.5 IV	$4.86^{+0.14}_{-0.14}$	33840^{+880}_{-880}	$3.90^{+0.10}_{-0.10}$	40^{+30}_{-30}	−	$20.0^{+1.6}_{-1.5}$	70^{+39}_{-38}	$5.0^{+0.5}_{-0.6}$	$19.6^{+1.7}_{-1.2}$	$7.8^{+0.9}_{-0.9}$	...*	$6.89^{+0.04}_{-0.01}$ (68%) (3)
046	O9.7 II((n))	$5.10^{+0.10}_{-0.10}$	28850^{+842}_{-689}	$3.33^{+0.10}_{-0.10}$	172^{+30}_{-30}	−	$22.8^{+1.9}_{-1.9}$	180^{+52}_{-42}	$6.2^{+0.5}_{-0.5}$	$23.4^{+0.6}_{-2.9}$	$14.8^{+1.8}_{-1.3}$	...*	$7.37^{+0.30}_{-0.11}$ (68%) (1)
065	O8 V(n)	$4.80^{+0.15}_{-0.15}$	37050^{+1079}_{-1079}	$4.06^{+0.16}_{-0.16}$	165^{+30}_{-30}	−	$22.2^{+1.8}_{-1.6}$	170^{+48}_{-46}	$2.4^{+0.9}_{-1.4}$	$22.2^{+1.7}_{-1.6}$	$6.2^{+0.9}_{-0.5}$	...*	$6.89^{+0.20}_{-0.01}$ (68%) (3)
067	O9.5 Vz	$4.56^{+0.17}_{-0.17}$	35200^{+1100}_{-1100}	$4.12^{+0.19}_{-0.19}$	40^{+30}_{-30}	−	$18.6^{+1.5}_{-1.4}$	70^{+38}_{-38}	$2.0^{+1.2}_{-1.4}$	$18.6^{+1.5}_{-1.4}$	$5.5^{+0.6}_{-0.6}$	...*	$6.89^{+0.01}_{-0.01}$ (71%) (3)
072	O2 V-III(n)((f*))	$6.07^{+0.13}_{-0.13}$	54000^{+1500}_{-1500}	$4.00^{+0.10}_{-0.10}$	185^{+30}_{-30}	−	$80.0^{+31.7}_{-14.4}$	460^{+0}_{-0} a	$0.4^{+1.9}_{-0.4}$	$94.0^{+17.2}_{-35.6}$	$13.4^{+2.0}_{-1.9}$	...*	$8.98^{+0.05}_{-0.79}$ (68%) (3)
074	O9 Vn	$4.69^{+0.15}_{-0.15}$	35140^{+1349}_{-1349}	$4.18^{+0.21}_{-0.21}$	265^{+30}_{-30}	−	$19.6^{+1.8}_{-1.4}$	270^{+61}_{-45}	$2.1^{+1.2}_{-1.7}$	$19.6^{+1.8}_{-1.4}$	$6.0^{+0.6}_{-0.6}$	...*	$6.90^{+0.61}_{-0.01}$ (68%) (3)
076	O9.2 III	$5.09^{+0.10}_{-0.10}$	32500^{+663}_{-500}	$3.59^{+0.10}_{-0.10}$	86^{+30}_{-30}	−	$23.6^{+1.9}_{-1.6}$	100^{+41}_{-37}	$5.3^{+0.3}_{-0.3}$	$23.2^{+1.9}_{-1.4}$	$11.3^{+1.3}_{-1.0}$	...*	$6.93^{+0.14}_{-0.05}$ (68%) (1)
089	O6.5 V((f))z Nstr	$5.09^{+0.18}_{-0.18}$	39700^{+700}_{-700}	$4.02^{+0.12}_{-0.12}$	50^{+30}_{-30}	−	$28.0^{+2.6}_{-1.9}$	70^{+45}_{-32}	$2.5^{+0.4}_{-0.8}$	$28.0^{+2.2}_{-2.0}$	$7.5^{+1.2}_{-0.8}$	...*	$6.89^{+0.04}_{-0.01}$ (68%) (3)
091	O9.5 IIIn	$4.82^{+0.10}_{-0.10}$	32850^{+510}_{-663}	$3.92^{+0.10}_{-0.10}$	306^{+30}_{-30}	−	$19.4^{+1.1}_{-1.0}$	310^{+47}_{-43}	$5.1^{+0.5}_{-0.5}$	$19.2^{+1.1}_{-0.9}$	$7.8^{+0.7}_{-0.7}$	...*	$7.72^{+0.19}_{-0.16}$ (68%) (1)
103	O8.5 III((f))	$5.23^{+0.10}_{-0.10}$	34700^{+500}_{-500}	$3.89^{+0.10}_{-0.10}$	112^{+30}_{-30}	−	$25.2^{+2.0}_{-1.6}$	120^{+44}_{-39}	$4.4^{+0.2}_{-0.2}$	$24.8^{+1.8}_{-1.5}$	$10.2^{+1.1}_{-0.9}$	...*	$6.93^{+0.24}_{-0.05}$ (68%) (1)
108	WN7h	$5.70^{+0.10}_{-0.10}$	53088^{+1907}_{-1907}	−	< 200	$0.78^{+0.05}_{-0.05}$	$35.0^{+1.6}_{-6.3}$	500^{+30}_{-18}	$6.3^{+1.2}_{-0.8}$	$26.2^{+4.0}_{-3.3}$	$7.7^{+1.5}_{-0.8}$	$0.81^{+0.02}_{-0.04}$	$9.06^{+0.03}_{-0.10}$ (68%) (2)
110	O6 V((n))z	$5.40^{+0.20}_{-0.20}$	39850^{+1049}_{-1049}	$3.86^{+0.10}_{-0.10}$	175^{+30}_{-30}	−	$34.4^{+5.0}_{-4.0}$	180^{+52}_{-43}	$2.7^{+0.3}_{-0.3}$	$33.4^{+4.8}_{-3.5}$	$10.6^{+1.5}_{-1.5}$	...*	$7.35^{+0.35}_{-0.23}$ (68%) (3)
117	O6: Vz	$5.02^{+0.26}_{-0.26}$	41300^{+1500}_{-1500}	$4.14^{+0.16}_{-0.16}$	75^{+30}_{-30}	−	$29.2^{+3.7}_{-3.2}$	90^{+41}_{-37}	$1.3^{+0.7}_{-1.0}$	$29.0^{+3.7}_{-3.1}$	$6.9^{+1.2}_{-0.6}$	...*	$6.89^{+0.04}_{-0.01}$ (69%) (3)
123	O6.5 Vz	$4.99^{+0.13}_{-0.13}$	40400^{+680}_{-680}	$4.10^{+0.12}_{-0.12}$	65^{+30}_{-30}	−	$28.2^{+1.6}_{-1.6}$	80^{+44}_{-33}	$1.4^{+0.6}_{-0.9}$	$28.0^{+1.6}_{-1.5}$	$6.9^{+0.7}_{-0.6}$	...*	$6.89^{+0.03}_{-0.02}$ (70%) (3)
130	O8.5 V((n))	$5.06^{+0.12}_{-0.12}$	36500^{+1330}_{-1330}	$4.09^{+0.19}_{-0.19}$	170^{+30}_{-30}	−	$24.2^{+2.1}_{-1.9}$	170^{+54}_{-41}	$3.4^{+0.7}_{-1.0}$	$24.0^{+2.1}_{-1.8}$	$7.6^{+1.1}_{-1.0}$	...*	$6.90^{+0.40}_{-0.01}$ (68%) (3)
132	O9.5 Vz	$4.71^{+0.13}_{-0.13}$	35640^{+680}_{-680}	$4.18^{+0.10}_{-0.10}$	40^{+30}_{-30}	−	$19.8^{+1.1}_{-0.9}$	70^{+39}_{-38}	$2.3^{+0.9}_{-1.2}$	$19.8^{+1.1}_{-0.9}$	$5.7^{+0.6}_{-0.4}$	...*	$6.90^{+0.01}_{-0.01}$ (68%) (3)
149	O9.5 V	$4.68^{+0.15}_{-0.15}$	34995^{+1395}_{-1395}	$4.12^{+0.24}_{-0.24}$	125^{+30}_{-30}	−	$19.0^{+1.7}_{-1.5}$	130^{+44}_{-40}	$2.9^{+1.3}_{-1.9}$	$19.0^{+1.7}_{-1.5}$	$5.8^{+0.8}_{-0.6}$	...*	$6.90^{+0.06}_{-0.01}$ (68%) (3)
165	O9.7 Iab	$5.49^{+0.10}_{-0.10}$	28650^{+765}_{-765}	$3.26^{+0.10}_{-0.10}$	75^{+30}_{-30}	−	$31.2^{+3.6}_{-3.0}$	100^{+40}_{-41}	$4.7^{+0.4}_{-0.4}$	$29.8^{+3.5}_{-2.3}$	$21.0^{+2.9}_{-1.8}$	...*	$6.99^{+0.16}_{-0.10}$ (68%) (1)
168	O8.5 Vz	$4.92^{+0.11}_{-0.11}$	37270^{+510}_{-510}	$4.02^{+0.10}_{-0.10}$	40^{+30}_{-30}	−	$23.6^{+1.2}_{-1.2}$	70^{+38}_{-38}	$3.0^{+0.5}_{-0.7}$	$23.4^{+1.2}_{-1.1}$	$7.0^{+0.8}_{-0.6}$	...*	$6.89^{+0.02}_{-0.02}$ (70%) (3)
169	O2.5 V(n)((f*))	$5.91^{+0.13}_{-0.13}$	47000^{+1500}_{-1500}	$3.90^{+0.10}_{-0.10}$	200^{+30}_{-30}	−	$64.8^{+12.0}_{-8.6}$	210^{+71}_{-47}	$1.4^{+0.3}_{-0.3}$	$62.0^{+11.2}_{-7.9}$	$13.7^{+1.7}_{-1.8}$	...*	$7.98^{+0.31}_{-0.40}$ (68%) (3)
185	O7.5 III((f))	$5.31^{+0.10}_{-0.10}$	35050^{+500}_{-500}	$3.51^{+0.10}_{-0.10}$	124^{+30}_{-30}	−	$30.8^{+3.1}_{-2.4}$	130^{+49}_{-38}	$4.0^{+0.2}_{-0.3}$	$30.4^{+2.3}_{-2.6}$	$13.1^{+1.6}_{-1.1}$	...*	$6.95^{+0.40}_{-0.03}$ (68%) (1)
190	O7 Vnn((f))p	$5.28^{+0.10}_{-0.10}$	35700^{+500}_{-500}	$3.45^{+0.10}_{-0.10}$	444^{+44}_{-44}	−	−	−	−	−	−	−	− (1)
210	O9.7 II-III((n))	$4.61^{+0.10}_{-0.10}$	32300^{+500}_{-536}	$4.05^{+0.10}_{-0.10}$	166^{+30}_{-30}	−	$16.8^{+0.8}_{-0.8}$	170^{+48}_{-44}	$5.1^{+0.7}_{-0.9}$	$16.8^{+0.8}_{-0.8}$	$6.2^{+0.6}_{-0.5}$	...*	$6.92^{+0.25}_{-0.03}$ (68%) (1)
216	O4 V((fc))	$5.83^{+0.13}_{-0.13}$	43000^{+1500}_{-1500}	$3.80^{+0.10}_{-0.10}$	100^{+30}_{-30}	−	$55.4^{+9.0}_{-7.5}$	110^{+48}_{-48}	$2.0^{+0.3}_{-0.2}$	$52.8^{+8.3}_{-6.6}$	$14.4^{+1.9}_{-1.8}$	...*	$6.99^{+0.47}_{-0.10}$ (73%) (3)
249	O8 Vn	$4.78^{+0.14}_{-0.14}$	36480^{+759}_{-759}	$4.04^{+0.11}_{-0.11}$	300^{+30}_{-30}	−	$22.4^{+1.4}_{-1.4}$	300^{+74}_{-43}	$2.7^{+0.9}_{-1.3}$	$22.2^{+1.4}_{-1.3}$	$6.4^{+0.8}_{-0.5}$	...*	$7.63^{+0.41}_{-0.39}$ (68%) (3)
250	O9.2 V((n))	$4.76^{+0.12}_{-0.12}$	35415^{+805}_{-805}	$4.12^{+0.15}_{-0.15}$	155^{+30}_{-30}	−	$20.2^{+1.3}_{-1.1}$	160^{+47}_{-45}	$3.0^{+0.9}_{-1.4}$	$20.2^{+1.2}_{-1.1}$	$6.1^{+0.7}_{-0.6}$	...*	$6.90^{+0.16}_{-0.01}$ (68%) (3)
251	O9.5 IV	$4.72^{+0.11}_{-0.11}$	33710^{+559}_{-559}	$4.01^{+0.10}_{-0.10}$	40^{+30}_{-30}	−	$18.4^{+1.1}_{-0.8}$	70^{+39}_{-38}	$4.7^{+0.5}_{-0.8}$	$18.6^{+0.8}_{-0.9}$	$6.7^{+0.6}_{-0.7}$	...*	$6.89^{+0.03}_{-0.01}$ (68%) (3)

VFTS No.	SpT	$\log L/L_\odot$	T_{eff} (K)	$\log g$ (cgs)	$v \sin i$ (km s^{-1})	Y_{obs}	M_{ini} (M$_\odot$)	v_{ini} (km s^{-1})	Age (Myr)	M_{present} (M$_\odot$)	R (R$_\odot$)	Y	$\log \mathrm{N/H} + 12$ (dex)
252	O8.5 Vz	$4.73^{+0.12}_{-0.12}$	36955^{+500}_{-500}	$4.21^{+0.10}_{-0.10}$	100^{+30}_{-30}	–	$21.6^{+1.0}_{-0.8}$	110^{+40}_{-39}	$1.1^{+0.8}_{-0.8}$	$21.6^{+1.0}_{-0.8}$	$5.8^{+0.5}_{-0.3}$	$\cdots$ *	$6.89^{+0.02}_{-0.02}$ (70%) (3)
266	O8 V((f))z	$5.05^{+0.12}_{-0.12}$	38045^{+500}_{-500}	$4.01^{+0.10}_{-0.10}$	40^{+30}_{-30}	–	$25.6^{+1.7}_{-1.4}$	70^{+39}_{-38}	$3.0^{+0.3}_{-0.6}$	$25.4^{+1.6}_{-1.3}$	$7.6^{+0.9}_{-0.7}$	$\cdots$ *	$6.90^{+0.03}_{-0.02}$ (69%) (3)
280	O9 V((n))	$4.88^{+0.12}_{-0.12}$	34360^{+560}_{-560}	$3.82^{+0.10}_{-0.10}$	150^{+30}_{-30}	–	$21.4^{+1.6}_{-1.3}$	150^{+48}_{-39}	$4.7^{+0.3}_{-0.3}$	$21.2^{+1.6}_{-1.3}$	$8.3^{+0.9}_{-0.8}$	$\cdots$ *	$6.92^{+0.34}_{-0.02}$ (68%) (3)
285	O7.5 Vnnn	$4.77^{+0.20}_{-0.20}$	35280^{+919}_{-919}	$3.63^{+0.10}_{-0.10}$	600^{+60}_{-60}	–	–	–	–	–	–	–	– (3)
290	O9.5 IV	$4.76^{+0.10}_{-0.10}$	33950^{+500}_{-500}	$3.99^{+0.10}_{-0.10}$	40^{+30}_{-30}	–	$19.0^{+1.0}_{-0.8}$	70^{+39}_{-38}	$4.7^{+0.5}_{-0.6}$	$19.2^{+0.7}_{-1.0}$	$6.9^{+0.7}_{-0.6}$	$\cdots$ *	$6.91^{+0.02}_{-0.02}$ (70%) (3)
306	O8.5 II((f))	$5.42^{+0.10}_{-0.10}$	32400^{+500}_{-500}	$3.43^{+0.10}_{-0.10}$	88^{+30}_{-30}	–	$31.4^{+3.3}_{-2.7}$	100^{+48}_{-33}	$4.3^{+0.3}_{-0.3}$	$30.8^{+2.5}_{-2.9}$	$16.1^{+2.0}_{-1.5}$	$\cdots$	$6.96^{+0.23}_{-0.06}$ (68%) (1)
356	O6: V(n)z	$5.14^{+0.20}_{-0.20}$	39250^{+1250}_{-1250}	$3.99^{+0.13}_{-0.13}$	215^{+30}_{-30}	–	$28.2^{+3.2}_{-2.9}$	220^{+58}_{-46}	$2.6^{+0.6}_{-0.9}$	$28.0^{+3.0}_{-2.9}$	$8.0^{+1.1}_{-1.3}$	$\cdots$ *	$7.56^{+0.22}_{-0.46}$ (68%) (3)
361	O8.5 V	$5.27^{+0.15}_{-0.15}$	36895^{+674}_{-674}	$4.07^{+0.10}_{-0.10}$	70^{+30}_{-30}	–	$25.2^{+2.2}_{-1.8}$	80^{+48}_{-30}	$3.5^{+0.3}_{-0.5}$	$25.2^{+1.8}_{-2.0}$	$8.2^{+1.1}_{-0.9}$	$\cdots$ *	$6.90^{+0.08}_{-0.01}$ (68%) (3)
369	O9.7 V	$4.67^{+0.14}_{-0.14}$	33360^{+1200}_{-1200}	$4.10^{+0.18}_{-0.18}$	40^{+30}_{-30}	–	$17.6^{+1.4}_{-1.3}$	70^{+39}_{-38}	$4.4^{+1.2}_{-1.8}$	$17.6^{+1.4}_{-1.3}$	$5.8^{+0.9}_{-0.7}$	$\cdots$ *	$6.90^{+0.01}_{-0.01}$ (70%) (3)
380	O6-7 Vz	$4.92^{+0.15}_{-0.15}$	39120^{+680}_{-680}	$4.13^{+0.10}_{-0.10}$	65^{+30}_{-30}	–	$25.6^{+1.7}_{-1.3}$	80^{+44}_{-33}	$1.7^{+0.7}_{-0.9}$	$25.6^{+1.5}_{-1.3}$	$6.6^{+0.7}_{-0.5}$	$\cdots$ *	$6.91^{+0.02}_{-0.01}$ (71%) (3)
382	O4-5 V((fc))z	$5.31^{+0.13}_{-0.13}$	40000^{+1500}_{-1500}	$3.80^{+0.10}_{-0.10}$	75^{+30}_{-30}	–	$32.8^{+4.0}_{-3.3}$	90^{+42}_{-36}	$3.0^{+0.4}_{-0.4}$	$32.2^{+3.7}_{-3.1}$	$10.3^{+1.4}_{-1.1}$	$\cdots$ *	$6.90^{+0.13}_{-0.01}$ (68%) (3)
392	O6-7 V((f))z	$5.11^{+0.23}_{-0.23}$	37560^{+840}_{-840}	$3.87^{+0.10}_{-0.10}$	40^{+30}_{-30}	–	$27.0^{+3.3}_{-2.6}$	70^{+39}_{-38}	$3.4^{+0.3}_{-0.3}$	$26.2^{+3.6}_{-2.0}$	$9.2^{+1.3}_{-1.4}$	$\cdots$ *	$6.91^{+0.04}_{-0.01}$ (69%) (3)
406	O6 Vnn	$5.55^{+0.10}_{-0.10}$	37800^{+500}_{-561}	$3.54^{+0.10}_{-0.10}$	356^{+36}_{-36}	–	$38.6^{+3.3}_{-7.3}$	380^{+46}_{-46}	$3.3^{+1.6}_{-0.4}$	$37.4^{+3.4}_{-7.2}$	$13.8^{+1.7}_{-1.1}$	$0.27^{+0.20}_{-0.02}$ [b]	$8.47^{+0.26}_{-0.40}$ (91%) (1)
418	O5 V((n))((fc))z	$5.24^{+0.18}_{-0.18}$	43220^{+1740}_{-1740}	$4.09^{+0.13}_{-0.13}$	135^{+30}_{-30}	–	$34.2^{+4.6}_{-3.9}$	140^{+48}_{-43}	$1.4^{+0.6}_{-0.9}$	$33.8^{+4.6}_{-3.6}$	$7.8^{+1.1}_{-0.7}$	$\cdots$ *	$6.90^{+0.21}_{-0.01}$ (68%) (3)
419	O9: V(n)	$5.07^{+0.24}_{-0.24}$	33100^{+899}_{-899}	$3.61^{+0.10}_{-0.10}$	145^{+30}_{-30}	–	$24.4^{+3.5}_{-2.9}$	150^{+48}_{-41}	$4.9^{+0.6}_{-0.5}$	$25.0^{+2.3}_{-3.6}$	$11.3^{+2.2}_{-1.4}$	$\cdots$ *	$7.33^{+0.08}_{-0.39}$ (70%) (3)
427	WN8(h)	$6.10^{+0.10}_{-0.10}$	41687^{+1497}_{-1497}	–	< 200	$0.93^{+0.05}_{-0.05}$	$90.4^{+9.5}_{-17.9}$	410^{+18}_{-37}	$3.1^{+0.3}_{-0.3}$ [c]	$53.2^{+12.3}_{-2.1}$ [d]	$27.6^{+2.9}_{-4.6}$	$0.84^{+0.04}_{-0.04}$	$9.09^{+0.22}_{-0.08}$ (68%) (2)
435	O7-8 V	$5.12^{+0.13}_{-0.13}$	36000^{+1500}_{-1500}	$3.90^{+0.10}_{-0.10}$	80^{+30}_{-30}	–	$24.6^{+2.7}_{-2.1}$	90^{+45}_{-33}	$3.9^{+0.6}_{-0.6}$	$24.4^{+2.5}_{-1.5}$	$8.9^{+1.1}_{-0.9}$	$\cdots$ *	$6.91^{+0.11}_{-0.01}$ (68%) (3)
436	O7-8 V	$4.87^{+0.13}_{-0.13}$	35000^{+1500}_{-1500}	$3.90^{+0.10}_{-0.10}$	60^{+30}_{-30}	–	$20.8^{+1.9}_{-1.8}$	80^{+40}_{-36}	$4.6^{+0.8}_{-0.8}$	$20.4^{+2.1}_{-1.5}$	$7.8^{+0.9}_{-0.8}$	$\cdots$ *	$6.90^{+0.04}_{-0.01}$ (68%) (3)
457	O3.5 If*/WN7	$6.20^{+0.10}_{-0.10}$	39811^{+1430}_{-1430}	–	< 200	$0.40^{+0.05}_{-0.01}$	$78.6^{+18.9}_{-12.3}$	320^{+23}_{-16}	$2.4^{+0.2}_{-0.4}$	$68.6^{+16.7}_{-11.6}$ [e]	$26.0^{+3.8}_{-3.7}$	$0.41^{+0.05}_{-0.03}$ [f]	$8.52^{+0.05}_{-0.04}$ (79%) (2)
466	O9 III	$5.24^{+0.10}_{-0.10}$	34250^{+500}_{-500}	$3.72^{+0.10}_{-0.10}$	86^{+30}_{-30}	–	$26.4^{+2.2}_{-1.9}$	100^{+41}_{-38}	$4.5^{+0.2}_{-0.2}$	$25.8^{+2.4}_{-1.5}$	$11.4^{+1.2}_{-1.0}$	$\cdots$ *	$6.95^{+0.15}_{-0.05}$ (68%) (1)
470	O6: V((f))z	$4.97^{+0.18}_{-0.18}$	39330^{+630}_{-630}	$3.93^{+0.10}_{-0.10}$	75^{+30}_{-30}	–	$28.0^{+2.6}_{-1.9}$	90^{+41}_{-37}	$2.8^{+0.3}_{-0.6}$	$27.8^{+2.4}_{-1.8}$	$8.1^{+1.1}_{-0.9}$	$\cdots$ *	$6.90^{+0.08}_{-0.01}$ (68%) (3)
472	O6 Vz	$5.01^{+0.15}_{-0.15}$	40365^{+855}_{-855}	$4.12^{+0.12}_{-0.12}$	40^{+30}_{-30}	–	$28.0^{+2.0}_{-1.8}$	70^{+39}_{-38}	$1.5^{+0.6}_{-0.9}$	$27.8^{+2.1}_{-1.7}$	$6.9^{+0.8}_{-0.6}$	$\cdots$ *	$6.91^{+0.02}_{-0.01}$ (69%) (3)
482	O2.5 If*/WN6	$6.40^{+0.10}_{-0.10}$	42170^{+1515}_{-1515}	–	< 200	$0.33^{+0.05}_{-0.05}$	$124.4^{+24.9}_{-19.2}$	100^{+102}_{-36}	$1.3^{+0.2}_{-0.2}$	$113.8^{+22.8}_{-17.7}$	$28.1^{+4.4}_{-3.7}$	$\cdots$ *	$8.23^{+0.02}_{-1.06}$ (74%) (2)
483	O9 V	$4.59^{+0.15}_{-0.13}$ †	33655^{+854}_{-854}	$4.09^{+0.11}_{-0.11}$	40^{+30}_{-30}	–	$17.4^{+1.6}_{-1.3}$	70^{+38}_{-38}	$4.3^{+0.8}_{-1.7}$	$17.4^{+1.6}_{-1.3}$	$5.8^{+0.9}_{-0.8}$	$\cdots$ *	$6.91^{+0.01}_{-0.01}$ (70%) (3)
484	O6-7 V((n))	$5.41^{+0.14}_{-0.14}$	35680^{+680}_{-680}	$3.67^{+0.10}_{-0.10}$	120^{+30}_{-30}	–	$31.6^{+3.9}_{-3.3}$	130^{+45}_{-40}	$3.8^{+0.3}_{-0.3}$	$31.0^{+3.4}_{-3.1}$	$12.7^{+1.9}_{-1.4}$	$\cdots$ *	$6.96^{+0.49}_{-0.06}$ (81%) (3)
488	O6 V((f))z	$5.33^{+0.25}_{-0.25}$	40700^{+659}_{-659}	$3.87^{+0.10}_{-0.10}$	55^{+30}_{-30}	–	$35.4^{+5.4}_{-3.8}$	80^{+39}_{-38}	$2.5^{+0.2}_{-0.2}$	$34.6^{+5.0}_{-3.3}$	$10.3^{+1.7}_{-1.5}$	$\cdots$ *	$6.90^{+0.08}_{-0.01}$ (68%) (3)
491	O6 V((fc))	$5.43^{+0.16}_{-0.16}$	40360^{+799}_{-799}	$3.84^{+0.10}_{-0.10}$	50^{+30}_{-30}	–	$36.4^{+4.7}_{-3.7}$	70^{+46}_{-31}	$2.6^{+0.2}_{-0.2}$	$35.4^{+4.5}_{-3.3}$	$10.9^{+1.5}_{-1.4}$	$\cdots$ *	$6.90^{+0.07}_{-0.01}$ (68%) (3)
493	O9 V	$5.06^{+0.16}_{-0.16}$	37050^{+950}_{-950}	$4.28^{+0.10}_{-0.10}$	200^{+30}_{-30}	–	$23.4^{+1.6}_{-1.6}$	200^{+64}_{-42}	$1.5^{+0.8}_{-1.0}$	$23.2^{+1.8}_{-1.4}$	$6.3^{+0.6}_{-0.5}$	$\cdots$ *	$6.90^{+0.31}_{-0.01}$ (68%) (3)
498	O9.5 V	$4.88^{+0.14}_{-0.14}$	33230^{+810}_{-810}	$4.12^{+0.15}_{-0.15}$	40^{+30}_{-30}	–	$18.6^{+1.4}_{-1.3}$	70^{+39}_{-38}	$5.0^{+0.7}_{-0.9}$	$18.6^{+1.3}_{-1.2}$	$6.9^{+0.9}_{-1.0}$	$\cdots$ *	$6.90^{+0.02}_{-0.01}$ (69%) (3)
505	O9.5 V-III	$4.66^{+0.13}_{-0.14}$	34040^{+680}_{-680}	$4.30^{+0.10}_{-0.10}$	100^{+30}_{-30}	–	$17.8^{+0.9}_{-0.8}$	110^{+41}_{-39}	$1.8^{+1.1}_{-1.2}$	$17.8^{+0.9}_{-0.8}$	$5.3^{+0.5}_{-0.4}$	$\cdots$ *	$6.89^{+0.02}_{-0.01}$ (70%) (3)
513	O6-7 II(f)	$4.93^{+0.10}_{-0.10}$	36600^{+500}_{-500}	$4.16^{+0.10}_{-0.10}$	114^{+30}_{-30}	–	$22.4^{+1.1}_{-1.0}$	120^{+45}_{-39}	$2.8^{+0.6}_{-0.9}$	$22.4^{+0.9}_{-1.0}$	$6.6^{+0.7}_{-0.5}$	$\cdots$ *	$6.89^{+0.08}_{-0.01}$ (69%) (1)
517	O9.5 V-III((n))	$5.09^{+0.10}_{-0.10}$	33000^{+500}_{-500}	$4.01^{+0.10}_{-0.10}$	120^{+30}_{-30}	–	$21.0^{+1.5}_{-1.2}$	120^{+51}_{-34}	$5.2^{+0.3}_{-0.3}$	$20.8^{+1.6}_{-1.4}$	$8.9^{+0.9}_{-0.8}$	$\cdots$ *	$6.92^{+0.24}_{-0.03}$ (68%) (3)
536	O6 Vz	$5.19^{+0.17}_{-0.17}$	41500^{+1540}_{-1540}	$4.24^{+0.15}_{-0.15}$	40^{+30}_{-30}	–	$30.4^{+3.5}_{-2.8}$	70^{+39}_{-38}	$0.9^{+0.7}_{-0.8}$	$30.2^{+3.5}_{-2.7}$	$7.1^{+0.9}_{-0.6}$	$\cdots$ *	$6.89^{+0.02}_{-0.01}$ (69%) (3)
537	O5 V((fc))z	$5.19^{+0.13}_{-0.13}$	39000^{+1500}_{-1500}	$3.80^{+0.10}_{-0.10}$	60^{+30}_{-30}	–	$29.4^{+3.3}_{-2.9}$	80^{+41}_{-36}	$3.3^{+0.5}_{-0.5}$	$29.0^{+3.0}_{-2.8}$	$9.8^{+1.2}_{-1.1}$	$\cdots$ *	$6.90^{+0.07}_{-0.01}$ (68%) (3)
542	O2 If*/WN5	$6.20^{+0.10}_{-0.10}$	44668^{+2006}_{-2006}	–	< 200	$0.47^{+0.05}_{-0.05}$	$81.4^{+17.3}_{-13.4}$	340^{+16}_{-31}	$2.2^{+0.3}_{-0.4}$	$71.4^{+15.8}_{-11.4}$	$20.3^{+3.2}_{-3.1}$	$0.44^{+0.06}_{-0.04}$	$8.57^{+0.07}_{-0.06}$ (68%) (2)

Table 5.6: continued.

VFTS No.	SpT	$\log L/L_\odot$	$T_{\rm eff}$ (K)	$\log g$ (cgs)	$v \sin i$ (km s^{-1})	$Y_{\rm obs}$	$M_{\rm ini}$ (M$_\odot$)	$v_{\rm ini}$ (km s^{-1})	Age (Myr)	$M_{\rm present}$ (M$_\odot$)	R (R$_\odot$)	Y	$\log {\rm N/H} + 12$ (dex)
545	O2 If*/WN5	$6.30^{+0.10}_{-0.10}$	47315^{+1700}_{-1700}	–	< 200	$0.25^{+0.05}_{-0.01}$	$109.8^{+19.2}_{-15.6}$	100^{+66}_{-49}	$1.1^{+0.2}_{-0.2}$	$103.2^{+18.2}_{-14.0}$	$19.4^{+3.1}_{-2.4}$	... *	$6.91^{+0.70}_{-0.02}$ (68%) (2)
546	O8-9 III:((n))	$4.97^{+0.10}_{-0.10}$	32100^{+500}_{-663}	$3.51^{+0.10}_{-0.10}$	96^{+30}_{-30}	–	$22.0^{+1.7}_{-1.5}$	110^{+38}_{-40}	$5.7^{+0.4}_{-0.3}$	$21.8^{+1.5}_{-1.5}$	$11.1^{+1.2}_{-1.0}$	... *	$6.94^{+0.17}_{-0.06}$ (68%) (1)
549	O6.5 Vz	$5.09^{+0.15}_{-0.15}$	39760^{+1159}_{-1159}	$4.04^{+0.16}_{-0.16}$	110^{+30}_{-30}	–	$27.8^{+2.6}_{-2.3}$	120^{+41}_{-42}	$2.2^{+0.6}_{-1.1}$	$27.6^{+2.5}_{-2.2}$	$7.3^{+1.0}_{-0.8}$	... *	$6.91^{+0.11}_{-0.01}$ (68%) (3)
550	O5 V((fc))z	$5.20^{+0.13}_{-0.13}$	39000^{+1500}_{-1500}	$3.80^{+0.10}_{-0.10}$	50^{+30}_{-30}	–	$29.6^{+3.3}_{-3.0}$	70^{+45}_{-32}	$3.3^{+0.5}_{-0.4}$	$29.0^{+3.2}_{-2.7}$	$9.9^{+1.2}_{-1.1}$	... *	$6.90^{+0.06}_{-0.01}$ (68%) (3)
554	O9.7 V	$4.51^{+0.09}_{-0.10}$ †34130^{+770}_{-770}	$4.30^{+0.10}_{-0.10}$	45^{+30}_{-30}	–	$17.4^{+1.0}_{-1.1}$	70^{+40}_{-35}	$0.4^{+1.7}_{-0.4}$	$17.4^{+1.0}_{-1.1}$	$5.0^{+0.5}_{-0.3}$	... *	$6.90^{+0.01}_{-0.01}$ (69%) (3)
560	O9.5 V	$4.52^{+0.18}_{-0.18}$	33565^{+1154}_{-1154}	$4.20^{+0.16}_{-0.16}$	40^{+30}_{-30}	–	$16.8^{+1.3}_{-1.3}$	70^{+38}_{-38}	$2.6^{+1.5}_{-1.9}$	$16.8^{+1.3}_{-1.3}$	$5.2^{+0.7}_{-0.5}$	... *	$6.90^{+0.01}_{-0.01}$ (70%) (3)
564	O6-8 V((f))	$5.33^{+0.13}_{-0.13}$	37000^{+1500}_{-1500}	$4.10^{+0.10}_{-0.10}$	40^{+30}_{-30}	–	$27.8^{+2.9}_{-2.5}$	70^{+40}_{-38}	$3.0^{+0.5}_{-0.6}$	$27.6^{+2.6}_{-2.5}$	$8.4^{+1.1}_{-0.9}$	... *	$6.89^{+0.04}_{-0.01}$ (68%) (3)
566	O3 III(f*)	$5.66^{+0.10}_{-0.10}$	39400^{+500}_{-500}	$3.72^{+0.10}_{-0.10}$	118^{+30}_{-30}	–	$44.2^{+4.9}_{-4.2}$	130^{+46}_{-41}	$2.7^{+0.1}_{-0.2}$	$42.6^{+4.1}_{-4.0}$	$14.5^{+1.3}_{-1.8}$	... *	$6.99^{+0.47}_{-0.07}$ (70%) (1)
577	O6 V((fc))z	$5.21^{+0.13}_{-0.13}$	42000^{+1500}_{-1500}	$4.00^{+0.10}_{-0.10}$	40^{+30}_{-30}	–	$32.2^{+3.4}_{-2.9}$	70^{+39}_{-38}	$2.1^{+0.5}_{-0.7}$	$32.0^{+3.2}_{-2.9}$	$8.3^{+1.0}_{-0.8}$	... *	$6.90^{+0.02}_{-0.01}$ (68%) (3)
581	O4-5 V((fc))	$5.38^{+0.13}_{-0.13}$	40000^{+1500}_{-1500}	$3.70^{+0.10}_{-0.10}$	70^{+30}_{-30}	–	$35.4^{+4.8}_{-3.8}$	90^{+40}_{-39}	$3.0^{+0.4}_{-0.3}$	$34.2^{+4.7}_{-3.2}$	$11.8^{+1.4}_{-1.4}$	... *	$6.91^{+0.14}_{-0.01}$ (68%) (3)
582	O9.5 V((n))	$4.58^{+0.10}_{-0.09}$ †34950^{+750}_{-750}	$4.29^{+0.10}_{-0.10}$	115^{+30}_{-30}	–	$18.6^{+1.2}_{-1.2}$	120^{+43}_{-37}	$0.4^{+1.5}_{-0.4}$	$18.6^{+1.2}_{-1.2}$	$5.2^{+0.5}_{-0.3}$	... *	$6.89^{+0.02}_{-0.01}$ (70%) (3)
586	O4 V((n))((fc))z	$5.42^{+0.13}_{-0.13}$	45000^{+1500}_{-1500}	$4.00^{+0.10}_{-0.10}$	100^{+30}_{-30}	–	$41.4^{+4.8}_{-4.2}$	110^{+44}_{-39}	$1.5^{+0.4}_{-0.6}$	$40.8^{+4.6}_{-4.0}$	$9.2^{+1.2}_{-0.9}$	... *	$6.89^{+0.17}_{-0.01}$ (68%) (3)
592	O9.5 Vn	$4.69^{+0.13}_{-0.13}$	33560^{+1000}_{-1000}	$4.25^{+0.13}_{-0.13}$	295^{+30}_{-30}	–	$18.4^{+1.3}_{-1.1}$	300^{+63}_{-44}	$2.5^{+1.2}_{-1.6}$	$18.4^{+1.3}_{-1.0}$	$5.8^{+0.9}_{-0.6}$	... *	$6.91^{+0.68}_{-0.04}$ (68%) (3)
597	O8-9 V(n)	$4.87^{+0.14}_{-0.14}$	35400^{+720}_{-720}	$3.90^{+0.11}_{-0.11}$	210^{+30}_{-30}	–	$22.0^{+1.7}_{-1.5}$	210^{+57}_{-42}	$4.0^{+0.5}_{-0.6}$	$21.8^{+1.7}_{-1.4}$	$7.7^{+0.9}_{-0.9}$	... *	$7.38^{+0.20}_{-0.28}$ (68%) (3)
601	O5-6 V((n))z	$5.55^{+0.18}_{-0.18}$	40275^{+500}_{-500}	$3.93^{+0.10}_{-0.10}$	125^{+30}_{-30}	–	$35.8^{+4.7}_{-3.5}$	130^{+47}_{-38}	$2.6^{+0.1}_{-0.2}$	$35.2^{+4.0}_{-3.4}$	$10.5^{+1.7}_{-1.3}$	... *	$6.95^{+0.33}_{-0.06}$ (68%) (3)
609	O9-9.5 V-III	$4.52^{+0.13}_{-0.13}$	33000^{+1500}_{-1500}	$3.80^{+0.10}_{-0.10}$	100^{+30}_{-30}	–	$16.4^{+1.5}_{-1.3}$	110^{+40}_{-38}	$6.5^{+1.5}_{-1.0}$	$16.4^{+1.5}_{-1.2}$	$7.1^{+0.9}_{-0.7}$	... *	$6.90^{+0.11}_{-0.01}$ (68%) (3)
611	O8 V(n)	$4.79^{+0.14}_{-0.14}$	37410^{+900}_{-900}	$4.09^{+0.14}_{-0.14}$	210^{+30}_{-30}	–	$23.0^{+1.5}_{-1.6}$	210^{+62}_{-43}	$1.9^{+0.9}_{-1.2}$	$22.8^{+1.6}_{-1.4}$	$6.3^{+0.6}_{-0.6}$	... *	$6.89^{+0.38}_{-0.01}$ (68%) (3)
617	WN5ha	$6.30^{+0.10}_{-0.10}$	53088^{+1907}_{-1907}	–	< 200	$0.62^{+0.05}_{-0.05}$	$93.0^{+21.7}_{-13.1}$	370^{+63}_{-10}	$2.1^{+0.4}_{-0.4}$	$80.4^{+18.6}_{-11.8}$	$15.0^{+3.0}_{-1.5}$	$0.63^{+0.05}_{-0.06}$	$8.75^{+0.05}_{-0.07}$ (68%) (2)
620	O9.7 III(n)	$4.34^{+0.10}_{-0.10}$	32150^{+510}_{-765}	$4.10^{+0.10}_{-0.10}$	206^{+30}_{-30}	–	$15.4^{+0.7}_{-0.8}$	210^{+52}_{-44}	$3.3^{+1.3}_{-1.6}$	$15.4^{+0.7}_{-0.8}$	$5.1^{+0.5}_{-0.3}$	... *	$6.92^{+0.18}_{-0.04}$ (68%) (1)
627	O9.7 V	$4.67^{+0.13}_{-0.13}$	33600^{+639}_{-639}	$4.11^{+0.12}_{-0.12}$	50^{+30}_{-30}	–	$17.8^{+0.9}_{-1.0}$	70^{+45}_{-32}	$4.2^{+0.8}_{-1.3}$	$17.8^{+0.9}_{-0.9}$	$6.0^{+0.6}_{-0.7}$	... *	$6.91^{+0.02}_{-0.01}$ (71%) (3)
638	O8.5 Vz	$4.68^{+0.13}_{-0.13}$	36920^{+500}_{-500}	$4.20^{+0.10}_{-0.10}$	45^{+30}_{-30}	–	$21.4^{+0.9}_{-0.9}$	70^{+40}_{-35}	$1.0^{+0.8}_{-0.8}$	$21.4^{+0.9}_{-0.9}$	$5.7^{+0.5}_{-0.3}$	... *	$6.89^{+0.02}_{-0.02}$ (71%) (3)
639	O9.7 V	$4.78^{+0.12}_{-0.12}$	33710^{+500}_{-500}	$4.18^{+0.10}_{-0.10}$	65^{+30}_{-30}	–	$18.2^{+0.8}_{-0.9}$	80^{+45}_{-33}	$4.1^{+0.7}_{-1.1}$	$18.2^{+0.8}_{-0.9}$	$6.0^{+0.7}_{-0.6}$	... *	$6.90^{+0.02}_{-0.01}$ (70%) (3)
660	O9.5 Vnn	$4.73^{+0.20}_{-0.20}$	32259^{+1019}_{-1019}	$3.95^{+0.16}_{-0.16}$	515^{+52}_{-52}	–	$17.2^{+1.3}_{-0.8}$	500^{+52}_{-33}	$6.3^{+2.1}_{-2.4}$	$17.0^{+1.4}_{-0.7}$	$5.8^{+1.5}_{-0.3}$	... *	$8.41^{+0.06}_{-0.28}$ (68%) (3)
663	O8.5 V	$4.77^{+0.12}_{-0.12}$	36465^{+1715}_{-1715}	$4.02^{+0.29}_{-0.29}$	90^{+30}_{-30}	–	$20.6^{+2.0}_{-1.6}$	100^{+42}_{-36}	$2.5^{+1.3}_{-1.7}$	$20.6^{+1.9}_{-1.6}$	$6.0^{+0.8}_{-0.5}$	... *	$6.89^{+0.03}_{-0.01}$ (69%) (3)
664	O7 II(f)	$5.51^{+0.10}_{-0.10}$	35000^{+638}_{-500}	$3.63^{+0.10}_{-0.10}$	96^{+30}_{-30}	–	$34.4^{+3.7}_{-3.0}$	110^{+44}_{-38}	$3.7^{+0.3}_{-0.2}$	$34.0^{+2.3}_{-3.6}$	$14.3^{+1.9}_{-1.1}$	... *	$6.97^{+0.28}_{-0.07}$ (72%) (1)
679	O9.5 V	$4.72^{+0.20}_{-0.20}$	33220^{+900}_{-900}	$4.10^{+0.15}_{-0.15}$	40^{+30}_{-30}	–	$17.4^{+1.3}_{-1.3}$	70^{+39}_{-38}	$4.7^{+0.9}_{-1.7}$	$17.4^{+1.3}_{-1.3}$	$5.9^{+0.9}_{-0.8}$	... *	$6.90^{+0.02}_{-0.01}$ (71%) (3)
682	WN5h	$6.50^{+0.10}_{-0.10}$	54450^{+1956}_{-1956}	–	< 200	$0.45^{+0.05}_{-0.05}$	$149.2^{+17.8}_{-24.3}$	320^{+74}_{-46}	$1.1^{+0.2}_{-0.3}$	$134.8^{+19.7}_{-19.7}$	$19.6^{+2.1}_{-2.5}$	$0.44^{+0.05}_{-0.05}$	$8.56^{+0.05}_{-0.04}$ (68%) (2)
695	WN6h + ?	$6.50^{+0.10}_{-0.10}$	39811^{+1430}_{-1430}	–	< 200	$0.85^{+0.05}_{-0.05}$	$171.4^{+78.0}_{-41.8}$	350^{+36}_{-311}	g$2.2^{+0.1}_{-0.3}$	$109.0^{+21.7}_{-13.7}$	$42.2^{+5.8}_{-3.9}$	$0.89^{+0.05}_{-0.03}$	$9.31^{+0.14}_{-0.15}$ (68%) (2)
704	O9.2 V(n)	$4.65^{+0.25}_{-0.19}$ †34150^{+1450}_{-1450}	$3.98^{+0.22}_{-0.22}$	240^{+30}_{-30}	–	$18.4^{+3.1}_{-2.2}$	240^{+61}_{-40}	$4.2^{+2.1}_{-1.1}$	$18.6^{+2.8}_{-2.4}$	$5.5^{+2.2}_{-0.7}$	... *	$6.90^{+0.65}_{-0.01}$ (68%) (3)
706	O6-7 Vnnz	$5.02^{+0.26}_{-0.26}$	38030^{+1169}_{-1169}	$3.80^{+0.13}_{-0.13}$	375^{+38}_{-38}	–	$26.2^{+4.5}_{-2.8}$	370^{+75}_{-40}	$3.5^{+1.4}_{-0.9}$	$25.4^{+4.7}_{-2.2}$	$9.1^{+1.3}_{-1.7}$	$0.27^{+0.07}_{-0.01}$	$8.25^{+0.29}_{-0.33}$ (79%) (3)
710	O9.5 IV	$4.57^{+0.10}_{-0.10}$	35010^{+750}_{-750}	$4.24^{+0.12}_{-0.12}$	60^{+30}_{-30}	–	$18.4^{+1.0}_{-0.8}$	80^{+39}_{-36}	$1.1^{+1.1}_{-0.8}$	$18.4^{+1.0}_{-0.8}$	$5.4^{+0.4}_{-0.4}$	... *	$6.89^{+0.01}_{-0.01}$ (70%) (3)
717	O9 IV	$5.09^{+0.12}_{-0.12}$	35030^{+500}_{-500}	$3.89^{+0.10}_{-0.10}$	50^{+30}_{-30}	–	$23.4^{+1.8}_{-1.6}$	70^{+45}_{-32}	$4.4^{+0.3}_{-0.2}$	$23.6^{+1.2}_{-1.9}$	$9.0^{+1.0}_{-1.0}$	... *	$6.90^{+0.05}_{-0.02}$ (69%) (3)
722	O7 Vnnz	$4.91^{+0.13}_{-0.13}$	36640^{+770}_{-770}	$3.84^{+0.10}_{-0.10}$	405^{+40}_{-40}	–	$23.6^{+2.0}_{-2.5}$	410^{+66}_{-51}	$3.9^{+2.0}_{-2.0}$	$23.4^{+1.8}_{-0.8}$	$8.1^{+1.0}_{-0.8}$	$0.27^{+0.08}_{-0.01}$ h$8.43^{+0.17}_{-0.39}$ (81%) (3)
724	O7 Vnnz	$5.01^{+0.47}_{-0.47}$	37600^{+3299}_{-3299}	$3.78^{+0.41}_{-0.41}$	370^{+37}_{-37}	–	$22.0^{+5.2}_{-4.0}$	370^{+70}_{-45}	$3.6^{+1.4}_{-2.6}$	$21.4^{+5.4}_{-3.5}$	$6.8^{+1.8}_{-1.5}$	... *	$8.03^{+0.44}_{-0.28}$ (68%) (3)
737	O9 V	$5.11^{+0.12}_{-0.12}$	37515^{+735}_{-735}	$4.30^{+0.10}_{-0.10}$	50^{+30}_{-30}	–	$24.0^{+1.5}_{-1.2}$	70^{+46}_{-33}	$2.1^{+0.7}_{-1.0}$	$24.0^{+1.3}_{-1.3}$	$6.5^{+0.7}_{-0.5}$	... *	$6.90^{+0.02}_{-0.01}$ (71%) (3)

VFTS No.	SpT	$\log L/L_\odot$	$T_{\rm eff}$ (K)	$\log g$ (cgs)	$v \sin i$ (km s^{-1})	$Y_{\rm obs}$	$M_{\rm ini}$ (M$_\odot$)	$v_{\rm ini}$ (km s^{-1})	Age (Myr)	$M_{\rm present}$ (M$_\odot$)	R (R$_\odot$)	Y	$\log {\rm N/H} + 12$ (dex)
746	O6 Vnn	$5.29^{+0.24}_{-0.24}$	39885^{+1154}_{-1154}	$3.86^{+0.10}_{-0.10}$	275^{+30}_{-30}	–	$33.0^{+5.5}_{-3.9}$	290^{+54}_{-48}	$2.8^{+0.4}_{-0.4}$	$32.2^{+5.1}_{-3.5}$	$10.1^{+1.5}_{-1.5}$	$\ldots$ *	$7.90^{+0.25}_{-0.24}$ (70%) (3)
751	O7-8 Vnnz	$5.01^{+0.31}_{-0.31}$	36045^{+1494}_{-1494}	$3.90^{+0.25}_{-0.25}$	360^{+36}_{-44}	–	$22.0^{+3.4}_{-2.3}$	360^{+67}_{-44}	$3.8^{+1.1}_{-2.0}$	$22.0^{+3.1}_{-2.3}$	$6.4^{+2.2}_{-0.7}$	$\ldots$ *	$7.98^{+0.46}_{-0.24}$ (73%) (3)
753	O9.7 II-III	$4.78^{+0.10}_{-0.10}$	32300^{+867}_{-765}	$4.02^{+0.11}_{-0.10}$	38^{+30}_{-30}	–	$17.8^{+1.2}_{-0.9}$	60^{+48}_{-29}	$5.6^{+0.6}_{-0.7}$	$18.0^{+0.9}_{-1.1}$	$7.1^{+0.7}_{-0.7}$	$\ldots$ *	$6.90^{+0.02}_{-0.01}$ (69%) (1)
755	O3 Vn((f*))	$5.65^{+0.13}_{-0.13}$	46000^{+1500}_{-1500}	$3.90^{+0.10}_{-0.10}$	285^{+30}_{-30}	–	$51.6^{+4.8}_{-11.9}$	410^{+38}_{-147}	$^i 1.8^{+1.7}_{-0.8}$ ^{j}	$50.2^{+5.1}_{-12.8}$ ^{k}	$11.1^{+1.5}_{-1.2}$	$0.27^{+0.15}_{-0.02}$	$8.65^{+0.09}_{-0.71}$ (85%) (3)
758	WN5h	$6.40^{+0.10}_{-0.10}$	47315^{+1700}_{-1700}	–	< 200	$0.78^{+0.05}_{-0.05}$	$133.4^{+17.1}_{-35.1}$	420^{+35}_{-28}	$2.2^{+0.4}_{-0.2}$	$82.4^{+18.3}_{-14.0}$ ^{l}	$24.6^{+2.3}_{-4.0}$	$0.79^{+0.04}_{-0.05}$	$8.97^{+0.11}_{-0.08}$ (68%) (2)
761	O6.5 V((n))((f))z Nstr	$4.99^{+0.13}_{-0.13}$	40280^{+680}_{-680}	$4.15^{+0.10}_{-0.10}$	110^{+30}_{-30}	–	$28.0^{+1.6}_{-1.6}$	120^{+40}_{-42}	$1.2^{+0.6}_{-0.8}$	$27.8^{+1.6}_{-1.4}$	$6.9^{+0.6}_{-0.6}$	$\ldots$ *	$6.89^{+0.05}_{-0.02}$ (69%) (3)
770	O7 Vnn	$4.98^{+0.27}_{-0.27}$	37815^{+1125}_{-1125}	$3.95^{+0.15}_{-0.15}$	350^{+35}_{-35}	–	$25.0^{+3.0}_{-2.6}$	350^{+75}_{-41}	$3.2^{+0.9}_{-1.6}$	$24.8^{+3.0}_{-2.4}$	$7.0^{+0.7}_{-0.9}$	$\ldots$ *	$7.92^{+0.55}_{-0.16}$ (75%) (3)
775	O9.2 V	$4.72^{+0.12}_{-0.12}$	35940^{+1329}_{-1329}	$4.14^{+0.20}_{-0.20}$	40^{+30}_{-30}	–	$20.0^{+1.6}_{-1.4}$	70^{+38}_{-38}	$2.3^{+1.2}_{-1.5}$	$20.0^{+1.5}_{-1.4}$	$5.8^{+0.7}_{-0.5}$	$\ldots$ *	$6.90^{+0.01}_{-0.01}$ (70%) (3)
777	O9.2 II	$5.31^{+0.10}_{-0.10}$	29300^{+500}_{-663}	$3.28^{+0.10}_{-0.12}$	152^{+30}_{-30}	–	$27.2^{+2.7}_{-2.4}$	160^{+55}_{-38}	$5.2^{+0.5}_{-0.4}$	$25.8^{+3.1}_{-1.6}$	$18.3^{+1.6}_{-2.2}$	$\ldots$ *	$7.41^{+0.21}_{-0.28}$ (68%) (1)
778	O9.5 V	$4.81^{+0.18}_{-0.18}$	34215^{+1375}_{-1375}	$4.18^{+0.21}_{-0.21}$	125^{+30}_{-30}	–	$19.0^{+1.9}_{-1.7}$	130^{+45}_{-40}	$3.9^{+1.1}_{-1.9}$	$19.0^{+1.8}_{-1.7}$	$5.9^{+1.1}_{-0.7}$	$\ldots$ *	$6.90^{+0.10}_{-0.01}$ (68%) (3)
782	O8.5 III	$5.22^{+0.10}_{-0.10}$	33800^{+638}_{-500}	$3.57^{+0.10}_{-0.10}$	78^{+30}_{-30}	–	$27.2^{+2.3}_{-2.2}$	90^{+46}_{-33}	$4.6^{+0.3}_{-0.3}$	$25.6^{+3.1}_{-1.6}$	$12.2^{+1.5}_{-1.0}$	$\ldots$ *	$6.96^{+0.10}_{-0.09}$ (68%) (1)
797	O3.5 V((n))((fc))	$5.60^{+0.13}_{-0.13}$	45000^{+1500}_{-1500}	$3.80^{+0.10}_{-0.10}$	140^{+30}_{-30}	–	$49.0^{+7.5}_{-6.3}$	150^{+55}_{-50}	$1.9^{+0.3}_{-0.3}$	$47.8^{+6.7}_{-6.1}$	$12.1^{+1.4}_{-1.1}$	$\ldots$ *	$6.94^{+0.69}_{-0.04}$ (68%) (3)
807	O9.5 III Nstr	$4.86^{+0.10}_{-0.10}$	33800^{+663}_{-1199}	$3.92^{+0.10}_{-0.12}$	20^{+30}_{-30}	–	$19.6^{+1.4}_{-1.1}$	50^{+47}_{-30}	$5.0^{+0.7}_{-0.5}$	$19.4^{+1.4}_{-1.1}$	$7.7^{+0.9}_{-0.7}$	$\ldots$ *	$6.90^{+0.02}_{-0.01}$ (69%) (1)
819	ON8 III((f))	$4.88^{+0.10}_{-0.10}$	36750^{+740}_{-536}	$3.81^{+0.12}_{-0.10}$	66^{+30}_{-30}	–	$23.4^{+1.3}_{-1.3}$	80^{+44}_{-32}	$3.5^{+0.4}_{-0.6}$	$23.0^{+1.5}_{-1.1}$	$7.5^{+0.8}_{-0.7}$	$\ldots$ *	$6.90^{+0.05}_{-0.02}$ (68%) (1)
843	O9.5 IIIn	$4.46^{+0.10}_{-0.10}$	30650^{+714}_{-500}	$3.93^{+0.10}_{-0.10}$	312^{+30}_{-30}	–	$15.8^{+0.7}_{-0.8}$	310^{+54}_{-37}	$5.9^{+0.7}_{-1.0}$	$15.8^{+0.7}_{-0.8}$	$6.2^{+0.6}_{-0.5}$	$\ldots$ *	$7.65^{+0.17}_{-0.18}$ (68%) (1)
849	O7 Vz	$5.02^{+0.13}_{-0.13}$	39800^{+639}_{-639}	$4.16^{+0.11}_{-0.11}$	95^{+30}_{-30}	–	$27.2^{+1.6}_{-1.4}$	100^{+47}_{-33}	$1.5^{+0.6}_{-0.9}$	$27.2^{+1.4}_{-1.4}$	$6.8^{+0.7}_{-0.6}$	$\ldots$ *	$6.90^{+0.03}_{-0.02}$ (69%) (3)
892	O9 V	$4.85^{+0.12}_{-0.12}$	35765^{+595}_{-595}	$3.98^{+0.10}_{-0.10}$	40^{+30}_{-30}	–	$21.4^{+1.4}_{-1.1}$	70^{+38}_{-38}	$3.8^{+0.5}_{-0.7}$	$21.2^{+1.4}_{-1.0}$	$7.1^{+0.8}_{-0.7}$	$\ldots$ *	$6.91^{+0.02}_{-0.01}$ (70%) (3)
1001	WN6(h)	$6.20^{+0.10}_{-0.10}$	42170^{+1515}_{-1515}	–	< 200	$0.85^{+0.05}_{-0.05}$	$78.2^{+20.7}_{-7.9}$	410^{+20}_{-33}	$3.3^{+0.1}_{-0.5}$	$53.2^{+13.8}_{-2.6}$	$24.9^{+5.0}_{-1.9}$	$0.81^{+0.04}_{-0.05}$	$8.98^{+0.18}_{-0.06}$ (68%) (2)
1017	O2 If*/WN5	$6.20^{+0.10}_{-0.10}$	50119^{+1800}_{-1800}	–	< 200	$0.55^{+0.05}_{-0.05}$	$75.8^{+20.1}_{-7.1}$	360^{+22}_{-24}	$2.2^{+0.4}_{-0.4}$	$66.6^{+18.3}_{-6.1}$	$15.7^{+2.5}_{-2.3}$	$0.53^{+0.06}_{-0.05}$ ^{m}	$8.64^{+0.06}_{-0.05}$ (68%) (2)
1022	O3.5 If*/WN7	$6.50^{+0.10}_{-0.10}$	42170^{+1515}_{-1515}	–	< 200	$0.25^{+0.05}_{-0.01}$	$148.0^{+29.4}_{-23.7}$	100^{+59}_{-49}	$1.2^{+0.2}_{-0.2}$	$135.6^{+26.5}_{-4.1}$	$31.6^{+4.8}_{-4.1}$	$\ldots$ *	$8.08^{+0.16}_{-0.64}$ (68%) (2)
1025	WN5h	$6.60^{+0.15}_{-0.15}$	42170^{+1894}_{-1894}	–	< 200	$0.70^{+0.05}_{-0.05}$	$198.8^{+32.6}_{-85.0}$ ^{n}	360^{+39}_{-17}	$1.8^{+0.4}_{-0.2}$	$102.4^{+77.2}_{-29.2}$ ^{o}	$37.9^{+7.2}_{-6.3}$	$0.73^{+0.04}_{-0.06}$	$8.87^{+0.07}_{-0.08}$ (68%) (2)

(1) Amsterdam, (2) Armagh, (3) Tenerife

(a) 97% CI, (b) 83% CI, (c) 69% CI, (d) 72% CI, (e) 72% CI, (f) 86% CI, (g) 93% CI, (h) 71% CI, (i) 85% CI, (j) 70% CI, (k) 70% CI, (l) 69% CI, (m) 70% CI, (n) 78% CI, (o) 91% CI

(*) not enriched in helium on surface, i.e. the models predict $Y \approx 0.26$

(†) luminosity predicted by the stellar models

Outlook

> The important thing is not to stop questioning.
>
> *(Albert Einstein)*

Massive stars are key agents in the Universe and important for many aspects of astrophysics such as the reionisation of the early Universe and the chemical enrichment and evolution of galaxies. However, as discussed in this thesis, their evolution is seriously hampered by uncertain wind mass loss rates, interior mixing and duplicity (Sec. 1.2). Improving these aspects of massive star evolution is therefore of utmost importance. As is done in this thesis, a continuous comparison of theoretical predictions with observations is essential to improve the models as well as our understanding of observed stars and stellar populations. The statistical methods developed in this thesis will be of great help as a starting point to accomplish these aims. In the following we want to illustrate possible ways to tackle some of the open questions of massive star evolution and how results and methods described in this thesis may contribute to these efforts.

As discussed in Sec. 1.2.1, our theoretical understanding of the winds of massive stars is incomplete. There is the "weak-wind" problem for early B and late O stars, the likely overestimated wind mass loss rates of O stars because of wind clumping and the challenge with the high wind mass loss rates of the most massive stars because of their proximity to the Eddington limit. Current state-of-the-art stellar evolutionary models typically use wind mass loss prescriptions that do not account for these new empirical constraints. One way to update the wind mass loss rates used in stellar evolutionary computations would be to use robust empirical constrains as a function of effective temperature and luminosity, and of the surface helium mass fraction for the most massive stars. There are currently probably not enough robust empirical constraints available to obtain a complete picture of wind mass loss for massive stars but it may be worth starting to build a table of wind mass loss rates in which one can interpolate to fill some gaps and implement this table into stellar models. With time and help from wind experts it could then be possible to construct a flexible system that can be easily updated whenever new constraints are available. The transition to other metallicities may be accomplished by the usual scaling of the wind mass loss rates with a factor that depends on a power of the metallicity.

Another big challenge for massive star evolution is the internal mixing of chemical elements

and angular momentum. There are various physical processes that may lead to mixing, e.g. convection, internal gravity waves and magnetic fields, but we focus on rotational induced mixing here. The Hunter diagram, i.e. the diagram showing the surface nitrogen abundance of stars as a function of projected rotational velocity (Fig. 1.4), is thought to be an excellent probe of rotational mixing in stellar models. The slowly rotating, nitrogen enhanced and rapidly rotating, nitrogen normal stars pose a serious challenge for our understanding of rotational mixing (Hunter et al. 2008b; Brott et al. 2011b; Aerts et al. 2014; Maeder et al. 2014). With the statistical methods developed in this thesis, we already have the tools at hand to test the hypothesis that some of these stars are binary products and therefore may not follow the expectations of rotational mixing in single stars. As mentioned in Sec. 1.2.3, mergers are expected to be enriched in nitrogen on their surface and may produce magnetic fields that have the potential to efficiently spin-down stars. This may be a viable channel to explain some of the slowly rotating, nitrogen enriched stars. The structure of merger products may not differ greatly from genuine single stars, making it hard to distinguish between single stars and binary products. However, merger products are expected to be rejuvenated as discussed in this thesis (Chapters 2 and 3). So if the slowly rotating, nitrogen enriched stars are indeed merger products, we may expect that their average age is younger than that of the slowly rotating, non-enriched stars. Hence, computing the age probability distributions of stars in the different boxes of the Hunter diagram (Fig. 1.4) as done in Chapter 5 for the stars in the VLT-FLAMES Tarantula Survey and comparing their average ages may be a direct probe of the binary merger hypothesis. Such computations likely have to be accompanied by Monte Carlo calculations to check the odds of obtaining different average ages just by chance.

Identifying some of the stars in the Hunter diagram as potential binary products would be a great step forward but can yet not tell us whether our understanding of rotational mixing is correct or not. Improving upon the complex interplay between rotational mixing and binary mass transfer is not straightforward because rotationally induced mixing and binary mass transfer result, in some regards, in similar observational consequences. For example, a trend of higher nitrogen enrichment with faster rotational velocities is expected to occur because of rotational mixing as well as binary mass transfer and both mechanisms can prolong stellar lives. It is therefore essential to disentangle these degenerate physical processes. There may be at least two possible ways of doing so and both complement each other:

- On the observational site, a sample of genuine single stars, i.e. those stars for which past binary mass transfer can be for sure excluded, has to be selected to remove the signal of binary star evolution. This may be achieved by picking a sample of detached main-sequence binary stars or cluster stars that are below the main-sequence turn-off because they are mostly pre-interaction binaries as shown in Chapter 2. The drawback in the latter case is that these cluster members may yet not be evolved enough to show signs of rotational mixing. The drawback in the former case is that analysing composite spectra is difficult and likely requires new techniques. There are already methods to disentangle spectra and it is also possible to combine Monte Carlo sampling techniques with pre-computed grids of atmosphere models to determine the best-fitting atmospheric parameters of composite spectra. Having a sample of genuine single stars is probably the only way to obtain a clean observational picture of single star evolution, e.g. in the Hunter diagram as well as Hertzsprung–Russell diagram to tackle some problems in massive star research.

- On the theoretical site, detailed population synthesis predictions of single *and* binary

stars need to be made. Population synthesis models of single stars are already available but similar predictions for binary stars are yet lacking. In a first step, a grid of binary stars has to be computed. However, this is not enough because about half of the binaries interacting by mass transfer from a main-sequence donor are expected to merge. Hence, a complete grid of binary stars would also have to take mergers into account which is a very challenging problem. Entropy sorting techniques may be applied to take some first steps in this direction. In any case, at least two population synthesis models have to be made, one model with and one without rotational mixing. A comparison with observations will then allow us to conclude whether rotational mixing is needed at all or whether binary star evolution is sufficient to explain the observations.

Computing detailed models of massive binary stars is a very pressing problem given that there is a lack of such models and that binary stars are now recognized to be such an important part of massive star evolution. There are many open questions in binary star evolution, for example how efficient is mass transfer, which binaries merge and how does common envelope evolution work. Once we have a complete picture of single and binary star evolution, Bonnsai (Chapter 4) can be extended to binary stars opening up possibilities never seen before. For example it would be possible to assess the likelihood of individual stars being binary products and to highlight shortcomings in our models. This would yet be another way to disentangle genuine single stars from binary products. Actually, there already exists an extension of Bonnsai to binary stars that is not described in this thesis because it has yet not been tested thoroughly. However, the extension of Bonnsai to binary stars shows that it may be beneficial to drop the grid approach and move to a Monte Carlo technique and efficient interpolation routines to sample the huge binary parameter space.

There are further key ingredients of stellar evolution, such as the extent of convective core overshooting, that can yet not be derived from first principles or sophisticated state-of-the-art simulations but are very important for the mixing of stars. For example, the extent of convective core overshooting is uncertain and may even be mass dependent (e.g. Castro et al. 2014). Given the immense progress of observations and newly developed statistical methods like Bonnsai we are in the fortunate situation that we can calibrate stellar models with the help of observations. Detached main-sequence binaries with accurately measured masses and radii are ideally suited for this purpose (e.g. the sample of Milky Way binaries of Torres et al. 2010). Making the metallicity and the extent of convective core overshooting free parameters beside mass and age in a grid of stellar models will enable us to determine the overshooting parameter including robust uncertainties from a large sample of binary stars using Bonnsai and to study a possible mass dependence. Efforts in this direction are already underway.

Besides these suggested paths to advance our understanding of massive star evolution, this thesis reveals further shortcomings of current models and suggests solutions that may be worth investigating in the future. For example, the criterion for stable mass transfer from giant-like stars in binary population synthesis models likely needs to be modified (Chapter 2). The modification has the potential to explain the observed trend of the frequency of blue straggler stars with cluster age and the observed blue straggler star binaries with white dwarf companions in wide orbits in NGC 188 (e.g. Chen & Han 2008; Geller & Mathieu 2011; Geller et al. 2013).

The comparison of the observed massive stars ($\log L/\mathrm{L}_\odot \gtrsim 6.0$) in the VLT-FLAMES Tarantula Survey with theoretical models in Chapter 5 shows that the models lack important physics to properly describe the observations. A first step could be updating the wind mass loss prescriptions for these stars such that the models follow the observed and theoretically

predicted trend of stronger winds when approaching the Eddington limit.

Furthermore Bonnsai opened up a totally new dimension of comparing observed stars to theoretical models but this method is currently limited to massive stars. Hence, an extension of Bonnsai to stars below $5\,M_\odot$ is desirable as well as the inclusion of other widely used stellar models to enable comparisons between different models to, e.g., asses uncertainties in inferred stellar parameters that are purely related to the calibrations and numerics applied in different stellar codes.

In the future, new instruments such as Gaia, the European Extremely Large Telescope (E-ELT), the James Webb Space Telescope (JWST), the Square Kilometre Array (SKA) and the Large Synoptic Survey Telescope (LSST) will bring unprecedented observations of stars in the Galaxy, massive stars up to large distances, the explosions of the first stars, the reionisation of the Universe and transients over the whole sky. We should expect the unexpected and be prepared for big discoveries that will trigger innovative developments, provide novel insights and demand improved models on our way to unravel the laws of nature.

Curriculum Vitae

Awards, prices and fellowships

2009–2014	Stipendiary Fellowship (honours branch) of the Bonn-Cologne Graduate School of Physics and Astronomy (BCGS)
2007–2011	Stipendiary Fellowship of the German National Academic Foundation (Studienstiftung des Deutschen Volkes)
2005	Book-award of the German Physical Society (Deutsche Physikalische Gesellschaft, DPG)

List of publications

Refereed publications

1. Fossati, L., Castro, N., Morel, T., Langer, N., Briquet, M., Carroll, T. A., Hubrig, S., Nieva, M. F., Oskinova, L. M., Przybilla, N., **Schneider, F. R. N.**, Schöller, M., Simón-Díaz, S., Ilyin, I., de Koter, A., Reisenegger, A., Sana, H. & the BOB collaboration 2014, A&A submitted, *B fields in OB stars (BOB): on the detection of weak magnetic fields in the two early B-type stars βCMa and εCMa—Possible lack of a "magnetic desert" in massive stars*

2. Neilson, H. R., **Schneider, F. R. N.**, Izzard, R. G., Evans, N. R. & Langer, N. 2014, A&A submitted, *The occurrence of classical Cepheids in binary systems*

3. Clark, J. S., Taylor, W. D., Townsley, L. K., Walborn, N. R., Bird, A. J., Sana, H., Broos, P. S., de Mink, S. E., Dufton, P. L., Evans, C. J., Langer, N., Maíz Apellániz, J., **Schneider, F. R. N.** & Soszyński, I. 2014, A&A submitted, *The VLT-FLAMES Tarantula Survey XIX. The nature of the X-ray bright emission line star VFTS 399*

4. **Schneider, F. R. N.**, Izzard, R. G., Langer, N. & de Mink, S. E. 2014, ApJ submitted, *Evolution of mass functions of coeval stars through wind mass loss and binary interactions*

5. Castro, N., Fossati, L., Langer, N., Simón-Díaz, S., **Schneider, F. R. N.** & Izzard, R. G. 2014, A&A Letter, in press, *The spectroscopic Hertzsprung–Russell diagram of Galactic massive stars*

6. **Schneider, F. R. N.**, Langer, N., de Koter, A., Brott, I., Izzard, R. G. & Lau, H. H. B. 2014, A&A, in press, *BONNSAI: a Bayesian tool for comparing stars with stellar evolution models*

7. Lau, H. H. B., Izzard, R. G. & **Schneider, F. R. N.** 2014, A&A, in press, *Numerical Tests of Rotational Mixing in Massive Stars with the new Population Synthesis Code BONNFIRES*

8. Bestenlehner, J. M., Gräfener, G., Vink, J. S., Najarro, F., de Koter, A., Sana, H., Evans, C. J., Crowther, P. A., Hénault-Brunet, V., Herrero, A., Langer, N., **Schneider, F. R. N.**, Simón-Díaz, S., Taylor, W. D. & Walborn, N. R. 2014, A&A, in press, *The VLT-FLAMES Tarantula Survey XVII. Physical and wind properties of massive stars at the top of the main sequence*

9. Koenigsberger, G., Morrell, N., Hillier, D. J., Gamen, R., **Schneider, F. R. N.**, González-Jiménez, N., Langer, N. & Barbá, R. 2014, AJ, 148, 62, *The HD 5980 multiple system: masses and evolutionary status*

10. de Mink, S. E., Sana, H., Langer, N., Izzard, R. G. & **Schneider, F. R. N.** 2014, ApJ, 782, 7, *The Incidence of Stellar Mergers and Mass Gainers among Massive Stars*

11. Fossati, L., Zwintz, K., Castro, N., Langer, N., Lorenz, D., **Schneider, F. R. N.**, Kuschnig, R., Matthews, J. M., Alecian, E., Wade, G. A., Barnes, T. G. & Thoul, A. A. 2014, A&A, 562, 143, *Two spotted and magnetic early B-type stars in the young open cluster NGC 2264 discovered by MOST and ESPaDOnS*

12. **Schneider, F. R. N.**, Izzard, R. G., de Mink, S. E., Langer, N., Stolte, A., de Koter, A., Gvaramadze, V. V., Hußmann, B., Liermann, A. & Sana, H. 2014, ApJ, 780, 117, *Ages of Young Star Clusters, Massive Blue Stragglers, and the Upper Mass Limit of Stars: Analyzing Age-dependent Stellar Mass Functions*

13. Doran, E. I., Crowther, P. A., de Koter, A., Evans, C. J., McEvoy, C., Walborn, N. R., Bastian, N., Bestenlehner, J. M., Gräfener, G., Herrero, A., Köhler, K., Maíz Apellániz, J., Najarro, F., Puls, J., Sana, H., **Schneider, F. R. N.**, Taylor, W. D., van Loon, J. Th. & Vink, J. S. 2013, A&A, 558, 134, *The VLT-FLAMES Tarantula Survey. XI. A census of the hot luminous stars and their feedback in 30 Doradus*

14. Sana, H., van Boeckel, T., Tramper, F., Ellerbroek, L. E., de Koter, A., Kaper, L., Moffat, A. F. J., Schnurr, O., **Schneider, F. R. N.** & Gies, D. R. 2013, MNRAS, 432, L26, *R144 revealed as a double-lined spectroscopic binary*

15. Sana, H., de Mink, S. E., de Koter, A., Langer, N., Evans, C. J., Gieles, M., Gosset, E., Izzard, R. G., Le Bouquin, J.-B. & **Schneider, F. R. N.** 2012, Science, 337, 444, *Binary Interaction Dominates the Evolution of Massive Stars*

Non-refereed Publications

1. Morel, T., Castro, N., Fossati, L., Hubrig, S., Langer, N., Przybilla, N., Schöller, M., Carroll, T., Ilyin, I., Irrgang, A., Oskinova, L., **Schneider, F. R. N.**, Simón-Díaz, S., Briquet, M., González, J. F., Kharchenko, N., Nieva, M.-F., Scholz, R.-D., de Koter, A., Hamann, W.-R., Herrero, A., Maíz Apellániz, J., Sana, H., Arlt, R., Barbá, R., Dufton, P., Kholtygin, A., Mathys, G., Piskunov, A., Reisenegger, A., Spruit, H. & Yoon, S.-C. 2014, in proceedings of IAU Symposium 307, New Windows on Massive Stars (Geneva, June 2014), *The B Fields in OB Stars (BOB) Survey*

2. **Schneider, F. R. N.**, Langer, N., Lau, H. H. B. & Izzard, R. G. 2013, in EAS Publications Series, Vol. 64, EAS Publications Series, 423–424, *The BONNSAI Project: A Statistical Comparison of Stars with Stellar Evolution Models*

3. Lau, H. H. B., Izzard, R. G. & **Schneider, F. R. N.** 2013, in EAS Publications Series, Vol. 64, EAS Publications Series, 55–58, *Modelling binary rotating stars by new population synthesis code BONNFIRES*

4. de Koter, A., Bestenlehner, J. M., de Mink, S. E., Evans, C. J., Gräfener, G., Izzard, R. G., Langer, N., Ramírez-Agudelo, O. H., Sana, H., **Schneider, F. R. N.**, Simón-Díaz, S. & Vink, J. S. 2013, in EAS Publications Series, Vol. 64, EAS Publications Series, 21–28, *On the possibility that the most massive stars result from binary mergers*

5. Sana, H., de Mink, S. E., de Koter, A., Langer, N., Evans, C. J., Gieles, M., Gosset, E., Izzard, R. G., Le Bouquin, J.-B. & **Schneider, F. R. N.** 2013, in Astronomical Society of the Pacific Conference Series, Vol. 470, 370 Years of Astronomy in Utrecht, ed. G. Pugliese, A. de Koter, & M. Wijburg, 141, *Multiplicity of massive O stars and evolutionary implications*

Acknowledgements

When starting to write these acknowledgements I really realised for the first time: I made it! Three years of hard work are brought to an end and written up in this thesis. However, it is not just the work of three years that culminates in this moment but rather all the work and effort since I began to study physics in Bonn with the distant aim of conducting professional research and finishing a PhD. Back then, the way to the PhD looked endless with many hurdles waiting to be taken—and to be honest, I am still wondering how I managed to pass some of them. Now, when looking back, it feels as if it was yesterday when I attended the "Vorkurs Mathematik und Physik" in preparation for the upcoming studies and sat together with several colleagues in the library desperately trying to solve some hard exercises. Since then I met many wonderful people without whom I would have never managed to get that far. I hope I do not forget to mention anybody but I am more or less sure that it will happen unintentionally—my honest apology.

First of all, I want to express my deepest gratitude to my advisers Norbert and Rob. They guided me through my Master project and also my PhD. It is my absolute pleasure to work with you and I learned so much from you. Norbert, your support and advise in every possible respect is outstanding. You gave me a lot of freedom to follow my own ideas and I very much appreciate that. From the first day on when I joined your group I felt at home. Science is a labyrinth in which it is easy to get lost but you have the ability to always see the bigger picture while still finding the details that will show the way out and bring us one step ahead. You have been a never drying up source of ideas and knowledge. Rob, your skills are astonishing and I tried my best to acquire a tiny part of them. Your innovative and efficient computing is admirable, just as is your smartness and concise writing.

From my first day on, when doing a small project during a four week internship before starting to work on my Master thesis, I experienced support from several people that immediately treated me as one of their colleagues and helped me a lot in various respects. In particular, I would like to thank Selma, Alex and Hugues for many useful discussions, inspiration, help and support. I am not overstating when saying that you became something like third advisers to me but also close colleagues and friends.

I also want to thank all our group members in Bonn that made working a joy. In no special order these are Hilding, Enrique, Matteo, Vincent, Jonathan M., Jonathan B., Shazrene, Tyl, Sung-Chul, Thomas, Selma, Herbert, Karen, Sasha, Luis, Dominique, Denise, Sutirtha, Stefan

Bibliography

Abate, C., Pols, O. R., Izzard, R. G., Mohamed, S. S., & de Mink, S. E. 2013, A&A, 552, A26

Abt, H. A., Levato, H., & Grosso, M. 2002, ApJ, 573, 359

Aerts, C., Molenberghs, G., Kenward, M. G., & Neiner, C. 2014, ApJ, 781, 88

Ahumada, J. A., & Lapasset, E. 2007, A&A, 463, 789

Andersen, J. 1991, A&A Rev., 3, 91

Andersen, M., Zinnecker, H., Moneti, A., et al. 2009, ApJ, 707, 1347

Anderson, C. N., Meier, D. S., Ott, J., et al. 2014, ApJ, 793, 37

Antoniadis, J., Freire, P. C. C., Wex, N., et al. 2013, Science, 340, 448

Asplund, M., Grevesse, N., Sauval, A. J., & Scott, P. 2009, ARA&A, 47, 481

Banerjee, S., Kroupa, P., & Oh, S. 2012a, ApJ, 746, 15

—. 2012b, MNRAS, 426, 1416

Barbá, R. H., Gamen, R., Arias, J. I., et al. 2010, in Revista Mexicana de Astronomia y Astro-
fisica Conference Series, Vol. 38, Revista Mexicana de Astronomia y Astrofisica Conference
Series, 30–32

Barnes, S. A. 2007, ApJ, 669, 1167

Bastian, N., Covey, K. R., & Meyer, M. R. 2010, ARA&A, 48, 339

Batten, A. H. 1991, JRASC, 85, 43

Bazot, M., Bourguignon, S., & Christensen-Dalsgaard, J. 2012, MNRAS, 427, 1847

Beck, P. G., Montalban, J., Kallinger, T., et al. 2012, Nature, 481, 55

Bergemann, M., Ruchti, G. R., Serenelli, A., et al. 2014, A&A, 565, A89

Bestenlehner, J. M., Vink, J. S., Gräfener, G., et al. 2011, A&A, 530, L14

Bestenlehner, J. M., Gräfener, G., Vink, J. S., et al. 2014, A&A, in press, arXiv:1407.1837

Bethe, H. A. 1939, Physical Review, 55, 434

Bethe, H. A., & Critchfield, C. L. 1938, Physical Review, 54, 248

Bica, E., Bonatto, C., Dutra, C. M., & Santos, J. F. C. 2008, MNRAS, 389, 678

Bica, E. L. D., Schmitt, H. R., Dutra, C. M., & Oliveira, H. L. 1999, AJ, 117, 238

Blind, N., Boffin, H. M. J., Berger, J.-P., et al. 2011, A&A, 536, A55

Blum, R. D., Schaerer, D., Pasquali, A., et al. 2001, AJ, 122, 1875

Bode, M. F., & Evans, A. 2012, Classical Novae

Boffin, H. M. J. 2014, ArXiv e-prints, arXiv:1406.3473

Bondi, H. 1952, MNRAS, 112, 195

Bosch, G., Terlevich, E., & Terlevich, R. 2009, AJ, 137, 3437

Brandl, B., Sams, B. J., Bertoldi, F., et al. 1996, ApJ, 466, 254

Brandner, W., Clark, J. S., Stolte, A., et al. 2008, A&A, 478, 137

Brandner, W., Grebel, E. K., Barbá, R. H., Walborn, N. R., & Moneti, A. 2001, AJ, 122, 858

Braun, H., & Langer, N. 1995, A&A, 297, 483

Bressert, E., Bastian, N., Evans, C. J., et al. 2012, A&A, 542, A49

Brott, I., de Mink, S. E., Cantiello, M., et al. 2011a, A&A, 530, A115

Brott, I., Evans, C. J., Hunter, I., et al. 2011b, A&A, 530, A116

Burbidge, E. M., Burbidge, G. R., Fowler, W. A., & Hoyle, F. 1957, Reviews of Modern Physics, 29, 547

Burnett, B., & Binney, J. 2010, MNRAS, 407, 339

Cantiello, M., Mankovich, C., Bildsten, L., Christensen-Dalsgaard, J., & Paxton, B. 2014, ApJ, 788, 93

Cantiello, M., Yoon, S.-C., Langer, N., & Livio, M. 2007, A&A, 465, L29

Cardelli, J. A., Clayton, G. C., & Mathis, J. S. 1989, ApJ, 345, 245

Casagrande, L., Schönrich, R., Asplund, M., et al. 2011, A&A, 530, A138

Cassinelli, J. P., Mathis, J. S., & Savage, B. D. 1981, Science, 212, 1497

Castor, J. I., Abbott, D. C., & Klein, R. I. 1975, ApJ, 195, 157

Castro, N., Fossati, L., Simón-Díaz, S., et al. 2014, A&A, in press

Ceverino, D., & Klypin, A. 2009, ApJ, 695, 292

Charbonneau, P. 1995, ApJS, 101, 309

Chatterjee, S., Rasio, F. A., Sills, A., & Glebbeek, E. 2013, ApJ, 777, 106

Chen, X., & Han, Z. 2008, MNRAS, 387, 1416

—. 2009, MNRAS, 395, 1822

Chen, Y., Wang, Q. D., Gotthelf, E. V., et al. 2006, ApJ, 651, 237

Chesneau, O., Meilland, A., Chapellier, E., et al. 2014, A&A, 563, A71

Chiosi, C., & Maeder, A. 1986, ARA&A, 24, 329

Clarkson, W. I., Ghez, A. M., Morris, M. R., et al. 2012, ApJ, 751, 132

Clausen, J. V., Frandsen, S., Bruntt, H., et al. 2010, A&A, 516, A42

Collier, A. C., & Jenkins, C. R. 1984, MNRAS, 211, 391

Conroy, C., & Kratter, K. M. 2012, ApJ, 755, 123

Conti, P. S., & Ebbets, D. 1977, ApJ, 213, 438

Crowther, P. A., Schnurr, O., Hirschi, R., et al. 2010, MNRAS, 408, 731

Crowther, P. A., & Walborn, N. R. 2011, MNRAS, 416, 1311

Cucchiara, A., Levan, A. J., Fox, D. B., et al. 2011, ApJ, 736, 7

da Silva, L., Girardi, L., Pasquini, L., et al. 2006, A&A, 458, 609

De Gennaro, S., von Hippel, T., Jefferys, W. H., et al. 2009, ApJ, 696, 12

de Grijs, R., Gilmore, G. F., Johnson, R. A., & Mackey, A. D. 2002, MNRAS, 331, 245

de Koter, A., Heap, S. R., & Hubeny, I. 1997, ApJ, 477, 792

—. 1998, ApJ, 509, 879

De Marchi, G., Paresce, F., Panagia, N., et al. 2011, ApJ, 739, 27

de Mink, S. E., Langer, N., Izzard, R. G., Sana, H., & de Koter, A. 2013, ApJ, 764, 166

de Mink, S. E., Pols, O. R., & Hilditch, R. W. 2007, A&A, 467, 1181

de Mink, S. E., Sana, H., Langer, N., Izzard, R. G., & Schneider, F. R. N. 2014, ApJ, 782, 7

Dib, S. 2014, MNRAS, 444, 1957

Doran, E. I., Crowther, P. A., de Koter, A., et al. 2013, A&A, 558, A134

Dray, L. M., & Tout, C. A. 2007, MNRAS, 376, 61

Duchêne, G., & Kraus, A. 2013, ARA&A, 51, 269

Dufton, P. L., Dunstall, P. R., Evans, C. J., et al. 2011, ApJ, 743, L22

Dufton, P. L., Langer, N., Dunstall, P. R., et al. 2013, A&A, 550, A109

Eggleton, P. P. 1983, ApJ, 268, 368

Ekström, S., Georgy, C., Eggenberger, P., et al. 2012, A&A, 537, A146

Eldridge, J. J., Izzard, R. G., & Tout, C. A. 2008, MNRAS, 384, 1109

Elmegreen, B. G. 2000, ApJ, 530, 277

Elmegreen, B. G. 2011, in EAS Publications Series, Vol. 51, EAS Publications Series, ed. C. Charbonnel & T. Montmerle, 45–58

Espinoza, P., Selman, F. J., & Melnick, J. 2009, A&A, 501, 563

Evans, C. J., Lennon, D. J., Smartt, S. J., & Trundle, C. 2006, A&A, 456, 623

Evans, C. J., Smartt, S. J., Lee, J.-K., et al. 2005, A&A, 437, 467

Evans, C. J., Walborn, N. R., Crowther, P. A., et al. 2010, ApJ, 715, L74

Evans, C. J., Taylor, W. D., Hénault-Brunet, V., et al. 2011, A&A, 530, A108

Feigelson, E. D., Townsley, L. K., Broos, P. S., et al. 2013, ApJS, 209, 26

Ferrario, L., Pringle, J. E., Tout, C. A., & Wickramasinghe, D. T. 2009, MNRAS, 400, L71

Figer, D. F. 2005, Nature, 434, 192

Figer, D. F., McLean, I. S., & Morris, M. 1999, ApJ, 514, 202

Figer, D. F., Najarro, F., Morris, M., et al. 1998, ApJ, 506, 384

Figer, D. F., Najarro, F., Gilmore, D., et al. 2002, ApJ, 581, 258

Fitzpatrick, E. L., & Garmany, C. D. 1990, ApJ, 363, 119

Fujii, M. S., & Portegies Zwart, S. 2011, Science, 334, 1380

Gal-Yam, A., Mazzali, P., Ofek, E. O., et al. 2009, Nature, 462, 624

Gatti, H. 2002, Giordano Bruno and Renaissance Science, 1st edn. (Cornell University Press)

Geller, A. M., Hurley, J. R., & Mathieu, R. D. 2013, AJ, 145, 8

Geller, A. M., & Mathieu, R. D. 2011, Nature, 478, 356

Getman, K. V., Feigelson, E. D., & Kuhn, M. A. 2014a, ApJ, 787, 109

Getman, K. V., Feigelson, E. D., Kuhn, M. A., et al. 2014b, ApJ, 787, 108

Ghez, A. M., Salim, S., Weinberg, N. N., et al. 2008, ApJ, 689, 1044

Gies, D. R., & Bolton, C. T. 1986, ApJS, 61, 419

Gilmore, G., Randich, S., Asplund, M., et al. 2012, The Messenger, 147, 25

Glebbeek, E., Gaburov, E., Portegies Zwart, S., & Pols, O. R. 2013, MNRAS, 434, 3497

Glebbeek, E., & Pols, O. R. 2008, A&A, 488, 1017

Gräfener, G., & Hamann, W.-R. 2008, A&A, 482, 945

Gräfener, G., Vink, J. S., de Koter, A., & Langer, N. 2011, A&A, 535, A56

Gratton, R. G., Carretta, E., & Bragaglia, A. 2012, A&A Rev., 20, 50

Grebel, E. K., & Chu, Y.-H. 2000, AJ, 119, 787

Grevesse, N., & Sauval, A. J. 1998, Space Sci. Rev., 85, 161

Gruberbauer, M., Guenther, D. B., & Kallinger, T. 2012, ApJ, 749, 109

Grunhut, J. H., Wade, G. A., Leutenegger, M., et al. 2013, MNRAS, 428, 1686

Gvaramadze, V. V., & Bomans, D. J. 2008a, A&A, 485, L29

—. 2008b, A&A, 490, 1071

Gvaramadze, V. V., Kniazev, A. Y., Kroupa, P., & Oh, S. 2011, A&A, 535, A29

Gvaramadze, V. V., Langer, N., & Mackey, J. 2012, MNRAS, 427, L50

Habibi, M., Stolte, A., Brandner, W., Hußmann, B., & Motohara, K. 2013, A&A, 556, A26

Haiman, Z., & Loeb, A. 1997, ApJ, 483, 21

Hainich, R., Rühling, U., Todt, H., et al. 2014, A&A, 565, A27

Hall, P. D., Tout, C. A., Izzard, R. G., & Keller, D. 2013, MNRAS, 435, 2048

Harfst, S., Portegies Zwart, S., & Stolte, A. 2010, MNRAS, 409, 628

Heger, A., Fryer, C. L., Woosley, S. E., Langer, N., & Hartmann, D. H. 2003, ApJ, 591, 288

Heger, A., Langer, N., & Woosley, S. E. 2000, ApJ, 528, 368

Heger, A., & Woosley, S. E. 2002, ApJ, 567, 532

Heger, A., Woosley, S. E., & Spruit, H. C. 2005, ApJ, 626, 350

Hénault-Brunet, V., Evans, C. J., Sana, H., et al. 2012, A&A, 546, A73

Henyey, L. G., Forbes, J. E., & Gould, N. L. 1964, ApJ, 139, 306

Henyey, L. G., Wilets, L., Böhm, K. H., Lelevier, R., & Levee, R. D. 1959, ApJ, 129, 628

Herrero, A., Corral, L. J., Villamariz, M. R., & Martín, E. L. 1999, A&A, 348, 542

Herrero, A., Kudritzki, R. P., Vilchez, J. M., et al. 1992, A&A, 261, 209

Hillebrandt, W., & Niemeyer, J. C. 2000, ARA&A, 38, 191

Hillenbrand, L. A., Massey, P., Strom, S. E., & Merrill, K. M. 1993, AJ, 106, 1906

Hillier, D. J., & Miller, D. L. 1998, ApJ, 496, 407

Hills, J. G., & Day, C. A. 1976, Astrophys. Lett., 17, 87

Holmberg, J., Nordström, B., & Andersen, J. 2007, A&A, 475, 519

Howarth, I. D., Siebert, K. W., Hussain, G. A. J., & Prinja, R. K. 1997, MNRAS, 284, 265

Hoyle, F., & Lyttleton, R. A. 1941, MNRAS, 101, 227

Huang, W., Gies, D. R., & McSwain, M. V. 2010, ApJ, 722, 605

Humphreys, R. M., & Davidson, K. 1979, ApJ, 232, 409

—. 1994, PASP, 106, 1025

Hunter, D. A., Shaya, E. J., Holtzman, J. A., et al. 1995, ApJ, 448, 179

Hunter, D. A., Vacca, W. D., Massey, P., Lynds, R., & O'Neil, E. J. 1997, AJ, 113, 1691

Hunter, I., Lennon, D. J., Dufton, P. L., et al. 2008a, A&A, 479, 541

Hunter, I., Brott, I., Lennon, D. J., et al. 2008b, ApJ, 676, L29

Hurley, J. R., Pols, O. R., Aarseth, S. J., & Tout, C. A. 2005, MNRAS, 363, 293

Hurley, J. R., Pols, O. R., & Tout, C. A. 2000, MNRAS, 315, 543

Hurley, J. R., Tout, C. A., Aarseth, S. J., & Pols, O. R. 2001, MNRAS, 323, 630

Hurley, J. R., Tout, C. A., & Pols, O. R. 2002, MNRAS, 329, 897

Hußmann, B., Stolte, A., Brandner, W., Gennaro, M., & Liermann, A. 2012, A&A, 540, A57

Hyland, A. R., Straw, S., Jones, T. J., & Gatley, I. 1992, MNRAS, 257, 391

Iglesias, C. A., & Rogers, F. J. 1996, ApJ, 464, 943

Indebetouw, R., Brogan, C., Chen, C.-H. R., et al. 2013, ApJ, 774, 73

Ivanova, N. 2014, ArXiv e-prints, arXiv:1406.3475

Izzard, R. G., Dray, L. M., Karakas, A. I., Lugaro, M., & Tout, C. A. 2006, A&A, 460, 565

Izzard, R. G., Glebbeek, E., Stancliffe, R. J., & Pols, O. R. 2009, A&A, 508, 1359

Izzard, R. G., Tout, C. A., Karakas, A. I., & Pols, O. R. 2004, MNRAS, 350, 407

Jørgensen, B. R., & Lindegren, L. 2005, A&A, 436, 127

Kasliwal, M. M. 2011, PhD thesis, California Institute of Technology

Kennicutt, Jr., R. C. 1984, ApJ, 287, 116

Kennicutt, Jr., R. C., & Chu, Y.-H. 1988, AJ, 95, 720

Kim, S. S., Figer, D. F., Kudritzki, R. P., & Najarro, F. 2006, ApJ, 653, L113

Kippenhahn, R., & Meyer-Hofmeister, E. 1977, A&A, 54, 539

Kippenhahn, R., & Weigert, A. 1967, ZAp, 65, 251

Koen, C. 2006, MNRAS, 365, 590

Köhler, K., Borzyszkowski, M., Brott, I., Langer, N., & de Koter, A. 2012, A&A, 544, A76

Köhler, K., Langer, N., de Koter, A., et al. 2014, A&A, submitted

Kozyreva, A., Blinnikov, S., Langer, N., & Yoon, S.-C. 2014, A&A, 565, A70

Kroupa, P. 2001, MNRAS, 322, 231

Kroupa, P., Tout, C. A., & Gilmore, G. 1993, MNRAS, 262, 545

Kroupa, P., Weidner, C., Pflamm-Altenburg, J., et al. 2013, The Stellar and Sub-Stellar Initial Mass Function of Simple and Composite Populations, ed. T. D. Oswalt & G. Gilmore, 115

Krtička, J., Owocki, S. P., & Meynet, G. 2011, A&A, 527, A84+

Kudritzki, R. P., Pauldrach, A., Puls, J., & Abbott, D. C. 1989, A&A, 219, 205

Kudryavtseva, N., Brandner, W., Gennaro, M., et al. 2012, ApJ, 750, L44

Kulkarni, S. R., Ofek, E. O., Rau, A., et al. 2007, Nature, 447, 458

Lai, D. 2001, in Lecture Notes in Physics, Berlin Springer Verlag, Vol. 578, Physics of Neutron Star Interiors, ed. D. Blaschke, N. K. Glendenning, & A. Sedrakian, 424

Langer, N. 1992, A&A, 265, L17

—. 1998, A&A, 329, 551

—. 2009, Nature, 462, 579

—. 2012, ARA&A, 50, 107

Langer, N. 2014, in IAU Symposium, Vol. 302, IAU Symposium, 1–9

Langer, N., & Maeder, A. 1995, A&A, 295, 685

Langer, N., Norman, C. A., de Koter, A., et al. 2007, A&A, 475, L19

Larson, R. B., & Starrfield, S. 1971, A&A, 13, 190

Lattimer, J. M., & Prakash, M. 2004, Science, 304, 536

Lauterborn, D. 1970, A&A, 7, 150

Leigh, N., Sills, A., & Knigge, C. 2011, MNRAS, 415, 3771

Leitherer, C., & Chavarria-K., C. 1987, A&A, 175, 208

Lejeune, T., & Schaerer, D. 2001, A&A, 366, 538

Levenberg, K. 1944, Quart. Applied Math., 2, 164

Liermann, A., Hamann, W.-R., & Oskinova, L. M. 2009, A&A, 494, 1137

—. 2012, A&A, 540, A14

Liermann, A., Hamann, W.-R., Oskinova, L. M., Todt, H., & Butler, K. 2010, A&A, 524, A82

Lim, B., Chun, M.-Y., Sung, H., et al. 2013, AJ, 145, 46

Lin, D. N. C., & Pringle, J. E. 1976, in IAU Symposium, Vol. 73, Structure and Evolution of Close Binary Systems, ed. P. Eggleton, S. Mitton, & J. Whelan, 237–+

Loeb, A., & Barkana, R. 2001, ARA&A, 39, 19

Lombardi, Jr., J. C., Rasio, F. A., & Shapiro, S. L. 1995, ApJ, 445, L117

Lucy, L. B., & Solomon, P. M. 1970, ApJ, 159, 879

Maeder, A. 1987, A&A, 178, 159

Maeder, A., & Meynet, G. 2000, ARA&A, 38, 143

Maeder, A., Przybilla, N., Nieva, M.-F., et al. 2014, A&A, 565, A39

Maercker, M., & Burton, M. G. 2005, A&A, 438, 663

Maíz Apellániz, J. 2008, ApJ, 677, 1278

Maíz Apellániz, J., Sota, A., Walborn, N. R., et al. 2011, in Highlights of Spanish Astrophysics VI, ed. M. R. Zapatero Osorio, J. Gorgas, J. Maíz Apellániz, J. R. Pardo, & A. Gil de Paz, 467–472

Maíz Apellániz, J., & Úbeda, L. 2005, ApJ, 629, 873

Maíz Apellániz, J., Sota, A., Morrell, N. I., et al. 2013, in Massive Stars: From alpha to Omega

Maoz, D., & Mannucci, F. 2012, PASA, 29, 447

Marigo, P., Girardi, L., Bressan, A., et al. 2008, A&A, 482, 883

Marquardt, D. W. 1963, SIAM Journal on Applied Mathematics, 11, 431

Martayan, C., Frémat, Y., Hubert, A.-M., et al. 2006, A&A, 452, 273

—. 2007, A&A, 462, 683

Martini, P., Wagner, R. M., Tomaney, A., et al. 1999, AJ, 118, 1034

Martins, F., Hillier, D. J., Paumard, T., et al. 2008, A&A, 478, 219

Massey, P. 2003, ARA&A, 41, 15

Massey, P., & Hunter, D. A. 1998, ApJ, 493, 180

McCrea, W. H. 1964, MNRAS, 128, 147

McEvoy et al., C. in prep.

McLaughlin, D. E., & Fall, S. M. 2008, ApJ, 679, 1272

Meylan, G. 1993, in Astronomical Society of the Pacific Conference Series, Vol. 48, The Globular Cluster-Galaxy Connection, ed. G. H. Smith & J. P. Brodie, 588

Mohamed, S., & Podsiadlowski, P. 2007, in Astronomical Society of the Pacific Conference Series, Vol. 372, 15th European Workshop on White Dwarfs, ed. R. Napiwotzki & M. R. Burleigh, 397

Mokiem, M. R., de Koter, A., Puls, J., et al. 2005, A&A, 441, 711

Monteiro, H., Dias, W. S., & Caetano, T. C. 2010, A&A, 516, A2

Morton, D. C. 1967a, ApJ, 150, 535

—. 1967b, ApJ, 147, 1017

Mosser, B., Goupil, M. J., Belkacem, K., et al. 2012, A&A, 548, A10

Muijres, L. E., Vink, J. S., de Koter, A., Müller, P. E., & Langer, N. 2012, A&A, 537, A37

Munari, U., Henden, A., Kiyota, S., et al. 2002, A&A, 389, L51

Naylor, T., & Jeffries, R. D. 2006, MNRAS, 373, 1251

Negueruela, I., Marco, A., Herrero, A., & Clark, J. S. 2008, A&A, 487, 575

Neo, S., Miyaji, S., Nomoto, K., & Sugimoto, D. 1977, PASJ, 29, 249

Nieuwenhuijzen, H., & de Jager, C. 1990, A&A, 231, 134

Nishiyama, S., Tamura, M., Hatano, H., et al. 2009, ApJ, 696, 1407

O'Connell, R. W., Gallagher, III, J. S., & Hunter, D. A. 1994, ApJ, 433, 65

Oey, M. S., & Clarke, C. J. 2005, ApJ, 620, L43

Öpik, E. 1924, Publications of the Tartu Astrofizica Observatory, 25, 1

Packet, W. 1981, A&A, 102, 17

Paczynski, B. 1976, in IAU Symposium, Vol. 73, Structure and Evolution of Close Binary Systems, ed. P. Eggleton, S. Mitton, & J. Whelan, 75

Pang, X., Grebel, E. K., Allison, R. J., et al. 2013, ApJ, 764, 73

Pang, X., Grebel, E. K., & Altmann, M. 2010, in IAU Symposium, Vol. 266, IAU Symposium, ed. R. de Grijs & J. R. D. Lépine, 24–28

Parker, J. W., Clayton, G. C., Winge, C., & Conti, P. S. 1993, ApJ, 409, 770

Pasquali, A., Nota, A., Langer, N., Schulte-Ladbeck, R. E., & Clampin, M. 2000, AJ, 119, 1352

Penny, L. R., & Gies, D. R. 2009, ApJ, 700, 844

Perets, H. B., & Šubr, L. 2012, ApJ, 751, 133

Perlmutter, S., Aldering, G., Goldhaber, G., et al. 1999, ApJ, 517, 565

Petit, V., & Wade, G. A. 2012, MNRAS, 420, 773

Petrovic, J., Langer, N., & van der Hucht, K. A. 2005, A&A, 435, 1013

Pietrzyński, G., Graczyk, D., Gieren, W., et al. 2013, Nature, 495, 76

Podsiadlowski, P. 2010, Astronomische Nachrichten, 331, 218

—. 2013, Supernovae and Gamma-Ray Bursts, ed. T. D. Oswalt & M. A. Barstow, 693

Podsiadlowski, P., Joss, P. C., & Hsu, J. J. L. 1992, ApJ, 391, 246

Pols, O. R. 1994, A&A, 290, 119

Pols, O. R., & Marinus, M. 1994, A&A, 288, 475

Pols, O. R., Schroder, K.-P., Hurley, J. R., Tout, C. A., & Eggleton, P. P. 1998, MNRAS, 298, 525

Pols, O. R., Tout, C. A., Schroder, K.-P., Eggleton, P. P., & Manners, J. 1997, MNRAS, 289, 869

Pont, F., & Eyer, L. 2004, MNRAS, 351, 487

Popham, R., & Narayan, R. 1991, ApJ, 370, 604

Portegies Zwart, S., Gaburov, E., Chen, H.-C., & Gürkan, M. A. 2007, MNRAS, 378, L29

Portegies Zwart, S. F., Makino, J., McMillan, S. L. W., & Hut, P. 1999, A&A, 348, 117

Psaltis, D. 2006, Accreting neutron stars and black holes: a decade of discoveries, ed. W. H. G. Lewin & M. van der Klis, 1–38

Puls, J., Urbaneja, M. A., Venero, R., et al. 2005, A&A, 435, 669

Puls, J., Vink, J. S., & Najarro, F. 2008, A&A Rev., 16, 209

Ramírez-Agudelo, O. H., Simón-Díaz, S., Sana, H., de Koter, A., & Sabín-Sanjulían, C. in prep.

Ramírez-Agudelo, O. H., Simón-Díaz, S., Sana, H., et al. 2013, A&A, 560, A29

Repolust, T., Puls, J., & Herrero, A. 2004, A&A, 415, 349

Rieke, G. H., & Lebofsky, M. J. 1985, ApJ, 288, 618

Riess, A. G., Filippenko, A. V., Challis, P., et al. 1998, AJ, 116, 1009

Rosenberg, H. 1910, Astronomische Nachrichten, 186, 71

Rubio, M., Barbá, R. H., Walborn, N. R., et al. 1998, AJ, 116, 1708

Russell, H. N. 1914a, The Observatory, 37, 165

—. 1914b, Popular Astronomy, 22, 275

Sabbi, E., Lennon, D. J., Gieles, M., et al. 2012, ApJ, 754, L37

Sabbi, E., Anderson, J., Lennon, D. J., et al. 2013, AJ, 146, 53

Sabín-Sanjulián, C., Simón-Díaz, S., Herrero, A., et al. 2014, A&A, 564, A39

Sagar, R., & Richtler, T. 1991, A&A, 250, 324

Salpeter, E. E. 1955, ApJ, 121, 161

Sana, H., Ramírez-Agudelo, O. H., Simón-Díaz, S., de Koter, A., & Sabín-Sanjulían, C. in prep.

Sana, H., de Mink, S. E., de Koter, A., et al. 2012, Science, 337, 444

Sana, H., de Koter, A., de Mink, S. E., et al. 2013, A&A, 550, A107

Sandage, A. R. 1953, AJ, 58, 61

Sanyal et al., D. in prep.

Sathyaprakash, B. S., & Schutz, B. F. 2009, Living Reviews in Relativity, 12, 2

Savaglio, S., Glazebrook, K., & Le Borgne, D. 2009, ApJ, 691, 182

Scalo, J. M. 1986, Fund. Cosmic Phys., 11, 1

Schaye, J., Dalla Vecchia, C., Booth, C. M., et al. 2010, MNRAS, 402, 1536

Schneider, F. R. N., Izzard, R. G., Langer, N., & de Mink, S. E. subm., ApJ

Schneider, F. R. N., Langer, N., de Koter, A., et al. 2014a, A&A, in press, arXiv:1408.3409

Schneider, F. R. N., Izzard, R. G., de Mink, S. E., et al. 2014b, ApJ, 780, 117

Schnurr, O., Casoli, J., Chené, A.-N., Moffat, A. F. J., & St-Louis, N. 2008, MNRAS, 389, L38

Schönberg, M., & Chandrasekhar, S. 1942, ApJ, 96, 161

Schönrich, R., & Bergemann, M. 2014, MNRAS, 443, 698

Schroder, K.-P., Pols, O. R., & Eggleton, P. P. 1997, MNRAS, 285, 696

Selman, F., Melnick, J., Bosch, G., & Terlevich, R. 1999, A&A, 347, 532

Serenelli, A. M., Bergemann, M., Ruchti, G., & Casagrande, L. 2013, MNRAS, 429, 3645

Shkedy, Z., Decin, L., Molenberghs, G., & Aerts, C. 2007, MNRAS, 377, 120

Sills, A., Faber, J. A., Lombardi, Jr., J. C., Rasio, F. A., & Warren, A. R. 2001, ApJ, 548, 323

Sills, A., Glebbeek, E., Chatterjee, S., & Rasio, F. A. 2013, ApJ, 777, 105

Sills, A., Lombardi, Jr., J. C., Bailyn, C. D., et al. 1997, ApJ, 487, 290

Simón-Díaz, S., Castro, N., Garcia, M., Herrero, A., & Markova, N. 2011a, Bulletin de la Societe Royale des Sciences de Liege, 80, 514

Simón-Díaz, S., Castro, N., Herrero, A., et al. 2011b, Journal of Physics Conference Series, 328, 012021

Simón-Díaz, S., & Herrero, A. 2014, A&A, 562, A135

Smith, N. 2014, ARA&A, 52, 487

Smith, N., Gehrz, R. D., Hinz, P. M., et al. 2003, AJ, 125, 1458

Soderblom, D. R. 2010, ARA&A, 48, 581

Steinmetz, M., Zwitter, T., Siebert, A., et al. 2006, AJ, 132, 1645

Stolte, A., Brandner, W., Grebel, E. K., Lenzen, R., & Lagrange, A.-M. 2005, ApJ, 628, L113

Stolte, A., Grebel, E. K., Brandner, W., & Figer, D. F. 2002, A&A, 394, 459

Stone, R. C. 1991, AJ, 102, 333

Suijs, M. P. L., Langer, N., Poelarends, A.-J., et al. 2008, A&A, 481, L87

Taam, R. E., & Sandquist, E. L. 2000, ARA&A, 38, 113

Takeda, G., Ford, E. B., Sills, A., et al. 2007, ApJS, 168, 297

Tanvir, N. R., Fox, D. B., Levan, A. J., et al. 2009, Nature, 461, 1254

Tauris, T. M., & van den Heuvel, E. P. J. 2006, Formation and evolution of compact stellar X-ray sources, ed. Lewin, W. H. G. & van der Klis, M., 623–665

Testor, G., Llebaria, A., & Debray, B. 1988, The Messenger, 54, 43

Torres, G., Andersen, J., & Giménez, A. 2010, A&A Rev., 18, 67

Torres, G., Vaz, L. P. R., Sandberg Lacy, C. H., & Claret, A. 2014, AJ, 147, 36

Tout, C. A., Aarseth, S. J., Pols, O. R., & Eggleton, P. P. 1997, MNRAS, 291, 732

Tout, C. A., & Eggleton, P. P. 1988, MNRAS, 231, 823

Tout, C. A., Pols, O. R., Eggleton, P. P., & Han, Z. 1996, MNRAS, 281, 257

Tout, C. A., Wickramasinghe, D. T., Liebert, J., Ferrario, L., & Pringle, J. E. 2008, MNRAS, 387, 897

Tramper, F., Ramírez-Agudelo, O. H., Sana, H., & de Koter, A. in prep.

Tramper, F., Sana, H., de Koter, A., & Kaper, L. 2011, ApJ, 741, L8

Tylenda, R., Hajduk, M., Kamiński, T., et al. 2011, A&A, 528, A114

Ulrich, R. K., & Burger, H. L. 1976, ApJ, 206, 509

Unsöld, A., & Baschek, B. 2001, The new cosmos : an introduction to astronomy and astrophysics

van Bever, J., & Vanbeveren, D. 1998, A&A, 334, 21

van Dyk, D. A., Degennaro, S., Stein, N., Jefferys, W. H., & von Hippel, T. 2009, Annals of Applied Statistics, 3, 117

van Leeuwen, F. 2007, A&A, 474, 653

Vanbeveren, D. 1991, A&A, 252, 159

Vanbeveren, D., De Loore, C., & Van Rensbergen, W. 1998, A&A Rev., 9, 63

Vink, J. S., de Koter, A., & Lamers, H. J. G. L. M. 2000, A&A, 362, 295

—. 2001, A&A, 369, 574

Vink, J. S., Muijres, L. E., Anthonisse, B., et al. 2011, A&A, 531, A132

Vogelsberger, M., Genel, S., Springel, V., et al. 2014, Nature, 509, 177

von Hippel, T., Jefferys, W. H., Scott, J., et al. 2006, ApJ, 645, 1436

Wade, G. A., Grunhut, J., Alecian, E., et al. 2014, in IAU Symposium, Vol. 302, IAU Symposium, 265–269

Walborn, N. R., & Blades, J. C. 1987, ApJ, 323, L65

—. 1997, ApJS, 112, 457

Walborn, N. R., Maíz-Apellániz, J., & Barbá, R. H. 2002, AJ, 124, 1601

Walborn, N. R., Sana, H., Simón-Díaz, S., et al. 2014, A&A, 564, A40

Walch, S. K. 2014, in Astrophysics and Space Science Proceedings, Vol. 36, The Labyrinth of Star Formation, ed. D. Stamatellos, S. Goodwin, & D. Ward-Thompson (Springer International Publishing), 173

Walmswell, J. J., Eldridge, J. J., Brewer, B. J., & Tout, C. A. 2013, MNRAS, 435, 2171

Wang, B., & Han, Z. 2012, New A Rev., 56, 122

Weidner, C., & Kroupa, P. 2004, MNRAS, 348, 187

Weidner, C., Kroupa, P., & Maschberger, T. 2009, MNRAS, 393, 663

Weisz, D. R., Fouesneau, M., Hogg, D. W., et al. 2013, ApJ, 762, 123

Weizsäcker, C. F. v. 1937, Physikalische Zeitschrift, 38, 176

—. 1938, Physikalische Zeitschrift, 39, 633

Wellstein, S., Langer, N., & Braun, H. 2001, A&A, 369, 939

Whalen, D. J., Joggerst, C. C., Fryer, C. L., et al. 2013a, ApJ, 768, 95

Whalen, D. J., Even, W., Frey, L. H., et al. 2013b, ApJ, 777, 110

Wickramasinghe, D. T., Tout, C. A., & Ferrario, L. 2014, MNRAS, 437, 675

Woosley, S. E. 1993, ApJ, 405, 273

Woosley, S. E., & Heger, A. 2006, ApJ, 637, 914

Yanny, B., Rockosi, C., Newberg, H. J., et al. 2009, AJ, 137, 4377

Yoon, S.-C., & Langer, N. 2005, A&A, 443, 643

Yusof, N., Hirschi, R., Meynet, G., et al. 2013, MNRAS, 433, 1114